Title
Fermi-LAT Observations of Gamma-Ray Emission Towards the Galactic Center and the Outer Halo of M31

Author
Karwin, Chris

Publication Date
2019

UNIVERSITY OF CALIFORNIA,
IRVINE

Fermi-LAT Observations of γ-ray Emission Towards the Galactic Center and the Outer Halo of M31

DISSERTATION

submitted in partial satisfaction of the requirements
for the degree of

DOCTOR OF PHILOSOPHY

in Physics

by

Christopher M. Karwin

Dissertation Committee:
Professor Simona Murgia, Chair
Professor Mike Cooper
Professor Manoj Kaplinghat

2019

DEDICATION

For my Mom and Dad.

TABLE OF CONTENTS

LIST OF FIGURES

LIST OF TABLES

ACKNOWLEDGMENTS

I would like to thank my advisor, Simona Murgia; my dissertation committee, Mike Cooper and Manoj Kaplinghat; my co-authors, Igor Moskalenko, Sheldon Campbell, Tim Tait, Flip Tanedo, and Troy Porter; and my fellow classmates, Ketron Mitchell-Wynne and Sean Fillingham.

My Ph.D. dissertation work was supported in part by Department of Energy grant DESC0014431.

A portion of this dissertation is a reprint of the material as it appears in Physical Review D and the Astrophysical Journal.

CURRICULUM VITAE

Christopher M. Karwin

EDUCATION

Ph.D., Physics	**2019**
University of California, Irvina	*Irvine, CA*
M.S., Physics	**2017**
University of California, Irvine	*Irvine, CA*
B.S., Physics	**2013**
University of Colorado at Colorado Springs	*Colorado Springs, CO*

RESEARCH EXPERIENCE

Graduate Research Assistant	**2014–2019**
University of California, Irvine	*Irvine, California*
Undergraduate Research Assistant	**2012–2013**
University of Colorado at Colorado Springs	*Colorado Springs, Colorado*

TEACHING EXPERIENCE

Teaching Associate	**2017**
University of California, Irvine	*Irvine, CA*
Teaching Assistant	**2013–2019**
University of California, Irvine	*Irvine, CA*
Math and Physics Tutor	**2010–2013**
University of Colorado at Colorado Springs	*Colorado Springs, CO*

REFEREED JOURNAL PUBLICATIONS

***Fermi*-LAT Observations of γ-Ray Emission Towards the Outer Halo of M31** First author, The Astrophysical Journal	**2019**
Search for Gamma-Ray Emission from P-Wave Dark Matter Annihilation in the Galactic Center Contributing author, The Astrophysical Journal	**2019**
Dark Matter Interpretation of the *Fermi*-LAT Observation Towards the Galactic Center First author, Physical Review D	**2017**
***Fermi*-LAT Observations of High-Energy γ-Ray Emission Toward the Galactic Center** Contributing author, The Astrophysical Journal	**2016**

Microwave Properties of Twisted and Supertwisted Nematic Liquid Crystals with Weak Anchoring **2014**
First author, Liquid Crystals

Liquid Crystal Phase Shifters with a Twist **2013**
First author, Applied Physics Letters

ABSTRACT OF THE DISSERTATION

Fermi-LAT Observations of γ-ray Emission Towards the Galactic Center and the Outer Halo of M31

By

Christopher M. Karwin

Doctor of Philosophy in Physics

University of California, Irvine, 2019

Professor Simona Murgia, Chair

An excess γ-ray signal coming from the direction of the Galactic center (GC) has been detected by the *Fermi* Large Area Telescope (*Fermi*-LAT). Possible explanations for the excess include inaccuracies in the foreground/background model, an unresolved population of millisecond pulsars, and/or dark matter (DM) annihilation. However, the GC is a complicated region, and the true nature of the excess currently remains uncertain.

M31 is the closest spiral galaxy to us and has been the subject of numerous studies. Because it is both massive and relatively nearby, M31 is an ideal target for studying galaxies, and historically it has played a major role in the development of our understanding of the Universe. γ-ray radiation coming from the inner region of M31 was first detected in 2010 by *Fermi*-LAT. Since the initial detection, all studies to date have focused on the innermost region, where the galactic disk can be observed. However, M31's galactic disk only amounts to roughly 10% of the galaxy's total mass, with the other 90% being in the form of DM, which extends well beyond the inner region of the galaxy.

In this dissertation, a detailed study of the γ-ray emission towards M31's outer halo is made. Using the cosmic ray propagation code GALPROP, specialized interstellar emission models are constructed to characterize the foreground emission from the Milky Way (MW), including a self-consistent determination of the isotropic component, and an in-depth analysis of the systematic uncertainties related to the observations. Evidence is found for an extended excess that appears to be distinct from the conventional MW foreground, having a total radial extension upwards of $\sim$120-200 kpc from the center of M31. A DM interpretation is found to provide a good description of the observed emission and is consistent with the GC excess DM interpretation. However, uncertainties in the MW foreground, and in particular, modeling of the H I-related components, have not been fully explored and may impact the results.

Chapter 1

Introduction

This section begins with a brief overview of DM, since the observations presented in this dissertation are motivated in large part by searching for a DM signal. An overview of *Fermi*-LAT is then given. The discussion of *Fermi*-LAT includes a brief review of the primary sources and mechanisms that generate high-energy γ-ray radiation. Next, a synopsis of space-based high-energy γ-ray astronomy is provided. The main intention of the synopsis is to outline some of the relevant history and background for the *Fermi*-LAT observations towards the Galactic center and the outer halo of M31. Lastly, an introduction to the M31 system is given. Note that the main work of this dissertation is the M31 study, which is presented in Chapter 4.

1.1 Dark Matter

One of the main motivations for the observations presented in this dissertation is to search for an indirect signal from the annihilation of cold DM. There exist in the literature a large body of work discussing the DM problem in great detail (for example, see Trimble (1987); Feng (2010); Bertone & Hooper (2018), and references therein). This section gives a brief outline of the collection of complementary evidence that supports the standard DM paradigm, with the main intention of providing an intuitive sense of the DM problem and its significance. This section also reviews the three general experimental methods used to search for DM, including the general process by which γ-ray emission may arise from DM annihilation.

The DM problem can be illustrated quite clearly by considering a spiral galaxy. The rotation of a spiral galaxy results in its constituent parts (i.e. the gas, stars, and dust) experiencing an outward force. However, what holds the galaxy together is the mutual gravitational attraction. If most of the mass were contained within the visible part of the galaxy, at large radii the rotational speed should decrease, based on classical Newtonian dynamics. However, by measuring the rotations of galaxies to large radii, it was found that they were systematically rotating too quickly in the outer regions to be held together by the amount of visible matter. This finding ultimately leads to two possible conclusions. One possibility is that galaxies may contain a significant amount of matter that is not being detected through conventional astrophysical methods, otherwise known as DM. The other possibility is that these types of measurements may be an indication that the laws of gravity are modified for very small accelerations, otherwise known as modified Newtonian dynamics (MOND) (Milgrom, 1983). In fact, MOND seems to be a suitable explanation on local scales. However, as discussed below, evidence for DM is found at all cosmological scales (which is difficult to explain with MOND), and because of this the DM hypothesis seems to be the most likely explanation.

Historically, the DM problem began in 1933 when Fritz Zwicky found that the velocity dispersion measurements of galaxies in the Coma Cluster implied a light-to-mass ratio of 400 $M_\odot/L_\odot$, which exceeded the value measured in the solar neighborhood by two orders of magnitude (Zwicky, 1933). Shortly after that Sinclair Smith estimated the total mass of the Virgo Cluster, which when divided by the total number of galaxies in the cluster, implied that the galaxies were two orders of magnitude more massive than the estimates made by Hubble, which led him to suggest that there may be a ”great mass of internebular material within the cluster” (Smith, 1936). The modern era of DM research then began in the 1970’s with the measurements of rotational velocity curves. These measurements showed a flat rotational speed at large radii (Rubin & Ford, 1970; Roberts & Whitehurst, 1975; Bosma, 1978; Rubin et al., 1978), which implied that galaxies were more massive than previously had been thought, and that there was a significant amount of mass in the outer regions (Einasto et al., 1974; Ostriker et al., 1974; Faber & Gallagher, 1979).

Since these early days evidence for DM has been accumulating at all cosmological scales, and from numerous complementary probes. This evidence includes type Ia supernovae (Riess et al., 1998; Perlmutter et al., 1999), the Bullet Cluster (Clowe et al., 2006) (and more generally, gravitational lensing measurements), the cosmic microwave background (Hinshaw et al., 2013; Ade et al., 2016), baryon acoustic oscillations (Eisenstein et al., 2005; Anderson et al., 2014), Big Bang nucleosynthesis (BBN) (Tanabashi et al., 2018), and large scale structure (Peacock et al., 2001). Collectively, these observations inform the standard model of cosmology, known as ΛCDM, which describes the observable Universe.

In ΛCDM cosmology the Universe is comprised of ∼5% baryonic matter (i.e. matter corresponding to the elements of the periodic table), ∼26% DM, and ∼69% dark energy (DE) (Ade et al., 2016). The observations presented in this dissertation broadly relate to the indirect detection of DM. The topic of DE is not mandatory for such studies and will not be discussed in any detail. DE ultimately relates to the accelerating expansion of the Universe, and it connects theoretically to the Big Bang Theory. DM and DE are related in the sense that they are two of the main components that make up the Universe, and it is possible that they may even be related on a more intimate level, but very little is currently understood about the true nature of DE.

The Standard Model (SM) of particle physics very elegantly summarizes the known particles and interactions of nature, which includes just 12 fermions and 5 bosons. The properties required of DM essentially rule out the possibility that the DM particle is one of the known SM particles. This implies that DM may be a new particle, and the main goal then is to learn about its properties, i.e. its mass, how it interacts with the other particles of the SM (if it interacts at all), its interaction cross-section, how it broadly fits within the SM, and how it is distributed throughout the Universe. Thus, in addition to being a problem of astrophysics and cosmology, DM is also a problem of particle physics, and likewise it connects the very large scales with the very small scales. In a sense, DM represents a union of these two opposites.

DM searches are motivated in large part by open problems in particle physics (for a detailed discussion on this topic see Feng (2010)). One of the leading DM theories postulates that DM is a massive particle that interacts weakly with the other particles of the SM. This type of DM is known as a weakly interacting massive particle (WIMP). For all practical purposes a WIMP is generally a particle with a mass in the range from ∼10 GeV - 1 TeV, that has an interaction cross section on the scale of the weak force. If a WIMP exists and is stable, it is naturally produced with a relic density consistent with that required of DM, sometimes referred to as the ”WIMP miracle” (Feng, 2010). Moreover, the gauge hierarchy problem implies new physics at the weak scale, for which the WIMP miracle independently provides a strong motivation. It should be noted that although WIMPs can quite naturally account for all of the thermal relic density, it is also possible that they only account for some fraction of it, with the remaining fraction being accounted for by other types of DM. And of course it may be the case that DM is not a WIMP at all (for example, see the ”WIMPless miracle” (Feng & Kumar, 2008)).

There are three main experimental methods by which WIMP DM can be searched for, as illustrated in Figure 1.1[1]. The process going from left to right in the diagram is known as indirect detection, and it is the method employed in this dissertation. The corresponding physics is as follows. A DM particle (χ) and its anti-particle annihilate through some unknown annihilation process (as depicted by the circle enclosing the two question marks). Note that this diagram only considers the initial and final states. More specifically, it is also of interest to learn the details of the annihilation process, and this can be probed through the use of simplified DM models, as detailed in Chapter 3. In general, the annihilation of DM may generate any of the SM particles. For example, it may result in a final state bottom quark and anti-bottom quark. In this case, the particle pair then undergoes a process known as hadronization, in which a particle

---

[1] Image downloaded from `https://fermi.gsfc.nasa.gov/science/eteu/dm/`

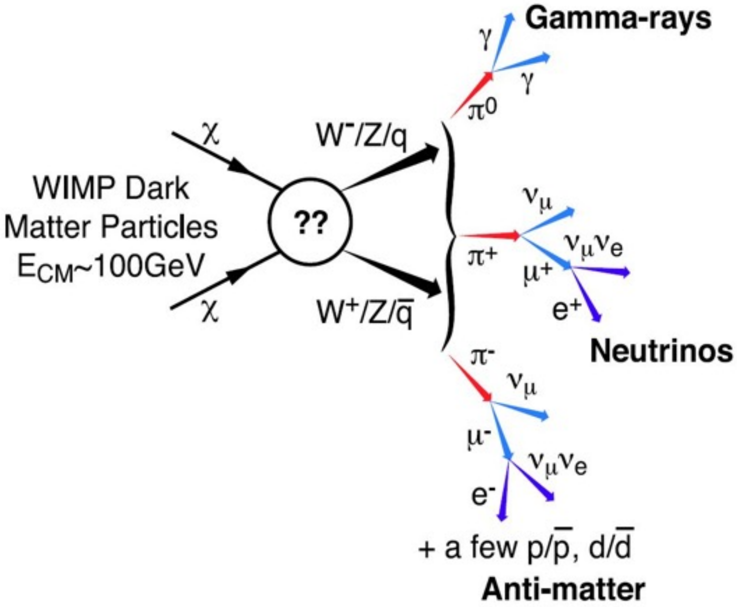

Figure 1.1 The basic mechanisms by which DM may be searched for. Going from left to right in the diagram corresponds to indirect detection, which is the method employed in this dissertation. Going from right to left corresponds to production, and going from bottom to top (or top to bottom) corresponds to direct detection. See text for more details.

shower takes place. This process ultimately results in neutral and charged pions, which then quickly decay, as shown in the diagram. The neutral pions decay to γ-ray photons, and these photons can be detected by γ-ray telescopes. The charged pions decay to electrons, positrons, and neutrinos, as well as some other particles, which can also be detected by the appropriate detectors.

The process just described can also occur from the right to left, as well as from bottom to top (or top to bottom), with respect to the diagram. Going from the right to left is known as DM production, and in this case DM may be produced through colliding two SM particles at very high energies. Going from top to bottom (or bottom to top) is known as direct detection, and in this case the DM may interact with a SM particle thereby imparting some momentum, and the recoil of the SM particle can then potentially be detected. There are pros and cons to each of the different search methods, and each comes with its own unique difficulties and limitations. Ideally, the goal is to detect complementary signals from all three detection methods and as many different targets as possible, in order to establish a definite discovery of the DM's particle nature.

The γ-ray intensity and spectrum from DM annihilation is given by the following equation:

$$\frac{dN_\gamma}{dE} = \left[\sum_f \frac{\langle \sigma_f v \rangle}{4\pi\eta\, m_\chi^2} \frac{dN_\gamma^f}{dE}\right] \times \left\{\sum_i \int_{\Delta\Omega} d\Omega \int_{\mathrm{LoS}} ds \rho_i^2(\mathbf{r}_i(s,\mathbf{n}))\right\}, \tag{1.1}$$

where the first summation is over annihilation final states f (i.e. up-type quarks, down-type quarks, leptons, etc.), dN_γ^f/dE is the number of photons produced for a single annihilation into final state f, $\langle\sigma_f v\rangle$ is the thermally averaged cross section for final state f, m_χ is the DM particle mass, and $\eta = 2(4)$ for self-conjugate (non-self-conjugate) DM. The total cross section $\langle\sigma v\rangle$ is the sum of the cross sections for all final states $\langle\sigma_f v\rangle$. The quantity in large square brackets depends on the particle nature of the DM and is referred to as the *DM attribute quantity*. The quantity in large curly brackets depends on the spatial distribution of the DM and is known as the J-factor (J), given by the integral of the mass density squared, over the line of sight. When describing the DM distribution as an ensemble of disjoint dark matter halos, the J-factor is summed over all halos i in the line of sight.

The spherically-averaged DM halo density profile $\rho(r)$ for each halo is often taken to be a generalized NFW profile, as detailed in Chapters 3 and 4 (however, other profiles are also possible):

$$\rho(r) = \rho_s \left(\frac{r}{R_s}\right)^{-\gamma} \left(1 + \frac{r}{R_s}\right)^{\gamma-3}. \tag{1.2}$$

Here, γ specifies the inner spectral slope of the profile, R_s is the scale radius, and ρ_s is the scale density, often determined for the MW halo from the local DM density.

J-factors determined from these spherically-averaged profiles (denoted J) are an underestimate of the total J-factor (denoted J') because of the effect of the non-spherical structure. This underestimate is typically encoded with a boost factor (B) such that

$$J' = BJ, \tag{1.3}$$

with B determined from the model of halo substructure.

1.2 The *Fermi* Large Area Telescope

The Fermi Gamma-Ray Space Telescope was launched on June 11, 2008. The main instrument onboard is *Fermi*-LAT, which consists of an array of 16 tracker modules, 16 calorimeter modules, and a segmented anti-coincidence detector. *Fermi*-LAT is sensitive to γ-rays in the energy range 20 MeV - 300 GeV. The telescope works by converting an incident γ-ray photon into an electron-positron pair in the tracker module, and the corresponding energy is then deposited into the calorimeter. These measurements allow for the reconstruction of the direction in the sky from which the photon originated, as well as the photon's incident energy. The all-sky map[2] of the γ-ray emission observed by *Fermi*-LAT is

---

[2] Image downloaded from `https://svs.gsfc.nasa.gov/11342`

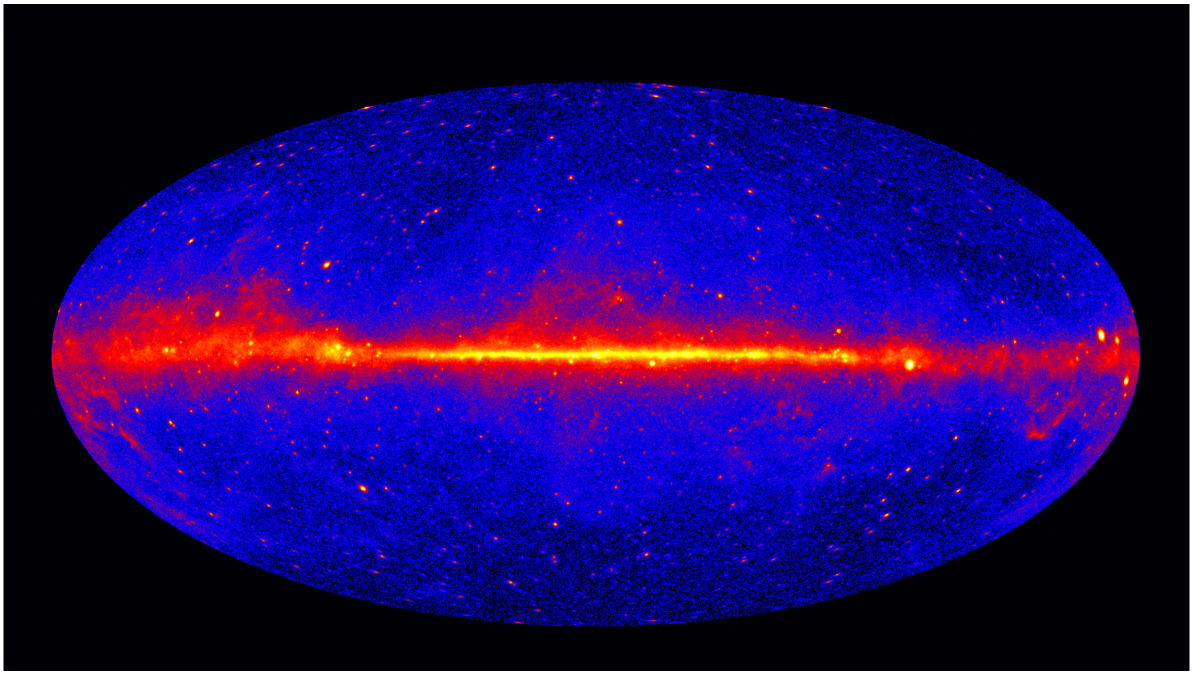

Figure 1.2 The five-year all-sky γ-ray emission observed by *Fermi*-LAT, for energies above 1 GeV.

shown in Figure 1.2. The bright emission along the center of the map corresponds to the disk of the MW. In addition, diffuse emission can be observed over the entire sky, as well as a large number of point sources.

In general, the three main components of the γ-ray emission are point sources, Galactic diffuse emission, and the isotropic emission. The γ-ray emission also contains the Fermi Bubbles, which are two large bubble-like features centered at the Galactic center, positioned above and below the Galactic plane. Lastly, there are a number of other sub-dominant sources including emission associated with radio loops, extended sources, and possibly emission from DM annihilation or decay. A major aspect of this dissertation entails the construction of specialized models that describe the Galactic diffuse emission. This construction also requires a self-consistent determination of the isotropic component and the point sources, as will be detailed in later chapters.

A majority of the Galactic diffuse emission is due to the interaction of high-energy cosmic rays (CRs) with the interstellar gas and radiation fields. There are three main mechanisms that give rise to this emission. CR electrons up-scatter low-energy photons of the interstellar radiation field producing inverse Compton (IC) emission. CR electrons are also accelerated by the protons of the gas generating Bremsstrahlung emission. Lastly, CR protons interact with the protons of the gas generating π^0 mesons, which then decay to γ-ray photons.

The 3FGL point source catalogue (which contains all of the point sources detected by *Fermi*-LAT) contains over 3000 sources (Acero et al., 2015). The extragalactic sources are primarily active galactic nuclei (AGN, i.e. blazars and quasars.) In the galactic plane a majority of the point sources are pulsars. A number of additional source classes have also been identified, including supernova remnants, pulsar wind nebulae, and unassociated sources.

After subtracting the Galactic diffuse emission and point sources from the γ-ray data, a residual all-sky signal is found, which is roughly the same in all directions, i.e. the isotropic emission. This component includes unresolved extragalactic emission (AGN, star-forming galaxies, and radio galaxies), residual instrumental background, and possibly contributions from other Galactic components that have a roughly isotropic distribution, as discussed in detail in Chapter 4.

1.3 A Synopsis[3] of Space-Based High-Energy γ-Ray Astronomy: From the Pioneering Mission of Explorer 11 to the Galactic Center Excess, Milky Way Satellites, and Milky Way Halo

On April 27, 1961 the satellite Explorer 11 was launched into orbit carrying the first space-based experiment designed to detect high-energy γ-rays with energies above $\sim$50 MeV (Kraushaar & Clark, 1962). This pioneering mission resulted in roughly 141 hours of useful observing time, during which 1012 events were accepted as γ-rays (Kraushaar et al., 1965). Explorer 11 gave an apparent average all-sky γ-ray intensity that was 10–20 times higher than the predictions made for γ-rays from π^0-decay, resulting from CR collisions with the interstellar hydrogen, which was estimated to be the most important production mechanism in interstellar space. In addition to π^0-decay, other important production mechanisms that were expected included IC emission and Bremsstrahlung emission. The signal detected by Explorer 11 was found to be roughly isotropic over the sky. All of the internal tests performed at the time indicated that the measured intensity was in fact the true intensity of the γ-ray emission, as opposed to being due to background; however, lacking evidence of anisotropy in the signal, only an upper-limit measurement was claimed.

Following the Explorer 11 mission was a γ-ray detector aboard the third Orbiting Solar Observatory, OSO-3 (Kraushaar et al., 1972). These observations, carried out in 1967-1968, confirmed the discovery of high-energy γ-rays with energies above $\sim$50 MeV. The spatial distribution showed a Galactic component concentrated along the disk with an extended region of high intensity toward the Galactic center. An isotropic component was also detected. In total 621 γ-ray events were observed. The all-sky intensity map from Kraushaar et al. (1972) is shown in Figure 1.3.

---

[3] This synopsis is primarily intended to help motivate this dissertation, while at the same time providing some of the relevant history and background. It is by no means exhaustive, and it by no means encompasses the many different areas of high-energy γ-ray astronomy.

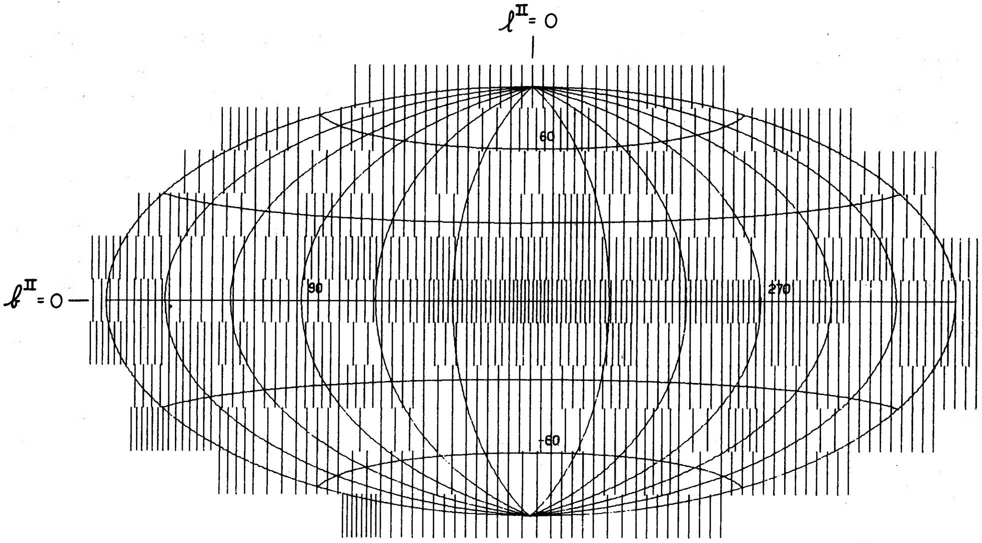

Figure 1.3 Sky-map of the γ-ray intensity observed by OSO-3 taken from Kraushaar et al. (1972). The number of events recorded per solid angle on the sky is indicated by the density of vertical lines. The map shows bright emission along the Galactic plane and towards the Galactic center.

The second Small Astronomy Satellite (SAS-2) (Fichtel et al., 1975a) (launched on November 15, 1972) and later the COS B satellite (Bennett et al., 1976) (launched on August 9, 1975) provided the first detailed views of the diffuse γ-ray emission from the Galactic plane above 30 MeV (Hunter et al., 1997). These observations provided clear evidence of a correlation between the distributions of high-energy γ-rays and the interstellar gas (H I and H_2) (see Acero et al. (2016) and references therein). The diffuse Galactic emission thus provided information about the distribution of CRs in the Galaxy, as well as the structure of the interstellar medium. A 'gradient model' approach was employed for analysis of the COS B data (see Bloemen et al. (1986); Strong et al. (1988); Hunter et al. (1997); and references therein), which marked the first realistic modeling of the high-energy interstellar emission (Acero et al., 2016). This approach was based on the assumption of a cylindrically symmetric distribution of emissivity per gas atom, where the Galactic structure was included through the use of H I and CO surveys, as well as dust extinction maps. The diffuse model also included contributions from IC emission and the isotropic emission. The γ-ray emission from the Galactic plane observed by COS B[4] is shown in Figure 1.4.

Improvements in the sensitivity and spatial and energy resolution, relative to SAS-2 and COS B, came from the Energetic Gamma-Ray Experiment Telescope (EGRET), aboard the Compton Gamma-Ray Observatory. The left panel of Figure 1.5 shows an image of the spacecraft[5], and the right panel of Figure 1.5 shows the all-sky γ-ray emission observed by EGRET[6]. The EGRET observations of the diffuse γ-ray emission from the Galactic plane

---

[4] Image downloaded from `http://sci.esa.int/cos-b/36193-milky-way-in-gamma-rays/`

[5] Image downloaded from `https://heasarc.gsfc.nasa.gov/docs/cgro/images/epo/gallery/cgro/index.html`

[6] Image downloaded from `https://heasarc.gsfc.nasa.gov/docs/cgro/images/epo/gallery/skymaps/index.html`

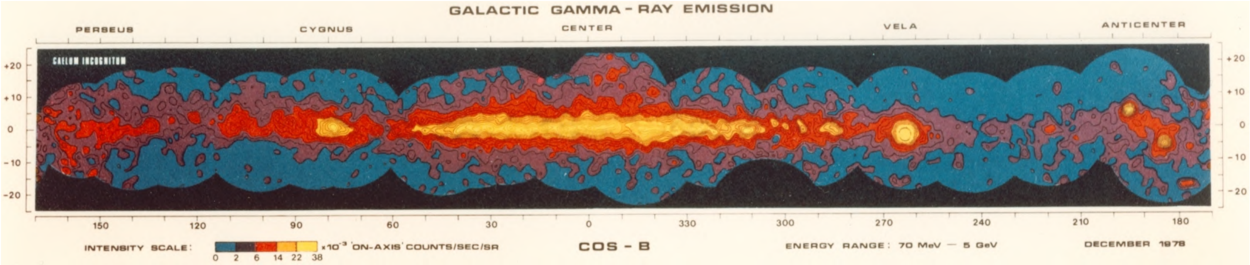

Figure 1.4 The γ-ray emission from the Galactic plane observed by COS B, for an energy range of 70 MeV to 5 GeV.

indicated that in the energy range above $\sim$1 GeV the γ-ray flux was up to 60% higher than the theoretical predictions (see Strong & Mattox (1996); Hunter et al. (1997); Stecker et al. (2008), and references therein). Possible explanations for the excess emission included inaccuracies in the interstellar emission model (the gas-related emission, the IC emission, and/or the CR properties) and an unresolved point source population. It was also argued that the excess was the long awaited signal of supersymmetric DM annihilation (de Boer et al., 2005; Elsaesser & Mannheim, 2005).

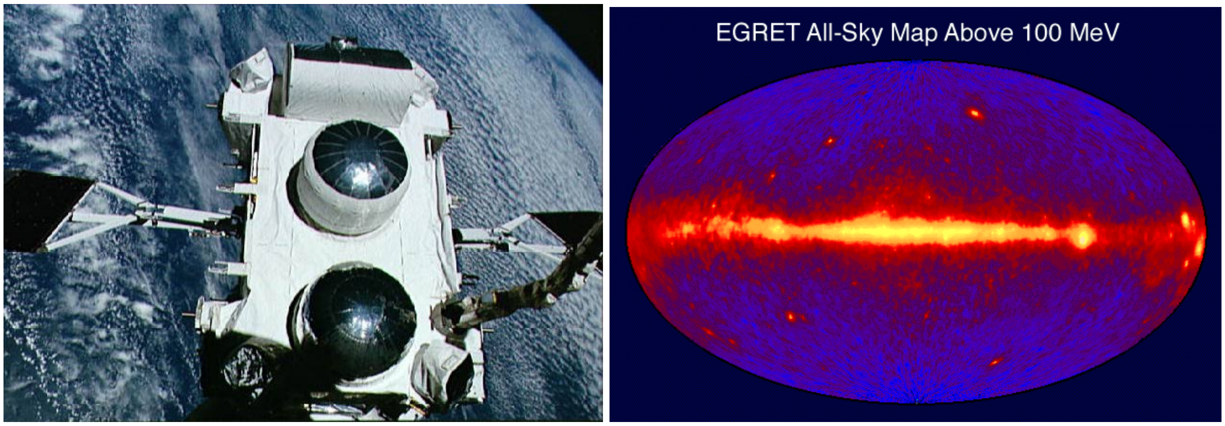

Figure 1.5 **Left:** The Compton Gamma-Ray Observatory, which contained four main telescopes: EGRET (back), COMPTEL (middle), OSSE (front), and BATSE. **Right:** The all-sky γ-ray map observed by EGRET.

A new all-sky analysis of the EGRET data was given in Stecker et al. (2008). This study found the GeV excess to be uniform over the entire sky. There was no apparent structure related to the Galactic plane, Galactic center, anti-center, nor halo. This led Stecker et al. (2008) to the conclusion that the GeV excess (dubbed the 'GeV anomaly') was likely due to a systematic error in the EGRET calibration, rather than being a real astronomical effect: "In this paper, we will make the case that a problem in the analysis of the EGRET sensitivity calibration is the most likely explanation for the 'GeV anomaly' and that the dark matter hypothesis can be ruled out by an examination of the GeV spectrum over the whole sky."

EGRET was the predecessor to *Fermi*-LAT. The *Fermi*-LAT measurements of the diffuse γ-ray emission at intermediate latitudes were first published in Abdo et al. (2009b). This study found that the LAT spectrum was well produced by a model consisting of standard astrophysical processes and was inconsistent with the EGRET GeV excess. However, while the LAT spectral shape was consistent with the diffuse Galactic emission (DGE) model, the overall model emission was too low, thus giving rise to a $\sim$10–15% excess over the energy range 100 MeV – 10 GeV. The DGE model employed in this study was based on pre-*Fermi* data, which was the main explanation given for the discrepancy.

A more detailed study of the DGE was conducted in Ackermann et al. (2012a). It was found that all of the models considered under-predicted the data in the Galactic plane above a few GeV, with the difference being most pronounced in the inner Galaxy. However, compared to the EGRET anomaly, the magnitude of the difference was much less, and was also confined mostly to the plane. The two possible explanations given for the excess were undetected sources and variations in the CR spectra. A systematic excess was also seen in the outer Galaxy. Possible explanations for this were modifications of the assumed distributions of CR sources or of CR propagation in the outer Galaxy, or even the presence of much greater amounts of interstellar gas than currently assumed.

The γ-ray excess towards the GC observed by *Fermi*-LAT (known as the GC excess) was first reported by Goodenough and Hooper Goodenough & Hooper (2009); Hooper & Goodenough (2011), and has since been the subject of numerous studies (Hooper & Linden, 2011; Abazajian & Kaplinghat, 2012; Hooper & Slatyer, 2013; Gordon & Macias, 2013; Huang et al., 2013; Abazajian et al., 2014; Zhou et al., 2015; Calore et al., 2015b; Abazajian et al., 2015; Calore et al., 2015a; Huang et al., 2016; Ajello et al., 2016; Daylan et al., 2016; Carlson et al., 2016; Ajello et al., 2017; Karwin et al., 2017; Ackermann et al., 2017a; Agrawal & Randall, 2017). The first dedicated study of the inner Galaxy by the *Fermi*-LAT Collaboration was published in Ajello et al. (2016). This study confirmed the presence of the excess, characterized the properties of the signal, and quantified the systematic uncertainties related to the observations, as summarized in Chapter 2.

The true nature of the GC excess remains uncertain. The leading explanations for the excess include inaccuracies in the modeling of the foreground/background emission, an unresolved population of point sources (i.e. millisecond pulsars), and/or DM annihilation. If the GC excess is in fact due to DM, and in particular, cold DM, then a complementary signal should also be coming from the MW's satellite galaxies and the MW halo. Correspondingly, the MW halo is expected to contain a high level of substructures, a subset of which hosts the MW's population of satellite galaxies.

No systematic signal has been detected from the MW's dwarf spheroidal galaxies, and this non-detection is in tension with the DM interpretation of the GC excess, but it does not rule it out. The strongest constraints come from Ackermann et al. (2015a) and they result from the combined analysis of 15 dwarf spheroidal galaxies using Pass-8 data. Most recently new constraints were published in Albert et al. (2017) and they result from the combined analysis of

45 stellar systems, including 28 kinematically confirmed dark-matter-dominated dwarf spheroidal galaxies, and 17 recently discovered systems that are dwarf candidates. In the DM mass range corresponding to the GC excess these constraints are weakened by a factor of $\sim$2, relative to the limits given in Ackermann et al. (2015a).

Standard astrophysical γ-ray emission is expected from both the LMC and SMC, and both have previously been detected by *Fermi*-LAT (Abdo, 2010; Abdo et al., 2010a). Note that the first detection of high-energy γ-ray emission from the LMC was made by EGRET (Sreekumar et al., 1992) (the SMC was not detected by EGRET). The emission from the LMC observed by *Fermi*-LAT is modeled using the so-called ”emissivity model” (Ackermann et al., 2016). On top of this model, and the model of the foreground emission from the MW, a statistical excess is detected at the level of 4-5σ (Buckley et al., 2015). The excess is exactly in the DM range required to the explain the GC excess, and it is located near the peak of the DM density profile. The significance is quoted at 1-2σ after including systematics. The true nature of the γ-ray emission from the LMC remains an open question. DM limits from the SMC were published in Caputo et al. (2016). These limits were weaker than expected due to a strong correlation between a component of the SMC model and DM.

The *Fermi*-LAT Collaboration published constraints for a Galactic DM signal in Ackermann et al. (2012b). The study used a region with Galactic longitude and latitude values of $|l| \leq 80°$ and $5° \leq |b| \leq 15°$. After modeling the diffuse emission, the residuals did not seem obviously related to DM, and so the focus of the analysis was to set limits on a possible DM signal, rather than conducting a search. Upper limits were derived requiring that the DM contribution did not exceed the observed diffuse emission. In deriving upper limits the study did not consider substructure contribution. The greatest uncertainty in this analysis was the value of the local DM density.

The *Fermi*-LAT measurement of the isotropic gamma-ray background (IGRB) did not show any signature of a dominant contribution from DM (Abdo et al., 2010c,d). In Abdo et al. (2010d) the absolute size and spectral shape of the measured flux were used to derive limits for an extragalactic DM signal. In Blanchet & Lavalle (2012) the IGRB was used to set limits on a Galactic DM signal, which involved a detailed modeling of the predicted signal, including predictions for substructure contribution. A number of other studies have also employed a similar methodology, using the measured IGRB to set limits on different DM models Abazajian et al. (2010, 2012). Improvements in event selection and characterization of the DGE, as well as a longer data accumulation, allowed for a refinement and extension of the IGRB measurement in Ackermann et al. (2015b). The spectrum was still found to be predominantly featureless, but contained a cutoff at $\sim$279 GeV. In Ajello et al. (2015) a study was made regarding the origin of the IGRB. It was shown that unresolved blazars, star-forming galaxies, and radio galaxies can naturally account for the amplitude and spectral shape of the background, leaving only modest room for other contributions. It has also been argued that CR interactions with the circumgalactic gas in the MW may also contribute to the IGRB at the level of $\sim$10%, for energies above 1 GeV (Feldmann et al., 2013). Likewise, a similar extragalactic component may also contribute at a similar level.

A summary plot of the DM parameter space corresponding to the GC excess is given in Section 5.1, and it contains a number of relevant complementary studies, including DM limits from the MW satellites and halo, as just discussed. It also contains complementary measurements for radio emission from the centers of M31 and the MW, as well as the detection regions corresponding to a recently reported excess in the spectrum of antiprotons.

1.4 Introduction to the M31 System

The Andromeda Galaxy is the closest spiral galaxy to us and has been the subject of numerous studies. Other names for the Andromeda Galaxy are Messier 31, M31, and NGC 224. Because M31 is both massive and relatively nearby (its distance is roughly 785 kpc or 2.5 million light years), it has a large extension on the sky, thus making it a prime target for studying galaxies. A great deal of information has been obtained from observations of M31 in all wavelengths of the electromagnetic spectrum, as will be further discussed in Chapter 4. This section provides a brief (and selective) observational history of M31[7], and also gives additional background and motivation for the observations presented in Chapter 4.

The left panel in Figure 1.6 shows an image of M31 taken from the São Domingos Mine in Portugal by Miguel Claro in 2018. M31 is located in the constellation Andromeda, which is indicated in the Figure. The Triangulum Galaxy (M33) can also be seen. The right panel in Figure 1.6 shows a zoomed in view of M31's galactic disk. M31 is a spiral galaxy very similar to the MW. The blue and purple light in the outer arms is the star-forming region of the galaxy, which is mixed in with dark lanes of dust, and towards the center of the galaxy the yellow and orange light is from the old stellar population. Two satellites of M31 can also be seen in the image; below the galactic disk in NGC 205, and above the galactic disk is M32.

M31 has associated with it a very rich observational history, and correspondingly it has played a major role in the development of our understanding of the Universe. The upper-left panel in Figure 1.7 shows the first-ever published image of M31, published by Issac Roberts in 1893 (Roberts, 1893). The photograph was taken with a 20-inch reflector telescope on December 29, 1888, with an exposure time of four hours. The image revealed for the first time the spiral structure of M31, which at this point in history was referred to as ”The Great Nebula in Andromeda”, the true nature of which was unknown.

---

[7] This brief history by no means encompasses the large body of work that has been done on M31.

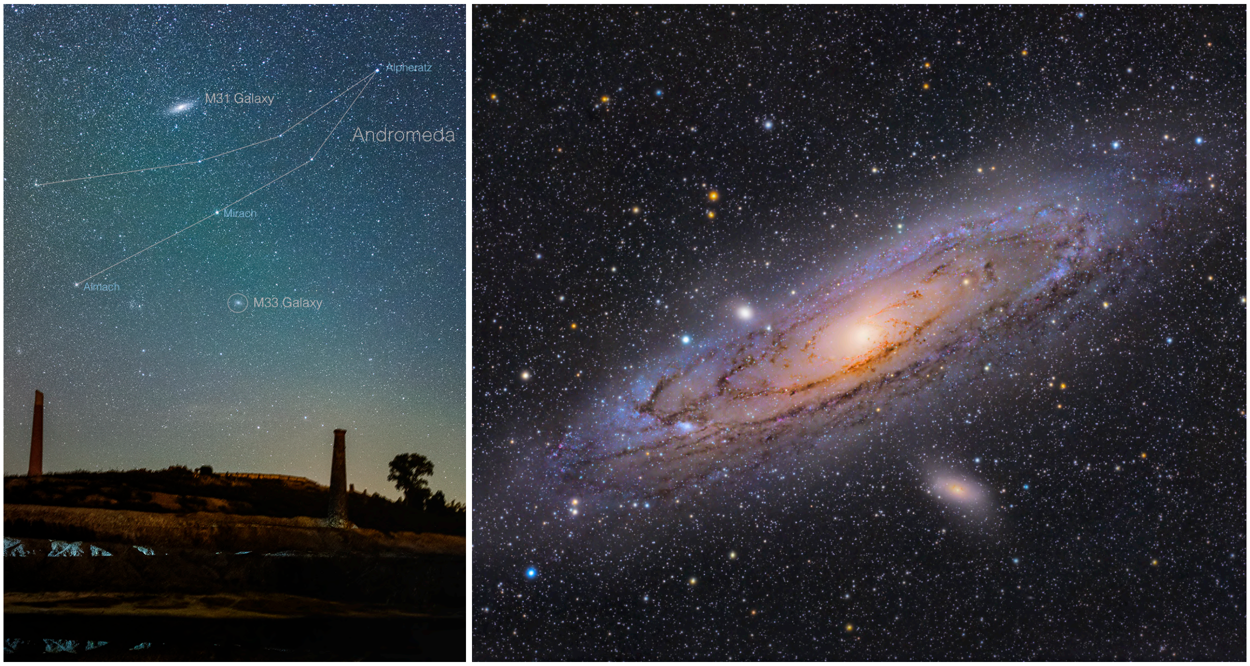

Figure 1.6 Credit (both): © Miguel Claro (`www.miguelclaro.com`). The left panel shows an image of M31 taken from the São Domingos Mine in Portugal in 2018. M31 is located in the constellation of Andromeda. M33 (which is a satellite galaxy of M31) can also be seen in the image. The right panel is a zoomed in view of M31's galactic disk also taken in 2018. Two other satellites of M31 can also be seen, NGC 205 is below the galactic disk, and M32 is above the galactic disk.

In 1914 Vesto Slipher made the discovery that M31 rotates, based on the detection of inclined spectral lines in M31's nuclear spectra (Slipher, 1914; Sofue & Rubin, 2001; Brémond, 2009). This also marked the discovery of galaxy rotation in general (together with similar measurements in the Sombrero Galaxy and M81) (Sofue & Rubin, 2001; Brémond, 2009). Slipher's observations led Francis Pease to measure the rotation of the central region of M31 out to an angular radius of 2.5 arcminutes (Pease, 1918). Other early studies of M31's rotation were made by Horace Babcock in his Ph.D. dissertation (Babcock, 1939) and Nicholas Mayall (Mayall, 1951).

The top middle panel in Figure 1.7 shows a plate from Edwin Hubble's classic study published in 1929 (Hubble, 1929). Before the publication of this work there occurred what is known as ”The Great Debate”. The debate was held between the American astronomers Harlow Shapley and Heber Curtis on April 26, 1920 at the Smithsonian Museum of Natural History[8]. The topic of debate pertained to the nature of the spiral nebulae that had been observed (M31 and others) and the scale of the Universe. Curtis argued that the Universe was composed of many galaxies like our own, and these were the spiral nebulae. Shapley argued that the spiral nebulae were just nearby gas clouds, and that the Universe was composed of just one large galaxy. This debate was partially settled with Hubble's observations of

---

[8] See NASA's dedicated webpage for more details and discussion pertaining to the Great Debate: `https://apod.nasa.gov/diamond_jubilee/debate20.html`

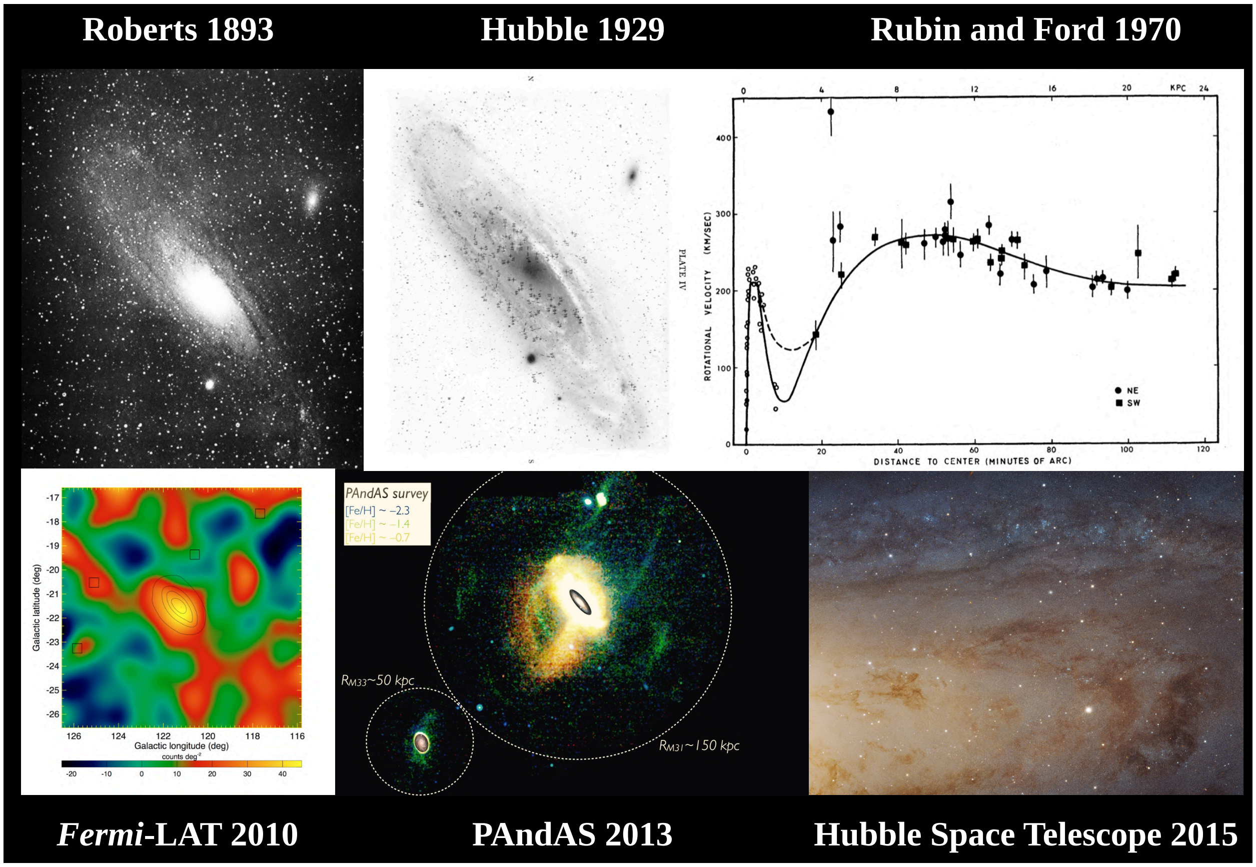

Figure 1.7 Some notable and historic observations of M31. See text for details and references.

M31 (Hubble, 1929). Using the 100 inch Hooker Telescope at Mount Wilson, Hubble identified 40 Cepheid variable stars in M31, which allowed him to calculate the distance to M31. He calculated a distance of 275 kpc. We now know that the distance to M31 is $\sim$785 kpc, but nevertheless, this put M31 outside of the MW, and indeed, as we know today, M31 is its own galaxy. Moreover, the Universe is very large and contains many such galaxies. Flash forward to almost 100 years later and the lower right panel in Figure 1.7 shows a high-definition panoramic view of M31 taken by the Hubble Space Telescope[9].

The upper right panel in Figure 1.7 shows the galactic rotational velocity curve published in the classic study by Vera Rubin and William Ford (Rubin & Ford, 1970). This measurement, and subsequent measurements (Roberts & Whitehurst, 1975; Carignan et al., 2006), are what indicate that M31 contains a large amount of DM.

The first high-energy γ-ray detection of M31 didn't come till 2010 (Abdo et al., 2010b; Ögelman et al., 2011). The lower-left panel in Figure 1.7 shows the residual map from the *Fermi*-LAT Collaboration study published in Abdo

---

[9] Image downloaded from:
`https://www.nasa.gov/content/goddard/hubble-s-high-definition-panoramic-view-of-the-andromeda-galaxy`

et al. (2010b). Note that all γ-ray studies of M31 so far have focused on the innermost region where the galactic disk resides. The study presented in Chapter 4 is the first to explore the furthest reaches of the M31 system in γ-rays.

The bottom middle panel in Figure 1.7 shows M31's extended stellar halo as observed by the Pan-Andromeda Archaeological Survey (PAndAS) (Martin et al., 2013). The PAndAS survey was a large program of the Canada-France-Hawaii Telescope (CFHT) conducted with the MegaPrime/MegaCam wide-field camera over the period 2008-2011. The region used for PAndAS is very similar to the region that is used for the γ-ray observations presented in Chapter 4. At the very center of the image is the galactic disk of M31. This is the region that all γ-ray studies so far have focused on. More generally, the M31 system extends well beyond the galactic disk, as can be seen in the image. M31's extended stellar halo contains numerous clouds and streams. Most notably, the Giant Stellar Stream can be seen to the south of the galactic disk. These features are fossil signatures of the hierarchical nature by which the M31 halo has been built, through accretions and mergers with other galaxies. In the lower left corner of the image is M33.

In addition to the galactic disk and stellar halo, the M31 system is also comprised of a circumgalactic medium, which is loosely defined as a halo of gas (primarily ionized hydrogen) in different phases which may extend as far as the galaxy's virial radius. There may also be a CR halo that extends well beyond the galactic disk region, but the density of CRs in the outer region is highly uncertain and depends on the strength of the galactic magnetic fields.

Lastly, the M31 system is thought to reside within a massive DM halo. The DM halo of M31 is predicted to extend to roughly 300 kpc from its center and have a mass on the order of $10^{12}\ M_{\odot}$, which amounts to $\sim$90% of the galaxy's total mass. To help illustrate this, Figure 1.8 shows an image of an M31-MW-like galaxy pair from Garrison-Kimmel et al. (2018). This image is from a set of high-resolution hydrodynamic cosmological zoom-in simulations that apply the Feedback In Realistic Environments (FIRE) physics to Local Group-like volumes (Garrison-Kimmel et al., 2018). This particular pair is affectionately known as Romeo and Juliet. The green and pink panel shows the DM, and it gives a sense of what the local DM structure may be like. There are the two main halos of M31 and the MW, with a high level of substructure, and a large filamentary structure connecting the two galaxies. In general, along the direction that connect M31 and the MW there is a high density of DM and gas.

For γ-ray observations towards M31's outer halo, the total signal ostensibly contains emission from the MW's DM halo in the line of sight, emission from the local filamentary structure connecting the MW and M31, and emission from the entire DM halo of M31, plus any secondary emission from M31. For the MW halo, a DM signal should be pretty bright, but since we see through the halo, the emission can be easily confused with the diffuse components of the interstellar emission model. For M31 we see the entire halo from the outside, and so we see the total integral signal. Thus M31 is advantages for halo searches with γ-rays because it breaks the observational degeneracy.

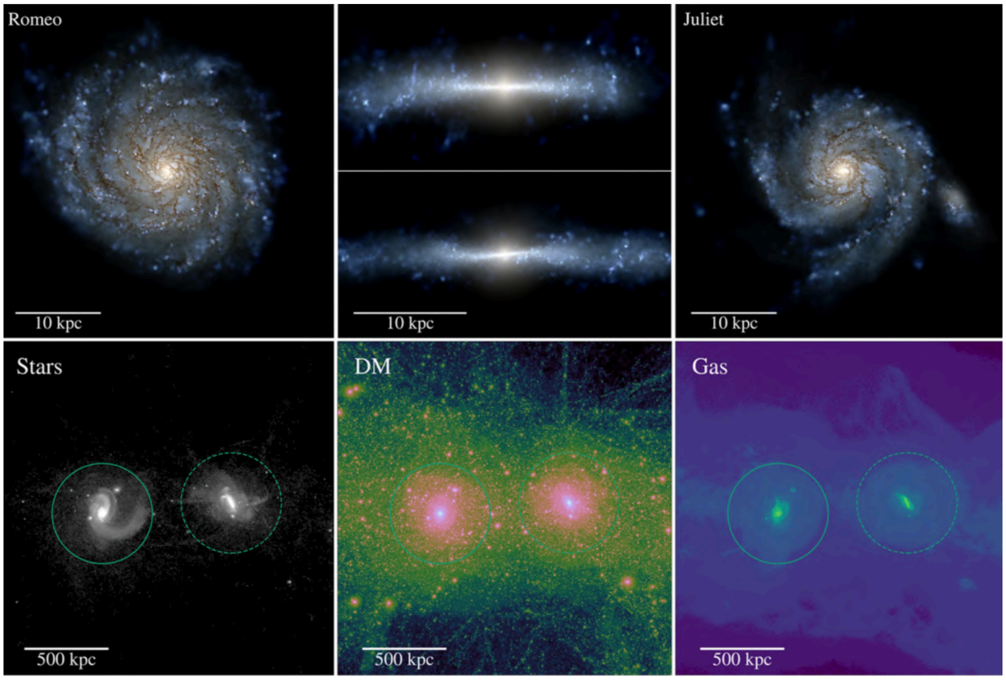

Figure 1.8 M31-MW-like galaxy pairs from Garrison-Kimmel et al. (2018). The green and pink image illustrates what the DM structure may look like in the Local Group.

There is currently a high level of uncertainty regarding the actual properties of the DM halos for both M31 and the MW, i.e. the geometry, extent, and substructure content. In general, the DM halos have both a smooth component and a substructure component. In regards to the latter, a subset of the satellites in M31 (which are thought to reside within DM substructures) are known to be positioned within a large thin plane (The Great Plane of Andromeda, GPoA); and likewise, a subset of the MW satellites are known to be part of a large planar structure as well (The Vast Polar Structure of the Milky Way) (Kroupa et al., 2005; Pawlowski et al., 2012; Conn et al., 2013; Ibata et al., 2013; Pawlowski et al., 2013a; Hammer et al., 2013; Pawlowski, 2018). In addition, the satellite system of M31 is highly lopsided, as about 80% of its satellites lie on the side closest to the MW (Conn et al., 2013; Pawlowski et al., 2017). M31's dwarf population is shown with red circles in Figure 1.9, overlaid to the γ-ray emission (which will be described in detail in Chapter 4). Note that for members of the GPoA, those to the north of M31 recede from us, and those to the south of M31 move toward us, in the plane of rotation.

Also shown in Figure 1.9 are two notable highly extended gas clouds in the direction of M31 which may be intrinsically related to the Local Group structure, namely, Complex H (Hulsbosch, 1975; Blitz et al., 1999; Lockman, 2003; Simon et al., 2006) and the M31 cloud (Blitz et al., 1999; Kerp et al., 2016). The M31 cloud is a highly extended lop-sided gas cloud centered in projection on M31, originally observed in Blitz et al. (1999). It remains uncertain whether the M31 cloud resides in M31 or the MW. Most recently Kerp et al. (2016) have argued that M31's disk is physically

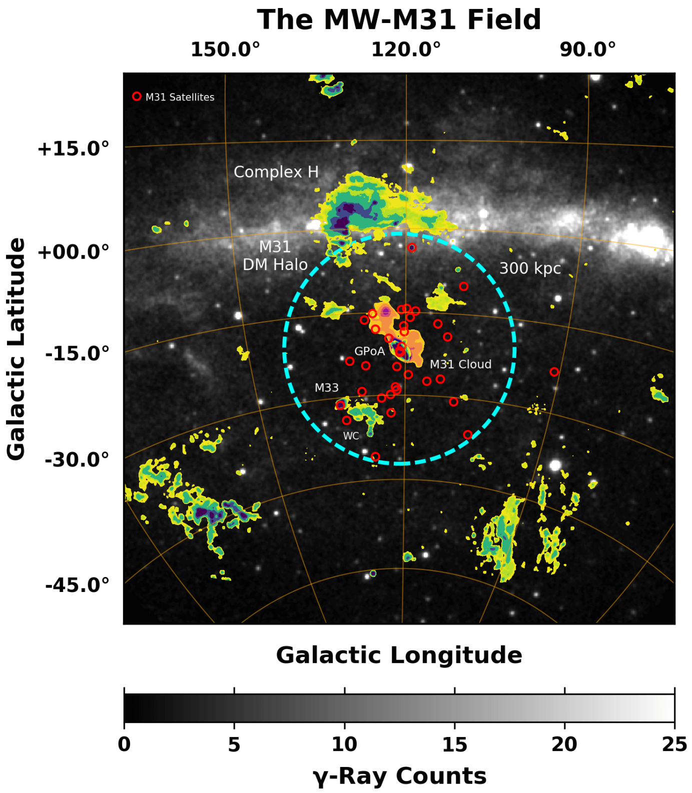

Figure 1.9 The line of sight looking towards the DM halo of M31. M31's population of satellite galaxies are shown with red open circles. A subset of these satellite are known to reside with a vast thin plane, known as the Great Plane of Andromeda (GPoA). M31's satellite system is also highly lopsided, with approximately 80% of its satellites lying on the side closest to the MW. The size of M31's DM halo is indicated with a dashed cyan circle, which corresponds to a projected radius of 300 kpc, for an M31-MW distance of 785 kpc. Also plotted are some notable gas clouds in the region, namely, the M31 cloud, M33, Wright's cloud (WC), and Complex H. See text for more details. Overall, these observations are a qualitative indication that M31's DM halo may not have a spherically symmetric distribution (at least for the substructure), and this is an important consideration for γ-ray observations towards M31's outer halo.

connected to the M31 cloud. If at the distance of M31 ($\sim$785 kpc) the total gas mass is estimated to be $\sim 10^8$–$10^9\ \mathrm{M}_\odot$. The M31 cloud can be seen in Figure 1.9, which shows H I emission contours from the HI4PI all-sky survey (based on EBHIS and GASS) (Bekhti et al., 2016), integrated over the velocity range $-600 \leq V_{\mathrm{LSR}} \leq -95\ \mathrm{km\,s^{-1}}$. The contour levels are 12%, 15%, 20%, 40%, 60%, 80%, 100%, and 200% of the log of the H I integrated line strength, clipped to a maximum value of 50 $\mathrm{K\ km\,s^{-1}}$. The systemic velocity of the M31 disk is $\sim$–300 $\mathrm{km\,s^{-1}}$, and its proper motion has been estimated to be approximately oriented from the top right corner to the lower left corner (Sohn et al., 2012; Kerp et al., 2016).

The large gas cloud towards the top of the map in Figure 1.9 is Complex H, first detailed by Hulsbosch (1975). Below the main structure, near $b{\sim}-15^\circ$, two additional mid-size clouds can also be seen (near the right and left edges of the main cloud), also labeled as members of Complex H. In particular, the contours show H I data from the HI4PI all-sky survey (based on EBHIS and GASS), integrated over the velocity range $-600 \leq V_{\rm LSR} \leq -170$ km s^{-1}, effectively excluding the conventional Galactic gaseous disk. The distance of Complex H from the MW is uncertain, although its likely distance has been estimated to be $\sim$30 kpc from the Galactic center, which corresponds to the cloud having a diameter of about $\sim$10 kpc and an H I mass of $\sim 10^7$ M$_\odot$ (Blitz et al., 1999; Lockman, 2003; Simon et al., 2006). Complex H does not appear to contain any stars, and it has been postulated to be either a dark galaxy of the Local Group or an example of a cold accretion flow (Simon et al., 2006).

Also shown in Figure 1.9 are H I emission contours corresponding to M33. The systemic velocity of M33 is ~ -180 km s^{-1}. The total H I mass of the M33 disk is $\sim 10^9$ M$_\odot$. The hook-shaped gas cloud to the right of M33 is Wright's cloud, as originally observed in Wright (1979). The distance of Wright's cloud remains uncertain (Braun & Thilker, 2004). The H I mass of Wright's cloud at the distance of M33 is $\sim 4.5 \times 10^7$ M$_\odot$ (Keenan et al., 2015). The systemic velocity of Wrights cloud is ~ -383 km s^{-1}. Although no contours are shown, note that below M33 is "the dark companion to M33", which is another highly extended gas cloud originally observed in Thilker et al. (2002), and labeled as a compact high-velocity cloud. The systemic velocity is ~ -374 km s^{-1}, comparable to that of Wright's cloud. If at the distance of M33, Keenan et al. (2015) estimate the H I mass to be $\sim 10^7$ M$_\odot$, and the size to be $\sim 18.2 \times 14.6$ kpc. See Keenan et al. (2015) for details of the cloud.

As indicated by DM simulations of MW-M31-like galaxy pairs, the GPoA, the VPOS, the lopsided distribution of M31 satellites (with $\sim 80\%$ being on the MW side), the M31 cloud, and Complex H, the overall DM subhalo population in the Local Group may not be uniformly distributed, and likewise, the DM halos of M31 and the MW may deviate significantly from spherical symmetry. Moreover, the DM halos of M31 and the MW may even be coupled, with an enhanced density of DM in the direction connecting the two galaxies. These realizations are important for γ-ray observations towards the outer halo of M31, as presented in Chapter 4.

Chapter 2

Fermi–LAT Observations of High-Energy γ-Ray Emission Toward the Galactic Center

This chapter gives a summary of the paper ”*Fermi*–LAT Observations of High-Energy γ-Ray Emission Toward the Galactic Center”, published in the *Astrophysical Journal* (Ajello et al., 2016). This was a *Fermi*-LAT Collaboration study, which was led by Simona Murgia and Troy Porter.

Abstract: The *Fermi* Large Area Telescope (LAT) has provided the most detailed view to date of the emission toward the Galactic center (GC) in high-energy γ-rays. This paper describes the analysis of data taken during the first 62 months of the mission in the energy range 1–100 GeV from a $15^\circ \times 15^\circ$ region about the direction of the GC. Specialized interstellar emission models (IEMs) are constructed to enable the separation of the γ-ray emissions produced by cosmic ray particles interacting with the interstellar gas and radiation fields in the Milky Way into that from the inner $\sim$1 kpc surrounding the GC, and that from the rest of the Galaxy. A catalog of point sources for the $15^\circ \times 15^\circ$ region is self-consistently constructed using these IEMs: the First *Fermi*-LAT Inner Galaxy Point Source Catalog (1FIG). After subtracting the interstellar emission and point-source contributions a residual is found. If templates that peak toward the GC are used to model the positive residual the agreement with the data improves, but none of the additional templates tried account for all of its spatial structure. The spectrum of the positive residual modeled with these templates has a strong dependence on the choice of IEM.

2.1 Introduction

The region surrounding the GC is among the brightest and most complex in high-energy γ-rays, with ongoing massive star formation providing all types of known or suspected cosmic ray and γ-ray sources. The GC also houses a $\sim 10^6\ M_\odot$ black hole, and the region is predicted to be the brightest source of γ-rays associated with dark matter (DM) annihilation or decay.

The γ-ray emission in the Galaxy is predominantly due to the interactions of CR particles with the interstellar gas and radiation fields. This interstellar emission is a fore-/background against which γ-ray point sources are detected. In the Galactic plane the intensity of this emission makes disentangling the contributions by γ-ray point sources and truly diffuse processes challenging. Particularly toward the GC, where the intensity of the interstellar emission and number of point sources is maximized, self-consistent modeling is necessary to deal with the strong confusion.

Since 2008 the Large Area Telescope instrument on the *Fermi* Gamma-Ray Space Telescope (*Fermi*-LAT) has been taking data in the range 20 MeV to more than 300 GeV energies. Analyses of the data toward the region surrounding the GC have been made by various authors (Goodenough & Hooper, 2009; Hooper & Goodenough, 2011; Hooper & Linden, 2011; Abazajian & Kaplinghat, 2012; Hooper & Slatyer, 2013; Gordon & Macias, 2013; Huang et al., 2013; Abazajian et al., 2014; Zhou et al., 2015; Calore et al., 2015b; Abazajian et al., 2015; Calore et al., 2015a; Huang et al., 2016; Daylan et al., 2016; Carlson et al., 2016). The results of these works have been interpreted as evidence for an unresolved point source population or annihilating DM. Versions of the IEMs distributed by the Fermi Science Support Center (FSSC) have typically been employed in these analyses, although some works have used IEMs (e.g., Calore et al. (2015b)) that are based on CR propagation calculations using the GALPROP[1] code (Moskalenko & Strong, 1998, 2000; Strong & Moskalenko, 1998; Strong et al., 2000; Ptuskin et al., 2006; Strong et al., 2007; Vladimirov et al., 2011; Jóhannesson et al., 2016; Porter et al., 2017; Jóhannesson et al., 2018; Génolini et al., 2018).

The FSSC IEMs are optimized to flatten residuals over large regions of the sky in support of the generation of the Fermi- LAT source catalogs. The optimizations vary according to the version of the FSSC IEM. The most widely used by the analyses cited above (supporting the generation of the Second Fermi-LAT Source Catalog; Nolan et al. (2012)) includes patches with spatially uniform spectral intensity to account for positive residuals. Some of these are in and about the GC, which makes interpretation of positive residuals after fitting additional templates and subtracting the IEM and point sources uncertain.

In this paper, an analysis is described of the γ-ray emission observed by the *Fermi*-LAT during the first 62 months of

---

[1] Available at `https://galprop.stanford.edu`

the mission toward the inner Milky Way that characterizes the $15^\circ \times 15^\circ$ region in Galactic coordinates centered on the GC. This encompasses the innermost $\sim$1 kpc where the CR intensities, interstellar gas and radiation field densities are highest but most uncertain, and signatures of new physics may be detectable. The analysis uses multiple IEMs together with an iterative fitting procedure to determine the contributions by diffuse and discrete sources of high-energy γ-ray emission. The GALPROP CR propagation code is used to calculate components of IEMs that are fit to the *Fermi*-LAT data to predict the interstellar emission fore-/background toward the $15^\circ \times 15^\circ$ region. Candidate locations of point sources are found using a wavelet-based algorithm (Damiani et al., 1997). These are used together with the IEMs to define a model for the emission of the region, which is then optimized in a maximum-likelihood fit to determine the contribution by CR-induced diffuse emission from the innermost $\sim$1 kpc and γ-ray point sources. This is the first self-consistent modeling balancing the various sources of γ-rays toward the inner Galaxy.

2.2 Data Selection

The analysis employs events with reconstructed energy in the range 1–100 GeV, where the effective area of the LAT is largest and not strongly dependent on energy. To allow the best separation between point sources and the structured interstellar emission , only front-converting events are used.

Events and IRFs for the standard low-residual CR background ”Clean” events from the Pass 7 event selections (Ackermann et al. 2012b) are used. To minimize the contribution from the very bright Earth limb, the event selection and exposure calculation is restricted to zenith angles less than 100°.

Events are selected from approximately 62 months of data from 2008 August 11 until 2013 October 15. Exposure maps and the PSF for the pointing history of the observations were generated using the standard Fermi-LAT ScienceTools package (version 09-34-02).

2.3 Systematic Uncertainties for the Interstellar Emission Models

Specialized IEMs are constructed which allow for the separation of the γ-ray emission from within $\sim$1 kpc of the GC. In total four different IEMs are used, corresponding to two systematic variations which quantify the uncertainty of the analysis.

The first uncertainty is due to the radial distribution of the CR source density. CRs are thought to be accelerated

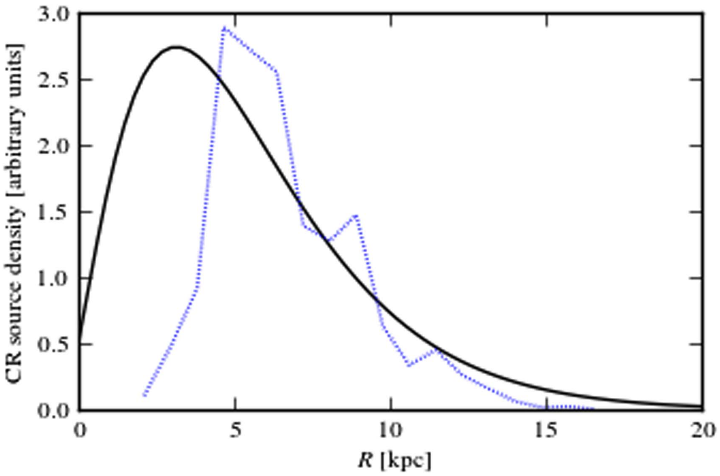

Figure 2.1 Galactocentric radial dependence of the spatial distribution of CR sources per unit volume. Line styles/colors: solid/black, Pulsars; dotted/blue, OB-stars.

primarily by supernova remnants. However, the radial distribution of supernova remnants is not well determined, and therefore, other tracers are used. This analysis uses two different distributions, namely, the distribution of pulsars, which are the end state of supernovae, and the distribution of OB stars, which are progenitors to supernovae. The two distributions are plotted in Figure 2.1.

The second uncertainty is due to the tuning procedure used for modeling the foreground/background emission. Two variations of the tuning procedure are employed. In one variation the normalization of the diffuse component are scaled (intensity-scaled). In the other variation additional freedom is allowed by also scaling the index of the gas-related components interior to the solar circle (index-scaled). The two tuning procedures, together with the two tracers of the CR source density, result in four different IEMs which quantify the systematic uncertainty of the observations.

The tuning is performed over a majority of the sky, as shown in Figure 2.2. The top row shows spatial residuals for the baseline Pulsars model, the middle row is the intensity-scaled Pulsars model, and the bottom row is the index-scaled Pulsars model. The green regions are masked for the entire tuning procedure. This includes the Cygnus region, the Fermi bubbles, and the $15° \times 15°$ signal region about the GC.

The IEMs are defined in Galactocentric annuli, and the tuning procedure is performed from the outermost annuli inwards. For each annuli, the scaling of the γ-ray intensity maps towards the GC region (foreground and background) is determined from the fit in the tuning region. Note that the gas (H I and H_2) is placed at Galactocentric radii based on Doppler shifted emission (21-cm for H I and CO for H_2). The kinematic resolution of this method vanishes for directions near the GC, and therefore, the corresponding gas distributions are linearly interpolated for each annulus

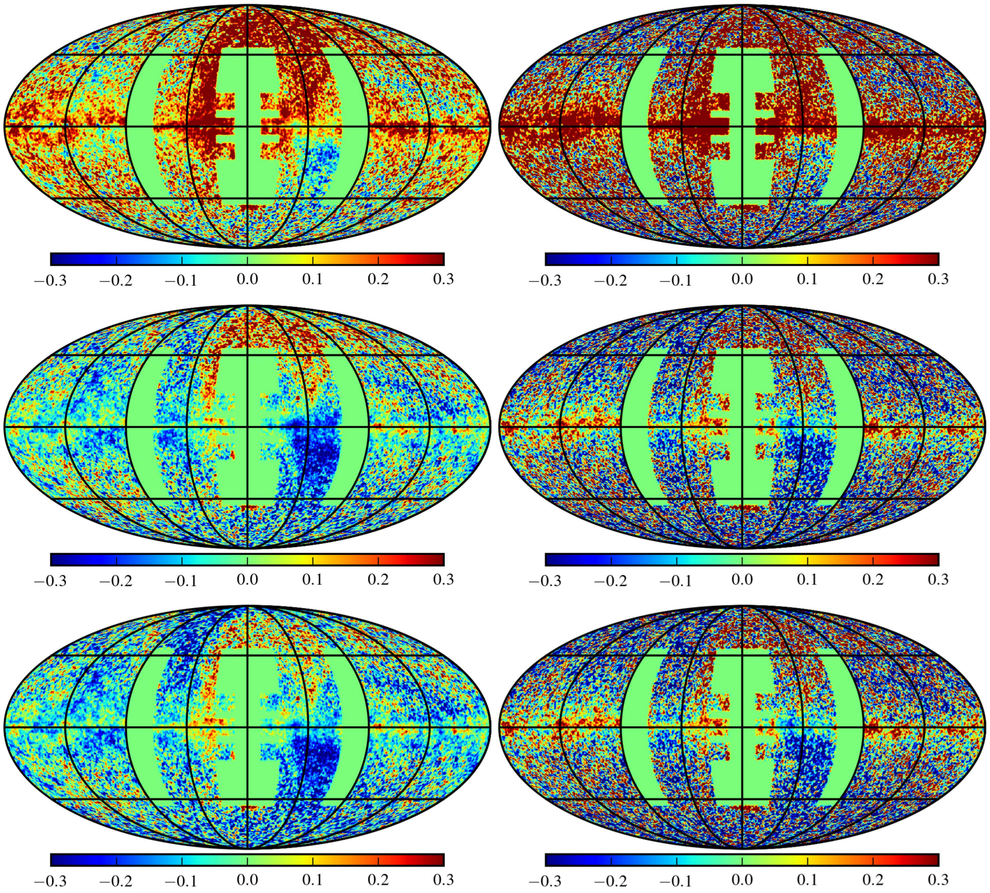

Figure 2.2 Residual fractional counts (data-model)/model in the 1–3.16 GeV (left) and 3.16–10 GeV (right) energy ranges for the baseline Pulsars model (upper), the intensity-scaled Pulsars model (center), and the index-scaled Pulsars model (lower). Regions not used for the IEM tuning procedure are masked.

towards the GC.

2.4 Baseline Fit for the Galactic Center

The IEM components for the inner annulus are fit in the $15^\circ \times 15^\circ$ region about the GC. Point sources in the region are also determined self-consistently with the IEM. Figure 2.3 shows the flux and remaining fractional count residuals for the baseline fit, for the four different IEMs. The red dashed curve labeled ”IEM” shows the emission coming from the foreground/background, as determined from the tuning procedure. As can be seen, this is the dominant contribution towards the GC. The blue dashed curve is the the IC component from the inner annulus, and the green dashed-dot curve is the gas-related emission from the inner annulus. Point sources are shown with the pink dash-dot curve. The IC component dominates the diffuse emission in the inner Galaxy, whereas the gas-related component is subdominant

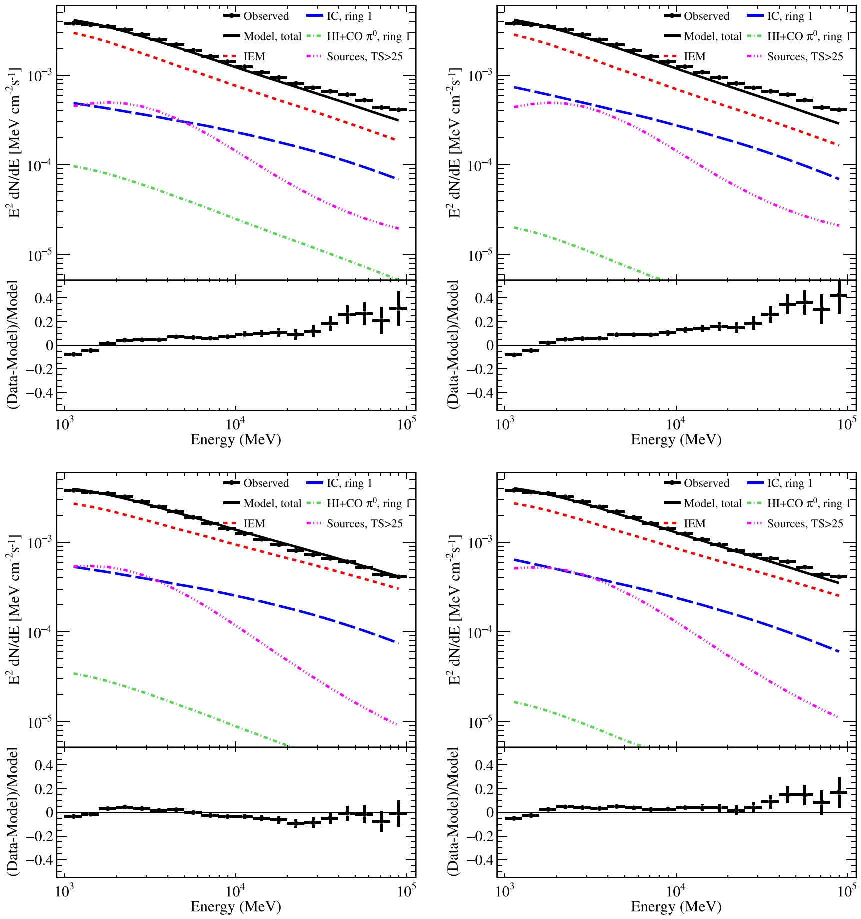

Figure 2.3 Differential fluxes for the $15^\circ \times 15^\circ$ region about the GC for the four IEMs. Upper row shows the results for the intensity-scaled IEMs based on the Pulsars (left) and OB stars (right) source distributions. Lower row shows the results for the index-scaled IEMs based on the Pulsars (left) and OB stars (right) source distributions. Line styles: solid black (total model), long-dash blue (IC, annulus 1), dot-dash green (H I and CO gas π^0-decay, annulus 1), dot-dot-dot-dash pink (point sources), dash red (Galactic interstellar emission excluding annulus 1 for IC, H I and CO gas π^0-decay). Solid black circles: data.

and also lower than the model prediction.

The fractional count residuals show that the baseline IEMs are not providing a very accurate description of the data. The intensity-scaled models (top row) show a high-energy excess reaching as high as ∼40%, whereas there is better agreement at high energies for the index-scaled models.

The spatial residuals resulting from the fit are shown in Figure 2.4. The columns correspond to the different IEMs, and the rows correspond to the energy bands 1–1.6 GeV, 1.6–10 GeV, and >10 GeV, from top to bottom, respectively. The first bin shows excess emission near the GC, and over-modeling along the Galactic plane. The middle bin coincides with the GC excess. The excess emission is roughly spherically symmetric with respect to the GC. The excess is also

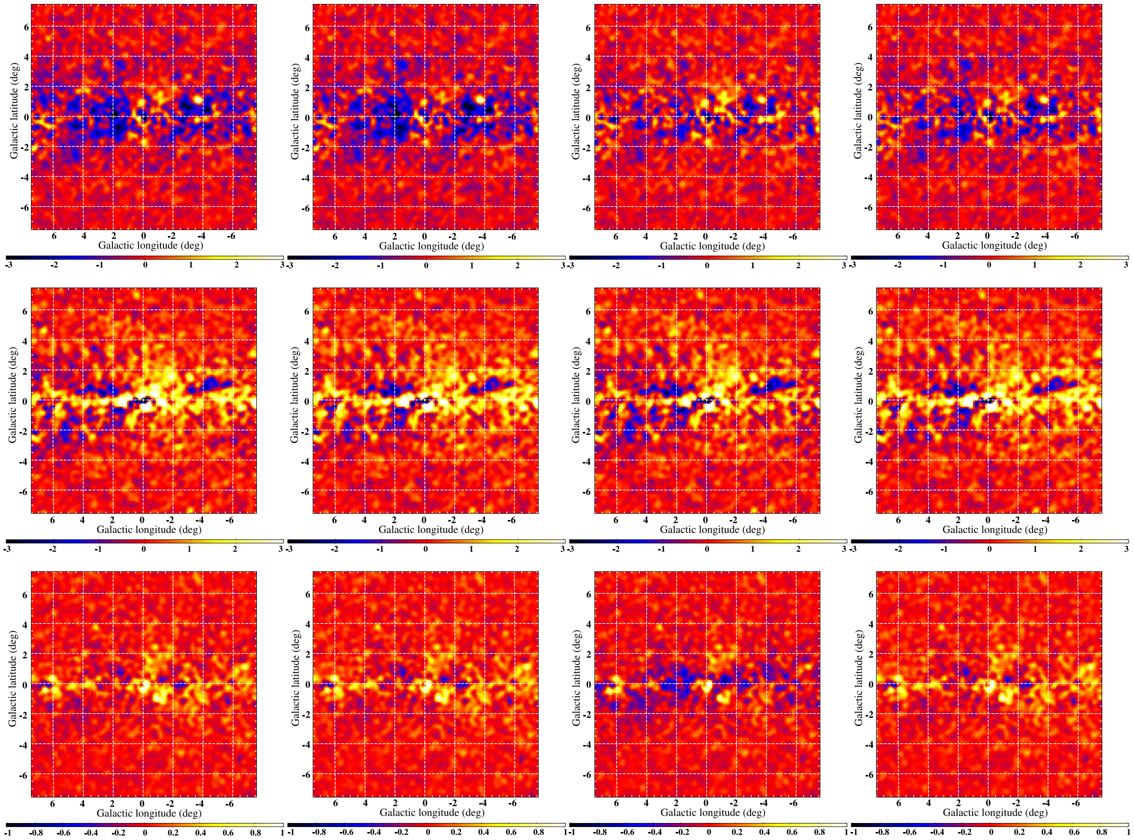

Figure 2.4 Residual counts for the 15° × 15° region about the GC for the Pulsars and OB stars IEMs for energy ranges 1–1.6 GeV (upper row), 1.6–10 GeV (middle row), and >10 GeV (bottom row). The two leftmost columns show the residual counts for the intensity-scaled variant for the Pulsars and OB stars, respectively. The two rightmost columns show the residual counts for the index-scaled variant for the Pulsars and OB stars, respectively. The color scale is in counts/0.1 deg^2 pixel.

seen along the plane as well, and in general there is more emission on the right side of the field compared to the left side. The last energy bin also shows excesses and deficits along the plane.

2.5 Characterizing the Galactic Center Excess

To characterize the properties of the excess emission, an additional component is added to the model and fit simultaneously with the diffuse components and point sources. The additional component is fit with a power law with exponential cutoff spectral model, and multiple spatial templates are tested. Of the spatial models tested an NFW DM profile provides the greatest improvement in the likelihood. Note, however, that only a limited number of spatial

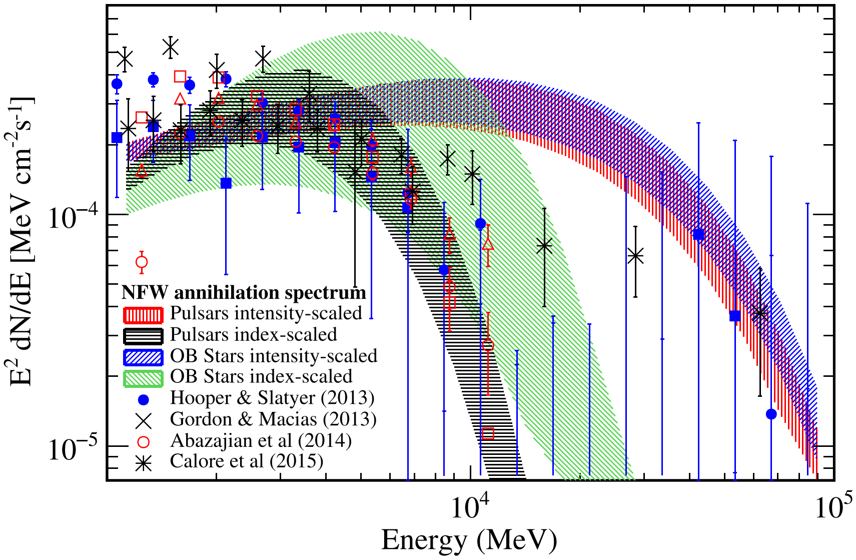

Figure 2.5 Differential fluxes for the 15° × 15° region about the GC, for an NFW component with an exponential cut-off power law spectral model. The envelopes include the fit uncertainties for the normalization and spectral index. Hatch styles: Pulsars, intensity-scaled (red, vertical); Pulsars, index-scaled (black, horizontal); OB stars, intensity-scaled (blue, diagonal-right); OB stars, index-scaled (green, diagonal-left). Results from selected other works are overlaid.

models were tested, and the NFW profile does not account for the entirety of the emission.

Figure 2.5 shows the spectrum of the GC excess. The four different bands correspond to the four different IEMs, and they quantify the uncertainty of the spectrum. The intensity-scaled IEMs have a higher cutoff compared to the index-scaled models, consistent with the high-energy excess seen in the fractional count residuals for the baseline fit. Results from other selected works are also overlaid, and the results found in this analysis are overall in agreement with these other studies.

2.6 Summary

This chapter summarized the study published in Ajello et al. (2016), which is the first study of the inner Galaxy published by the *Fermi*-LAT Collaboration. In this study specialized IEMs are constructed which allow for the separation of the γ-ray emission from within $\sim$1 kpc of the Galaxy. Point sources are also determined self-consistently with the IEMs. The presence of the GC excess, as reported in previous studies, is confirmed. However, this study finds a broader uncertainty in the properties of the excess, which reflects the broader range of systematics the analysis has probed. The excess emission is subdominant with respect to the foreground/background emission along the line of sight. The morphology has a roughly spherical distribution about the GC, and the spectrum is peaked between $\sim$2–20 GeV, with cutoffs at higher and lower energies, but the exact properties have a strong dependence on the IEM.

Chapter 3

Dark Matter Interpretation of the *Fermi*–LAT Observation Toward the Galactic Center

This chapter is from ”Dark Matter Interpretation of the *Fermi*–LAT Observation Toward the Galactic Center”, with Simona Murgia, Tim Tait, Troy Porter, and Philip Tanedo, published in *Physical Review D* (Karwin et al., 2017).

Abstract: The center of the Milky Way is predicted to be the brightest region of γ-rays generated by self-annihilating dark matter particles. Excess emission about the Galactic center above predictions made for standard astrophysical processes has been observed in γ-ray data collected by the *Fermi* Large Area Telescope. It is well described by the square of an NFW dark matter density distribution. Although other interpretations for the excess are plausible, the possibility that it arises from annihilating dark matter is valid. In this paper, we characterize the excess emission as annihilating dark matter in the framework of an effective field theory. We consider the possibility that the annihilation process is mediated by either pseudo-scalar or vector interactions and constrain the coupling strength of these interactions by fitting to the *Fermi* Large Area Telescope data for energies 1–100 GeV in the $15^\circ \times 15^\circ$ region about the Galactic center using self-consistently derived interstellar emission models and point source lists for the region. The excess persists and its spectral characteristics favor a dark matter particle with a mass in the range approximately from 50 to 190 (10 to 90) GeV and annihilation cross section approximately from $1{\times}10^{-26}$ to $4{\times}10^{-25}$ ($6{\times}10^{-27}$ to $2{\times}10^{-25}$) cm^3/s for pseudo-scalar (vector) interactions. We map these intervals into the corresponding WIMP-

neutron scattering cross sections and find that the allowed range lies well below current and projected direct detection constraints for pseudo-scalar interactions, but are typically ruled out for vector interactions.

3.1 Introduction

Despite the overwhelming evidence from astrophysics and cosmology that roughly 80% of the matter in our Universe is in the form of dark, non-baryonic particles, how this so-called dark matter (DM) fits with the Standard Model (SM) of particle physics is currently unknown. Determining the nature of DM is one of the most pressing questions in the physical sciences, and a wide array of experiments are underway which hope to shed light on its identity by observing its interactions with the better understood particles of the SM.

Indirect detection is one of the promising avenues to elucidate the nature of DM. This method attempts to detect and discriminate the SM particles produced by DM particle annihilations (or decays) from those produced by conventional astrophysical processes. γ-rays of $\sim$ GeV energies are a particularly effective messenger because they propagate unhindered on galactic scales, and thus can be effectively traced back along the direction of their origin. In recent years, the *Fermi* Large Area Telescope (*Fermi*-LAT) has mapped out the γ-ray sky with the highest sensitivity of space-borne detectors to date, leading to the current best limits on the annihilation cross section for $\sim$ 100 GeV DM annihilations that result in γ-rays.

Numerical simulations of galaxy formation offer clues as to where DM annihilation is expected to shine the most brightly. The simulations typically predict a large concentration of DM close to the Galactic center (GC), which smoothly falls off with Galactocentric radius. They also predict localized over-densities of DM, some of which correspond to dwarf spheroidal satellite galaxies. Both targets provide complementary regions of interest for DM searches. The DM related emission from the dwarf galaxies is expected to be of lower intensity, but to be relatively free of standard astrophysical backgrounds. Searches for γ-ray emission from dwarf satellites of the Milky Way have so far shown no convincing signal of DM annihilation (Ackermann et al., 2014, 2015a; Geringer-Sameth & Koushiappas, 2011). In contrast, the GC is expected to produce a higher intensity annihilation signal. However, the region about the GC is strongly confused because of the intense interstellar emission and numerous discrete sources of γ-rays that are summed along and through the line-of-sight toward the GC. The estimation of these fore-/background contributions pose a significant challenge for detection of DM annihilation at the GC.

There seems to be an excess of γ-rays from the direction of the GC, above the expectations from astrophysics. This feature was first observed by Goodenough and Hooper (Goodenough & Hooper, 2009; Hooper & Goodenough, 2011), and its general features, a spatial morphology remarkably consistent with predictions for a DM annihilation signal and a spectrum that peaks at a few GeV, persist in more recent analyses (Hooper & Linden, 2011; Abazajian & Kaplinghat, 2012; Hooper & Slatyer, 2013; Gordon & Macias, 2013; Huang et al., 2013; Daylan et al., 2016; Abazajian et al., 2014; Zhou et al., 2015; Calore et al., 2015b; Abazajian et al., 2015; Calore et al., 2015a; Huang et al., 2016; Carlson et al., 2016). The *Fermi*-LAT collaboration has released its own analysis (Ajello et al., 2016) of the γ-rays from the direction of the inner galaxy based on specialized interstellar emission models (IEMs) for estimating the fore-/background emissions, and enabling the analysis to make the first separation of the γ-ray emission of the ~ 1 kpc region about the GC from the rest of the Galaxy. Even with these IEMs, which represent the most sophisticated modeling to date, the excess persists. However, its spectral properties are strongly dependent on the assumed IEM, making it challenging to conclusively identify its origin. As a result, it remains unclear whether this signal arises from DM annihilation rather than from a currently unknown contribution from astrophysics such as a large population of milli-second pulsars, cosmic-ray (CR) proton or electron outbursts, additional cosmic ray sources, and/or emission from a stellar over-density in the Galactic bulge (Hooper et al., 2013; Abazajian et al., 2014; Carlson & Profumo, 2014; Petrović et al., 2014; Cholis et al., 2015; Carlson et al., 2016; Macias et al., 2016). An interesting development is the use of statistical tools which indicate that GeV photons from the direction of the inner galaxy region show significantly more clustering than would be expected from Poisson noise from smooth components (Lee et al., 2015; Bartels et al., 2016; Lee et al., 2016; McDermott et al., 2016). However, it remains difficult with the current models to disentangle whether this feature represents a property of the excess itself, or unmodelled variation in the background components (Horiuchi et al., 2016).

While it is clearly premature to claim that the GeV excess represents a confirmed signal of DM annihilation, in this paper we extract the properties of the excess under the assumption that it does. We make simultaneous fits to the parameters of generic, realistic particle physics model of DM annihilation together with those defining the broad characterization of the possible fore-/backgrounds determined using the methodology of Ajello et al. (2016). As a result, we can compare with the expectations for such models from direct searches for DM and colliders, finding that the null results of those searches play a significant role in shaping the allowed parameter space.

Our work is organized as follows. In Section 3.2, we very briefly review the methodology of the *Fermi*-LAT analysis (Ajello et al., 2016) to formulate realistic IEMs, which crucially define the fore- and backgrounds as well as the astrophysical contributions from the GC itself. This is followed in Section 3.3 by a revisitation of some of the most important morphological and spectral features of the signal: its centroid and whether there is evidence for two separate components with distinct morphologies and spectra. In Section 3.4, we define realistic flexible DM models described by effective field theories (EFTs), and perform a maximum likelihood (ML) fit to determine the ranges of their parameters capable of describing the excess together with the IEM parameters. We compare the ML regions of those models to direct and collider searches for DM in Section 3.5. Section 3.6 contains our conclusions and outlook.

3.2 Interstellar Emission Model and Analysis

3.2.1 Data

The analysis presented in this paper employs the same data as used by Ajello et al. (2016): front converting events corresponding to the P7REP_CLEAN_V15 selection (Ackermann et al., 2012c), in the energy range 1-100 GeV, and with zenith angles less than 100°. Exposure maps and the PSF for the pointing history of the observations were produced using the *Fermi*–LAT ScienceTools package (version 09-34-02)[1]. Events are selected from approximately 62 months of data, from 2008-08-11 until 2013-10-15. We note that for high statistics analyses such as the one presented here a notable difference is not expected in the results obtained with the P7REP_CLEAN_V15 data processing and those processed using Pass 8 (Atwood et al., 2013); this is confirmed by several previous analyses (Lee et al., 2016; Carlson et al., 2016).

3.2.2 Interstellar Emission Models

The interstellar emission is the largest contribution to the γ-ray emission toward and through the line-of-sight toward the GC. To separate the contribution by the Galaxy between our location and the inner 1 kpc region about the GC, and that on the other side of the GC, specialized IEMs (four in total) were developed for the analysis in Ajello et al. (2016). The methodology employed templates calculated using the well-known GALPROP CR propagation modeling code[2] that were scaled to the data outside of the inner $15^\circ \times 15^\circ$ region about the GC. Under the assumption of Galactocentric azimuthal symmetry, these IEMs were used to estimate the fore-/background emission over the $15^\circ \times 15^\circ$ region, enabling the separation. Employing this prescriptive methodology ensures that minimal biases are introduced when fitting to the inner region. In addition, point source lists were developed for each IEM with the properties of the individual point sources obtained in a combined ML fit over the $15^\circ \times 15^\circ$ region. The construction of each IEM and its associated point-source list/model is a critical improvement over earlier works because the residual emission is strongly dependent on modeling both the over the region self-consistently.

---

[1] Available at `http://fermi.gsfc.nasa.gov/ssc/data/analysis`

[2] A description of the GALPROP code is available at `http://galprop.stanford.edu`

The four distinct IEMs from Ref Ajello et al. (2016) are labeled:

- *Pulsars, intensity-scaled*
- *Pulsars, index-scaled*
- *OB stars, intensity-scaled*
- *OB stars, index-scaled*

The IEMs differ in the assumed distribution of the sources of CRs as tracing either the distributions of pulsars or OB stars; and in the procedure employed to scale the γ-ray intensity of the fore-/background components outside of the $15^\circ \times 15^\circ$ region to the data, either by scaling the normalization of the model templates for *intensity-scaled* IEMs, or scaling the normalization and spectral index (the latter only for gas-related templates interior to the solar circle) for the *index-scaled* IEMs. Notably, it was found that the data are compatible with a contribution from γ-rays from DM annihilation, and that the agreement between the data and the model significantly improves for all four IEMs when an additional component with a DM annihilation morphology is included in the fit.

3.2.3 Analysis Procedure

We employ the procedure developed by the *Fermi*–LAT Collaboration in Ajello et al. (2016), which performs a ML fit of a model consisting of one of the four IEMs and its corresponding list of point sources to the data in the $15^\circ \times 15^\circ$ region. For each model, we include a DM annihilation contribution (described below) and perform the fit using the *gtlike* package of the *Fermi*–LAT ScienceTools. The results of the fit are the coefficients of the interstellar emission components from within the the innermost $\sim$1 kpc, as well as those describing the DM model under consideration. All point sources with a test statistic (defined as in Mattox et al. (1996)) $TS > 9$ are included in the model. Their fluxes and spectra are determined by iterative fits, with each iteration freeing the spectral parameters for a subset of point sources in order of decreasing *TS*.

3.3 Morphology and Spectral Characteristics

The DM spatial distribution used in this paper is described in this section. Because Ajello et al. (2016) tested spatial templates fixed at the position of Sgr A* we investigate the possibility of an offset from this location by refitting the

DM spatial distribution and scanning the ML grid about the GC. If a large offset is found, it might challenge a DM interpretation of the excess. For some IEMs the DM spectrum obtained by Ajello et al. (2016) extended beyond 10 GeV, but a dedicated study of the spatial distribution > 10 GeV was not made; this is also investigated in this section.

3.3.1 Dark Matter Component

The results of numerical simulations for galaxy formation can broadly be described by the Navarro, Frenk, and White (NFW) profile (Navarro et al., 1997):

$$\rho(r) = \rho_0 \left(\frac{r}{R_s}\right)^{-\gamma} \left(1 + \frac{r}{R_s}\right)^{\gamma - 3} \tag{3.1}$$

For this analysis, we use a scale radius R_s = 20 kpc, and ρ_0 corresponding to a local DM density $\rho_\odot$ = 0.4 $\mathrm{GeV/cm^3}$. Two values for the inner slope γ of the DM distribution are considered, γ = 1, 1.2. The more cuspy distribution γ = 1.2 is motivated by the possibility of halo contraction due to the influence of baryons, which are typically not included in the simulations (Diemand et al., 2005). The square of the NFW distribution is used as a template for DM annihilation, and we refer to it as the "NFW profile" (for $\gamma = 1$) or "NFW-c" (for γ = 1.2).

3.3.2 NFW Centroid

The centroid of the Milky Way DM halo is conventionally centered at the location of Sgr A*. Because a large offset from this location might disfavor a DM interpretation, we verify that the centroid of the excess is sufficiently close. An offset between the centroid of the DM halo and Sgr A* as large as approximately 2° is consistent with numerical DM simulations, with the largest offsets tending to correlate with flatter central profiles (Kuhlen et al., 2013; Lena et al., 2014). An offset in the centroid position was previously reported in Calore et al. (2015b); Linden et al. (2016), while other studies of the GC excess have found it to be consistent with Sgr A*.

We investigate the centroid position of the excess by scanning the ML for different locations near Sgr A*, for each of the four IEMs. A power-law with exponential cut-off is employed for the spectral model, following Ajello et al. (2016). The scan is performed by making the ML fit following Sec. 3.2 with the DM template centered at each point of a grid with spacing $0.2°$ centered on Sag A*. The results of the scan are shown in Fig. 3.1, where the color scale shows the $2\Delta\mathrm{logL}$ as a function of Galactic latitude and longitude. The intersections of the dotted grid lines correspond to the points where the likelihood is evaluated. The circle indicates the position of Sgr A*, and the triangle is the most

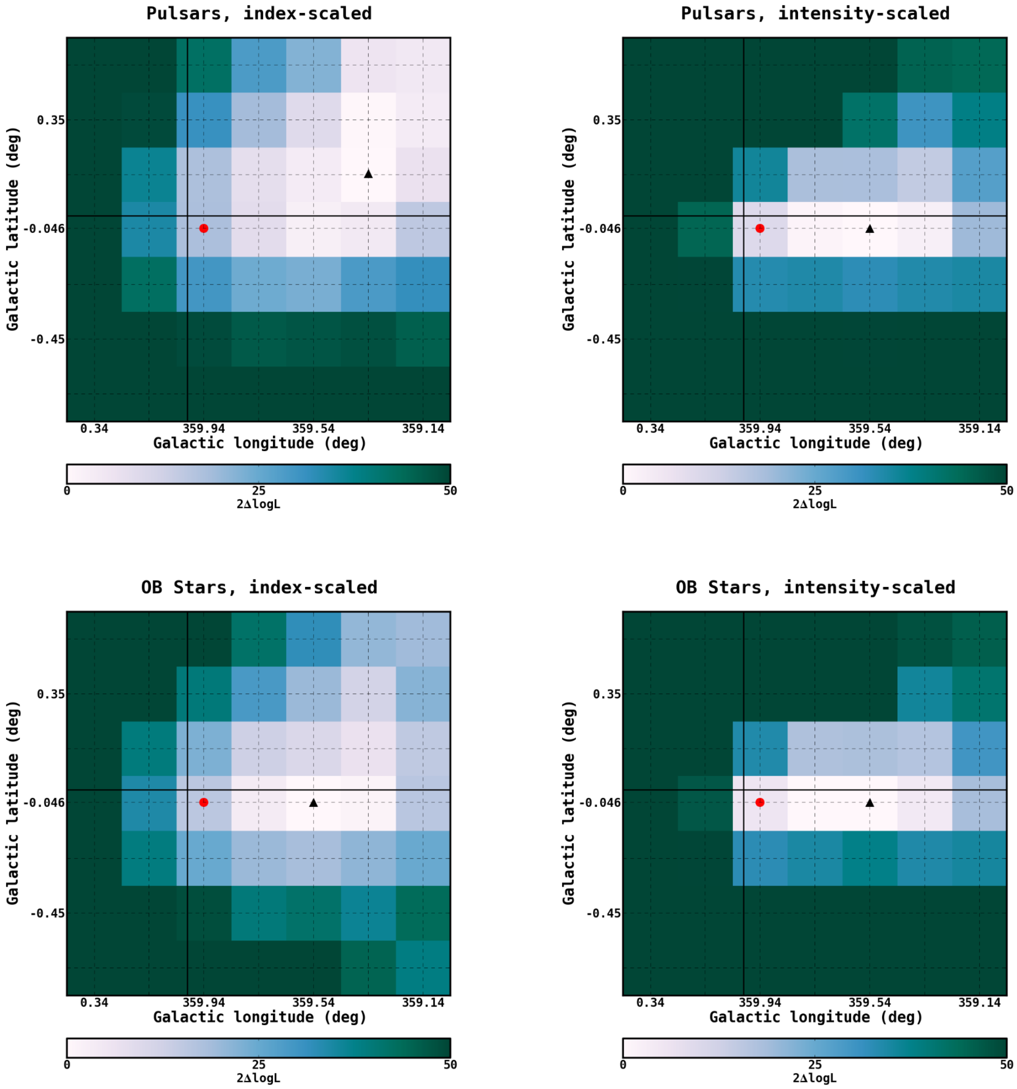

Figure 3.1 2Δlog Likelihood as a function of the centroid position of the NFW template, as described in the text. The results are shown for each of the four considered IEMs, as indicated. The triangle and the circle indicate the position of the ML and of Sag A*, respectively.

likely position of the centroid for that IEM. We find that the centroid position is offset from Sgr A* for all four IEMs, with the *Pulsars, index-scaled* model displaying the largest offset, both in longitude (0.6°) and latitude (0.2°). The other three models prefer an offset only in longitude (within 0.4° up to the grid accuracy). Based on the scan, Sgr A* is not favored as the location of the NFW centroid for all four IEMs, however its position is roughly consistent with a DM interpretation for the GC excess and imperfections in the IEMs could plausibly introduce an offset. We therefore assume for the remainder of this paper that the DM distribution is centered at Sgr A*.

3.3.3 Multiple Component Fit

Table 3.1 Results for the multiple component fit for the *Pulsars, intensity-scaled* IEM.

Fit components (1+2)	log L	2Δlog L
NFW + NFW	-82870	844
NFW + Gas template	-82942	700
NFW + 1° Gauss	-82968	648
NFW + 2° Gauss	-82932	720
NFW + 5° Gauss	-82951	682
NFW + 10° Gauss	-82950	684
NFW only	-82990	604
Null hypothesis	-83292	–

Table 3.2 Results for the multiple component fit for the *OB stars, intensity-scaled* IEM.

Fit components (1+2)	log L	2Δlog L
NFW + NFW	-82972	914
NFW + Gas template	-83068	722
NFW + 1° Gauss	-83096	666
NFW + 2° Gauss	-83065	728
NFW + 5° Gauss	-83147	564
NFW + 10° Gauss	-83111	636
NFW only	-83099	660
Null hypothesis	-83429	–

Whether the high-energy tail ($>$ 10 GeV) of the GeV excess spectrum is related to that at lower energies remains an open issue. In Ajello et al. (2016), the excess emission above 10 GeV is most prominent in the intensity-scaled IEMs. For the index-scaled variants however, it is largely attributed to interstellar emission (see also Daylan et al. (2016)). The origin of the $>$ 10 GeV excess has been previously investigated by several studies. In Horiuchi et al. (2016), the excess emission above 10 GeV is found to cut off in the innermost few degrees about the GC (unlike the excess at a few GeV) and therefore to have a different spatial morphology; secondary emission from unresolved millisecond pulsars is proposed as an interpretation. In Linden et al. (2016), the excess emission above 10 GeV is found to have a similar radial profile as the peak emission. Linden et al. (2016) also discusses the interplay with the Fermi Bubbles, although the bubble morphology close to the Galactic plane is uncertain.

Here we investigate the morphology of the $>$ 10 GeV excess emission present for the *Pulsars* and *OB stars, intensity-scaled* IEMs. We perform a ML fit over the 1-100 GeV energy range with two components to model the GC excess: an NFW template; and a second component that has either an NFW, gas, or a 2D gaussian (with half-width, half maximum of 1°, 2°, 5°, or 10°) morphology. These are the same templates that were employed by Ajello et al. (2016). Six template combinations for the two intensity-scaled models are therefore tested. The spectrum for each template is modeled as a power law with an exponential cutoff function. The ML fit is performed iteratively, as described in section 3.2, and the results are shown in Tables 3.1 and 3.2 for the *Pulsars* and *OB stars, intensity-scaled* IEM, respectively. The NFW + NFW combination is favored over all of the others considered, for both IEMs.

In Fig. 3.2 the differential fluxes integrated over the $15^\circ \times 15^\circ$ region for the two component fits, along with the fractional residuals, are shown for the *Pulsars, intensity-scaled* model. The contribution to the flux from each of the two spatial components and the IEM are shown, with the IEM broken down into the contributions from inverse Compton (IC), π^0 emission from the inner ~ 1 kpc ("ring 1" in the legend), and from the point sources. For each of the six combinations we consider, the low energy excess is better described by an NFW morphology. The more peaked 2D gaussian templates (1° and 2°) have spectra that peak in the few GeV energy range and cutoff at higher energies. Note that their contribution is always well below the contribution assigned to the NFW template. On the other hand, the spectra for the broader 2D gaussian templates (5° and 10°) are more prominent at higher energies, suggesting that the high-energy tail of the GeV excess is consistent with an extended component in the region. The NFW morphology, which is peaked towards the GC and broadly extended in the region, is better suited to model the excess emission over the full energy range compared to the other options we have considered. However, due to the limitations of the IEMs together with the limited statistics at the higher energies, it is difficult to conclude decisively whether or not the high-energy tail is a true feature of the GC excess. Given the current preference for a single NFW morphology for both low and high energy components, we include the full energy range when comparing with the DM scenarios in Section 3.4 below.

3.4 Dark Matter Interpretation

In this section we fit the parameters of particle physics models of DM, together with the parameters describing the fore-/backgrounds, extracting a comprehensive DM interpretation of the GC excess. As described in more detail below, we employ a parameterization of the DM particle physics model which allows for distinct annihilation rates into up-type quarks, down-type quarks, and leptons. Our parametrization has more flexibility than the often-considered annihilation into a single channel of SM particles and, in this sense, is better able to capture a wider array of realistic particle physics models for DM annihilation than those typically used in indirect searches.

3.4.1 EFT Description of Dark Matter Interactions

We consider two representative EFTs that describe the DM interactions with the SM fermions. These theories form part of a universal set of operators to which any theory of DM flows at low energies, well below the masses of the particles responsible for communicating between the SM and the dark matter (Beltran et al., 2009; Cao et al., 2011; Beltran

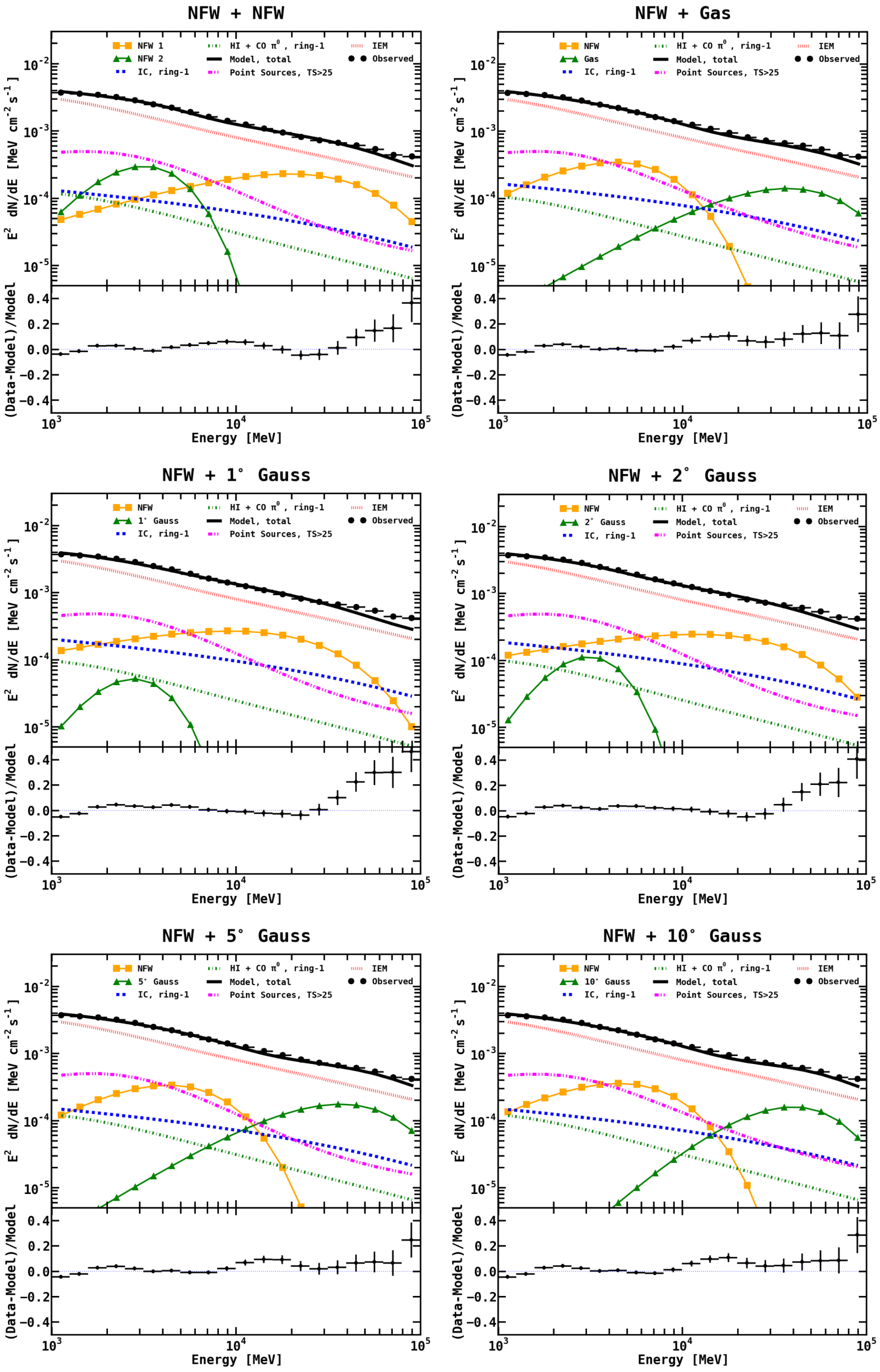

Figure 3.2 Differential fluxes (broken down into components, as indicated) integrated over the 15° × 15° region for the two component fits, along with their fractional residuals, for the *Pulsars, intensity-scaled* IEM.

et al., 2010; Goodman et al., 2010, 2011; Kumar & Marfatia, 2013). Such models have previously been considered to describe the GC excess (Alves et al., 2014; Liem et al., 2016). More generalized constructions are employed here, and their parameters are fit together with the IEM parameters as described in Section 3.2. Of course, models with light mediators are also interesting, and worthy of investigation in their own right (Boehm et al., 2014; Abdullah et al., 2014; Martin et al., 2014; Berlin et al., 2014; Balzs & Li, 2014; Ko & Tang, 2015; Fortes et al., 2016; Carpenter et al., 2016; Escudero et al., 2016). We leave exploration of such theories for future work.

Both of our considered EFTs are chosen such that they mediate s-wave (velocity-unsuppressed) annihilation, because a p-wave annihilation mechanism would require such strong interactions to overcome the innate $v^2 \sim 10^{-4}$ suppression that it is likely to already be ruled out by direct and/or collider searches. We further restrict them to follow the principle of minimal flavor violation (MFV), such that the most stringent constraints from flavor-violating observables are mitigated by small Yukawa interactions. We consider models containing either pseudo-scalar or vector Lorentz structures described by Lagrangians $\mathcal{L}_{\rm ps}$ and $\mathcal{L}_{\rm vec}$ (respectively, in the fermion mass basis),

$$\mathcal{L}_{\rm ps} = \overline{\chi}\gamma_5\chi \times \sum_i \left\{ \frac{m_{u_i}}{\Lambda_u^3}\,\overline{u}_i\gamma_5 u_i + \frac{m_{d_i}}{\Lambda_d^3}\,\overline{d}_i\gamma_5 d_i + \frac{m_{\ell_i}}{\Lambda_\ell^3}\,\overline{\ell}_i\gamma_5\ell_i \right\}, \tag{3.2}$$

$$\mathcal{L}_{\rm vec} = \overline{\chi}\gamma^\mu\chi \times \sum_i \left\{ \frac{1}{\Lambda_u^2}\overline{u}_i\gamma_\mu u_i + \frac{1}{\Lambda_d^2}\overline{d}_i\gamma_\mu d_i + \frac{1}{\Lambda_\ell^2}\overline{\ell}_i\gamma_\mu\ell_i \right\}, \tag{3.3}$$

where $i = 1, 2, 3$ is the sum over fermion flavor with the indicated relative weighting of m_{f_i} (1) for the pseudo-scalar (vector) interaction types, as dictated by the leading terms consistent with MFV. The $\Lambda_{u,d,\ell}$ are parameters with dimensions of energy which specify the separate interaction strengths between the DM and up-type quarks, down-type quarks, and charged leptons. Together with the DM mass, m_χ, these coefficients specify the point in parameter space for the DM model. They represent generalizations (in that they allow the couplings of up-type and down-type quarks and leptons to vary independently) of the commonly considered interactions D4 and D5 used in DM searches via direct detection and at colliders (Goodman et al., 2010).

3.4.2 γ-ray Flux from Dark Matter Annihilation

The interactions in both the pseudo-scalar and vector models defined in Eqs. (3.2,3.3) lead to cross sections for a pair of DM particles to annihilate $\chi\overline{\chi} \to f\overline{f}$ (where f is any SM fermion):

$$\langle \sigma_f v \rangle_{\rm ps} \;=\; \frac{N_f m_f^2 m_\chi^2}{\Lambda_f^6 \pi} \sqrt{1 - \frac{m_f^2}{m_\chi^2}} + \mathcal{O}(v^2), \tag{3.4}$$

$$\langle \sigma_f v \rangle_{\rm vec} \;=\; \frac{N_f (2m_\chi^2 + m_f^2)}{\Lambda_f^4 \pi} \sqrt{1 - \frac{m_f^2}{m_\chi^2}} + \mathcal{O}(v^2), \tag{3.5}$$

where $\langle \cdot \rangle$ indicates averaging over the DM velocity profile, $N_f = 3$ (1) for quarks (leptons) counts their color degrees of freedom, and Λ_f is the appropriate $\Lambda_{u,d,\ell}$ for the fermion under consideration. The inclusive cross section for annihilation into up-type quarks, down-type quarks, and charged leptons is the sum of the individual cross sections for all three flavors of each fermion type, and the total cross section $\langle \sigma v \rangle$ is the sum of the three inclusive cross sections. In presenting results, we typically trade the three parameters $\Lambda_{u,d,\ell}$ for $\langle \sigma v \rangle$ and the fractional cross sections f_u, f_d, and f_ℓ (with $f_u + f_d + f_\ell = 1$). It is easy to map these back into the $\Lambda_{u,d,\ell}$ parameters using the appropriate single channel cross section from Eqs. (3.4) and (3.5).

The γ-ray intensity and spectrum from DM annihilation is constructed by summing over all of the annihilation channels:

$$\frac{dN_\gamma}{dE} = \sum_f \frac{\langle \sigma_f v \rangle}{4\pi\eta\, m_\chi^2} \frac{dN_\gamma^f}{dE} \times \int_{\Delta\Omega} d\Omega' \int_{los} ds\, \rho^2(r(s,\psi)), \tag{3.6}$$

where dN_γ^f/dE is the number of γ rays per annihilation into the $f\overline{f}$ channel, generated from the PPPC 4 DM ID package (Cirelli et al., 2011) based on fits to Pythia 8.1 (Sjostrand et al., 2008), and η = 2(4) for Majorana (Dirac) DM. The integral is the *J*-factor, obtained by integrating the DM density $\rho^2(\vec{x})$ corresponding to either an NFW or NFW-c distribution, Eq. (A.1), over the line of sight (los) in direction ψ.

To determine the preferred DM model parameters for each IEM, we fix the DM mass in the range from 10 – 250 GeV in 10 GeV increments. For each mass hypothesis the analysis procedure of Section 3.2 determines the fitted values of the DM model parameters f_u, f_d, and f_ℓ, along with the coefficients of the interstellar emission components from within the innermost $\sim$1 kpc and point sources, as usual. We repeat this scan for both NFW and NFW-c annihilation morphologies and for both the pseudo-scalar and vector models described above. We find that the DM component is detected with high statistical significance for all IEMs, and for pseudo-scalar as well as vector interactions. The likelihood values for pseudo-scalar interactions are summarized in Table 3.3.

Table 3.3 Likelihood (log L) values for all IEMs for pseudo-scalar interactions and for NFW and NFW-c templates.

IEM	log L (null hypothesis)	log L (NFW)	log L (NFW-c)
Pulsars, index-scaled	-82926	-82738	-82739
Pulsars, intensity-scaled	-83292	-82965	-82956
OB stars, index-scaled	-82993	-82779	-82806
OB stars, intensity-scaled	-83429	-83081	-83117

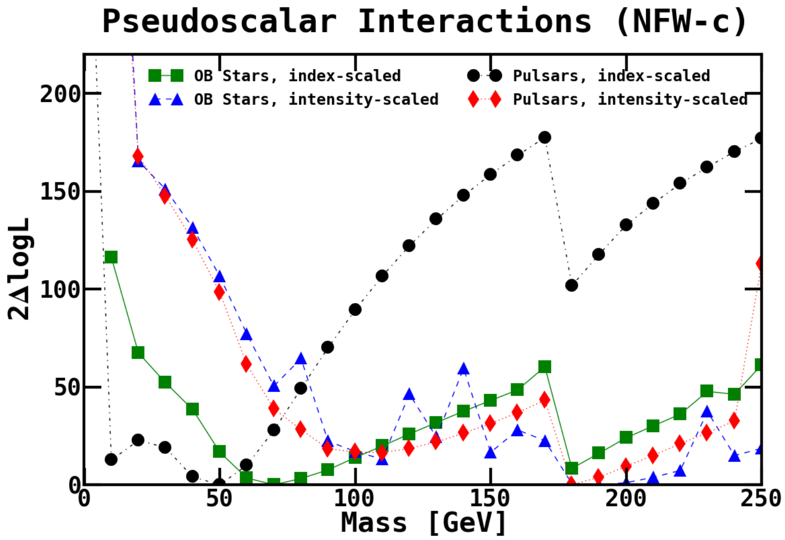

Figure 3.3 Likelihood (2ΔlogL) as a function of the DM mass for the pseudo-scalar interaction model with NFW-c morphology. Results are shown for all four IEMs, as indicated.

3.4.3 Results for Pseudo-scalar Interactions

In Fig. 3.3, we display the likelihood profile as a function of the DM mass for each of the IEMs for the NFW-c annihilation morphology. The results for the NFW morphology are qualitatively similar. Each of the four IEMs shows a clear preference for particular DM masses, but there is considerable variation between them, with the index-scaled models favoring a mass around $\sim$ 50 GeV, while the intensity-scaled models favor higher masses $\sim$ 200 GeV. The results are consistent with the results obtained by Ajello et al. (2016), where the spectrum of the GC excess for the index-scaled IEMs displays a lower energy cutoff compared to the intensity-scaled IEMs. The spectra we consider here correspond to motivated DM scenarios, in contrast with the simpler assumptions made for the spectral model by Ajello et al. (2016).

In Fig. 3.4, we present the ML fractions into the three annihilation channels as a function of the DM mass, for each of the IEMs with the NFW-c annihilation morphology. These also vary considerably from one IEM to another, and are characterized by one channel or another typically dominating at any given DM mass hypothesis: charged leptons at lower masses $\sim 10-20$ GeV; down-type quarks in the range $\sim 50-170$ GeV; and up-type quarks above 180 GeV

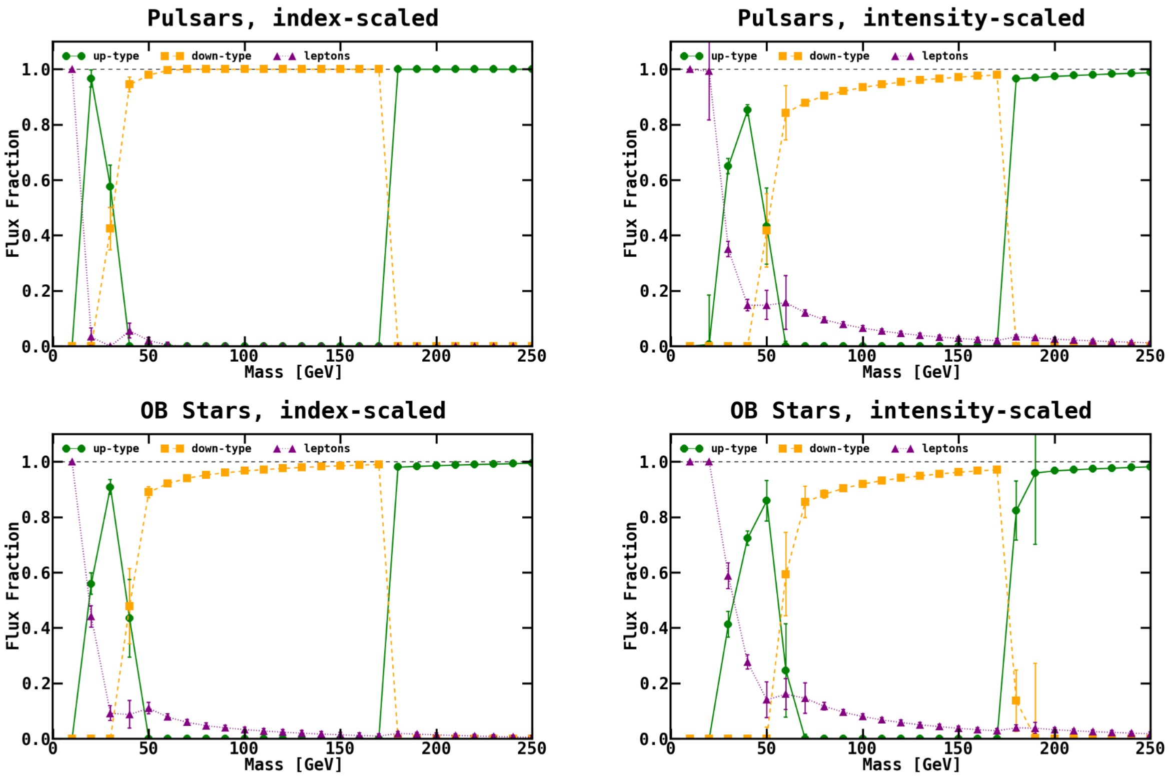

Figure 3.4 Flux fraction for annihilation into up-type quarks, down-type quarks, and charged leptons, for the pseudo-scalar interaction model with NFW-c morphology. Results are shown for all four IEMs, as indicated.

and at lower masses $\sim 20-40$ GeV. The lepton flux declines steeply above ~20 GeV, and its contribution to the flux is smaller for the index-scaled models (*Pulsars* in particular) compared to the intensity-scaled ones. This reflects in part the lower energy cutoff of the GC excess spectrum for the index-scaled models and the harder γ-ray spectra produced by charged leptons compared to quarks. Also of note is the sharp transition from annihilation into down-type quarks to up-type quarks at the top mass threshold, ~ 175 GeV. This follows because the pseudo-scalar model annihilations are dominated by the heaviest quark kinematically accessible, and top quarks produced close to at rest decay into ~ 60 GeV bottom quarks, corresponding to the ML region at $m_\chi \sim 50$ GeV.

The best-fit DM mass for the *Pulsars* (*OB stars*) index-scaled IEM is 50^{+10}_{-10} GeV (70^{+15}_{-10} GeV), and in both cases annihilation is predominantly into bottom quarks[3]. These results are compatible with the findings of previous studies (Agrawal et al., 2015; Balzs & Li, 2016) interpreting the spectrum of the excess as presented in Ajello et al. (2016). The intensity-scaled IEMs favor higher DM masses, 180^{+15}_{-5} GeV and 190^{+25}_{-15} GeV, for the *Pulsars* and *OB stars* variants, respectively, and primarily favor annihilation into top quarks. We note that the likelihood profile for the *OB stars, intensity-scaled* IEM is rather flat around the minimum, which yields a higher uncertainty in the best-fit DM mass, compared to the other IEMs. The uncertainties on the flux fractions into up-type and down-type quarks in this

---

[3] The grid spacing is taken into account in the quoted uncertainties on the DM mass.

mass range are also somewhat larger.

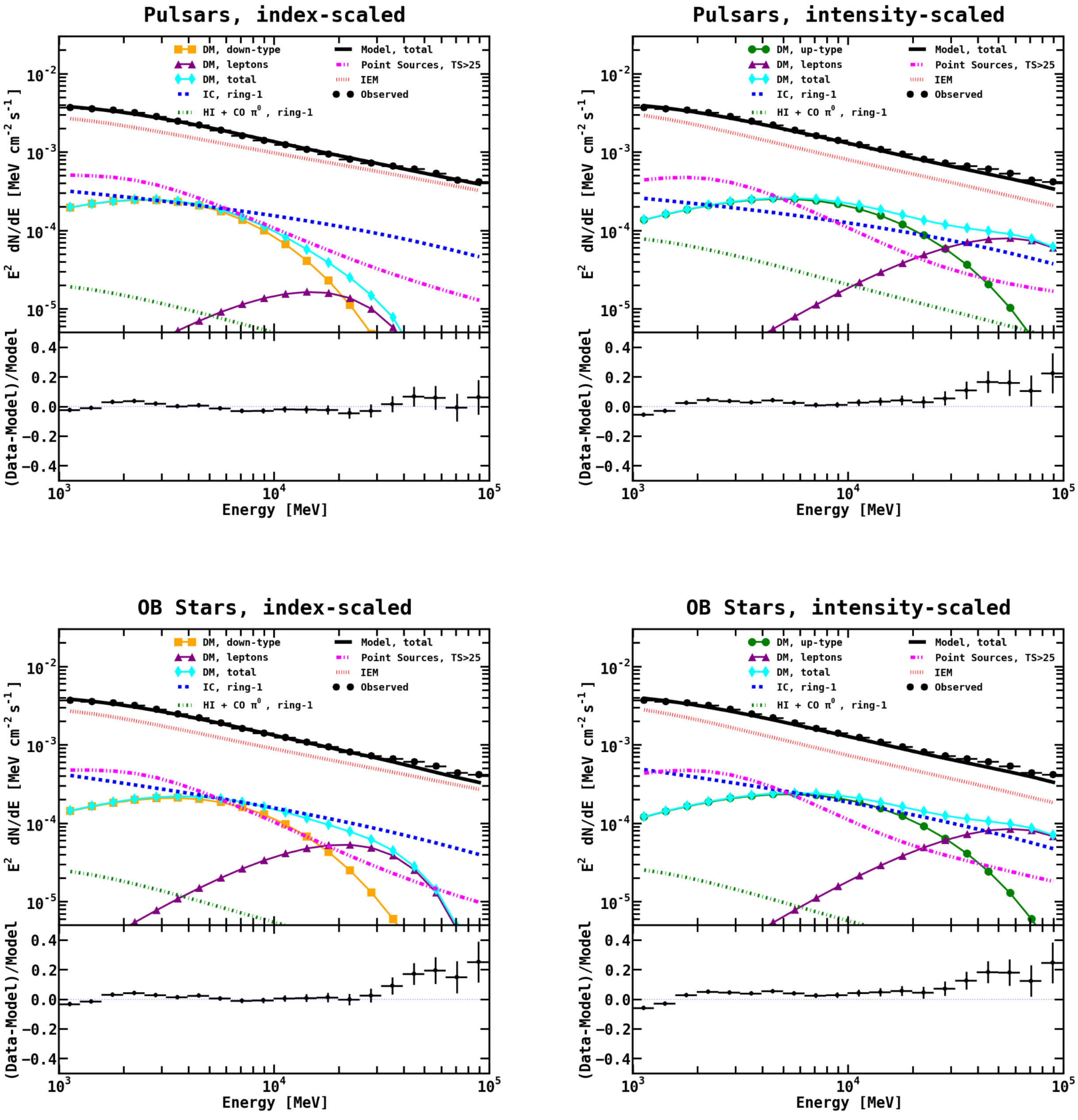
Pulsars, index-scaled

Pulsars, intensity-scaled

OB Stars, index-scaled

OB Stars, intensity-scaled

Figure 3.5 Differential fluxes (broken down into components, as indicated) integrated over the $15° \times 15°$ region and corresponding fractional residuals for pseudo-scalar interactions and for the four IEMs.

The differential fluxes for the ML model (and the data points) are shown for each IEM in Fig. 3.5. Individual model components are displayed separately, including the contribution to the DM flux from each annihilation final state, as well as their sum. The contribution from each DM annihilation channel illustrates the fact that the integrated DM flux originates primarily from annihilations into quarks with the harder spectrum from annihilation into leptons becoming

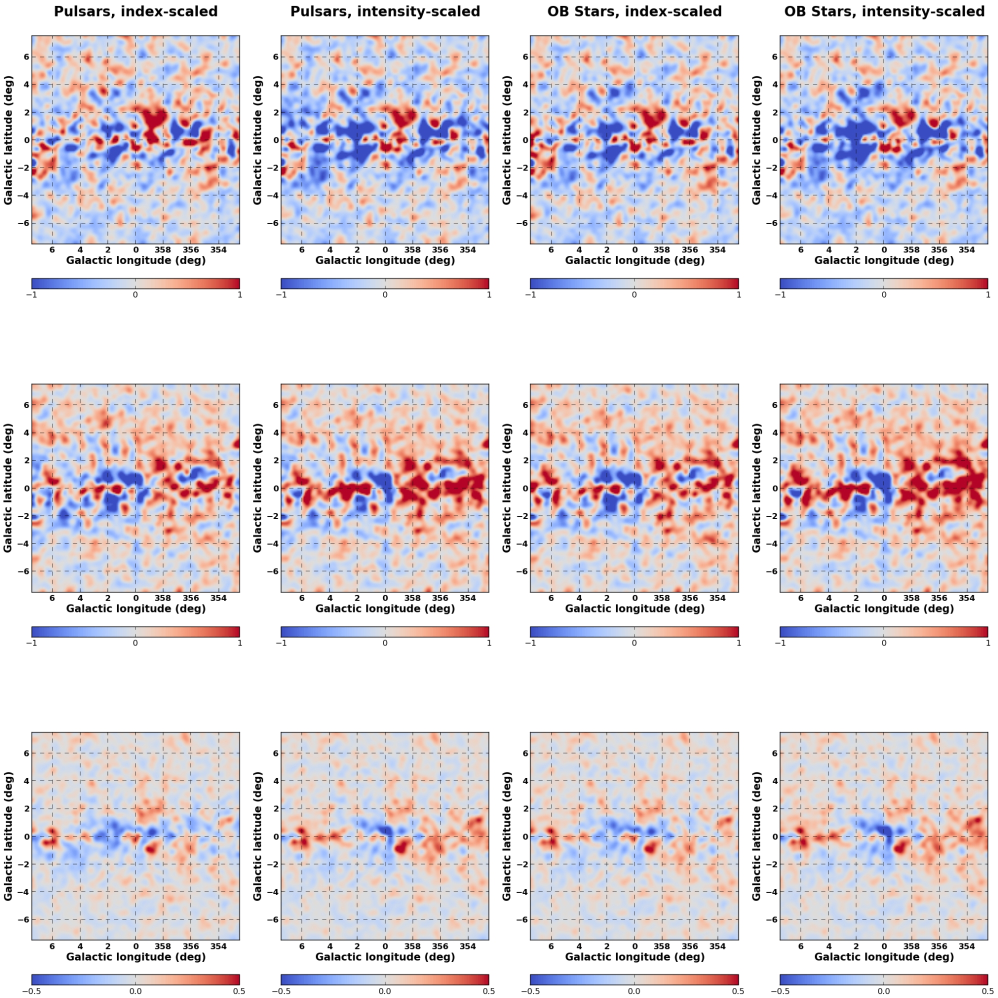

Figure 3.6 Residuals (data – model) in three energy bands, for the four IEMs. The rows correspond to the range 1 - 1.6 GeV (top), 1.6 - 10 GeV (center), and 10 - 100 GeV (bottom). The columns, going from left to right are: *Pulsars, index-scaled*; *Pulsars, intensity-scaled*; *OB stars, index-scaled*; *OB stars, intensity-scaled*.

important at higher energies, particularly for the intensity-scaled IEMs. The γ-ray emission correlated with gas from the innermost $\sim$1 kpc is sub-dominant in the region. Fig. 3.5 also shows the fractional residuals as a function of energy. The agreement between data and model is at the level of a few % or better up to $\sim$ 30 GeV for all IEMs, and is generally worse at higher energies for all but the *Pulsars, index-scaled* IEM. It is plausible that the energy cutoff at the DM mass in the annihilation spectrum limits its ability to describe the excess at the higher energies while simultaneously providing a good fit to the data in the few GeV range. We note that the fractional residuals based on realistic DM models including up-type, down-type, and lepton final states generally improve (for the same number of free parameters) over the results in Ajello et al. (2016) based on a power law with exponential cutoff spectrum.

Residual count (data-model) maps are shown in Fig. 3.6 for the energy bands $1 - 1.6$, $1.6 - 10$, and $10 - 100$ GeV, for each IEM. Structured excesses and deficits remain that may be attributed to imperfect modeling of the interstellar

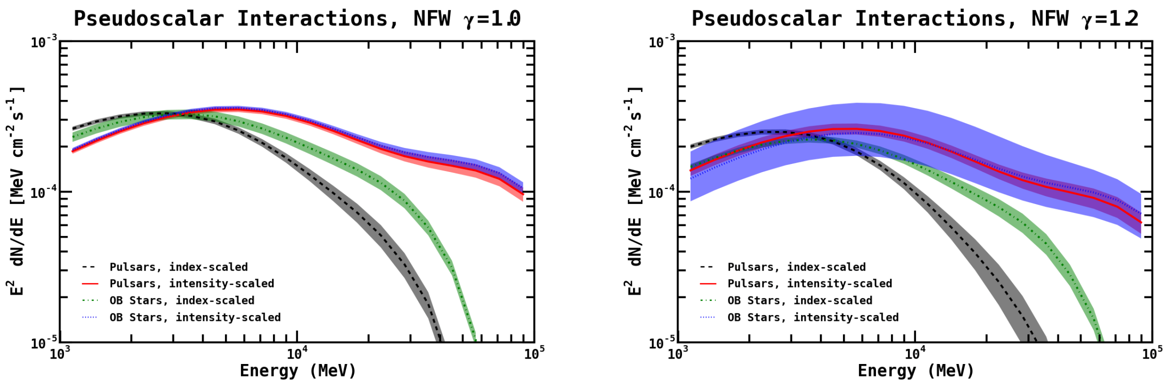

Figure 3.7 Differential flux integrated over the 15° × 15° region for the DM component for pseudo-scalar interactions, NFW and NFW-c profiles, for all four IEMs, as indicated. The bands represent the fit uncertainties on the normalization.

emission. Because of this, we do not rule out the DM models corresponding to IEMs with larger fractional residuals as these discrepancies might be explained by limitations in the IEMs. There is better agreement with the data when the DM spectrum is modeled with power law functions in 10 independent energy bins as done in Ajello et al. (2016); perhaps unsurprising given the larger number of free parameters for the spectral model.

The differential flux from the total DM annihilation component for both profiles (NFW, NFW-c) and all four IEMs are summarized in Fig. 3.7. The bands represent the 1σ fit uncertainty on the flux summing the up-type, down-type, and lepton final states. For the index-scaled variants of the IEMs, the spectrum peaks at a few GeV, while for the intensity-scaled counterparts the peak shifts to higher energies. This is consistent with the requirement that the high energy tail in the spectrum for the intensity-scaled IEMs, predominantly from annihilations into leptons, has to cutoff at the same energy (corresponding to the DM mass) as the contribution to the flux from annihilations into up-type and down-type quarks, which dominate the DM flux at lower energies. Finally, we note that the flux for NFW-c profile is smaller compared to the NFW profile. As a consequence, a simple rescaling based on $J-$factors when comparing fit results obtained with different profiles is not accurate, as the flux assigned to the DM component has a dependence on the specific morphology.

We translate the DM template flux for each IEM into the inclusive annihilation cross section, with the results shown in Fig. 3.8. Also shown for comparison is the $\langle\sigma v\rangle$ predicting saturation the measured DM relic density for a standard cosmology (Steigman et al., 2012). The results for the index-scaled models are comparable to those found in most of the earlier studies of the GeV excess (Hooper & Goodenough, 2011; Abazajian & Kaplinghat, 2012; Hooper & Slatyer, 2013; Gordon & Macias, 2013; Huang et al., 2013; Abazajian et al., 2014; Zhou et al., 2015; Calore et al., 2015b; Abazajian et al., 2015; Calore et al., 2015a; Carlson et al., 2016; Daylan et al., 2016). The intensity-scaled

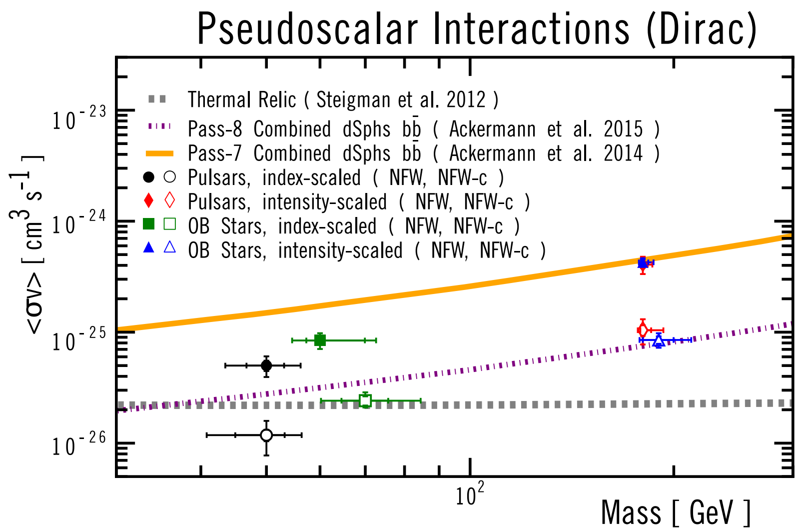

Figure 3.8 Masses and cross sections for pseudo-scalar interaction models (including one and two sigma uncertainties as the tick marks) for NFW and NFW-c DM profiles, and the four IEMs, as indicated. Also shown are the cross sections saturating the standard thermal relic density (grey dashed line) and the *Fermi*–LAT 95% C.L. bounds from dwarf spheroidal galaxies, for Pass–7 as well as Pass–8 data, assuming 100% annihilation into $b\bar{b}$.

models however are consistent with larger DM masses and cross sections, as first discussed in Agrawal et al. (2015), based on the spectra from Ajello et al. (2016).

3.4.4 Results for Vector Interactions

The analysis for the vector-type DM interactions proceeds very similarly to the analysis of the pseudo-scalar interactions described above. For each IEM and both NFW and NFW-c morphologies, the DM mass is scanned and the couplings to up-type quarks, down-type quarks, and charged leptons is fit. The results are presented in Figs. 3.9 and 3.10, respectively, for each IEM with the NFW-c profile (the results for the NFW profile are qualitatively similar.) Similarly to pseudo-scalar interactions, lower DM masses are favored by the index-scaled IEMs, compared to the intensity-scaled. However, in general, lower DM masses are favored for the vector interaction models than for the pseudo-scalar ones for the same IEM. In addition, because the coupling to SM fermions is assumed to be flavor-universal for the vector interaction model, there is no sharp transition in behavior at the top quark mass. For the *Pulsars, index-scaled* IEM, there are two close-to-degenerate minima in the likelihood profile, with the lower mass dominated by annihilations into leptons[4]. The fitted values of $\langle \sigma v \rangle$ and the DM mass for each of the IEMs and DM profiles are shown in Fig. 3.11.

---

[4] For annihilations into leptons, secondary γ-ray emission via IC processes is neglected. Note that for DM masses $\lesssim$ 10 GeV, IC photons are mainly produced at energies $<$ 1 GeV Cirelli et al. (2013b); Lacroix et al. (2014).

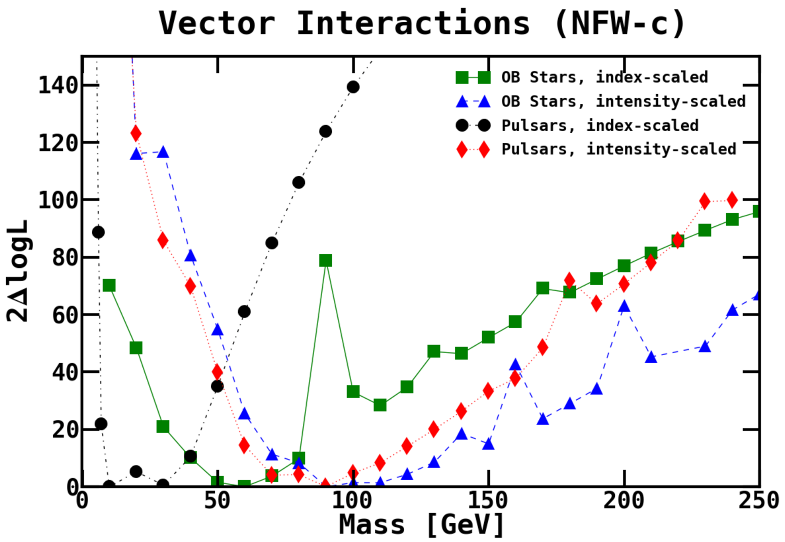

Figure 3.9 Likelihood (2ΔlogL) as a function of the DM mass for the vector interaction model with NFW-c morphology. Results are shown for all four IEMs, as indicated.

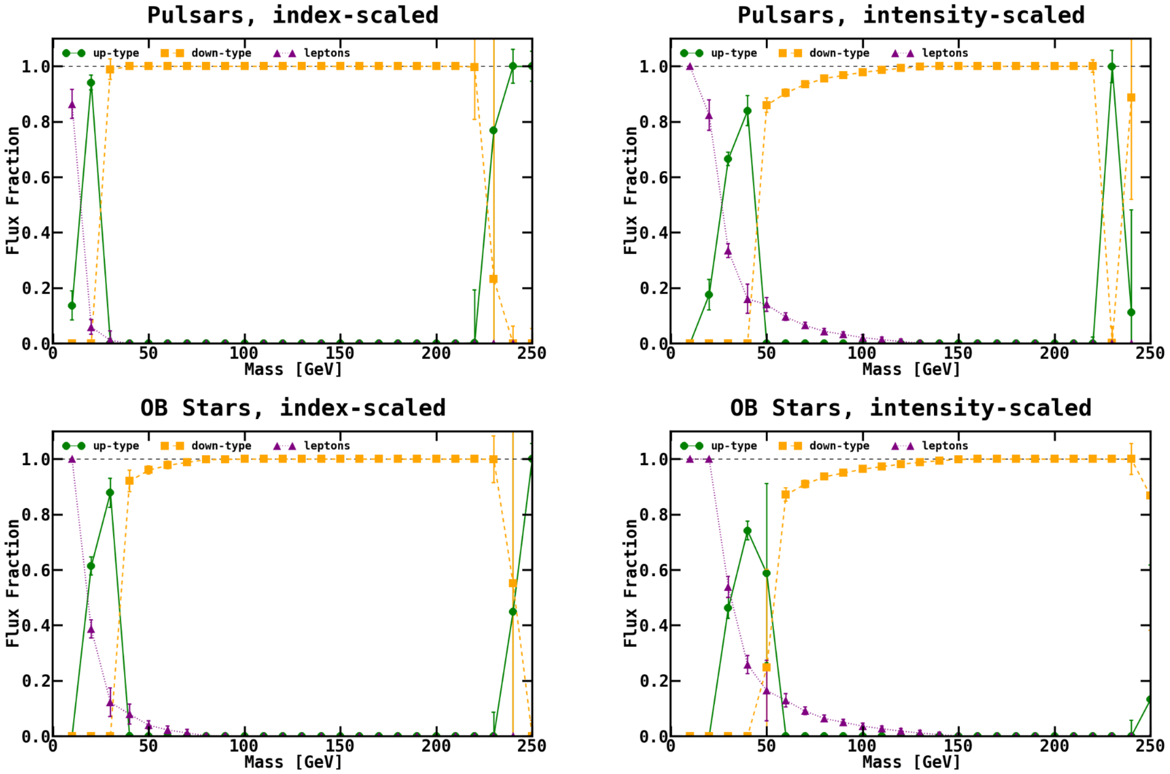

Figure 3.10 Flux fraction for annihilation into up-type quarks, down-type quarks, and charged leptons, for the vector interaction model with NFW-c morphology. Results are shown for all four IEMs, as indicated.

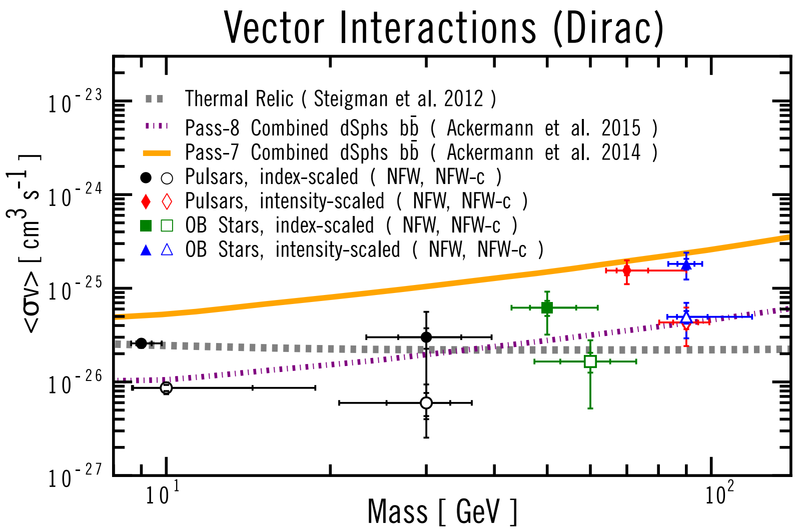

Figure 3.11 Masses and cross sections for vector interaction models (including one and two sigma uncertainties) for NFW and NFW-c DM profiles, and the four IEMs, as indicated. Also shown are the cross sections saturating the standard thermal relic density (grey dashed line) and the *Fermi*–LAT 95% C.L. bounds from dwarf spheroidal galaxies, for Pass–7 as well as Pass–8 data, assuming 100% annihilation into $b\bar{b}$.

3.5 Comparison with Other Searches

As seen in sections 3.4.3 and 3.4.4, DM interpretations of the GC excess cover a broad range of masses ($\sim 10-200$ GeV) and $\langle\sigma v\rangle$, depending on the IEM, DM profile, and interaction type. One crucial avenue toward exploring a DM hypothesis for the excess is to compare the regions of parameter space best describing the excess with the results from other searches for DM. Null results of such searches can sharpen the target parameter space or even exclude candidate explanations, whereas positive results could strengthen a DM interpretation of the excess and better define the characteristics of candidate models.

3.5.1 Indirect Searches

For masses in the range $10-200$ GeV, the strongest constraints from indirect detection are generally from *Fermi*–LAT observations of dwarf spheroidal galaxies (Geringer-Sameth & Koushiappas, 2011; Ackermann et al., 2014, 2015a). These limits appear to constrain the region relevant for explanations of the GC excess[5], but are derived from less theoretically motivated DM annihilation models where the DM annihilates into one species of SM fermion at a time. As such, they do not precisely apply to the models considered here, although similar conclusions are likely. The

---

[5] Note that an excess from the Reticulum II dwarf galaxy has been claimed Geringer-Sameth et al. (2015). We find that our interpretation of the GC excess is not in conflict with this observation.

bound based on the assumption of 100% annihilation into $b\bar{b}$, corrected to account for Dirac (rather than Majorana) DM particles, is shown on Figures 3.8 and 3.11 for reference. The dwarf spheroidal bounds for annihilations into leptons are not displayed in these figures. Although they would in principle be more pertinent to constrain our low mass, vector interaction results, they are still not adequate as the final state channel we consider here is an equal weight mixture of e^+e^-, $\mu^+\mu^-$, $\tau^+\tau^-$ and therefore not directly comparable.

The limitations in the IEMs, modeling uncertainties in the dwarf halos (Hayashi et al., 2016; Bernal et al., 2016; Ichikawa et al., 2016; Klop et al., 2016), modifications to the particle physics model for DM (Kopp et al., 2016), and large uncertainties in the *J*-factor for the GC (Abazajian & Keeley, 2016), all widen the relative uncertainties when confronting the parameters describing the GC excess with the limits from observations of dwarf spheroidal galaxies. Because of this, care must be taken when contrasting these limits with a DM interpretation of the GC excess.

The particle physics models under consideration also lead to annihilations producing anti-matter, such as positrons or anti-protons. Positrons in particular show excess production compared to naive expectations (Adriani et al., 2009; Aguilar et al., 2013), leading to limits which do not significantly constrain the parameters for the GC excess (Bergstrom et al., 2013). Recently Cuoco et al. (2016) (see also Cui et al. (2016)) performed a detailed analysis of the anti-proton spectrum measured by AMS-02 (Aguilar et al., 2016), and also found an indication for an excess component roughly consistent with the parameter space describing a DM interpretation of the GC excess (see Giesen et al. (2015) for a less optimistic view). The interpretation of CR anti-matter measurements is complicated by propagation, energy losses, and other modeling uncertainties related to particle fragmentation, as well as the spatial distribution of astrophysical sources. Consequently, the interpretation of these data in terms of DM is unclear.

3.5.2 Direct Searches

Coupling to quarks implies coupling to hadrons, and thus is bounded from direct searches for DM scattering with heavy nuclei. Models with pseudo-scalar interactions map onto a scattering cross section which is both suppressed by the small velocities of DM in the Galactic halo and are also spin-dependent. As a result, the expectation is that the null results of direct searches yield mild constraints which are roughly v^2 smaller than the constraints on $\sigma_{\rm SD}$ quoted by e.g. IceCube (Aartsen et al., 2017). In contrast, vector interactions lead to velocity-unsuppressed spin-independent scattering and are strongly constrained by direct searches. For the vector models, which contribute to the spin-independent cross section $\sigma_{\rm SI}$, we follow the usual convention mapping onto this quantity defined at zero relative velocity. For pseudo-scalar interactions, we compute the integrated cross section for DM scattering with a nucleon by integrating over the recoil energy of the nucleus and the velocity of the DM, which we assume follows

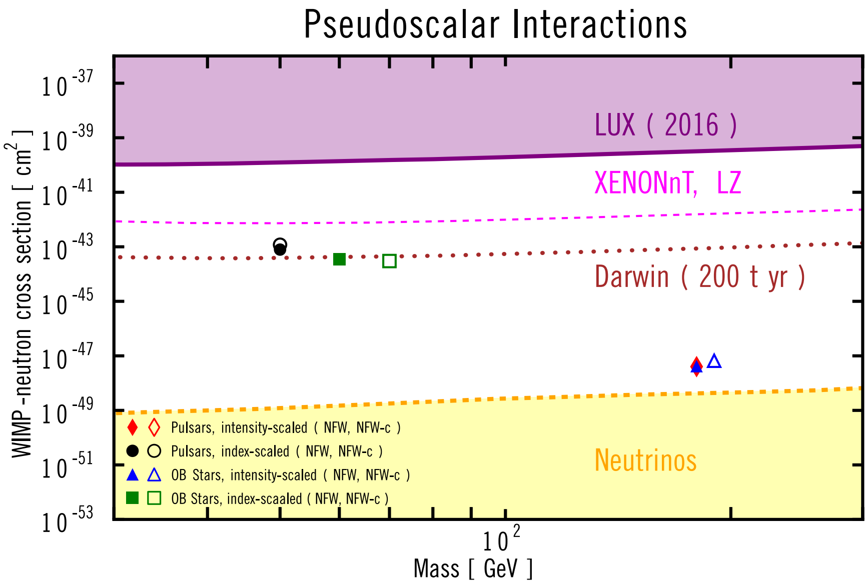

Figure 3.12 ML points for the pseudo-scalar models, for each IEM and profile considered, as indicated, mapped into the plane of the DM mass and the integrated cross section, as described in the text. Also shown are current constraints from LUX (upper shaded region) and projections from XENONnT, LZ, and Darwin (dashed and dotted lines). The lower shaded region indicates the neutrino floor.

a Maxwellian distribution, using techniques developed in Fitzpatrick et al. (2013); Cirelli et al. (2013a); Gresham & Zurek (2014); Anand et al. (2014), (specifically using the code presented in Cirelli et al. (2013a)). This integrated cross section should be distinguished from usual spin-dependent cross section $\sigma_{\rm SD}$, defined at zero velocity scattering, and is a more appropriate measure of scattering which is strongly velocity-dependent.

In Figs. 3.12 and 3.13, we show the ML points for the pseudo-scalar and vector models mapped into the WIMP-neutron spin-dependent integrated cross section, respectively, for each IEM and both NFW and NFW-c. For comparison, the limits from the LUX search for DM scattering with Xenon are presented (Akerib et al., 2016), also mapped into $\sigma_{\rm SI}$ or the integrated cross section for spin-dependent scattering with neutrons. For the vector models, the limits from LUX easily exclude all of the ML points except for the point with dark matter masses around 10 GeV which annihilates predominantly into leptons for the *Pulsars, index-scaled* IEM with NFW-c profile, which has sufficiently small coupling to quarks that the scattering with nuclei is highly suppressed. For the pseudo-scalar models, the predictions for the ML points lie well below below the LUX bounds, with the lower mass points potentially probed long-term by Darwin (Aalbers et al., 2016), while the higher mass points are slightly above the neutrino floor (Billard et al., 2014) and out of the reach of these experiments. These results illustrate the importance of the IEM modeling and its influence on characterization of the putative signal, which can lead to drastic differences in the expectations from complementary searches.

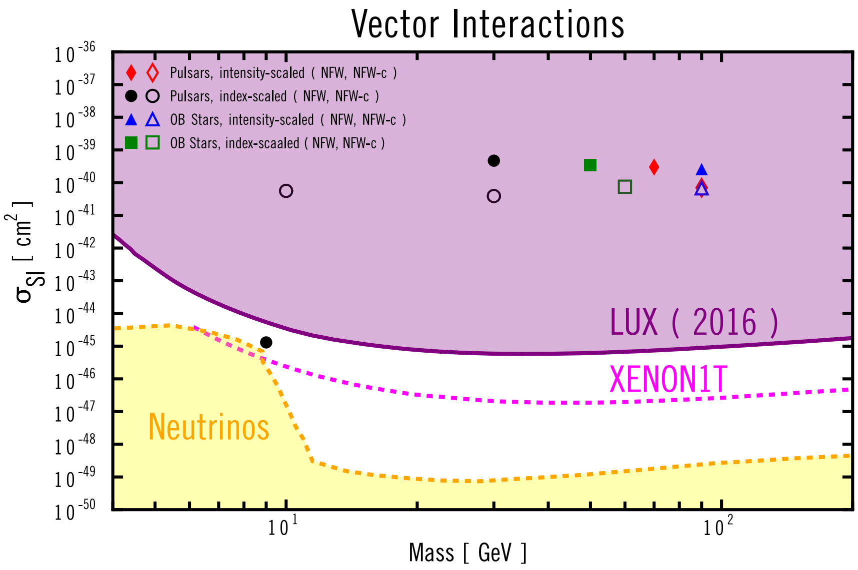

Figure 3.13 ML points for the vector models, for each IEM and profile considered, as indicated, mapped into the plane of the DM mass and σ_{SI}, as described in the text. Also shown are current constraints from LUX (upper shaded region) and projections from XENON1T (dashed line). The lower shaded region indicates the neutrino floor.

3.5.3 Collider Searches

Searches at the Large Hadron Collider (LHC) are more model-dependent, and can be classified based on the masses and couplings of the particles mediating the interaction. When such particles are heavy compared to the typical collider energies, they can be described by the same EFTs employed in this paper. The results of searches in this regime are typically not competitive with direct searches except at masses far below those of interest to describe the GC excess (Aad et al., 2013; Khachatryan et al., 2015). For lighter mediating particles, the limits depend sensitively on the specific couplings to the DM as well as to the SM fermions. In particular, for values of the cross sections similar to what has been found in past characterizations of the GeV excess, cases where a pseudo-scalar mediator's coupling to DM is significantly weaker than the coupling to quarks are mildly constrained by LHC data, and the opposite limit is essentially unconstrained (Fan et al., 2016). Given the wide range of parameter space (which is even larger for the specialized IEM analysis considered here), it seems possible that the LHC could eventually hope to observe an excess consistent with a pseudo-scalar mediator interpretation if parameters are favorable. Similar remarks apply to the vector mediator models, although all but the *Pulsars, index-scaled* IEM with NFW-c profile are already excluded by direct detection experiments. This latter model is consistent with vanishing coupling to quarks, and thus is unlikely to be excluded by searches at the LHC.

3.6 Summary

The excess of $\sim$ GeV γ-rays from the direction of the GC is an indication that there is something in the γ-ray sky beyond our current knowledge. Whether this source ultimately proves to originate from DM annihilation or from a more conventional astrophysical source still remains to be determined, and is likely to require further experimental input. As part of this process, we have examined key aspects of the putative signal using the specialized IEMs, developed by the *Fermi*–LAT Collaboration (Ajello et al., 2016). Our goal in characterizing potential DM explanations is to explore the implications from complementary searches, which can rule out or favor a DM interpretation.

Our results illustrate the impact of interstellar emission modeling on the extracted characteristics of the excess and highlight the need for improved modeling to capture a more realistic range of possibilities. As far as the gross characteristics of the excess are concerned, we find an offset of $\sim 0.5°$ of the excess centroid from Sgr A* for all four IEMs considered. We further find no significant evidence that the tail of the excess has a different spatial morphology than the few GeV bump, with both high energy and low energy components favoring an NFW morphology compared to the other morphologies we have considered.

We also consider flexible and realistic particle physics models for DM interacting with up-type quarks, down-type quarks, and charged leptons, for two separate interaction types (pseudo-scalar and vector) leading to s-wave annihilation. These theories are described by EFTs, valid when the momentum transfer is small compared to the masses of the particles mediating the interactions – to describe annihilation, this implies the mediators are heavier than the DM itself. We find that the choice of IEM has a large impact on the preferred DM mass, annihilation cross section, and primary annihilation channel. In particular, we identify regions with higher masses and annihilation predominantly into top quarks. Comparing the ML points in parameter space with direct and collider searches, we find that all of the vector models aside from one at DM mass ~ 10 GeV and annihilating into leptons are ruled out by null results from the LUX experiment. The pseudo-scalar models predict spin-dependent and velocity-dependent scattering with nuclei at a rate far below the current sensitivity, but in some cases within the grasp of future planned experiments. It would be interesting, but beyond the scope of this work, to extend our analysis beyond the EFT limit to the case of models where the DM can annihilate directly into the mediator particles themselves.

The GeV excess is a compelling hint that there is more to learn about the Galaxy. It is likely to take a combined effort of observation and interpretation to unravel its nature.

Chapter 4

Fermi-LAT Observations of γ-ray Emission Towards the Outer Halo of M31

This chapter is from ”*Fermi*-LAT Observations of γ-ray Emission Towards the Outer Halo of M31”, with Simona Murgia, Sheldon Campbell, and Igor Moskalenko, submitted for publication to the *Astrophysical Journal* (Karwin et al., 2019).

Abstract: The Andromeda Galaxy is the closest spiral galaxy to us and has been the subject of numerous studies. It harbors a massive dark matter (DM) halo which may span up to ∼600 kpc across and comprises ∼90% of the galaxy's total mass. This halo size translates into a large diameter of 42° on the sky for an M31–Milky Way (MW) distance of 785 kpc, but its presumably low surface brightness makes it challenging to detect with γ-ray telescopes. Using 7.6 years of *Fermi* Large Area Telescope (*Fermi*–LAT) observations, we make a detailed study of the γ-ray emission between 1–100 GeV towards M31's outer halo, with a total field radius of 60° centered at M31, and perform an in-depth analysis of the systematic uncertainties related to the observations. We use the cosmic ray (CR) propagation code GALPROP to construct specialized interstellar emission models (IEMs) to characterize the foreground γ-ray emission from the MW, including a self-consistent determination of the isotropic component. We find evidence for an extended excess that appears to be distinct from the conventional MW foreground, having a total radial extension upwards of ∼120–200 kpc from the center of M31. We discuss plausible interpretations of the excess emission but emphasize that uncertainties in the MW foreground, and in particular, modeling of the H I-related components, have not been fully explored and may impact the results.

4.1 Introduction

The Andromeda Galaxy, also known as M31, is very similar to the MW. It has a spiral structure and is comprised of multiple components including a central super-massive black hole, bulge, galactic disk (the disk of stars, gas, and dust), stellar halo, and circumgalactic medium, all of which have been studied extensively (Roberts, 1893; Slipher, 1913; Pease, 1918; Hubble, 1929; Babcock, 1939; Mayall, 1951; Arp, 1964; Rubin & Ford, 1970; Roberts & Whitehurst, 1975; Henderson, 1979; Beck & Gräve, 1982; Brinks & Burton, 1984; Blitz et al., 1999; Ibata et al., 2001; de Heij et al., 2002; Ferguson et al., 2002; Braun & Thilker, 2004; Galleti et al., 2004; Zucker et al., 2004; Ibata et al., 2005; Barmby et al., 2006; Gil de Paz et al., 2007; Ibata et al., 2007; Li & Wang, 2007; Faria et al., 2007; Huxor et al., 2008; Richardson et al., 2008; Braun et al., 2009; McConnachie et al., 2009; Garcia et al., 2010; Saglia et al., 2010; Corbelli et al., 2010; Peacock et al., 2010; Hammer et al., 2010; Mackey et al., 2010; Li et al., 2011; Lauer et al., 2012; McConnachie, 2012; Lewis et al., 2013; Bate et al., 2014; Veljanoski et al., 2014; Huxor et al., 2014; Ade et al., 2015; Bernard et al., 2015; Lehner et al., 2015; Bernard et al., 2015; McMonigal et al., 2015; Conn et al., 2016; Kerp et al., 2016). Furthermore, the Andromeda Galaxy, like all galaxies, is thought to reside within a massive DM halo (Rubin & Ford, 1970; Roberts & Whitehurst, 1975; Faber & Gallagher, 1979; Bullock et al., 2001; Carignan et al., 2006; Seigar et al., 2008; Banerjee & Jog, 2008; Tamm et al., 2012; Velliscig et al., 2015). The DM halo of M31 is predicted to extend to roughly 300 kpc from its center and have a mass on the order of $10^{12} M_{\odot}$, which amounts to approximately 90% of the galaxy's total mass (Klypin et al., 2002; Seigar et al., 2008; Corbelli et al., 2010; Tamm et al., 2012; Fardal et al., 2013; Shull, 2014; Lehner et al., 2015). For cold DM, the halo is also predicted to contain a large amount of substructure (Braun & Burton, 1999; Blitz et al., 1999; de Heij et al., 2002; Braun & Thilker, 2004; Diemand et al., 2007; Kuhlen et al., 2007; Springel et al., 2008; Zemp et al., 2009; Moliné et al., 2017), a subset of which hosts M31's population of satellite dwarf galaxies (McConnachie, 2012; Martin et al., 2013; Collins et al., 2013; Ibata et al., 2013; Pawlowski et al., 2013b; Conn et al., 2013). The combined M31 system, together with a similar system in the MW, are the primary components of the Local Group. The distance from the MW to M31 is approximately 785 kpc (Stanek & Garnavich, 1998; McConnachie et al., 2005; Conn et al., 2012), making it relatively nearby. Consequently, M31 appears extended on the sky. Because of this accessibility, M31 offers a prime target for studying galaxies; and indeed, a wealth of information has been gained from observations in all wavelengths of the electromagnetic spectrum, e.g., see the references provided at the beginning of the introduction.

The *Fermi* Large Area Telescope (*Fermi*–LAT) is the first instrument to significantly detect M31 in γ-rays (Abdo et al., 2010b; Ögelman et al., 2011). Prior to *Fermi*–LAT other pioneering experiments set limits on a tentative signal (Fichtel et al., 1975b; Pollock et al., 1981; Sreekumar et al., 1994; Hartman et al., 1999), with the first space-based γ-ray observatories dating back to 1962 (Kraushaar & Clark, 1962; Kraushaar et al., 1972). Note that M31 has not been significantly detected by any ground-based γ-ray telescopes, which are typically sensitive to energies above $\sim$100 GeV (Abeysekara et al., 2014; Funk, 2015; Bird, 2016; Tinivella, 2016).

The initial M31 analysis performed by the *Fermi*–LAT Collaboration modeled M31 both as a point source and an extended source, finding marginal preference for extension at the confidence level of 1.8σ (Abdo et al., 2010b). In order to search for extension, a uniform intensity elliptical template is employed, where the parameters of the ellipse are estimated from the IRIS 100 μm observation of M31 (Miville-Deschenes & Lagache, 2005). This emission traces a convolution of the interstellar gas and recent massive star formation activity (Yun et al., 2001; Reddy & Yun, 2004; Abdo et al., 2010b) and can be used as a template for modeling the γ-ray emission.

Since the initial detection further studies have been conducted (Dugger et al., 2010; Li et al., 2016; Pshirkov et al., 2016a,b; Ackermann et al., 2017b). A significant detection of extended γ-ray emission with a total extension of 0.9° was reported by Pshirkov et al. (2016b), where the morphology of the detected signal consists of two bubbles symmetrically located perpendicular to the M31 disk, akin to the MW Fermi bubbles. Most recently the *Fermi*-LAT Collaboration has published their updated analysis of M31 (Ackermann et al., 2017b). This study detects M31 with a significance of nearly 10σ, and evidence for extension is found at the confidence level of 4σ. Of the models tested, the best-fit morphology consists of a uniform-brightness circular disk with a radius of 0.4° centered at M31. The γ-ray signal is not found to be correlated with regions rich in gas or star formation activity, as was first pointed out by Pshirkov et al. (2016b).

In this work we make a detailed study of the γ-ray emission observed towards the outer halo of M31, including the construction of specialized interstellar emission models to characterize the foreground emission from the MW, and an in-depth evaluation of the systematic uncertainties related to the observations. Our ultimate goal is to test for a γ-ray signal exhibiting spherical symmetry with respect to the center of M31, since there are numerous physical motivations for such a signal.

In general, disk galaxies like M31 may be surrounded by extended CR halos (Feldmann et al., 2013; Pshirkov et al., 2016a). Depending on the strength of the magnetic fields in the outer galaxy, the CR halo may extend as far as a few hundred kpc from the galactic disk. However, the actual extent remains highly uncertain. The density of CRs in the outer halo is predicted to be up to 10% of that found in the disk (Feldmann et al., 2013). Disk galaxies like M31 are also surrounded by a circumgalactic medium, which is loosely defined as a halo of gas (primarily ionized hydrogen) in different phases which may extend as far as the galaxy's virial radius (Gupta et al., 2012; Feldmann et al., 2013; Lehner et al., 2015; Pshirkov et al., 2016a; Howk et al., 2017). In addition, the stellar halo of M31 is observed to have an extension $\gtrsim$50 kpc (Ibata et al., 2007; McConnachie et al., 2009; Mackey et al., 2010). CR interactions with the radiation field of the stellar halo and/or the circumgalactic gas could generate γ-ray emission.

Some hints of the extent and distribution of the M31 halo may be gained from observations of the distributions of well-studied objects, clearly tied to the M31 system. In Section 4.5 we compare the distribution of the observed γ-ray emission in the M31 field to such features as M31's population of globular clusters (Galleti et al., 2004; Huxor et al., 2008; Peacock et al., 2010; Mackey et al., 2010; Veljanoski et al., 2014; Huxor et al., 2014) and M31's population of satellite dwarf galaxies (McConnachie, 2012; Martin et al., 2013; Collins et al., 2013). We note that *Fermi*–LAT does not detect most of the MW dwarfs (Ackermann et al., 2015a), and likewise we do not necessarily expect to detect most of the individual M31 dwarfs. The dwarfs are included here primarily as a qualitative gauge of the extent of M31's DM halo, and more generally, in support of formulating the most comprehensive picture possible of the M31 region. We also compare the observed γ-ray emission to the M31 cloud (Blitz et al., 1999; Kerp et al., 2016), which is a highly extended lopsided gas cloud centered in projection on M31. It remains uncertain whether the M31 cloud resides in M31 or the MW, although most recently Kerp et al. (2016) have argued that M31's disk is physically connected to the M31 cloud.

Lastly, we note that due to its mass and proximity, the detection sensitivity of M31 to DM searches with γ-rays is competitive with the MW dwarf spheroidal galaxies, particularly if the signal is sufficiently boosted by substructures (Falvard et al., 2004; Fornengo et al., 2004; Mack et al., 2008; Dugger et al., 2010; Conrad et al., 2015; Gaskins, 2016). Moreover, M31 is predicted to be the brightest extragalactic source of DM annihilation (Lisanti et al., 2018a,b). At a distance of $\sim$785 kpc from the MW (Stanek & Garnavich, 1998; McConnachie et al., 2005; Conn et al., 2012) and with a virial radius of a few hundred kpc (Klypin et al., 2002; Seigar et al., 2008; Corbelli et al., 2010; Tamm et al., 2012; Fardal et al., 2013; Shull, 2014; Lehner et al., 2015), the diameter of M31's DM halo covers $\gtrsim 42^\circ$ across the sky. However, there is a high level of uncertainty regarding the exact nature of the halo geometry, extent, and substructure content (Kamionkowski & Kinkhabwala, 1998; Braun & Burton, 1999; Blitz et al., 1999; de Heij et al., 2002; Braun & Thilker, 2004; Helmi, 2004; Bailin & Steinmetz, 2005; Allgood et al., 2006; Bett et al., 2007; Hayashi et al., 2007; Kuhlen et al., 2007; Banerjee & Jog, 2008; Zemp et al., 2009; Saha et al., 2009; Law et al., 2009; Banerjee & Jog, 2011; Velliscig et al., 2015; Bernal et al., 2016; Garrison-Kimmel et al., 2017).

Our analysis proceeds as follows. In Section 4.2 we describe our data selection and modeling of the interstellar emission. In Section 4.3 we present the baseline analysis of the M31 field and perform a template fit, including the addition of M31-related components to the model. In Section 4.4 we compare the radial intensity profile and emission spectrum of the M31-related components to corresponding predictions for DM annihilation towards the outer halo of M31, including contributions from both the M31 halo and the MW halo in the line of sight. In Section 4.5 we compare the structured γ-ray emission in the M31 field to a number of complementary M31-related observations. Section 4.6

provides an extended summary of the analysis and results. Supplemental information is provided in Appendices. In Appendix A.1 we briefly describe the models for diffuse Galactic foreground emission. In Appendix A.2 we consider some additional systematics pertaining to the observations. Appendix A.3 provides the details of calculations of the DM profiles discussed in the paper.

4.2 Data and Models

4.2.1 Data

The *Fermi* Gamma-ray Space Telescope was launched on June 11, 2008. The main instrument on board *Fermi* is the Large Area Telescope. It consists of an array of 16 tracker modules, 16 calorimeter modules, and a segmented anti-coincidence detector. *Fermi*–LAT is sensitive to γ-rays in the energy range from approximately 20 MeV to above 300 GeV. A full description of the telescope, including performance specifications, can be found in Atwood et al. (2009), Abdo et al. (2009c), and Ackermann et al. (2012c).

Our region of interest (ROI) is a region with a radius of 60° centered at the position of M31, $(l, b) = (121.17^\circ, -21.57^\circ)$. We employ front and back converting events corresponding to the P8R2_CLEAN_V6 selection. The events have energies in the range 1–100 GeV and have been collected from 2008-08-04 to 2016-03-16 (7.6 years). The data are divided into 20 bins equally spaced in logarithmic energy, with $0.2^\circ \times 0.2^\circ$ pixel size. The analysis is carried out with the *Fermi*–LAT ScienceTools (version v10r0p5)[1]. In particular, the binned maximum likelihood fits are performed with the *gtlike* package.

Figure 4.1 shows the total observed counts between 1–100 GeV for the full ROI. Two different count ranges are displayed. The map on the left shows the full range. The bright emission along 0° latitude corresponds to the plane of the MW. The map on the right shows the saturated counts map, emphasizing the lower counts at higher latitudes. Overlaid is a green dashed circle (21° in radius) corresponding to a 300 kpc projected radius centered at M31, for an M31-MW distance of 785 kpc, i.e. the canonical virial radius of M31. Also shown is M31's population of dwarf galaxies. The primary purpose of the overlay is to provide a qualitative representation of the extent of M31's outer halo, and to show its relationship to the MW disk. Note that we divide the full ROI into subregions, and our primary field of interest is a $28^\circ \times 28^\circ$ square region centered at M31, which we refer to as field M31 (FM31), as further discussed below.

---

[1] Available at `http://fermi.gsfc.nasa.gov/ssc/data/analysis`

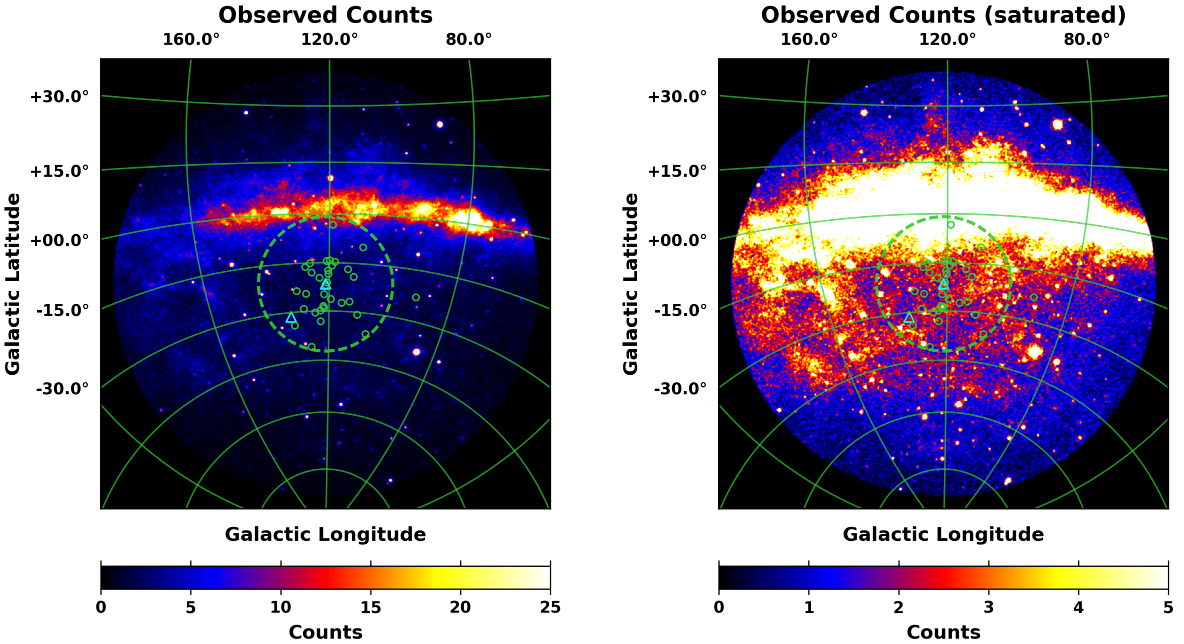

Figure 4.1 Observed counts (left) and saturated counts (right) for a 60° radius centered at M31, and an energy range of 1–100 GeV. The green dashed circle (21° in radius) corresponds to a 300 kpc projected radius centered at M31, for an M31–MW distance of 785 kpc, i.e. the canonical virial radius of M31. Also shown is M31's population of dwarf galaxies. M31 and M33 are shown with cyan triangles, and the other dwarfs are shown with 1° green circles, each centered at the optical center of the respective galaxy. The sizes of the circles are a bit arbitrary, although they roughly correspond to the PSF (68% containment angle) of *Fermi*-LAT, which at 1 GeV is $\sim 1°$. Most of the MW dwarfs are not detected by *Fermi*-LAT, and so we do not necessarily expect the individual M31 dwarfs to be detected. The primary purpose of the overlay is to provide a qualitative representation of the extent of M31's outer halo, and to show its relationship to the MW disk. Note that $\sim$3 dwarfs (which are thought to be gravitationally bound to M31) reach as for as $\sim$300 kpc, as seen in the Figure.

4.2.2 Foreground Model and Isotropic Emission

The foreground emission from the MW and the isotropic component (the latter includes unresolved extragalactic diffuse γ-ray emission, residual instrumental background, and possibly contributions from other Galactic components which have a roughly isotropic distribution) are the dominant contributions in γ-rays towards the M31 region. We use the CR propagation code GALPROP[2](v56) to construct specialized interstellar emission models (IEMs) to characterize the MW foreground emission, including a self-consistent determination of the isotropic component. These foreground models are physically motivated and *are not* subject to the same caveats[3] for extended source analysis as the FSSC IEM provided by the *Fermi*–LAT collaboration for point source analysis (Acero et al., 2016). Here we provide a brief description of the GALPROP model (Moskalenko & Strong, 1998, 2000; Strong & Moskalenko, 1998; Strong et al., 2000; Ptuskin et al., 2006; Strong et al., 2007; Vladimirov et al., 2011; Jóhannesson et al., 2016; Porter et al., 2017;

---

[2] Available at `https://galprop.stanford.edu`

[3] The list of caveats on the *Fermi*–LAT diffuse model is available at `https://fermi.gsfc.nasa.gov/ssc/data/analysis/LAT_caveats.html`

Jóhannesson et al., 2018; Génolini et al., 2018), and more details are given in Appendix A.1.

The GALPROP model calculates self-consistently spectra and abundances of Galactic CR species and associated diffuse emissions (radio, X-rays, γ-rays) in 2D and 3D. The CR injection and propagation parameters are derived from local CR measurements. The Galactic propagation includes all stable and long-lived particles and isotopes ($e^{\pm}$, $\bar{p}$, H-Ni) and all relevant processes in the interstellar medium. The radial distribution of the CR source density is parametrized as

$$\rho(r) = \left(\frac{r + r_1}{r_\odot + r_1}\right)^a \times \exp\left(-b \times \frac{r - r_\odot}{r_\odot + r_1}\right), \tag{4.1}$$

where r is the Galactocentric radius, $r_\odot = 8.5$ kpc, and the parameter r_1 regulates the CR density at $r = 0$. The injection spectra of CR species are described by the rigidity (R) dependent function

$$q(R) \propto (R/R_0)^{-\gamma_0} \prod_{i=0}^{2} \left[1 + (R/R_i)^{\frac{\gamma_i - \gamma_{i+1}}{s_i}}\right]^{s_i}, \tag{4.2}$$

where $\gamma_i (i = 0, 1, 2, 3)$ are the spectral indices, $R_i (i = 0, 1, 2)$ are the break rigidities, s_i are the smoothing parameters ($s_i = \mp 0.15$ for $|\gamma_i| \lessgtr |\gamma_{i+1}|$), and the numerical values of all parameters are given in Table 4.1. Some parameters are not in use, so for p and He, we have only $\gamma_{i=0,1,2}$ and $R_{i=0,1}$.

Heliospheric propagation is calculated using the dedicated code HelMod[4]. HelMod is a 2D Monte Carlo code for heliospheric propagation of CRs, which describes the solar modulation in a physically motivated way. It was demonstrated that the calculated CR spectra are in a good agreement with measurements including measurements outside of the ecliptic plane at different levels of solar activity and the polarity of the magnetic field. The result of the combined iterative application of the GALPROP and HelMod codes is a series of local interstellar spectra (LIS) for CR e^-, e^+, p, He, C, and O nuclei (Boschini et al., 2017, 2018a,b) that effectively disentangle two tremendous tasks such as Galactic and heliospheric propagation.

For our analysis we used a GALPROP-based combined diffusion-convection-reacceleration model with a uniform spatial diffusion coefficient and a single power law index over the entire rigidity range as described in detail in Boschini et al. (2017). Since the distribution of supernova remnants (SNRs), conventional CR sources, is not well determined due to the observational bias and the limited lifetime of their shells, other tracers are often employed. In our calculations we use the distribution of pulsars (Yusifov & Küçük, 2004) that are the final state of evolution of massive stars and can be observed for millions of years. The same distribution was used in the analysis of the γ-ray emission from the Inner Galaxy (IG) (Ajello et al., 2016).

---

[4] Available at `http://www.helmod.org/`

Table 4.1 GALPROP Model Parameters

Parameter	M31 IEM	IG IEM
$^{\mathrm{a}}z$ [kpc]	4	6
$^{\mathrm{a}}r$ [kpc]	20	30
$^{\mathrm{b}}a$	1.5	1.64
$^{\mathrm{b}}b$	3.5	4.01
$^{\mathrm{b}}r_1$	0.0	0.55
$^{\mathrm{c}}D_0$ [10^{28} cm^2 s^{-1}]	4.3	7.87
$^{\mathrm{c}}\delta$	0.395	0.33
$^{\mathrm{c}}\eta$	0.91	1.0
$^{\mathrm{c}}$Alfvén speed, v_{A} [km s^{-1}]	28.6	34.8
$^{\mathrm{d}}v_{\mathrm{conv},0}$ [km s^{-1}]	12.4	$\cdots$
$^{\mathrm{d}}dv_{\mathrm{conv}}/dz$ [km s^{-1} kpc^{-1}]	10.2	$\cdots$
$^{\mathrm{e}}R_{p,0}$ [GV]	7	11.6
$^{\mathrm{e}}R_{p,1}$ [GV]	360	$\cdots$
$^{\mathrm{e}}\gamma_{p,0}$	1.69	1.90
$^{\mathrm{e}}\gamma_{p,1}$	2.44	2.39
$^{\mathrm{e}}\gamma_{p,2}$	2.295	$\cdots$
$^{\mathrm{e}}R_{\mathrm{He},0}$ [GV]	7	$\cdots$
$^{\mathrm{e}}R_{\mathrm{He},1}$ [GV]	330	$\cdots$
$^{\mathrm{e}}\gamma_{\mathrm{He},0}$	1.71	$\cdots$
$^{\mathrm{e}}\gamma_{\mathrm{He},1}$	2.38	$\cdots$
$^{\mathrm{e}}\gamma_{\mathrm{He},2}$	2.21	$\cdots$
$^{\mathrm{e}}R_{e,0}$ [GV]	0.19	$\cdots$
$^{\mathrm{e}}R_{e,1}$ [GV]	6	2.18
$^{\mathrm{e}}R_{e,2}$ [GV]	95	2171.7
$^{\mathrm{e}}\gamma_{e,0}$	2.57	$\cdots$
$^{\mathrm{e}}\gamma_{e,1}$	1.40	1.6
$^{\mathrm{e}}\gamma_{e,2}$	2.80	2.43
$^{\mathrm{e}}\gamma_{e,3}$	2.40	4.0
$^{\mathrm{f}}J_p$ [10^{-9} cm^{-2} s^{-1} sr^{-1} MeV^{-1}]	4.63	4.0
$^{\mathrm{f}}J_e$ [10^{-11} cm^{-2} s^{-1} sr^{-1} MeV^{-1}]	1.44	0.011
$^{\mathrm{g}}$A5 [kpc]	8–10	8–10
$^{\mathrm{g}}$A6 [kpc]	10–11.5	10–50
$^{\mathrm{g}}$A7 [kpc]	11.5–16.5	$\cdots$
$^{\mathrm{g}}$A8 [kpc]	16.5–50	$\cdots$
$^{\mathrm{h}}$IC Formalism	Anisotropic	Isotropic

Note. — For reference, we also give corresponding values for the ("Yusifov") IEMs used in Ajello et al. (2016) for the analysis of the inner Galaxy (IG).

[a] Halo geometry: z is the height above the Galactic plane, and r is the radius.

[b] CR source density. The parameters correspond to Eq. (4.1).

[c] Diffusion: $D(R) \propto \beta^{\eta} R^{\delta}$. $D(R)$ is normalized to D_0 at 4.5 GV.

[d] Convection: $v_{\mathrm{conv}}(z) = v_{\mathrm{conv},0} + (dv_{\mathrm{conv}}/dz)z$.

[e] Injection spectra: The spectral shape of the injection spectrum is the same for all CR nuclei except for protons. The parameters correspond to Eq. (4.2).

[f] The proton and electron flux are normalized at the Solar location at a kinetic energy of 100 GeV. Note that for the IG IEM the electron normalization is at a kinetic energy of 25 GeV.

[g] Boundaries for the annuli which define the IEM. Only A5 (local annulus) and beyond contribute to the foreground emission for FM31.

[h] Formalism for the inverse Compton (IC) component.

We adopt the best-fit GALPROP parameters from Boschini et al. (2017, 2018a), which are summarized in Table 4.1. The spectral shape of the injection spectrum is the same for all CR nuclei except for protons. The corresponding CR spectra are plotted in Figure 4.2. Also plotted in Figure 4.2 are the latest AMS-02 measurements from Aguilar et al. (2014, 2015a,b) and Voyager 1 p and He data in the local interstellar medium (Cummings et al., 2016). The modulated LIS are taken from Boschini et al. (2017, 2018a) and correspond to the time frame of the published AMS-02 data. In addition, we plot the LIS for the ("Yusifov") IEMs used in Ajello et al. (2016) for the analysis of the inner Galaxy (IG), which we use as a reference model in our study of the systematics for the M31 field (see Appendix A.2.2). Overall, the LIS for the M31 model are in good agreement with the AMS-02 data.

We note that there is a small discrepancy in the modulated all-electron ($e^- + e^+$) spectrum between ∼4–10 GeV that, however, does not affect our results. Electrons in this energy range do not contribute much to the observed diffuse emission. The upscattered photon energy is $\epsilon_1 \sim \epsilon_0 \gamma^2$, where ϵ_0 and γ are the energy of the background photon and the Lorentz-factor of the CR electron, correspondingly. For our range of interest $\epsilon_1 \sim 5$ GeV, we need CR electrons of ∼35 GeV for $\epsilon_0 \sim 1$ eV optical photons and even higher for IR and CMB, meanwhile the number density of optical photons in the ISM is very small. Additionally, we perform several systematic tests throughout this work, including fits with three different IEMs (M31, IG, and FSSC IEMs), as well as a fit in a tuning region surrounding FM31 on the south.

Figure 4.3 shows the total IEM in the energy range 1–100 GeV. The model includes π^0-decay, inverse Compton (IC), and Bremsstrahlung components. Overlaid is the ROI used is this analysis. From the observed counts (Figure 4.1) we cut a $84^\circ \times 84^\circ$ ROI, which is centered at M31. The green dashed circle is the 300 kpc boundary corresponding to M31's canonical virial radius (of ∼21°), as also shown in Figure 4.1.

We label the field within the virial radius as FM31, and the region outside (and below latitudes of -21.57°) we label as the tuning region (TR). Longitude cuts are made on the ROI at $l = 168^\circ$ and $l = 72^\circ$. The former cut is made to stay away from the outer Galaxy, where the gas distribution becomes more uncertain, due to the method used for placing the gas at Galactocentric radii, i.e. Doppler shifted 21-cm emission. The latter cut is made to prevent the observations from including additional model component (i.e. A4, as described below), which would further complicate the analysis.

The γ-ray maps generated by GALPROP correspond to ranges in Galactocentric radii, and their boundaries are shown in Figure 4.4 (A1–A8), which also depicts an overhead view of the annuli. The line of sight for the ROI, as seen from the location of the Solar system, is indicated with dash-dot red lines. Maps for the individual processes are shown in Figures 4.5 and 4.6.

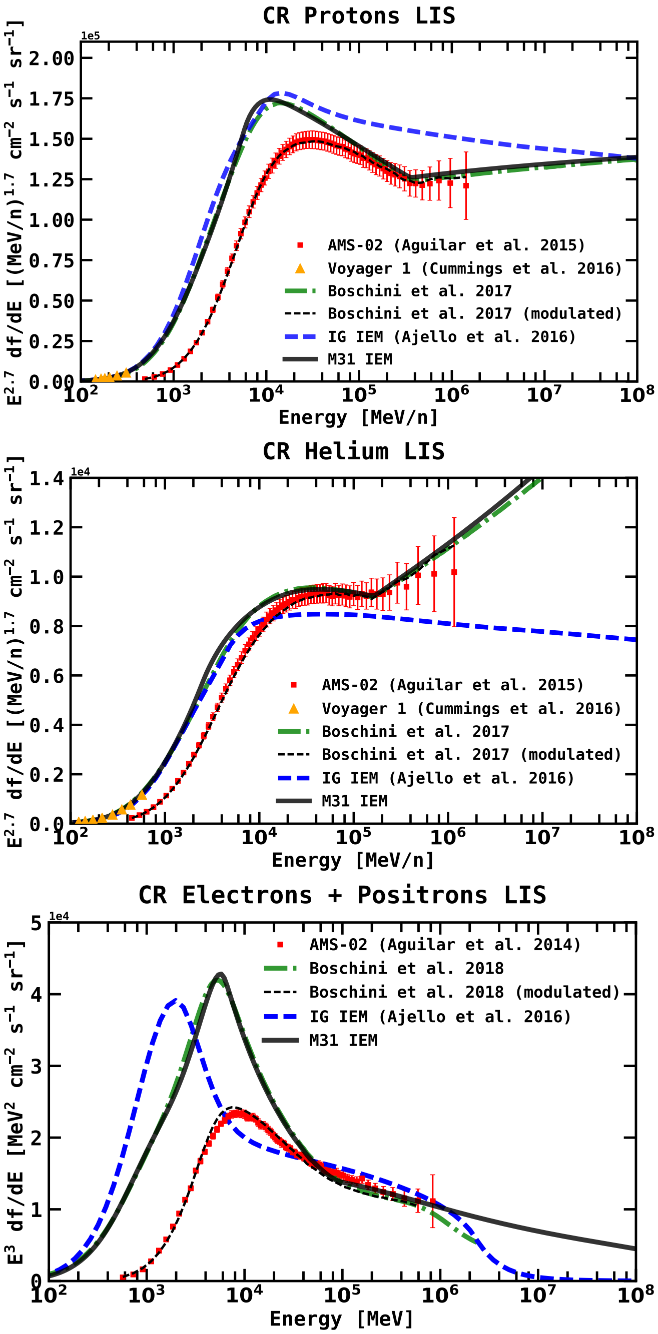

Figure 4.2 The LIS for CR protons (top), He (middle), and all electrons ($e^- + e^+$) (bottom). The latest AMS-02 measurements from Aguilar et al. (2014, 2015a,b) are shown with red squares. The green dashed line shows the results from Boschini et al. (2017, 2018a), which employ GALPROP and HelMod together in an iterative manner to derive the LIS. We adopt their derived GALPROP CR parameters, and the LIS for our IEM (M31 IEM: solid black line) are roughly the same. The thin dotted black line shows the LIS modulated with HelMod (Boschini et al., 2017, 2018a). Yellow triangles show the Voyager 1 p and He data in the local interstellar medium (Cummings et al., 2016). Voyager 1 electron data are below 100 MeV and, therefore, are not shown. In addition we show the LIS for the ("Yusifov") IEM in Ajello et al. (2016), which we use as a reference model in our study of the systematics for the M31 field (see Appendix A.2.2).

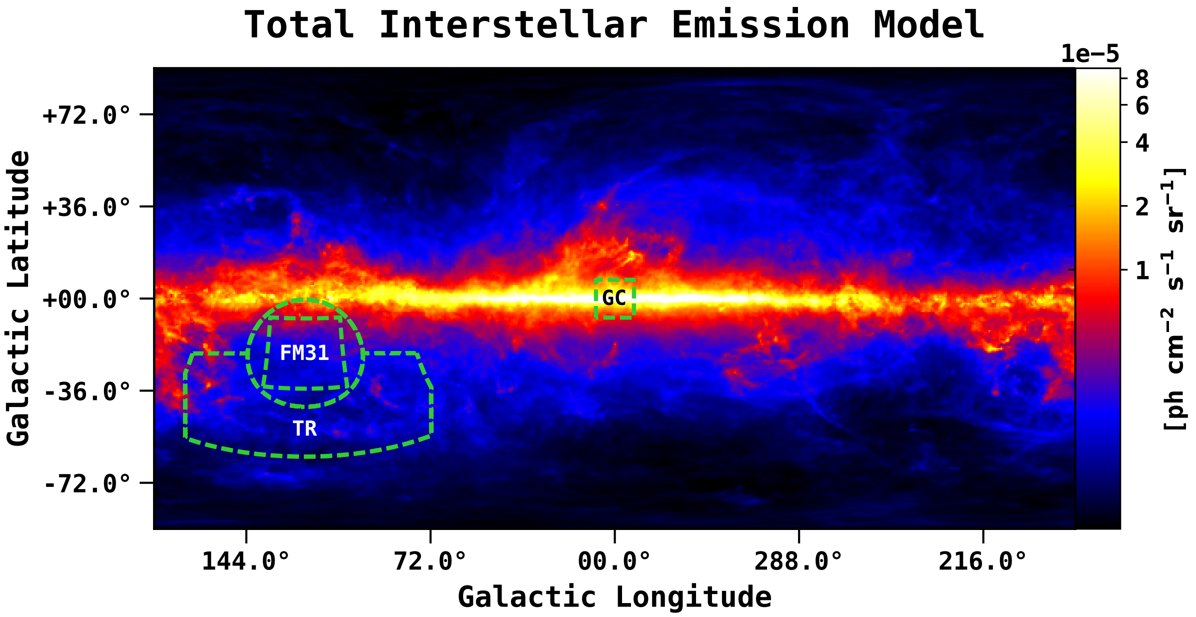

Figure 4.3 The total interstellar emission model (IEM) for the MW integrated in the energy range 1–100 GeV. The color corresponds to the intensity, and is shown in logarithmic scale. The intensity level is for the initial GALPROP output, before tuning to the γ-ray data. The map is shown in a Plate Carrée projection, and the pixel size is 0.25 deg/pix. The model has contributions from π^0-decay, (anisotropic) IC emission, and Bremsstrahlung. Overlaid is the region of interest (ROI) used in this analysis. From the observed counts (Figure 4.1) we cut an $84^\circ \times 84^\circ$ ROI, which is centered at M31. The green dashed circle is the 300 kpc boundary corresponding to M31's canonical virial radius (of $\sim 21^\circ$), as also shown in Figure 4.1. We label the field within the virial radius as field M31 (FM31), and the region outside (and south of latitudes of -21.57°) we label as the tuning region (TR). Longitude cuts are made on the ROI at $l = 168^\circ$ and $l = 72^\circ$, as discussed in the text. For reference we also show the Galactic center region (GC), which corresponds to a $15^\circ \times 15^\circ$ square centered at the GC.

The H I maps GALPROP employs are based on LAB[5] + GASS[6] data, which for our ROI corresponds to LAB data only (Kalberla et al., 2005). We note that there is a newer EBHIS[7] survey that covers the whole northern sky, but for our purposes the LAB survey suffices. Besides, the development of the new H I maps for GALPROP based on the EBHIS survey would require a dedicated study. The H I-related γ-ray emission depends on the H I column density, which depends on the spin temperature of the gas. We assume a uniform spin temperature of 150 K. The gas is placed at Galactocentric radii based on the Doppler-shifted velocity and Galactic rotation models. FM31 has a significant emission associated with H I gas. The emission is dominated by A5, with further contribution from A6–A7.

On the other hand, there is very little contribution from H_2, which is concentrated primarily along the Galactic disk. The emission in FM31 only comes from A5. The 2.6 mm line of the ^{12}CO molecular $J = 1 \rightarrow 0$ transition is used as a tracer of H_2, assuming a proportionality between the integrated line intensity of CO, $W(\mathrm{CO})$, and the column density of H_2, $N(\mathrm{H_2})$, given by the factor X_{CO}. We use the X_{CO} values from Ajello et al. (2016), which are tabulated

---

[5] The Leiden/Argentine/Bonn Milky Way H I survey
[6] GALEX Arecibo SDSS Survey; GALEX = the Galaxy Evolution Explorer, SDSS = Sloan Digital Sky Survey
[7] The Effelsberg-Bonn H I Survey

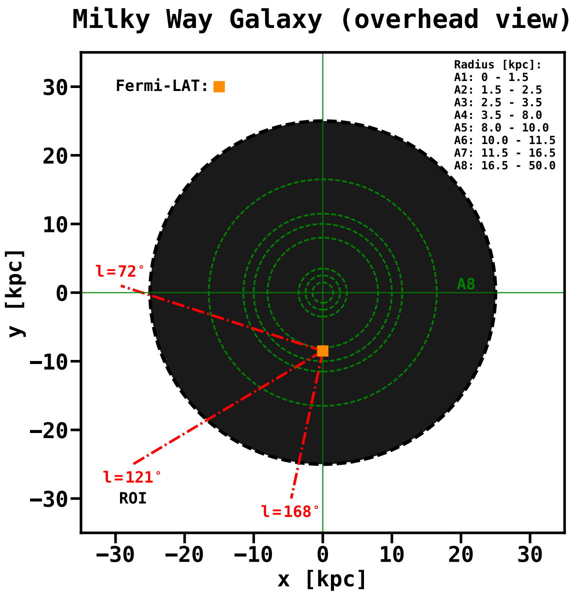

Figure 4.4 Schematic of the eight concentric circles which define the annuli (A1–A8) in the IEM, as described in the text. The ranges in Galactocentric radii are reported in the legend. Note that the full extension of A8 is not shown. Only A5–A8 contribute to the Galactic foreground emission for the field used in this analysis.

at different Galactocentric radii with power law interpolation. In particular, the values relevant for this analysis are 1.4×10^{20}, 7.2×10^{19}, and 7.0×10^{20} ($\mathrm{cm^{-2}\ K^{-1}\ km^{-1}\ s}$), for radii 7.5, 8.7, and 11.0 (kpc), respectively.

The foreground emission from H II is subdominant. Modeling of this component is based on pulsar dispersion measurements. We use the model from Gaensler et al. (2008). The distribution of He in the interstellar gas is assumed to follow that of hydrogen, with a He/H ratio of 0.11 by number. Heavier elements in the gas are neglected.

Our model also accounts for the dark neutral medium (DNM), or dark gas, which is a component of the interstellar medium that is not well traced by 21-cm emission or CO emission, as described in Grenier et al. (2005), Ackermann et al. (2012a), and Acero et al. (2016). For any particular region the DNM comprises unknown fractions of cold dense H I and CO-free or CO-quiet H_2. Details for the determination of the DNM component are described in Ackermann et al. (2012a).

In summary, a template for the DNM is constructed by creating a map of "excess" dust column density $\mathrm{E(B-V)_{res}}$. A gas-to-dust ratio is obtained for both H I and CO using a linear fit of the N(H I) map and W(CO) map to the $\mathrm{E(B-V)}$ reddening map of Schlegel et al. (1998). In general, the method is all-sky, and a constant gas-to-dust ratio is assumed throughout the Galaxy. Subtracting the correlated parts from the total dust results in the residual dust emission, $\mathrm{E(B-V)_{res}}$, which is then associated with the DNM. In the current study the DNM is incorporated into the H I templates; see Ackermann et al. (2012a) for details.

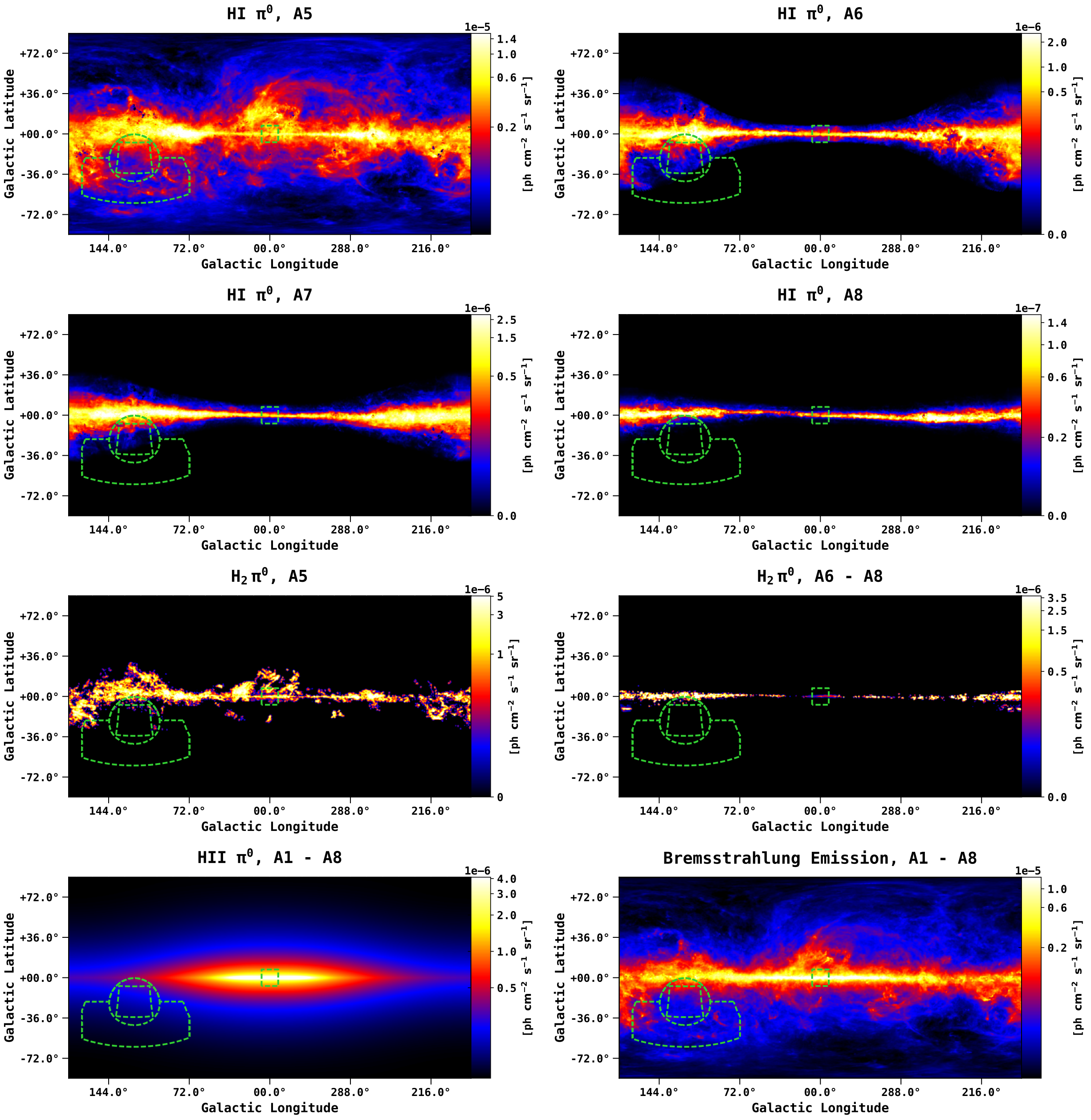

Figure 4.5 Gas-related components of the IEM (π^0-decay related to H I, H II, and H_2, and Bremsstrahlung emission) integrated in the energy range 1–100 GeV. The components correspond to different annuli, as indicated above each plot. The color corresponds to the intensity, and is shown in logarithmic scale. The intensity level is for the initial GALPROP outputs, before tuning to the γ-ray data. The maps are shown in a Plate Carrée projection, and the pixel size is 0.25 deg/pix. Overlaid is the ROI used in this analysis, as well as the GC region (see Figure 4.3).

The IC component arises from up-scattered low-energy photons of the Galactic interstellar radiation field (ISRF) by CR electrons and positrons. The ISRF (optical, infrared, and cosmic microwave background) is the result of the emission by stars, and scattering, absorption, and re-emission of absorbed starlight by dust in the interstellar medium. The ISRF is highly anisotropic since it is dominated by the radiation from the Galactic plane. An observer in the

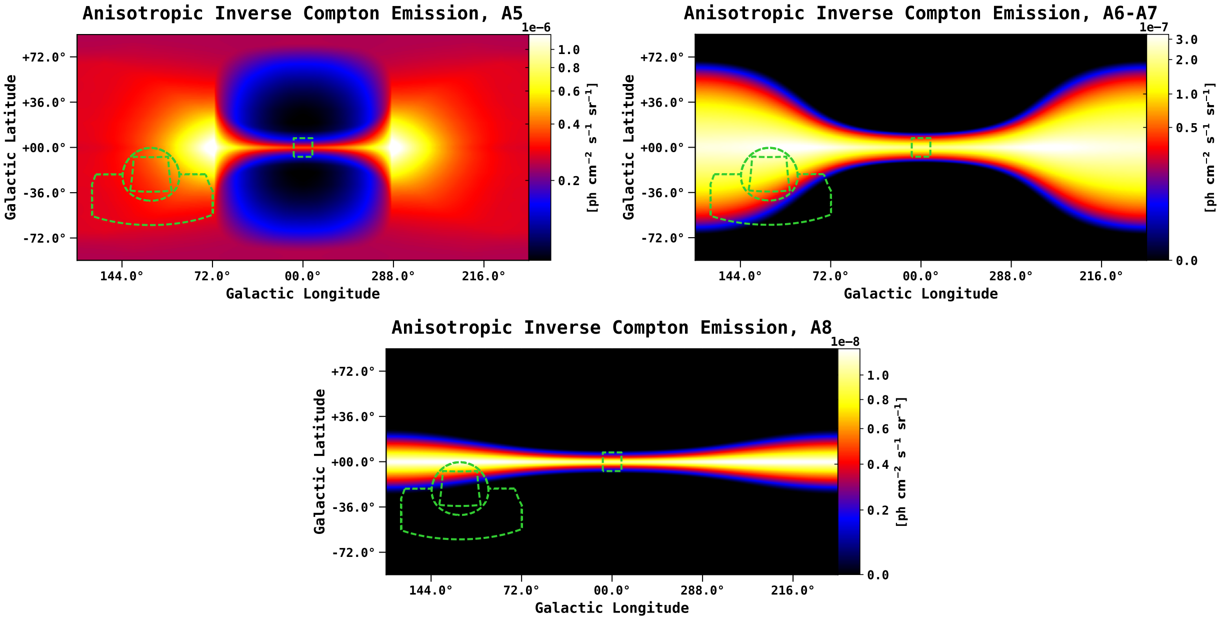

Figure 4.6 Anisotropic Inverse Compton (AIC) components of the interstellar emission model for the MW in the energy range 1–100 GeV. The color corresponds to the intensity, and is shown in logarithmic scale. The intensity level is for the initial GALPROP outputs, before tuning to the γ-ray data. The map is shown in a Plate Carrée projection, and the pixel size is 0.25 deg/pix. The IC A6 and A7 components are highly degenerate, and so we combine them into a single map A6+A7. Overlaid is the ROI used in this analysis, as well as the GC region (see Figure 4.3). Note that we use the anisotropic IC maps as our default component. Unless otherwise stated, all reference to the IC component implies the anisotropic formalism.

Galactic plane thus sees mostly head-on scatterings even if the distribution of the CR electrons is isotropic. This is especially evident when considering inverse Compton scattering by electrons in the halo, i.e. the diffuse emission at high Galactic latitudes.

We employ the anisotropic formalism of the IC component (Moskalenko & Strong, 2000). From the GALPROP code we use the standard ISRF model file (standard.dat) and standard scaling factors of 1.0 for optical, infrared, and microwave components. In Figure 4.7 we show the differential flux ratio (AIC/IC) between the anisotropic (AIC) and isotropic (IC) inverse Compton components (all-sky). The top figure shows the spatial variation of the ratio at 1 GeV. The ratio is close to unity towards the GC, increases with Galactic longitude and latitude, and reaches maximum at mid-latitudes towards the outer Galaxy. The bottom figure shows the energy dependence of the ratio for 4 different spatial points, including M31. Note that unless otherwise stated, *all reference to the IC component implies the anisotropic formalism.* Also, the γ-ray skymaps for IC A6 and A7 are highly degenerate, and so we combine them into a single map A6+A7.

The IC component anti-correlates with the isotropic component. The isotropic component includes unresolved extragalactic diffuse emission, residual instrumental background, and possibly contributions from other Galactic compo-

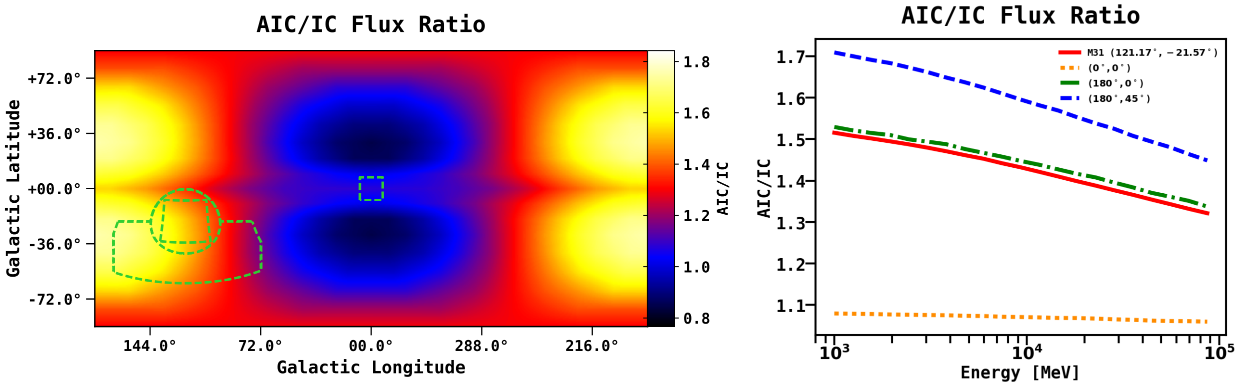

Figure 4.7 The IEM employs the anisotropic IC sky maps, as discussed in the text. For comparison we show the differential flux ratio (AIC/IC) between the anisotropic (AIC) and isotropic (IC) inverse Compton components (all-sky). The top figure shows the spatial variation of the ratio at 1 GeV. The bottom figure shows the energy dependence of the ratio for 4 different spatial points, including M31. The ratio is close to unity towards the GC, increases with Galactic longitude and latitude, and reaches maximum at mid-latitudes towards the outer Galaxy. Note that we use the anisotropic IC maps as our default component. Unless otherwise stated, all reference to the IC component implies the anisotropic formalism.

Table 4.2. Normalizations for Calculations of the Isotropic Component

Region	π^0	AIC
All-sky	1.319 ± 0.005	1.55 ± 0.04
North	1.430 ± 0.010	1.14 ± 0.05
South	1.284 ± 0.006	1.86 ± 0.05
East	1.397 ± 0.009	1.07 ± 0.05
West	1.287 ± 0.006	1.88 ± 0.05

Note. — See Figure 4.8 for definition of the regions.

nents which have a roughly isotropic distribution. The spectrum of the isotropic component depends on the IEM and the ROI used for the calculation. The spectrum also depends on the data set, since the residual instrumental background differs between data sets. We calculate the isotropic component self-consistently with the M31 IEM, and the spectrum is shown in Figure 4.8. Table 4.2 gives the corresponding best-fit normalizations for the diffuse components.

The main calculation is performed over the full sky excluding regions around the Galactic plane and the Inner Galaxy: $|b| \geq 30°,\ 45° \leq l \leq 315°$. We note that even though it is not actually an all-sky fit, we refer to it as 'all-sky' for simplicity hereafter. The fit includes 3FGL sources fixed, sun and moon templates fixed, Wolleben (2007) component (Loop I two-component spatial template), all-sky π^0-decay and (anisotropic) IC normalization scaled, and all-sky Bremsstrahlung fixed. Besides, we calculate the isotropic component in the different sky regions: north, south, east, and west, as detailed in Figure 4.8. Also shown are the isotropic components resulting from the M31 IEM using the

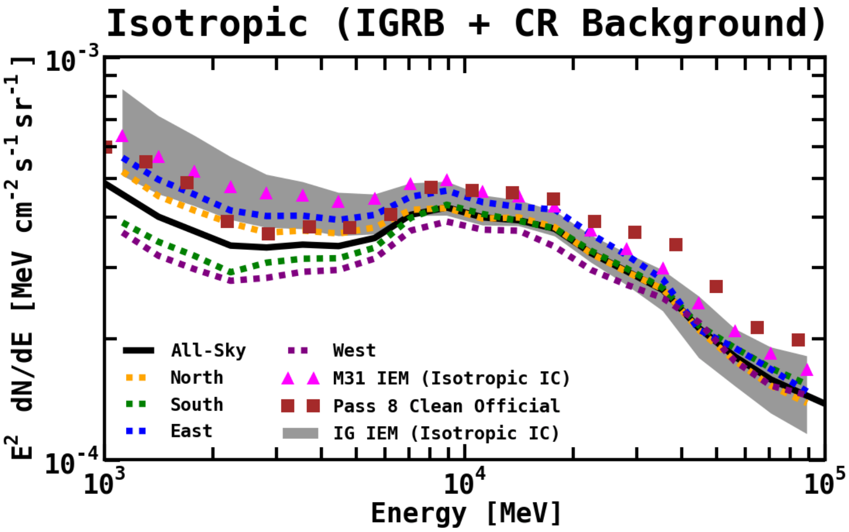

Figure 4.8 The spectrum of the isotropic component has a dependence on the IEM and the ROI used for the calculation, as well as the data set. For the M31 IEM (which uses the AIC sky maps) we calculate the **All-Sky** (solid black line) isotropic component in the following region: $|b| \geq 30°$, $45° \leq l \leq 315°$. We also calculate the isotropic component in the different sky regions: **north**: $b \geq 30°$, $45° \leq l \leq 315°$ (orange dashed line); **south**: $b \leq -30°$, $45° \leq l \leq 315°$ (green dashed line); **east**: $|b| \geq 30°$, $180° \leq l \leq 315°$ (blue dashed line); and **west**: $|b| \geq 30°$, $45° \leq l \leq 180°$ (purple dashed line). See Table 4.2 for the corresponding best-fit normalizations. Magenta triangles show the all-sky isotropic component for the M31 IEM derived using the isotropic IC formalism. The brown squares show the official FSSC isotropic spectrum (iso_P8R2_CLEAN_V6_v06). The grey band is our calculated isotropic systematic uncertainty for the IG IEM, which uses the isotropic IC formalism (see Appendix A.2.2).

isotropic IC formalism, the FSSC IEM, and the IG IEM (which uses the isotropic IC formalism). At lower energies the intensities of the spectra calculated in the south and west (both regions associated with the M31 system) are lower than that of the spectra calculated in the north and east. Correspondingly, the IC normalizations are higher for the south and west. Interestingly, independently on the IEM used in the fit, the isotropic spectrum features a bump at ∼10 GeV.

4.2.3 Tuning the IEM

Figure 4.9 shows the total model counts for the full ROI. The bottom panel shows the TR, for which we mask the 300 kpc circle around M31 and latitudes north of $-21.57°$. The primary purpose of the TR is to fit the normalization of the isotropic component. The isotropic component by definition is an all-sky average, but it may have some local spatial variations, since the instrumental background may also vary over the sky. The TR is also used to set the initial normalizations of the IC components, since they are anti-correlated with the isotropic component.

The fit is performed by uniformly scaling each diffuse component as well as all 3FGL sources in the region. Note that

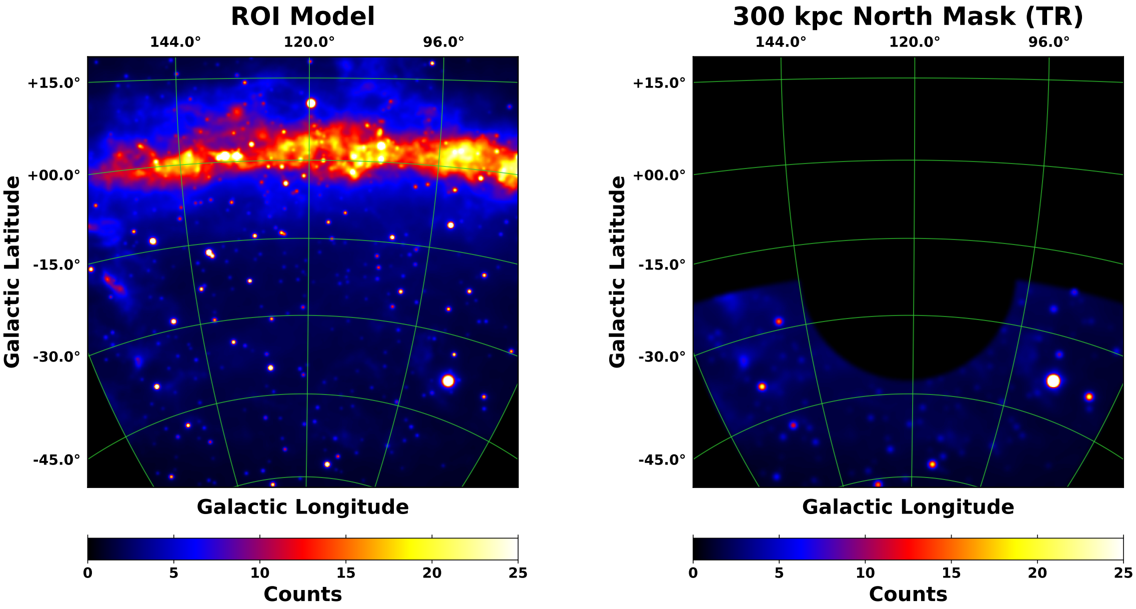

Figure 4.9 Total model counts for the full ROI. For the tuning region (TR) we mask within the 300 kpc circle and latitudes above $-21.57°$, as discussed in the text.

the model includes all sources within 70° of the ROI center, but only the sources in the TR are scaled in the fit. As a test, we also perform the fit by keeping fixed the 3FGL sources in the TR, and we find that the best-fit normalizations of the diffuse components are not very sensitive to the scaling of the point sources. Likewise, it is not necessary to scale the point sources outside of the TR, which are included in order to account for the spillover of the instrumental PSF. The fit uses the spectral shape of the isotropic spectrum derived from the all-sky analysis. The H II component is fixed to its GALPROP prediction, since it it subdominant compared to the other components. The Bremsstrahlung component possesses a normalization of 1.0 ± 0.6, consistent with the GALPROP prediction. In our further fits in the FM31 region these components remain fixed to their all-sky GALPROP predictions.

Figure 4.10 shows the best-fit spectra and fractional count residuals resulting from the fit in the TR. The corresponding best-fit normalizations and integrated flux are reported in Table 4.3. The isotropic component possesses a normalization of 1.06 ± 0.04, consistent with the all-sky average. The H I π^0 A6 component shows a fairly high normalization with respect to the model prediction, which is likely related to the fact that it only contributes near the edge of the region.

The fractional residuals are fairly flat over the entire energy range, but somewhat worsen at higher energies, although they remain consistent with statistical fluctuations. We note that there does appear to be a subtle systematic bias in the fractional residuals, where the data is being over-modeled between ∼6–20 GeV. This may be due to the spectral shape of the 3FGL sources in the region that is not properly accounted. For the sources we use their spectral parameterizations

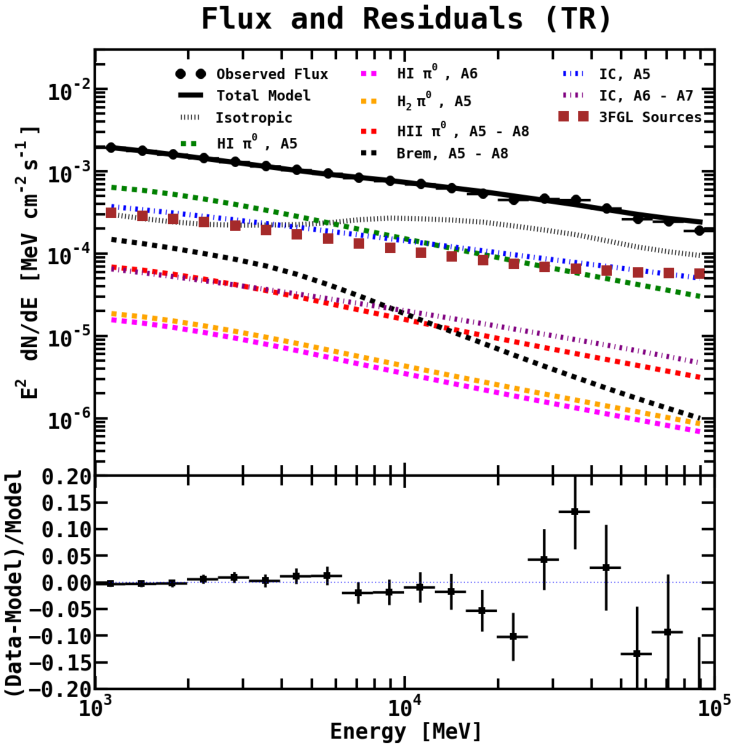

Figure 4.10 Flux (upper panel) and fractional count residuals (lower panel) for the fit in the TR. The H II component is fixed to its GALPROP prediction. The normalizations of all other diffuse components are freely scaled, as well as all 3FGL sources in the region. The residuals show fairly good agreement over the entire energy range.

rather than the binned data points.

Figure 4.11 shows the correlation matrix[8] for the fit. The isotropic component is anti-correlated with the IC components. The IC components are also anti-correlated with the H I A5 component. The H_2 component shows very little correlation with the other components, but its contribution is very minimal in the TR.

Figure 4.12 shows the spatial count residuals for three different energy bins, as indicated above each plot. The bins are chosen to coincide with positive residual emission which is observed in FM31, as discussed in Section 4.3. Residuals are shown using a colormap from the colorcet package (Kovesi, 2015).

Two notable features can be observed in the residuals. Near $(l, b){\approx}(156^\circ, -35^\circ)$ a deep hole can be seen in the first energy bin. Comparing to the H I column density maps (see Figure 4.5), this over-modeling is likely related to a feature in the gas. Note that the hole also contains a BL LAC (3FGL J0258.0+2030). The second notable feature is located near $(l, b){\approx}(84^\circ, -40^\circ)$. This is a flat spectral radio quasar (3FGL J2254.0+1608). As a test, these trouble-

---

[8] The correlation (C) of two parameters A and B is defined in terms of the covariance (cov) and the standard deviation (σ): $C = cov_{AB} \times (\sigma_A \sigma_B)^{-1}$.

Table 4.3. Baseline Values for the IEM Components in the TR

Component	Normalization	Flux ($\times 10^{-9}$) (ph cm^{-2} s^{-1})	Intensity ($\times 10^{-8}$) (ph cm^{-2} s^{-1} sr^{-1})
H I π^0, A5	1.10 ± 0.03	439.4 ± 11.0	153.1 ± 3.8
H I π^0, A6	5.0 ± 1.3	10.6 ± 2.8	3.7 ± 1.0
H_2 π^0, A5	2.1 ± 0.1	12.6 ± 0.7	4.4 ± 0.3
Bremsstrahlung	1.0 ± 0.6	100.4 ± 58.3	35.0 ± 20.3
IC, A5	2.3 ± 0.1	274.7 ± 14.0	95.7 ± 4.9
IC, A6 – A7	3.5 ± 0.4	45.7 ± 4.8	15.9 ± 1.7
Isotropic	1.06 ± 0.04	248.1 ± 10.4	86.4 ± 3.6

Note. — The normalizations of the diffuse components are freely scaled, as well as all 3FGL sources in the region. The fit uses the all-sky isotropic spectrum. Intensities are calculated by using the total area of the TR, which is 0.287 sr.

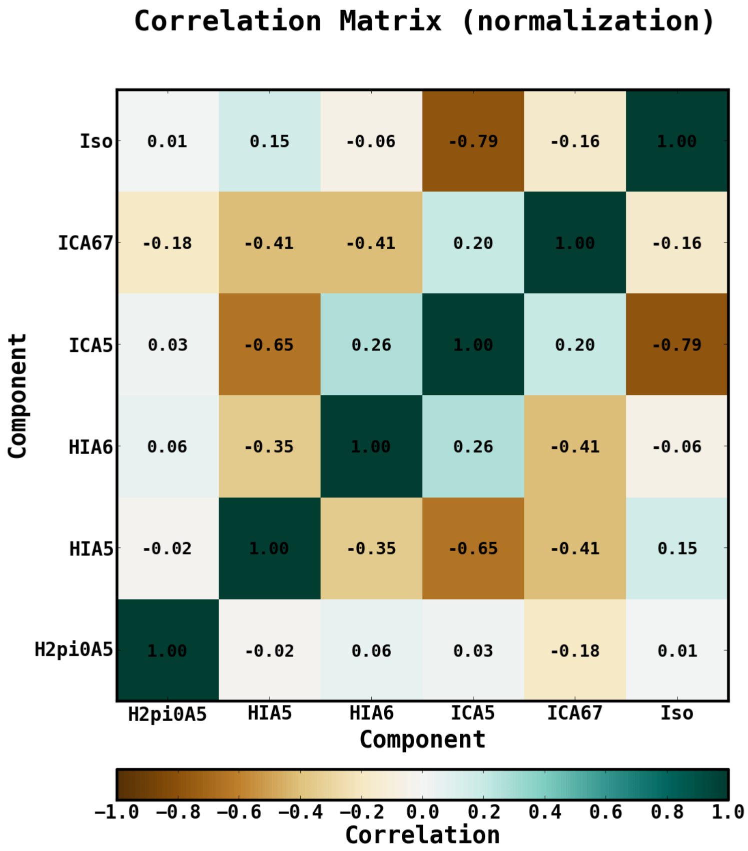

	H2pi0A5	HIA5	HIA6	ICA5	ICA67	Iso
Iso	0.01	0.15	-0.06	-0.79	-0.16	1.00
ICA67	-0.18	-0.41	-0.41	0.20	1.00	-0.16
ICA5	0.03	-0.65	0.26	1.00	0.20	-0.79
HIA6	0.06	-0.35	1.00	0.26	-0.41	-0.06
HIA5	-0.02	1.00	-0.35	-0.65	-0.41	0.15
H2pi0A5	1.00	-0.02	0.06	0.03	-0.18	0.01

Figure 4.11 Correlation matrix for the fit in the TR. For brevity IC A6 – A7 is labeled as ICA67, and the isotropic component is labeled as Iso.

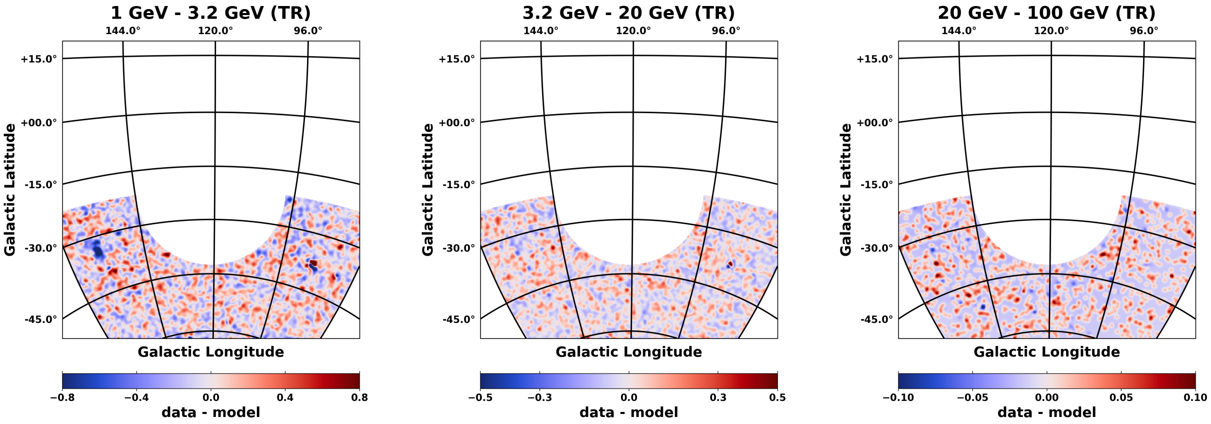

Figure 4.12 Spatial count residuals (data − model) resulting from the fit in the TR for three different energy bands, as indicated above each plot. The energy bins are chosen to coincide with an excess which is later observed in the fractional energy residuals for the fit in FM31, as discussed in the text. The color scale corresponds to counts/pixel, and the pixel size is $0.2° \times 0.2°$. The images are smoothed using a $1°$ Gaussian kernel. This value corresponds to the PSF (68% containment angle) of *Fermi*-LAT, which at 1 GeV is $\sim 1°$.

regions were masked and it's found that they do not significantly impact the normalizations of the diffuse components. Otherwise the residual maps in all three energy bins are pretty smooth, exhibiting no obvious features.

4.3 Analysis of the M31 Field

4.3.1 Baseline Fit and Point Source Finding Procedure

The data set employed in this work is approximately two times larger than the one used to derive the 3FGL. Therefore, in conjunction with the baseline fit, we search for additional point sources in FM31 to account for any un-modeled point-like structure that may otherwise contribute to the residual emission. The procedure we employ is similar to the one developed in Ajello et al. (2016). The point sources are initially modeled with the 3FGL. A maximum likelihood fit is performed by freeing the normalization of the 3FGL sources, as well as the H I- and H_2-related components. The top of FM31 also has contribution from IC A8, and its normalization is freed in the fit. The normalizations of the isotropic and IC components (A5 and A6 – A7) remain fixed to their best-fit values obtained in the TR. The H II and Bremsstrahlung components are fixed to their GALPROP predictions. Note that the Bremsstrahlung component possesses a normalization of 1.0 ± 0.6 in the TR, consistent with the GALPROP prediction.

A wavelet transform is applied to the residual map to find additional point source candidates. We employ PG-Wave (Damiani et al., 1997), included in the *Fermi*–LAT ScienceTools, which finds the positions of the point source candidates according to a user-specified signal-to-noise criterion (we use 3σ) based on the assumption of a locally flat background. Since PGWave does not provide spectral information, we model the spectrum of each point source candidate with a power law function and determine the initial values of the parameters via a maximum likelihood fit in the field, while all other components are held constant.

The determination of the spectrum is further refined by performing additional maximum likelihood fits concurrently with the other components in the region, i.e. 3FGL point sources, H I A5–A7, and H_2 A5. All point sources within a 30° radius of the field center are included in the model; however, only sources within a 20° radius are fit. The extra padding is included to account for the instrumental PSF. Owing to the large number of point sources involved, the fit is performed iteratively starting with the point sources (and point source candidates) with largest significance of detection. All point source candidates with a test statistic[9] $TS \geq 9$ are added to the model. Parameters for the additional point sources are summarized in Table 4.4.

Figure 4.13 shows the TS map calculated after the initial fit in FM31, before finding additional point sources. To reduce computational time, all components are held fixed to their best-fit values obtained in the initial fit. The TS map is calculated using the *gttsmap* function included in the ScienceTools. Note that we do not include an M31 template for the calculation. Overlaid on the map are the additional point sources that we found using our point source finding procedure. In total we found 4 sources with $TS \geq 25$ (besides the M31 source), and 17 sources with $9 \leq TS < 25$. A point source is found corresponding to the M31 disk, but this source is removed for the baseline fit, and no M31 component is included (likewise the M31 source is not listed in Table 4.4). Many of the new sources are correlated with large-scale structures which are also visible in the residual maps, and they are likely spurious sources which are actually features in the diffuse emission.

Figure 4.14 shows the final results for the flux and count residuals for the baseline fit in FM31, including additional point sources, with the normalizations of the isotropic and IC components fixed to their best-fit values obtained in the TR. The corresponding best-fit normalizations and integrated flux are reported in Table 4.5.

Below ~5 GeV the emission is dominated by H I A5, IC A5, and the isotropic component, in order of highest to lowest. A cross-over then occurs, and above ~5 GeV the order is reversed. The 3FGL sources also become more dominant at higher energies. The cumulative spectrum of the additional point sources is consistent with that of the 3FGL sources, although the flux is roughly an order of magnitude less.

The fractional residuals show an excess between ~3–20 GeV at the level of ~4%, and the data is being somewhat

---

[9] For a more complete explanation of the TS resulting from a likelihood fit see Mattox et al. (1996) and `https://fermi.gsfc.nasa.gov/ssc/data/analysis/documentation/Cicerone/Cicerone_Likelihood/`

Table 4.4. New point sources for FM31

Name	TS	l (degrees)	b (degrees)	Index α	Flux ($\times 10^{-10}$) (ph cm^{-2} s^{-1})
FM31_1	34	124.58	-32.60	2.61 ± 0.34	2.9 ± 0.7
FM31_2	31	122.66	-29.25	2.78 ± 0.33	2.8 ± 0.7
FM31_3	31	117.71	-26.83	2.33 ± 0.27	2.5 ± 0.6
FM31_4	29	131.86	-27.70	2.14 ± 0.24	1.9 ± 0.5
FM31_5	24	127.49	-9.62	3.81 ± 0.67	3.9 ± 0.9
FM31_6	23	129.91	-10.13	3.09 ± 0.39	3.4 ± 0.9
FM31_7	18	128.32	-10.58	2.25 ± 0.31	2.3 ± 0.8
FM31_8	18	111.53	-22.79	3.32 ± 0.55	2.7 ± 0.8
FM31_9	17	118.05	-31.02	2.41 ± 0.34	1.7 ± 0.6
FM31_10	17	119.73	-25.66	4.26 ± 1.26	2.1 ± 0.6
FM31_11	16	110.44	-25.71	2.90 ± 0.47	2.1 ± 0.7
FM31_12	15	108.73	-29.55	2.17 ± 0.36	1.5 ± 0.6
FM31_13	14	126.34	-11.63	3.12 ± 0.57	2.4 ± 0.8
FM31_14	14	118.27	-9.50	3.97 ± 0.96	2.7 ± 0.9
FM31_15	13	110.61	-33.64	3.90 ± 0.95	1.8 ± 0.6
FM31_16	13	120.13	-30.65	2.81 ± 0.55	1.7 ± 0.6
FM31_17	12	133.80	-8.37	2.29 ± 0.44	1.7 ± 0.8
FM31_18	11	126.84	-20.78	2.23 ± 0.37	1.3 ± 0.5
FM31_19	11	106.53	-28.95	4.85 ± 1.60	1.7 ± 0.6
FM31_20	11	116.65	-25.21	5.39 ± 1.48	1.6 ± 0.6
FM31_21	10	127.83	-27.92	2.48 ± 0.45	1.3 ± 0.5

Note. — The sources are fit with a power law spectral model $dN/dE \propto E^{-\alpha}$. The table gives the best-fit index, as well as the total flux, integrated between 1 GeV–100 GeV.

Table 4.5. Baseline Values for the IEM Components in FM31 (Tuned)

Component	Normalization	Flux ($\times 10^{-9}$) (ph cm^{-2} s^{-1})	Intensity ($\times 10^{-8}$) (ph cm^{-2} s^{-1} sr^{-1})
H I π^0, A5	0.82 ± 0.01	149.7 ± 2.5	63.6 ± 1.1
H I π^0, A6	0.1 ± 0.2	1.1 ± 2.4	0.5 ± 1.0
H I π^0, A7	3.2 ± 0.4	17.1 ± 2.0	7.3 ± 0.9
H_2 π^0, A5	2.9 ± 0.3	3.9 ± 0.4	1.7 ± 0.2
IC, A8	61.3 ± 13.0	11.3 ± 2.4	4.8 ± 1.0

Note. — The normalizations of the isotropic and IC components (A5 and A6 – A7) are held fixed to their best-fit values obtained in the TR. The normalizations of the π^0-related (H I and H_2) components are fit to the γ-ray data in FM31. Note that the top of FM31 has contribution from IC A8, and its normalization is also freely scaled. We also fit all 3FGL sources within 20° of M31, as well as additional point sources which we find using our point source finding procedure. Intensities are calculated by using the total area of FM31, which is 0.2352 sr.

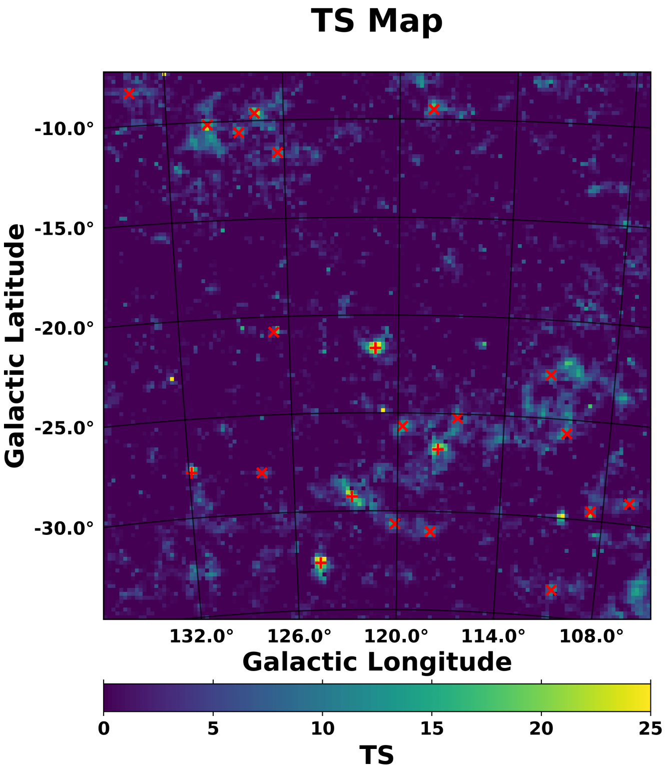

Figure 4.13 The TS map is calculated after the baseline fit in FM31 (tuned). Overlaid are the additional point sources that we found using our point source finding procedure. Red crosses represent new sources with TS≥25 and red slanted crosses represent new sources with 9≤TS<25.

over-modeled above and below this range. The over-modeling is expected as the fit tries to balance the excess with the negative residuals. This is in contrast to the TR which shows fairly good agreement over the entire energy range. The normalizations of H I A5 and A6 are low with respect to the GALPROP predictions, and likewise with respect to the values obtained in the TR and the all-sky fit. The normalization of H I A7 is high with respect to the GALPROP prediction. The normalization of H_2 is also high, but its contribution is minimal in FM31.

The spatial count residuals (data − model) resulting from the baseline fit are shown in Figures 4.15 and 4.16. The residuals are integrated in three different energy bins, as indicated above each plot. The energy bins are chosen to coincide with the positive residual emission observed in the fractional energy residuals. The residuals show structured excesses and deficits. In the first energy bin a large arc structure is observed. The upper-left corner shows bright excess emission, which extends around the field towards the projected position of M33. This structure is similar to what is seen in the TS map (Figure 4.13). Positive residual emission is also observed at the position of the M31 disk. In addition, the first energy bin shows deep over-modeling towards the top of the map and around the M31 disk. The second energy bin shows positive residual emission which is roughly uniform throughout the field, although the arc structure is also visible. In the third energy bin some holes can be seen corresponding to poorly modeled 3FGL

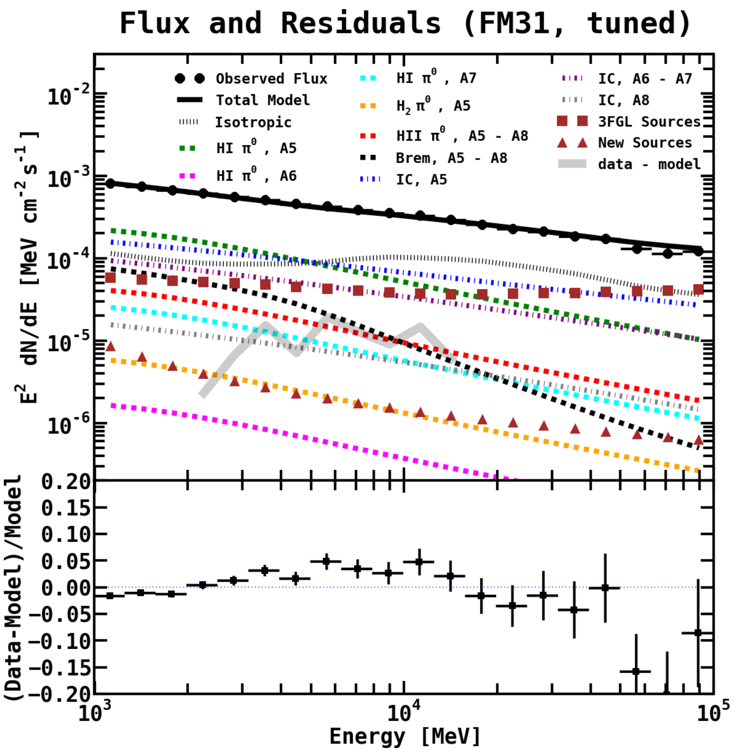

Figure 4.14 Flux (upper panel) and fractional count residuals (lower panel) for the fit in FM31 (tuned). The H II and Bremsstrahlung components are fixed to their GALPROP predictions. The normalizations of the IC (A5 and A6 – A7) and isotropic components are held fixed to the values obtained in the tuning region. The normalizations of the H I- and H_2-related components are fit to the γ-ray data in FM31, as well as 3FGL sources within 20° of M31, and additional point sources which we find using our point source finding procedure. Note that the top of FM31 has contribution from IC A8, and its normalization is also freed in the fit. The fractional residuals show an excess between ∼3–20 GeV reaching a level of ∼4%. Above and below this range the data is being over-modeled as the fit tries to balance the excess with the negative residuals. This is in contrast to the fit in the TR, which shows fairly good agreement over the entire energy range.

sources, but otherwise no obvious structures can be identified.

Figure 4.16 shows the same spatial residuals in gray scale, intentionally saturated in order to bring out weaker features. Overlaid are the point sources in the region, both 3FGL (green markers) and additional sources found in this analysis (red markers). Most of the additional sources are correlated with the arc structure. A majority of the 3FGL sources are AGN and are modeled with power-law (PL) spectra. We attempted to optimize the 3FGL spectra by fitting with a LogParabola spectral model, but this did not significantly change the positive residual emission, as discussed further in Appendix A.2.

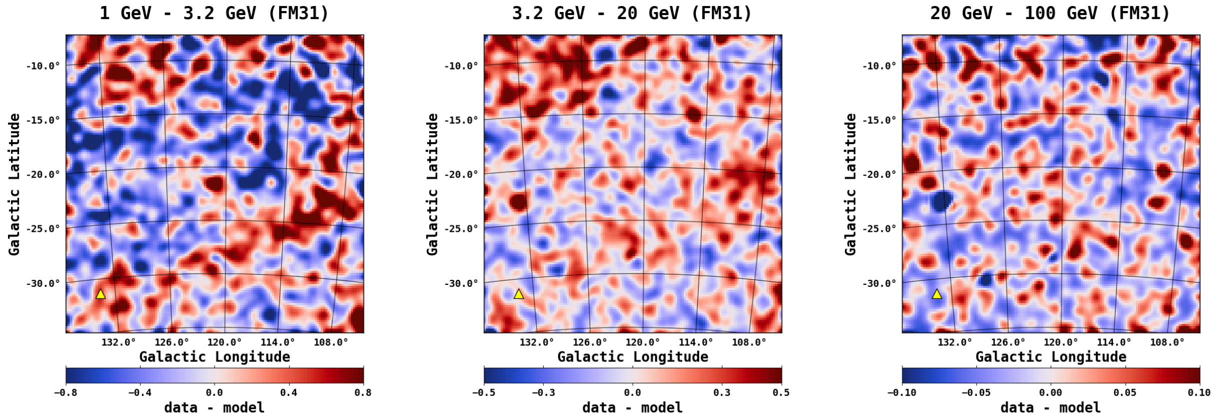

Figure 4.15 Spatial count residuals (data − model) resulting from the fit in FM31 (tuned) for three different energy bands, as indicated above each plot. The energy bins are chosen to coincide with the excess observed in the fractional residuals. The color scale corresponds to counts/pixel, and the pixel size is 0.2° × 0.2°. The images are smoothed using a 1° Gaussian kernel. This value corresponds to the PSF (68% containment angle) of *Fermi*-LAT, which at 1 GeV is $\sim 1^\circ$. For reference, the position of M33, $(l, b) = (133.61^\circ, -31.33^\circ)$, is shown with a yellow triangle.

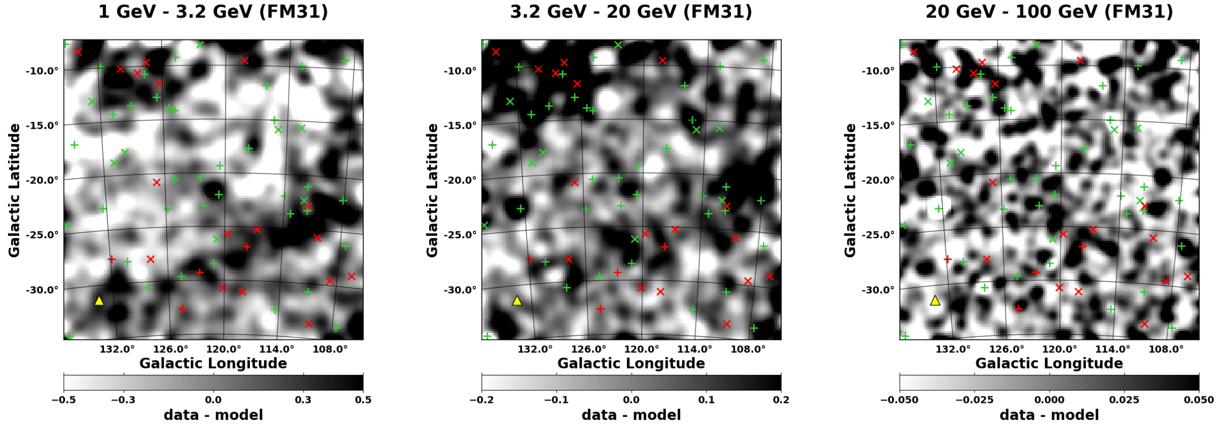

Figure 4.16 Same residual maps as shown in Figure 4.15. Here we show the maps in gray scale, and intentionally saturate the images to bring out weaker features. Overlaid are the point sources in the region. Crosses show sources with TS≥25 and slanted crosses show sources with 9≤TS<25. Fermi 3FGL sources are shown in green, and new sources found in this analysis are shown in red.

4.3.2 Analysis of the Galactic H I-related Emission in FM31

The structured excesses and deficits are an indication that the foreground emission may not be accurately modeled. In particular, the large arc structure observed in the first energy bin points to poorly modeled H I gas in the line of sight. The H I-related γ-ray emission depends on the column density of the gas, which in turn depends on the spin temperature. For this analysis the spin temperature is assumed to have a uniform value of 150 K, however, in reality it may vary over the region.

To further investigate the systematic uncertainty relating to the characterization of H I in the line of sight, we first compare the residual maps to the column densities for A5–A7, as shown in Figure 4.17. For visual clarity, the top row shows the column density filled contour maps. The units are 10^{20} cm^{-2}, and the levels are indicated on the maps. The second row shows the H I contours overlaid to the residual map integrated between 1–100 GeV. The residual emission is observed to be correlated with the column densities. In addition, the column densities of A6 and A7 are observed to be correlated with the major axis of M31 (the position angle of M31 is 38°).

The last row shows the same maps as the middle row, but for a 5° radius centered at M31. The IRIS 100 μm map of M31 is overlaid. Also overlaid are the regions corresponding to the two main spatial cuts which are made on the underlying H I maps when constructing the MW IEM. The spatial cuts correspond to cuts in velocity space, where the velocity is defined relative to the local standard of rest (LSR). Here we summarize all of the pertinent cuts made to the underlying H I gas maps:

- M31 cut (solid red box in Figure 4.17): $119^\circ \leq l \leq 123^\circ$, $-23.5^\circ \leq b \leq -19.5^\circ$, $V_{\mathrm{LSR}} < -120\ \mathrm{km\ s}^{-1}$;
- M31 cut (dashed green box in Figure 4.17): $121^\circ \leq l \leq 123^\circ$, $-22^\circ \leq b \leq -19.5^\circ$, $-120\ \mathrm{km\ s}^{-1} < V_{\mathrm{LSR}} < -50\ \mathrm{km\ s}^{-1}$;
- M33 cut:
  $132.5^\circ < l < 134.5^\circ, -33 < b < -30\ -460\ \mathrm{km\ s}^{-1} \leq V_{\mathrm{LSR}} \leq -60\ \mathrm{km\ s}^{-1}$;
- Anything above a given height z is assumed to be local gas (A5). The height is 1 kpc for R<8 kpc, but then increases linearly with R with a slope of 0.5 kpc/kpc. The cut is applied after determining the radial distance with the rotation curve and obtaining an estimate of z;
- Everything with $|V_{\mathrm{LSR}}| > 170\ \mathrm{km\ s}^{-1}$ and $|b| > 5^\circ$ is considered to be extragalactic;
- Everything with $V_{\mathrm{LSR}} < -100\ \mathrm{km\ s}^{-1}$ and $|b| > 30^\circ$ is considered to be extragalactic.

Note that these are the same cuts which are made for the official FSSC IEM. It was pointed out in Ackermann et al. (2017b) that for -50 km s^{-1}< V_{LSR} $<$ -30 km s^{-1}, foreground emission from the MW blends with the remaining signal from M31 at the north-eastern[10] tip of M31, and it is estimated that on some lines of sight in this direction up to $\sim$40% of the M31 signal might have been incorporated in the MW IEM. Besides, there may be additional H I gas in M31's outer regions which is wrongfully assigned to the MW, as discussed further in Section 4.5. Overall, the cuts (velocity and space) made to the underlying H I maps may be introducing systematics in the morphology of the extended M31 emission.

---

[10] For all directions relating to M31, north is up, and east is to the left.

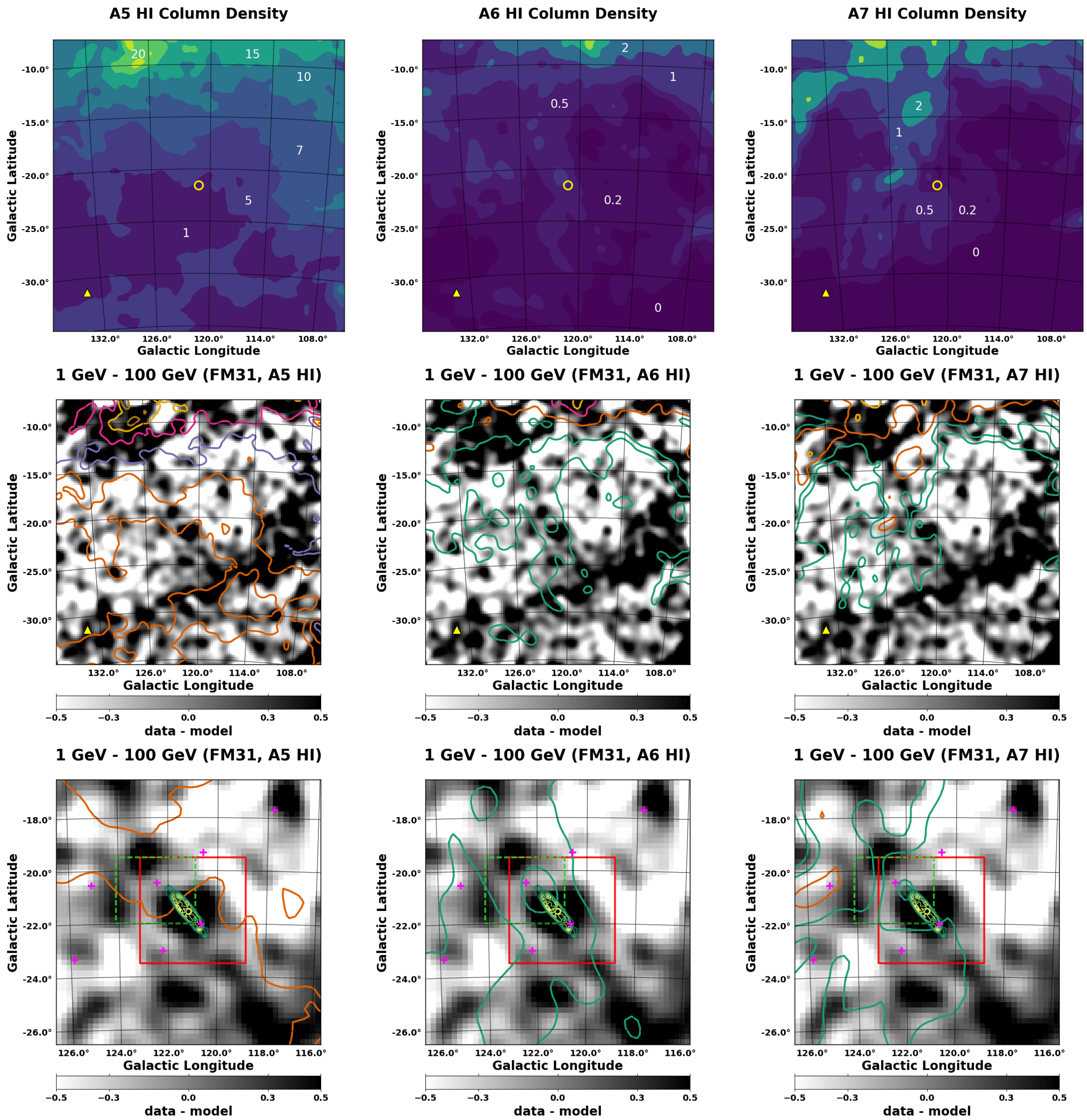
A5 HI Column Density

A6 HI Column Density

A7 HI Column Density

1 GeV - 100 GeV (FM31, A5 HI)

1 GeV - 100 GeV (FM31, A6 HI)

1 GeV - 100 GeV (FM31, A7 HI)

1 GeV - 100 GeV (FM31, A5 HI)

1 GeV - 100 GeV (FM31, A6 HI)

1 GeV - 100 GeV (FM31, A7 HI)

Figure 4.17 **Top Row:** H I column density contours for A5, A6, and A7, as indicated above each plot. For reference, a yellow circle ($0.4°$) centered at M31 is overlaid, and a yellow triangle is overlaid at the position of M33. The units are 10^{20} cm^{-2}, and the levels are indicated on the maps. **Middle Row:** The same H I column density contours are overlaid on the residual maps for FM31. The maps are integrated over the entire energy range 1–100 GeV. The residual emission is observed to be correlated with the column densities. In addition, the column densities of A6 and A7 are observed to be correlated with the major axis of M31 (the position angle of M31 is 38°). **Bottom Row:** The same maps as for the middle row but for a $5°$ radius centered at M31. Contours for the IRIS 100 μm map of M31 are overlaid. The levels shown range from 6–22 MJy sr^{-1}. Also overlaid are the regions corresponding to the two main cuts (space and velocity) which are made on the underlying gas maps when constructing the MW IEM, as detailed in the text. Lastly, we overlay the 3FGL sources (magenta crosses) in the region with TS$\geq$25. In particular, we consider the two point sources located closest to the M31 disk, since we are interested in the true morphology of the M31 emission. The source located to the right of the disk (3FGL J0040.3+4049) is a blazar candidate and has an association. The source located to the left of the disk (3FGL J0049.0+4224) is unassociated.

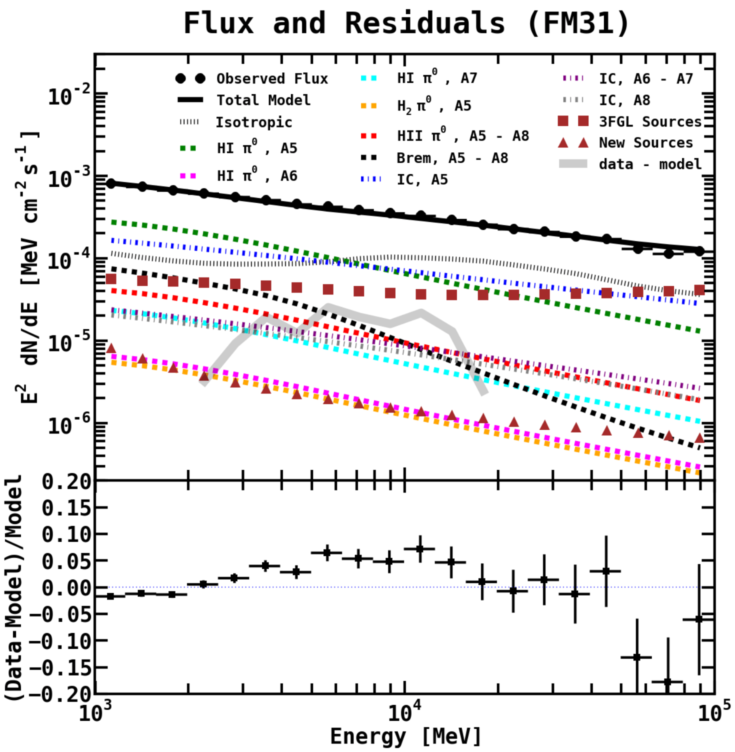

Figure 4.18 Additional freedom is given to the baseline fit. The IC components are fit simultaneously with the other contributing diffuse components and point sources. The isotropic component remains fixed to it's value obtained in the TR (1.06).

Also shown in Figure 4.17 are the 3FGL sources in the region with TS$\geq$25. In particular, we consider the two point sources located closest to the M31 disk, since we are ultimately interested in ascertaining the true morphology of the M31 emission. The source located to the right of the disk (3FGL J0040.3+4049) is a blazar candidate and has an association. The source located to the left of the disk (3FGL J0049.0+4224) is unassociated. We identify this source as conspicuous, in that it may actually be part of a larger diffuse structure.

Because of the poor data–model agreement and the poor description of the H I-related components, we allowed for additional freedom in the fit by also scaling the IC components (A5 and A6–A7) in FM31. The fit is performed just as for the baseline fit. Figure 4.18 shows the resulting flux and residuals, and the corresponding best-fit normalizations are reported in Table 4.6. Overall, a better fit is obtained. The likelihood value is $-\log L = 143268$, compared to the tuned fit which is $-\log L = 143302$.

The H I A5 component obtains a normalization of 1.04, which is comparable to the value obtained in the TR, and close to the GALPROP model prediction. The normalization of H I A6 is still low at $\sim$40% of the model prediction. We note that the H I A6 flux is less than that of H I A7, which is due to the fact that the radial extension of A6 is

Table 4.6. Baseline Values for the IEM Components in FM31 (IC scaled)

Component	Normalization	Flux ($\times 10^{-9}$) (ph cm^{-2} s^{-1})	Intensity ($\times 10^{-8}$) (ph cm^{-2} s^{-1} sr^{-1})
H I π^0, A5	1.04 ± 0.04	189.3 ± 6.9	80.5 ± 2.9
H I π^0, A6	0.4 ± 0.2	4.4 ± 2.5	1.9 ± 1.0
H I π^0, A7	2.9 ± 0.4	15.8 ± 2.1	6.7 ± 8.8
H_2 π^0, A5	2.7 ± 0.3	3.7 ± 0.4	1.6 ± 0.2
IC, A5	2.4 ± 0.1	125.0 ± 7.0	53.1 ± 3.0
IC, A6 – A7	0.9 ± 0.3	17.3 ± 6.4	7.3 ± 2.7
IC, A8	80.5 ± 16.4	14.8 ± 3.0	6.3 ± 1.3

Note. — The isotropic component is held fixed to the best-fit value obtained in the TR (1.06). All other diffuse sources and point sources are freely scaled in FM31, including the IC components. This is in contrast to the FM31 tuned fit, where the IC components are held fixed to the best-fit values obtained in the TR. Intensities are calculated by using the total area of FM31, which is 0.2352 sr.

1.5 kpc, compared to A7 which has a radial extension of 5 kpc. The normalization of IC A5 is consistent with the value obtained in the TR. On the other hand, the normalization of IC A6–A7 has a value of 0.9 ± 0.3, compared to the TR value of 3.5 ± 0.4. The normalization of IC A8 is very high, but this is a weak component with contribution only towards the top of the field. Despite the additional freedom the model is unable to flatten the positive residual emission between ∼3–20 GeV, and it actually becomes slightly more pronounced. The spatial residuals for this fit are qualitatively consistent with the residuals in Figure 4.15. The correlation matrix for the fit is given in Figure 4.19.

As already discussed, the H I column density depends on the value of the spin temperature, which is used to convert the observed 21-cm brightness temperature to column densities. In general the spin temperature may have some spatial variation. The CR density may also vary over the field, and likewise for the ISRF density. To account for these possibilities we divide FM31 into three equal subregions: top, middle, and bottom. Each subregion is then further divided equally into right and left. In each subregion we rescale the diffuse components. The point sources remain fixed to the best-fit values obtained in the baseline fit (with IC scaled).

The fractional count residuals that result from this rescaling are shown in Figure 4.20. The black data points show the residuals resulting from the baseline fit (over the entire field) calculated in the given subregion. The top row shows the residuals for the fit performed in the top, middle, and bottom regions, respectively. The second and third rows show the results for rescaling the normalizations in the regions which are further divided into right and left.

Even with these smaller subregions the model is unable to flatten the positive residual emission between ∼3–20 GeV. Note that for many of these subregions the best-fit normalizations of the diffuse components resulting from the

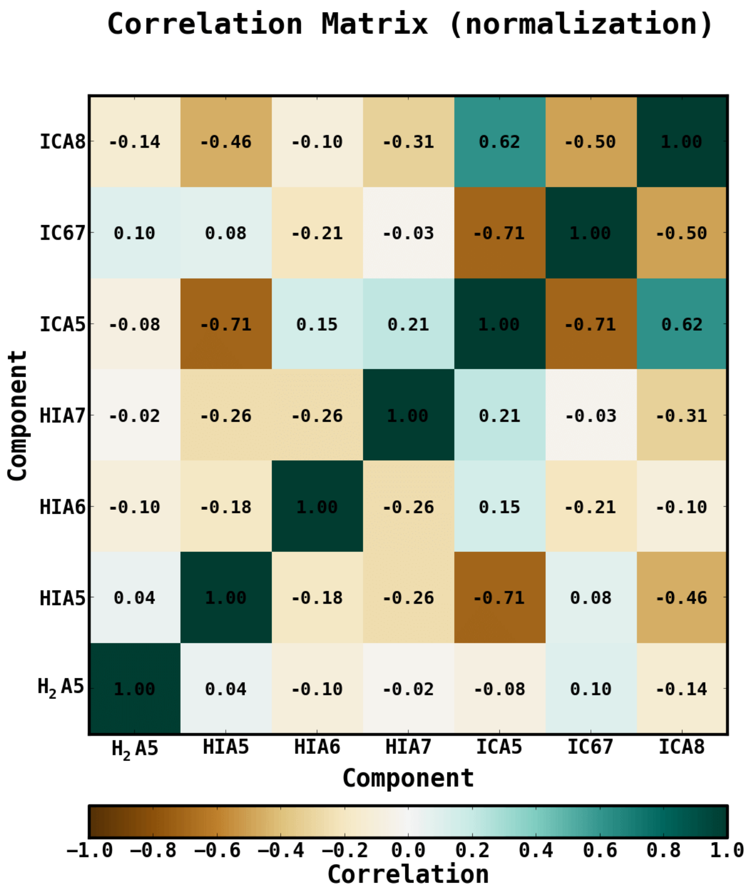

	H_2A5	HIA5	HIA6	HIA7	ICA5	IC67	ICA8
ICA8	-0.14	-0.46	-0.10	-0.31	0.62	-0.50	1.00
IC67	0.10	0.08	-0.21	-0.03	-0.71	1.00	-0.50
ICA5	-0.08	-0.71	0.15	0.21	1.00	-0.71	0.62
HIA7	-0.02	-0.26	-0.26	1.00	0.21	-0.03	-0.31
HIA6	-0.10	-0.18	1.00	-0.26	0.15	-0.21	-0.10
HIA5	0.04	1.00	-0.18	-0.26	-0.71	0.08	-0.46
H_2A5	1.00	0.04	-0.10	-0.02	-0.08	0.10	-0.14

Figure 4.19 Correlation matrix for the FM31 baseline fit with the IC components scaled.

rescaling are not very physical, as some of the components go to zero, since they are not very well constrained and the fit simply tries to optimize the likelihood. Nevertheless, the model is still unable to fully flatten the residuals.

Meanwhile, the residuals do start to become a bit more uniformly distributed. For example, when performing the fit over the entire field, the residuals in the top left are much more pronounced than the top right. For the rescaling in the different subregions, the top left residuals are decreased (between ∼3–20 GeV), whereas the top right residuals become a bit more pronounced. The same general trend can be seen in most of the subregions. The residuals are fairly flat in the bottom right, however, the bottom left (which contains M33) shows positive residual emission.

4.3.3 Arc Template

Thus far the model has been unable to flatten the positive residual emission observed between ∼3–20 GeV. Furthermore, the spatial residuals show structured excess and deficits. It may be due to some foreground MW gas that is not well traced by the 21-cm emission. On the other hand, or in addition, the positive residual emission may be re-

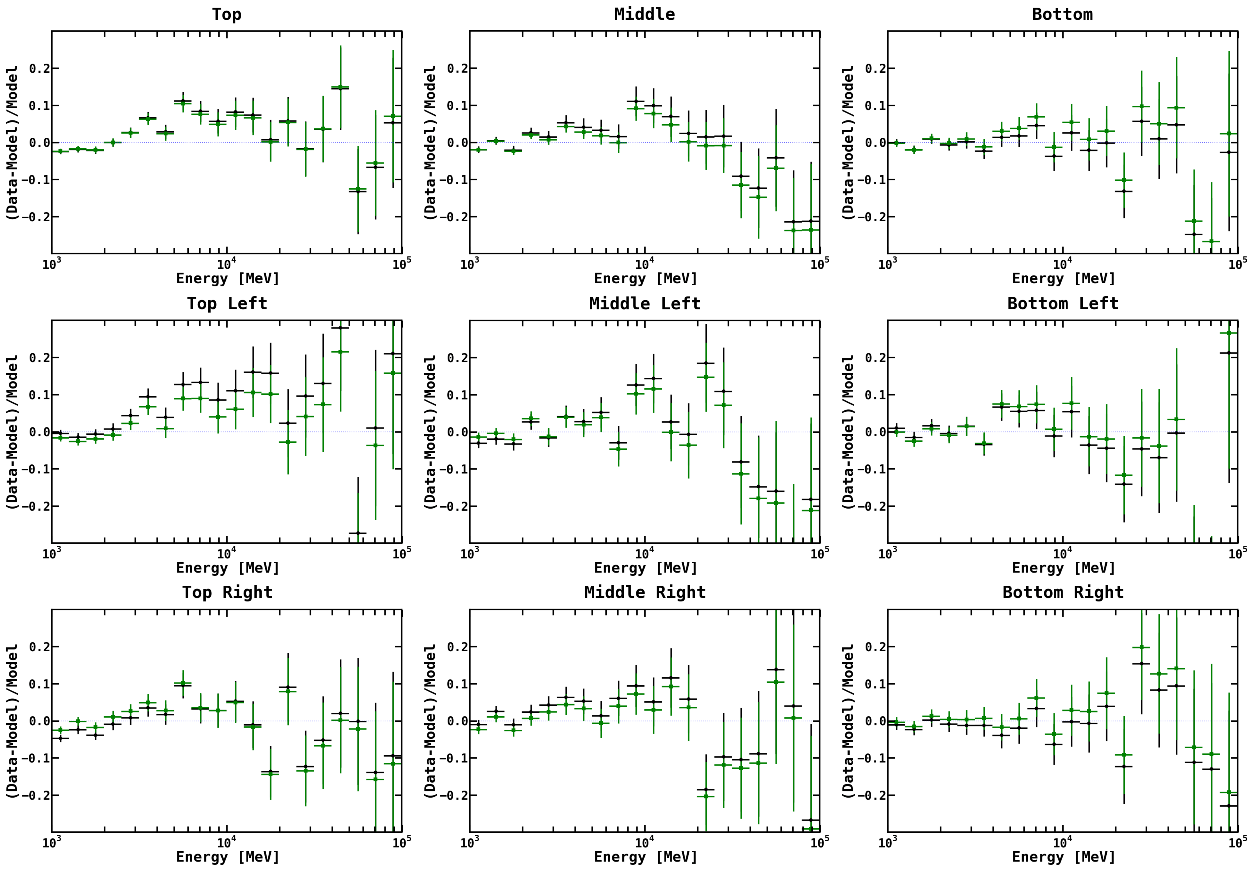

Figure 4.20 Fractional residuals calculated in different spatial regions. The field is evenly divided into top, middle, and bottom. Each slice is then further divided into right and left. The regions are indicated above each plot. Black data points show the residuals resulting from the baseline fit (which is over the entire field, with IC scaled in addition to the other contributing components). We then rescale the diffuse components in the different subregions (green data points), masking the rest of the region, and keeping the point sources fixed to their baseline values. This is done to allow for a spatially varying spin temperature and/or CR and ISRF densities, which would in turn change the normalizations of the γ-ray components. Even in these smaller regions the diffuse components are unable to flatten the residuals, with the exception of the bottom right, which is pretty flat.

lated to the M31 system, for which no model components are currently included. We note that the residuals behave qualitatively the same even when masking the inner region of the M31 disk (0.4°).

Our ultimate goal is to test for a γ-ray signal exhibiting spherical symmetry with respect to the center of M31, since there are numerous physical motivations for such a signal. However, before adding these components to the model, we employ a template approach to account for the arc-like feature observed in the spatial residuals, which may be related to foreground MW emission, and is not obviously related to the M31 system.

The first two panels in Figure 4.21 show the spatial residuals integrated between 1–100 GeV, resulting from the baseline fit (see Figure 4.18). In order to construct a template for the large arc extending from the top left corner to the projected position of M33 (arc template), we divide the total residual map into positive residuals (left) and negative

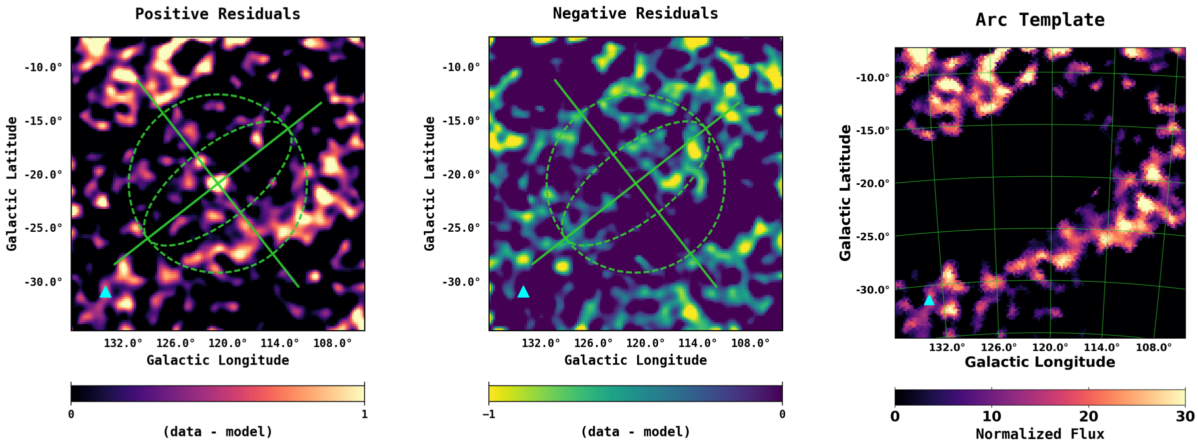

Figure 4.21 The first two panels show the spatial count residuals integrated between 1–100 GeV, resulting from the baseline fit (see Figure 4.18). In order to construct a template for the large arc extending from the top left corner to the projected position of M33 (arc template), we divide the total residual map into positive residuals (left) and negative residuals (middle). The maps show the geometry used to help facilitate the template construction, as detailed in the text. The corresponding geometrical parameters are given in Table 4.7. The resulting arc template is shown in the far right panel. In addition to fitting the full arc template, we also perform a variation of the fit in which the arc template is divided into a north component (arc north: $b > -16.5°$) and a south component (arc south: $b \leq -16.5°$), where the spectral parameters of each component are allowed to vary independently. The cut is made right below the bright emission in the upper-left corner, and it allows the north component to be at a different distance along the line of sight than the south component, as discussed in the text. The cyan triangle shows the projected position of M33.

residuals (middle). Overlaid is the geometry used to help facilitate the template construction. All geometry is plotted based on the general equation of an ellipse, which can be written as

$$a^{-2}\left\{(x-h)\cos\phi+(y-k)\sin\phi\right\}^2+\ b^{-2}\left\{(x-h)\sin\phi+(y-k)\cos\phi\right\}^2=1 \tag{4.3}$$

where the center is given by (h, k), a and b are the major and minor axes, respectively, and ϕ is the orientation angle of the ellipse. All geometrical parameters are given in Table 4.7. Note that the geometry corresponds to the γ-ray emission as observed in the stereographic projection, with the pole of the projection centered at M31. The plotted coordinate system (solid axes) is centered at M31 and oriented with respect to the position angle of the M31 disk (38°). The large dashed green circle has a radius of $8.5°$ ($R_{\text{tan}} = 117$ kpc). The corresponding border facilitates the cut for the north-east side, and the radius is determined by the bright emission in the upper-left corner. The inner ellipse is used to facilitate the cut on the south-west side. This cut follows the natural curvature of the arc. Any emission not connected to the large arc is removed.

The resulting normalized template is shown in the far right panel of Figure 4.21. By adding the arc template to the model we obtain a cleaner view towards M31's outer halo, and we are able to make inferences regarding the origin of the arc structure. We test two variations of the fit. In one variation we add a single template for the full arc. The arc is

Table 4.7. Geometrical Parameters for the Arc Template

Component	$2a$ [deg]	$2b$ [deg]	ϕ [deg]
M31 position angle axis	25	0	38
M31 perpendicular axis	25	0	128
Dashed circle	17	17	38
Dashed ellipse	17	7	38

Note. — M31 geometry is centered at $(h, k) = (121.17°, -21.57°)$. Angles are defined with respect to the positive x-axis (Cartesian plane), and they correspond to the major axis of the ellipse. Note that the geometry corresponds to the γ-ray emission as observed in the stereographic projection, with the pole of the projection centered at M31.

given a PL spectral model and the spectral parameters (normalization and index) are fit simultaneously with the other components in the region, just as for the baseline fit. In the second variation of the fit, the arc template is divided into a north component (arc north: $b > -16.5°$) and a south component (arc south: $b \leq -16.5°$). The cut is made right below the bright emission in the upper-left corner. Both components are given PLEXP spectral models (power law function with exponential cutoff), and the spectral parameters (normalization, index, and cutoff) of each component are allowed to vary independently. This allows the north component to be at a different distance along the line of sight than the south component, since different distances may correspond to different spectral parameters. Note that we also tried a number of different variations to the arc fit, and they all gave similar results as the two variations that we show here.

Results for the fits are given in Figure 4.22. The top panels show best-fit spectra, and bottom panels show the remaining fractional residuals. For comparison, black dashed lines show the best-fit H I spectra that result from the baseline fit, as shown in Figure 4.18. For visual clarity, we show just the arc template and gas-related components. Spectra for the other components are qualitatively consistent with the results shown in Figure 4.18. The arc template is unable to flatten the positive residual emission between ∼3–20 GeV, but the split arc fit with PLEXP spectral models does provide flatter residuals above ∼20 GeV. The correlation matrix for the arc north and south fit is shown in Figure 4.23.

Table 4.8 gives the best-fit normalizations for the diffuse components for both fits, as well as the overall likelihoods. Note that the normalizations are comparable for both fit variations. The last two columns report the total integrated flux and intensity for the arc north and south fit, which has the best likelihood. The corresponding best-fit parameters for the arc template components are reported in Table 4.9. For the baseline fit (Figure 4.18) the total integrated flux for H I A5 is 189.3 ± 6.9 ph cm^{-2} s^{-1}. For the arc north and south fit the total integrated flux for H I A5 plus the arc

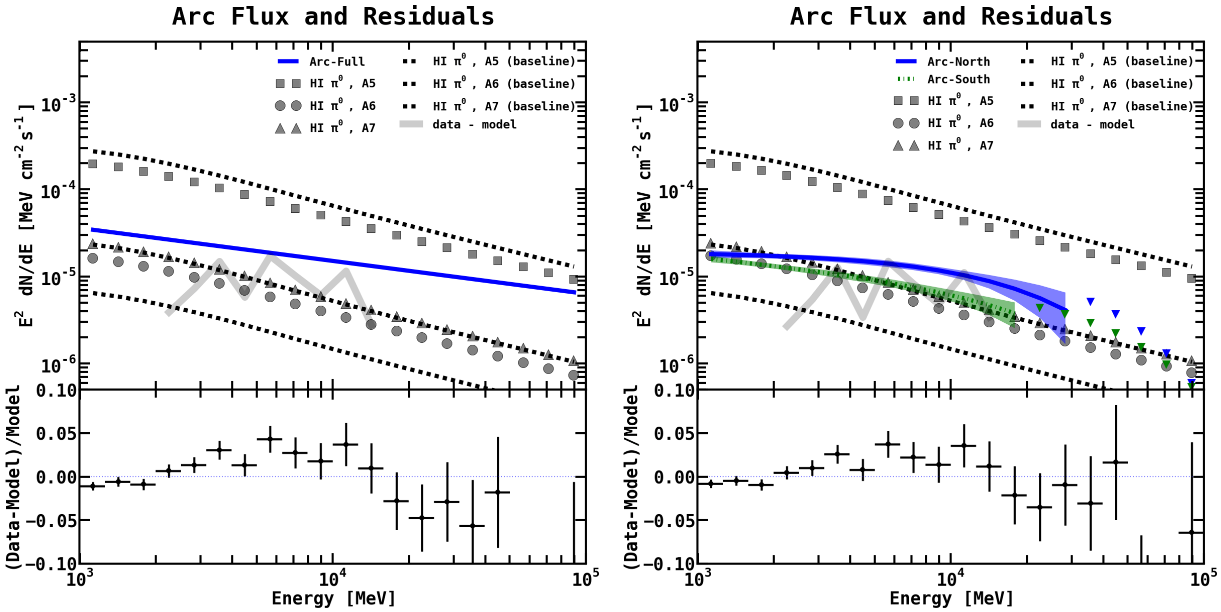

Figure 4.22 Spectra and fractional count residuals resulting from the arc fit. **Left:** The full arc component is given a PL spectrum, and the normalization and index are fit simultaneously with the other components in the region, just as for the baseline fit. Black dashed lines show the H I A5 (top), A6 (bottom), and A7 (middle) components from the baseline fit (not the arc fit). Note that A7 has a greater radial extension than that of A6, and likewise it has a greater overall flux. Correspondingly, the gray markers (squares, circles, and triangles) show the H I A5–A7 spectra resulting from the arc fit. The blue solid line is the best-fit spectrum for the arc template. The bottom panel shows the remaining fractional residuals. **Right:** The arc template is given additional freedom by dividing it into north and south components. The arc components are given PLEXP spectral models, and the spectral parameters (normalization, index, and cutoff) are freely scaled with the other components. Downward pointing blue and green triangles give upper-limits. Bands give the 1σ error. The arc template is unable to flatten the excess between ∼3–20 GeV.

Table 4.8. Normalizations of the Diffuse Components, Integrated Flux, and Likelihoods for the Arc Fits

Component	Arc Full (PL)	Arc North and South (PLEXP)	Flux ($\times 10^{-9}$) (ph cm^{-2} s^{-1})	Intensity ($\times 10^{-8}$) (ph cm^{-2} s^{-1} sr^{-1})
H I π^0, A5	0.74 ± 0.04	0.75 ± 0.04	137.3 ± 8.0	58.4 ± 3.4
H I π^0, A6	1.1 ± 0.2	1.2 ± 0.2	11.7 ± 2.5	5.0 ± 1.1
H I π^0, A7	3.0 ± 0.4	3.0 ± 0.4	16.2 ± 2.1	6.9 ± 0.9
H_2 π^0, A5	2.6 ± 0.3	2.7 ± 0.3	3.7 ± 0.4	1.6 ± 0.2
IC, A5	2.5 ± 0.1	2.6 ± 0.1	134.2 ± 7.4	57.1 ± 3.1
IC, A6 – A7	1.6 ± 0.3	1.5 ± 0.3	28.5 ± 6.4	12.1 ± 2.7
IC, A8	92.0 ± 17.0	62.0 ± 18.2	11.4 ± 3.3	4.8 ± 1.4
$-\log L$	142972	142954	⋯	⋯

Note. — Columns 2–3 give the best fit normalizations for the diffuse components. The last two columns report the total integrated flux and intensity between 1–100 GeV for the arc north and south fit, which is the fit with the best likelihood. Note that the normalizations for the diffuse components are comparable for both variations of the fit. The bottom row gives the resulting likelihood for each respective fit. Intensities are calculated by using the total area of FM31, which is 0.2352 sr.

Table 4.9.   Results for the Arc Templates

Template	area (sr)	TS	Flux ($\times 10^{-9}$) (ph cm^{-2} s^{-1})	Intensity ($\times 10^{-8}$) (ph cm^{-2} s^{-1} sr^{-1})	Counts	Index α	Cutoff (GeV)
AF	0.08	651	26.0 ± 1.4	32.4 ± 1.7	6872	2.38 ± 0.05	...
AN	0.03	457	15.7 ± 1.4	46.4 ± 4.1	4071	2.0 ± 0.2	18.3 ± 14.8
AS	0.05	416	12.0 ± 1.0	25.9 ± 2.2	3210	2.3 ± 0.1	24.6 ± 19.7

Note. — The components are listed as arc full (AF), arc north (AN), and arc south (AS). The TS is defined as $-2\Delta \log L$, and it is the value reported by *pylikelihood* (a fitting routine from the *Fermi*–LAT ScienceTools package), without refitting. Fits are made with a power-law spectral model $dN/dE \propto E^{-\alpha}$ and with a model with exponential cut off $dN/dE \propto E^{-\alpha} \exp{(-E/E_c)}$.

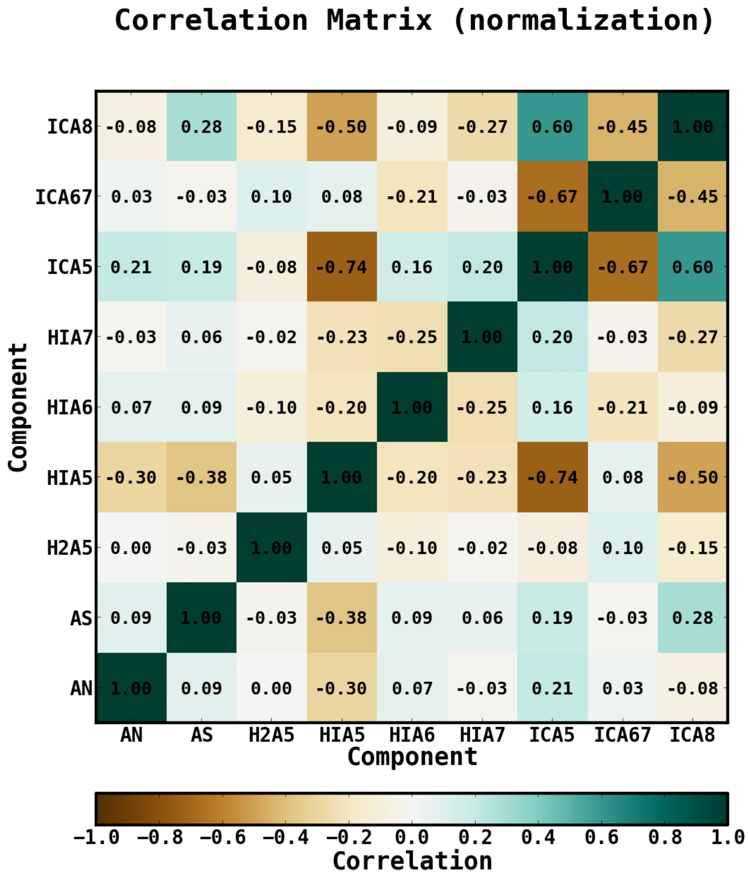

	AN	AS	H2A5	HIA5	HIA6	HIA7	ICA5	ICA67	ICA8
ICA8	-0.08	0.28	-0.15	-0.50	-0.09	-0.27	0.60	-0.45	1.00
ICA67	0.03	-0.03	0.10	0.08	-0.21	-0.03	-0.67	1.00	-0.45
ICA5	0.21	0.19	-0.08	-0.74	0.16	0.20	1.00	-0.67	0.60
HIA7	-0.03	0.06	-0.02	-0.23	-0.25	1.00	0.20	-0.03	-0.27
HIA6	0.07	0.09	-0.10	-0.20	1.00	-0.25	0.16	-0.21	-0.09
HIA5	-0.30	-0.38	0.05	1.00	-0.20	-0.23	-0.74	0.08	-0.50
H2A5	0.00	-0.03	1.00	0.05	-0.10	-0.02	-0.08	0.10	-0.15
AS	0.09	1.00	-0.03	-0.38	0.09	0.06	0.19	-0.03	0.28
AN	1.00	0.09	0.00	-0.30	0.07	-0.03	0.21	0.03	-0.08

Figure 4.23 The correlation matrix for the arc north (AN) and south (AS) fit.

flux is 165.0 ± 10.4 ph cm^{-2} s^{-1}. Thus with the arc template the total H I A5 flux is decreased by $\sim$13%. The flux is later increased when adding the M31-related components to the model, in addition to the arc template, as discussed in Section 4.3.4. With the arc template the H I A6 normalization has a value close to the GALPROP prediction. The normalization for IC A8 remains high, but this is a weak component with contribution only towards the top of the field.

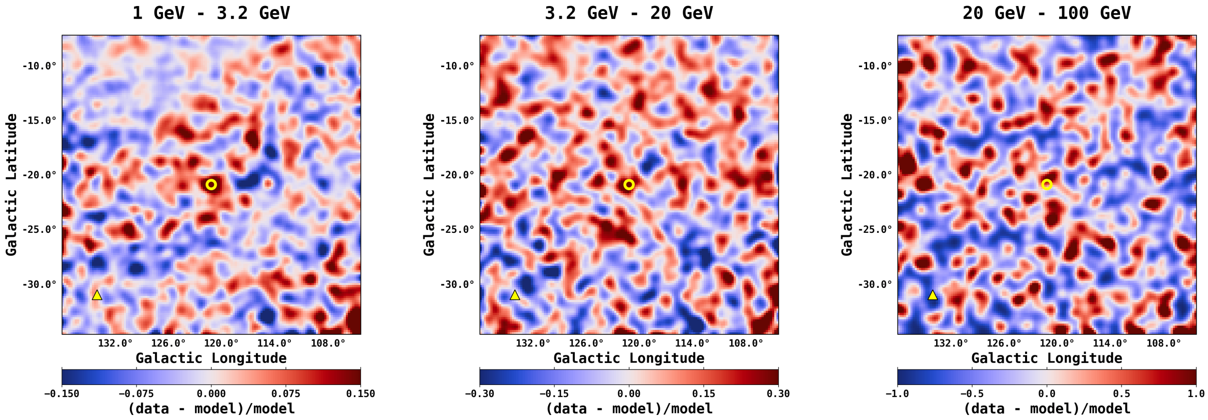

Figure 4.24 Spatial count residuals resulting from the arc fit. To give a sense of the deviations, here we show the fractional residuals, where we divide by the model counts for each pixel. The residuals are integrated in three energy bins, just as for the residuals in Figure 4.15. We show residuals from the arc north and south fit, with PLEXP spectral model. Residuals for the full arc fit with PL spectral model are very similar. The arc structure no longer dominates the residuals, as expected. The position of M33 is indicated with a yellow triangle, and the center of M31 is indicated with a 0.4° open circle.

Spatial residuals resulting from the arc north and south fit are shown in Figure 4.24. Results for the full arc fit are very similar. To give a sense of the deviations, we show the fractional residuals, where we divide by the model counts for each pixel. The residuals are divided into three energy bins, just as for the residuals in Figure 4.15. The arc structure no longer dominates the residuals, as expected. In the first energy bin bright emission can be seen at the center of the map, corresponding to the inner galaxy of M31. In addition, the residuals in the first bin still show structured excesses and deficits, possibly associated with emission from M31's outer disk and halo. The second energy bin coincides with the positive residual emission observed in the fractional energy residuals. The spatial distribution of the emission is roughly uniform throughout the field, although small-scale structures can be observed. The third energy bin is roughly uniform with no obvious features. The distribution of the residual emission in FM31 is further quantified in Section 4.3.5, where we consider the symmetry of the excess.

In Figure 4.25 we plot the measured local average emissivity per H atom, resulting from all fits in FM31. The dash-dot grey curve comes from the baseline fit with IC scaled, and gives the proper estimate of the emissivity in FM31. The dashed grey curve comes from the arc fit with PL spectral model, and it only includes the contribution from the H I A5 component, but not the emission associated with the arc. The best-fit normalizations are listed in the legend. Also plotted is the corresponding measurement made in Casandjian (2015), which is determined from a fit including absolute latitudes between 10°–70°. Additionally, we plot the results from Ackermann et al. (2012d), for which the emissivity is determined from different nearby molecular cloud complexes, within ∼300 pc from the solar system. Lastly, we plot the measurements from Abdo et al. (2009a), as determined from a mid-latitude region in the third Galactic quadrant, i.e. $200^\circ < l < 260^\circ$ and $22^\circ < |b| < 60^\circ$. The local emissivity as determined from

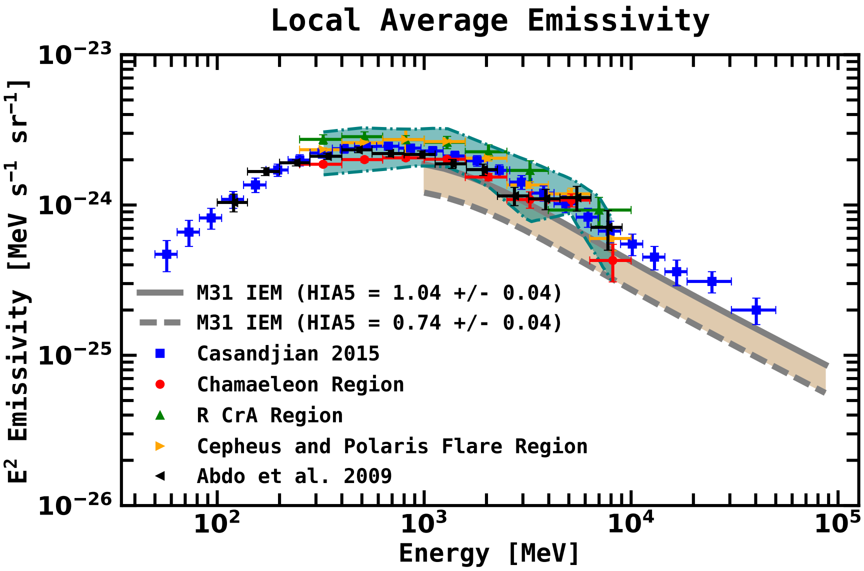

Figure 4.25 The average local (A5) emissivity per H atom. The dashed-dot grey curve comes from the baseline fit with IC scaled, and it gives the proper estimate of the emissivity in FM31. The dashed grey curve at the bottom comes from the arc fit with PL spectral model, and it only includes the contribution from the H I A5 component, but not the emission associated with the arc. The blue data points (squares) are from Casandjian (2015), and the corresponding error bars are systematic+statistical. The fit includes absolute latitudes between 10°–70°. The data points for the different regions (red circles, green upward-pointing triangles, and yellow rightward-pointing triangles) are from Ackermann et al. (2012d), and the corresponding error bars are statistical only (1σ). The teal band shows the total uncertainty (statistical+systematic) from the same analysis (from the erratum). The different regions are among the nearest molecular cloud complexes, within ∼300 pc from the solar system. We also plot the measurements from Abdo et al. (2009a) (black leftward-pointing triangles), as determined from a mid-latitude region in the third Galactic quadrant.

FM31 is slightly lower (referring to the baseline normalization of 1.04), but it is consistent within 1σ with these other measurements. This is not surprising since the analysis by Ackermann et al. (2012d) is based on observations of the well-defined gas clouds residing within ∼300 pc from the solar system. Meanwhile, our “local ring” is 2 kpc thick (Table 4.1), while FM31 is projected toward the outer Galaxy where the CR density is predictably low.

As we see, inclusion of the arc template into the fit improves its quality significantly. Meanwhile, the origin of the arc itself remains unknown. As we show below, the arc is most likely associated with the interstellar gas, its underpredicted column density, and/or with particles whose spectrum is distinctly flatter than the rest of CRs.

In Figure 4.26 we show the dust temperature map and the $\mathrm{E(B-V)}$ reddening map for FM31 from Schlegel et al. (1998). Overlaid are contours for the arc template. The levels correspond to the normalized flux, and they range from 1–20 in increments of 5. The dust temperature serves as a possible proxy for the gas temperature. In this analysis we have assumed a uniform spin temperature of 150 K, but as can be seen in the top panel of Figure 4.26, much of the arc template correlates with cold regions in the dust, indicating that at least part of the corresponding residuals may be

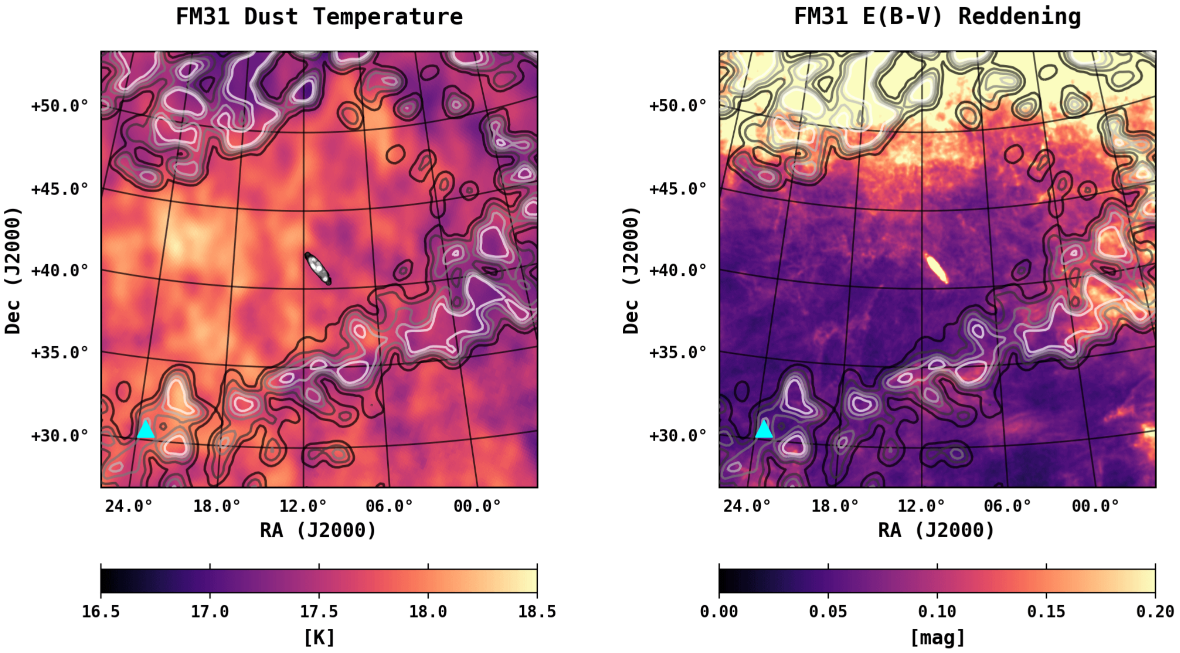

Figure 4.26 Top panel shows the dust temperature map for FM31, and the bottom panel shows the dust reddening map, from Schlegel et al. (1998), as discussed in the text. Overlaid are contours for the arc template. Contours for the IRIS 100 μm map of M31 are also overlaid in the top panel. The cyan triangle shows the (projected) position of M33.

caused by an under prediction of the H I column density.

As can be seen in Figure 4.26, much of the arc template closely correlates with the foreground dust, and likewise it correlates with the local H I column density, as seen in Figure 4.17, indicating that the corresponding emission is most likely due to inaccuracies in the foreground model. Although our model already corrects for the DNM, the method is full sky and may use an incorrect gas to dust ratio for this particular region. In addition, the method also assumes a linear conversion between gas and dust, which may not actually be the case. Also, we note that while the spatial correlation between the arc template and properties of the dust is clearly visible towards the Galactic plane and the extended arm at the far right of the map, the region associated closest with M33 (in projection) and its general vicinity is not as obviously correlated.

The analysis described in this section clearly shows that the arc is associated with the gas, but its components have the spectral index of ∼2.0–2.4, noticeably flatter than the rest of the H I gas ∼2.75 in the ROI (Figure 4.22). This may imply that the spectrum of CR particles interacting with gas in this direction is flatter than the spectrum of the old component of CRs that is altered by the long propagation history. Indeed, radio observations and sometimes X-rays and γ-rays reveal structures that cover a considerable area of the sky and are often referred to as “radio loops”. The most well-known is Loop I, which has a prominent part of its shell aligned with the North Polar Spur, but other

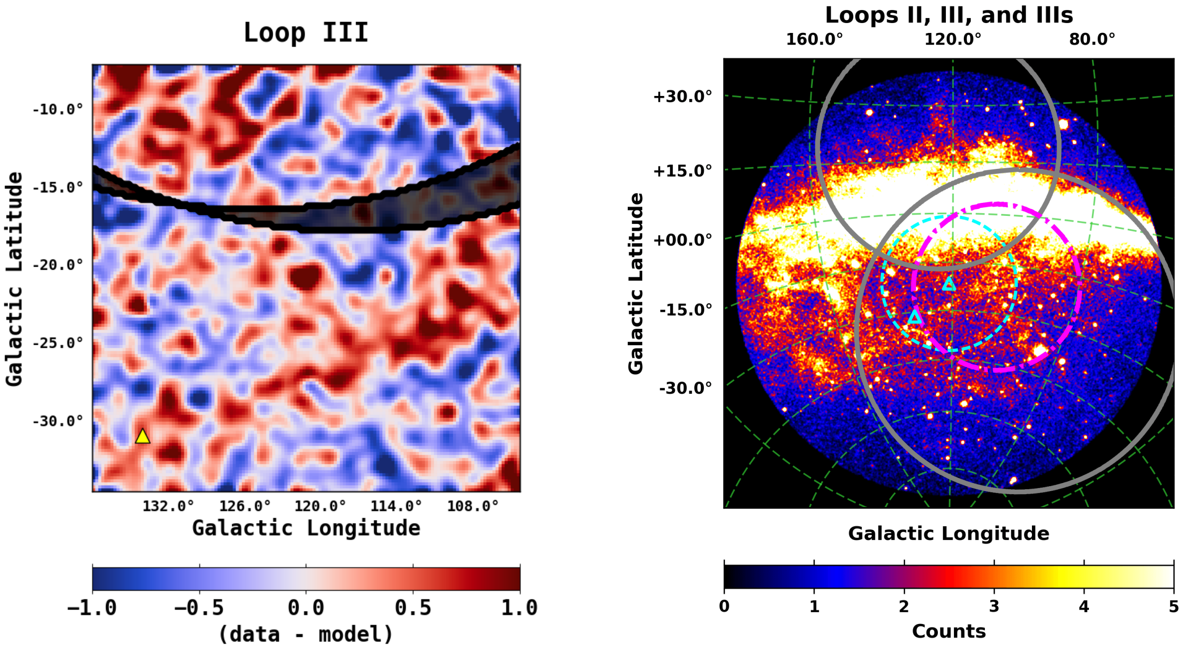

Figure 4.27 **Left:** FM31 residuals from the baseline fit (with IC scaled) with the Loop III shell plotted over it. The two lines correspond to two somewhat different positions and radii obtained from continuum and polarization observations (Vidal et al., 2015). The shell radius is approximate and the shell itself can be several degrees thick. The shaded area gives an idea of the error associated with the parameters of the shell. **Right:** M31's virial radius (300 kpc) is shown with a cyan dashed circle, and cyan triangles show the positions of M31 and M33. The grey circles show Loop III at the top and Loop II at the bottom. Loop IIIs (which is only visible in polarization) is shown with a dash-dot magenta circle.

circular structures and filaments also become visible in polarization skymaps. There are, at least, 17 known structures (for details see Vidal et al., 2015, and references therein) with the radii of tens of degrees that can be as large as ∼80° for the Loop XI. The spectral indices of these structures indicate a non-thermal (synchrotron) origin for the radio emission, but the origin of the loops is not completely clear. One of the major limitations is the lack of precise measurements of their distances. The current explanations include old and nearby SNR, bubbles/shells powered by OB associations, and some others.

It turns out that a part of the shell of Loop III seems to be associated with the north part of the arc (Figure 4.27) and Loops II and IIIs are covering the entire ROI. Presence of accelerated electrons associated with the Loop III shell hints that protons with a flat spectrum can also be present there. This may explain the distinctly different spectral index of the arc template and an exponential cutoff significantly below 50 GeV (Figure 4.22 right) that corresponds to the ambient particle energies below ∼1 TeV. Here we are not speculating further if the whole arc or only a part of it is associated with the Loop III shell or with other Loops, leaving a detailed analysis for a followup paper.

4.3.4 M31 Components

The baseline model seems unable to account for the total emission in FM31. We now proceeded to add to the model M31-related components, for which we make the simplifying assumption of spherical symmetry with respect to the center of M31. For the inner galaxy we add a uniform disk with a radius of 0.4°, consistent with the best-fit morphology in Ackermann et al. (2017b). We add a second uniform template centered at M31 with a radial extension of $0.4^\circ < r \leq 8.5^\circ$. This is the geometry as determined in Figure 4.21, which was used to help facilitate the construction of the arc template. We note that although the outer radius was set by the bright residual emission in the upper-left corner, it also happens to encompass a large H I cloud centered in projection on M31, possibly associated with the M31 system (i.e. the M31 cloud), as well as a majority of M31's globular cluster population and stellar halo, which will be further discussed in Section 4.5. The radial extension corresponds to a projected radius of 117 kpc. We label this component as FM31 spherical halo.

Lastly, we add a third uniform template with a radial extension of $r > 8.5^\circ$, covering the remaining extent of the field. This corresponds to M31's far outer halo, and likewise it begins to approach the MW plane towards the top of the field. This is the template that suffers most from Galactic confusion. We label this component as FM31 far outer halo.

All of the M31-related component are given PLEXP spectral models, and the spectral parameters (normalization, index, cutoff) are fit with the arc template and the other baseline components. We note that the spectra of the M31 components have also been fit with a power law per every other energy band, as well as a standard power law, and the results are consistent with the PLEXP model (for example see Figure A.10). The fit is performed in the standard way just as for the baseline fit. We perform two main variations of the fit, amounting to different variations of the arc template. For one variation we use the full arc template with PL spectral model. For the second variation we use the north and south arc templates with PLEXP spectral models.

The intensities and residuals resulting from the fits with the arc template and M31 components are shown in Figure 4.28. The left panel is for the full arc template with PL spectral model. The right panel is for the north and south arc templates with PLEXP spectral model. Black dashed lines show the best-fit spectra for the H I A5 (top), A6 (bottom), and A7 (middle) components. The black dashed-dot line shows the isotropic component, which remains fixed to its best-fit value obtained in the tuning region, just as for all other fits. The best-fit spectra of the remaining components are similar to that shown in Figure 4.18, and are left out here for visual clarity. The bottom panel shows the remaining fractional residuals, which are fairly flat over the entire energy range, and likewise show a normal distribution with a mean of zero. The best fit normalizations and flux for the diffuse components are reported in Table 4.10, as well as the fit likelihood. Best-fit parameters for the arc template and M31-related components are reported in Tables 4.11

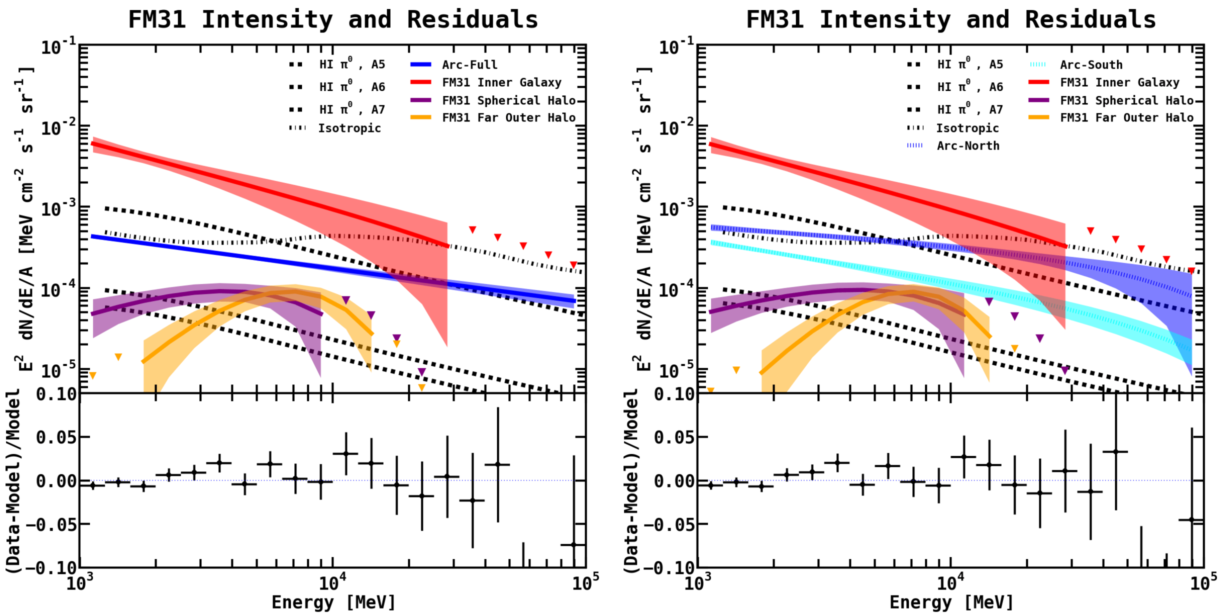

Figure 4.28 M31-related components are added to the model, in addition to the arc template, and standard baseline components. The left panel is for the full arc template with PL spectral model, and the right panel is for the north and south arc templates with PLEXP spectral model, just as in Figure 4.22. Black dashed lines show the best-fit spectra for the H I A5 (top), A6 (bottom), and A7 (middle) components. The black dashed-dot line shows the isotropic component, which remains fixed to its best-fit value obtained in the tuning region, just as for all other fits. The best-fit spectra of the remaining components are similar to that shown in Figure 4.18, and are left out here for visual clarity. Downward pointing triangles give upper-limits. Bands give the 1σ error. The bottom panel shows the remaining fractional residuals, which are fairly flat over the entire energy range, and likewise show a normal distribution with a mean of zero.

and 4.12.

We note that for the M31-related components the TS is defined as $-2\Delta\log L$, and it is the value reported by pylikelihood, without refitting. In order to obtain a more conservative estimate of the statistical significance of the M31-related components, and in particular, the components corresponding to the outer halo, we make the following calculation. We define the null model as consisting of the standard components (point sources and diffuse), arc template (north and south), and M31 inner galaxy component. Then for the alternative model we also include the spherical halo and far outer halo components. We find that the alternative model is preferred at the confidence level of roughly 8σ ($-2\Delta\log L$=65).

The total integrated flux for the H I A5 component plus the arc north and south components is 185.6 ± 12.9 ph cm^{-2} s^{-1}, consistent with that of the baseline fit (with IC scaled). The normalization of the H I A6 component is consistent with the GALPROP prediction. The normalization of the H I A7 component is still a bit high (2.8 ± 0.4). The normalizations of the IC A5 and A6-A7 components are consistent with the all-sky average obtained in the isotropic calculation (Table 4.2). The intensity of the arc south component at ∼10 GeV is at the same level as that of the

Table 4.10. Normalizations of the Diffuse Components, Integrated Flux, and Likelihoods for the Arc Fits with M31 Components

Component	Arc Full (PL)	Arc North and South	Flux ($\times 10^{-9}$) (ph cm^{-2} s^{-1})	Intensity ($\times 10^{-8}$) (ph cm^{-2} s^{-1} sr^{-1})
H I π^0, A5	0.85 ± 0.05	0.88 ± 0.05	159.8 ± 9.1	67.9 ± 3.9
H I π^0, A6	0.9 ± 0.2	1.0 ± 0.2	10.3 ± 2.5	4.4 ± 1.1
H I π^0, A7	2.8 ± 0.4	2.9 ± 0.4	15.3 ± 2.1	6.5 ± 0.9
H_2 π^0, A5	2.7 ± 0.3	2.7 ± 0.3	3.7 ± 0.4	1.6 ± 0.2
IC, A5	2.2 ± 0.2	2.2 ± 0.2	115.2 ± 8.6	49.0 ± 3.7
IC, A6 – A7	1.2 ± 0.4	1.0 ± 0.4	20.1 ± 7.0	8.6 ± 3.0
IC, A8	88.5 ± 19.0	59.7 ± 20.2	11.0 ± 3.6	4.7 ± 1.5
$-\log L$	142933	142919	···	···

Note. — Columns 2 and 3 give the best fit normalizations for the diffuse components. The last two columns report the total integrated flux and intensity between 1–100 GeV for the arc north and south fit. The bottom row gives the resulting likelihood for each respective fit. Intensities are calculated by using the total area of FM31, which is 0.2352 sr.

Table 4.11. Results for the Arc Template (Full, PL) and M31 Components

Template	area (sr)	TS	Flux ($\times 10^{-9}$) (ph cm^{-2} s^{-1})	Intensity ($\times 10^{-8}$) (ph cm^{-2} s^{-1} sr^{-1})	Counts	Index α	Cutoff, E_c (GeV)
AF	0.080232	616	25.5 ± 1.4	31.8 ± 1.7	6739	2.42 ± 0.05	···
IG	0.000144	55	0.5 ± 0.1	347.2 ± 69.4	141	2.8 ± 0.3	96.4 ± 151.6
SH	0.0684	34	4.2 ± 1.6	6.1 ± 2.3	1158	0.7 ± 1.1	2.9 ± 2.9
FOH	0.166656	32	4.3 ± 1.9	2.6 ± 1.1	1142	–1.4 ± 1.2	2.0 ± 0.7

Note. — The TS is defined as $-2\Delta \log L$, and it is the value reported by pylikelihood, without refitting. Fits are made with a power-law spectral model $dN/dE \propto E^{-\alpha}$ and with a model with exponential cut off $dN/dE \propto E^{-\alpha} \exp{(-E/E_c)}$. The components are labeled as arc full (AF), inner galaxy (IG), spherical halo (SH), and far outer halo (FOH).

Table 4.12. Results for the Arc Template (North and South, PLEXP) and M31 Components

Template	area (sr)	TS	Flux ($\times 10^{-9}$) (ph cm^{-2} s^{-1})	Intensity ($\times 10^{-8}$) (ph cm^{-2} s^{-1} sr^{-1})	Counts	Index α	Cutoff, E_c (GeV)
AN	0.033864	438	15.5 ± 1.3	45.8 ± 3.8	4027	2.2 ± 0.1	84.5 ± 100.4
AS	0.046368	395	11.8 ± 0.7	25.4 ± 1.5	3155	2.5 ± 0.1	100.0 ± 6.6
IG	0.000144	53	0.5 ± 0.08	347.2 ± 55.6	139	2.8 ± 0.3	100.0 ± 10.6
SH	0.0684	39	4.5 ± 1.2	6.6 ± 1.8	1223	0.9 ± 0.8	4.0 ± 3.6
FOH	0.166656	30	3.8 ± 1.3	2.3 ± 0.8	1020	–1.8 ± 1.3	1.8 ± 0.6

Note. — The TS is defined as $-2\Delta \log L$, and it is the value reported by pylikelihood, without refitting. Fits are made with a model with exponential cut off $dN/dE \propto E^{-\alpha} \exp{(-E/E_c)}$. The components are labeled as arc north and south (AN and AS), inner galaxy (IG), spherical halo (SH), and far outer halo (FOH).

Table 4.13. Results for the Symmetry Test

Template	area (sr)	TS	Flux ($\times10^{-9}$) (ph cm^{-2} s^{-1})	Intensity ($\times10^{-8}$) (ph cm^{-2} s^{-1} sr^{-1})	Counts	Index α	Cutoff, E_c (GeV)
SHN	0.0342	89	5.1 ± 1.3	14.9 ± 3.8	1388	1.2 ± 0.6	4.2 ± 3.3
SHS	0.0342	28	2.7 ± 1.2	7.9 ± 3.5	743	1.9 ± 0.5	11.6 ± 15.0
FOHN	0.0833	89	6.8 ± 2.1	8.2 ± 2.5	1805	-0.6 ± 0.8	2.4 ± 0.8
FOHS	0.0833	31	4.7 ± 2.4	5.6 ± 2.9	1233	2.7 ± 0.4	97.5 ± 21.9

Note. — The TS is defined as $-2\Delta \log L$, and it is the value reported by pylikelihood, without refitting. Fits are made with a model with exponential cut off $dN/dE \propto E^{-\alpha} \exp(-E/E_c)$. The components are labeled as spherical halo north and south (SHN and SHS), and far outer halo north and south (FOHN and FOHS).

M31-related components, and its spectrum is softer than the spectrum of the north component.

In Appendix A.2 we perform additional systematic checks. Using the M31 IEM we allow for extra freedom in the fit. We also repeat the analysis with two alternative IEMs, namely, the IG IEM and FSSC IEM. Each alternative IEM has its own self-consistently derived isotropic spectrum and additional point sources. Full details of these tests are given in Appendix A.2. Here we summarize the main findings.

Using the M31 IEM we allow for extra freedom in the fit by varying the index of the IC components with a PL scaling. In this case the IC components show a spectral hardening towards the outer Galaxy, for both the TR and FM31. However, this is unable to flatten the excess in FM31, and the properties of the excess remain qualitatively consistent with the results presented above.

Using the M31 IEM we also vary the index of the H I-related components using a PL scaling. In the TR the local annulus shows no change in the index. However, in FM31 there is a hardening of the index for the local annulus, with a significantly increasing hardening towards the outer Galaxy. This result is in direct contrast to the gradual softening which has been reported by other studies (Acero et al., 2016; Yang et al., 2016). FM31 clearly shows an anomaly with respect to these other measurements, as well as an anomaly with respect to the results in the TR and the GALPROP predictions (see Figure A.2). The anomaly is most clearly evident for the outer Galaxy rings, A6 and A7, and it is also these rings which are found to be partially correlated with the M31 system, as is clearly seen in Figure 4.17. In particular, the H I A7 component obtains a best-fit index $\Delta\alpha$ of –0.39 ± 0.11, which corresponds to an effective index of 2.37, compared to its GALPROP prediction of 2.76. This result further supports the conclusion that there is some significant anomaly in FM31. This particular fit is also able to do a better job at flattening the excess in the fractional energy residuals, however, some excess emission still remains. To quantify the remaining excess we fit the M31-related components. In this case the spherical halo is still detected at $\sim$3–4σ and the spectral properties are qualitatively consistent with the main results.

For the IG IEM the spectrum of the isotropic component is determined at high latitudes ($|b| > 50^{\circ}$), and the normalization is held fixed to its nominal value (1.0). This is in contrast to the M31 IEM, for which we use the all-sky isotropic spectrum, with the normalization determined in a tuning region directly below FM31. The fit is otherwise performed in the standard way. The residuals are qualitatively consistent with what we find for the M31 IEM.

We also repeat the fit using the FSSC IEM. We fit both the isotropic component and the Galactic diffuse component in the signal region, as well as the point sources. We perform the fit with and without freeing the index of the Galactic diffuse component. In the latter case the excess remains qualitatively consistent with what we find for the M31 IEM (both the fractional count residuals and the spatial residuals). However, in the former case the IEM is able to flatten the excess in the fractional count residuals (the spatial residuals remain qualitatively the same). This illustrates how the application of an improper IEM for analysis of largely extended emission can alter the physical results.

A summary of the excess in the fractional energy residuals for all fit variations tested in this analysis is shown in Figure 4.29. We conclude that a systematic excess is present between $\sim$3–20 GeV at the level of $\sim$3–5%. The signal is only flattened with the FSSC IEM (intended for point source analysis), when fitting all components in the signal region (including the index of the Galactic diffuse component), whereas all other fits result in an excess. Our benchmark model is the M31 IEM.

4.3.5 Symmetry of the Residual Emission in FM31

In this section we further test the symmetry of the residual emission in FM31. We divide the spherical halo and far outer halo templates into north and south components. The cut is made at the midpoint of FM31 along the horizontal direction (parallel to the Galactic plane), corresponding to a latitude of $\sim -21.5^{\circ}$. This allows for deviation from spherical symmetry, as well as a gradient with respect to the Galactic plane.

We first calculate the fractional count residuals in the different regions without fitting any of the M31-related templates. These results are shown in Figure 4.30, and they correspond to the spatial residuals shown in Figure 4.24, resulting from the baseline fit with the arc north and south templates. The excess can be seen for both the spherical halo and far outer halo regions. For the spherical halo region, the excess appears to be more prominent in the north compared to the south, although it is present in both. For the far outer halo region, the excess is prominent in the north, whereas the residuals in the south are pretty flat.

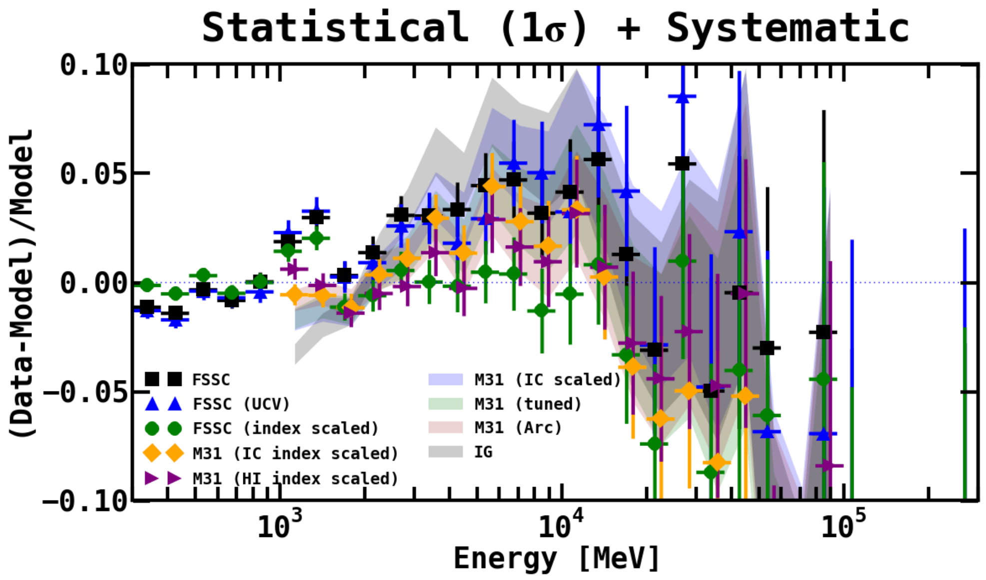

Figure 4.29 A systematic excess can be observed between ∼3–20 GeV at the level of ∼3–5%. Systematic over-modeling is also present above and below this range. We note that there is one model for which the signal can be flattened (shown with green circles). This results from using the FSSC IEM (intended for point source analysis) and fitting both the isotropic and Galactic diffuse (including the index) in the signal region. The FSSC IEM is not intended for extended source analysis, and this result illustrates how the application of an improper IEM for analysis of largely extended emission can alter the physical results. The M31 IEM is our benchmark model. The different models are as follows: **black squares:** FSSC IEM, fitting the isotropic and Galactic diffuse (with index fixed) in the signal region, using Clean data, corresponding to the fit in Figure A.8; **blue upward-pointing triangles:** same as for the black squares but using UltraCleanVeto (UCV) data; **green circles:** same as for the black squares but also freeing the index of the Galactic diffuse; **orange diamonds:** M31 IEM baseline fit, varying the index of the IC components A5-A8 using a power law scaling, corresponding to the fit in Figure A.1; **purple rightward-pointing triangles:** M31 IEM baseline fit, varying the index of the H I-related components A5–A8 using a power law scaling, corresponding to the fit in Figure A.2. Note that in this case FM31 shows a significant anomaly in the index of the gas-related emission towards the outer Galaxy, as is clearly shown in Figure A.2. **blue band:** M31 IEM baseline fit, corresponding to the fit in Figure 4.18; **green band:** M31 IEM tuned fit, corresponding to the fit in Figure 4.14; **pink band:** M31 IEM arc fit, corresponding to the fit in Figure 4.22 (this is our primary model); **black band:** inner Galaxy (IG) IEM, corresponding to the fit in Figure A.4.

We quantify the symmetry of the residual emission by fitting templates for the different regions simultaneously with the other components of the IEM. The M31-related components include the inner galaxy and the northern and southern regions of the spherical halo and far outer halo (5 components in total). Each component is given a PLEXP spectral model, and the spectral parameters are allowed to vary independently (although the components are fit simultaneously). The fit also includes the arc north and south components. Lastly, we scale the diffuse components and point sources in the standard way.

The resulting spectra for the northern and southern regions of the spherical halo and far outer halo are shown in Figure 4.31. For reference, we also overlay the spectra for the full M31-related components (from Figure 4.28). The spectra for the arc components are very similar to the results shown in Figure 4.28, and therefore we don't show them

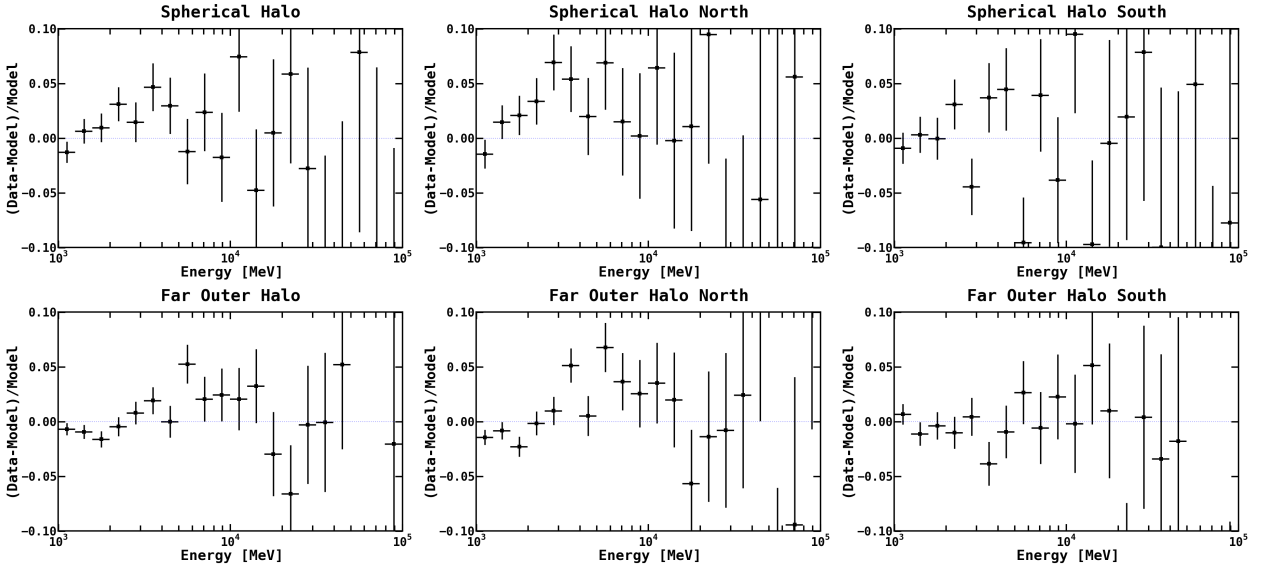

Figure 4.30 The fractional count residuals calculated over the different spatial regions corresponding to the spherical halo and far outer halo components, as indicated above each plot. Note that these are the residuals before adding the M31-related components, and they correspond to the spatial residuals shown in Figure 4.24, resulting from the baseline fit with the arc north and south templates. The goal here is to further examine the symmetry of the residual emission associated with the M31-related components. We consider the northern and southern regions of the templates, where the cut is made at the midpoint of FM31 along the horizontal direction (parallel to the Galactic plane), corresponding to a latitude of $-21.5°$. The first column shows the residuals calculated over the entire region, for the spherical halo and far outer halo, respectively. The second column shows the residuals in the north, and the third column shows the residuals in the south.

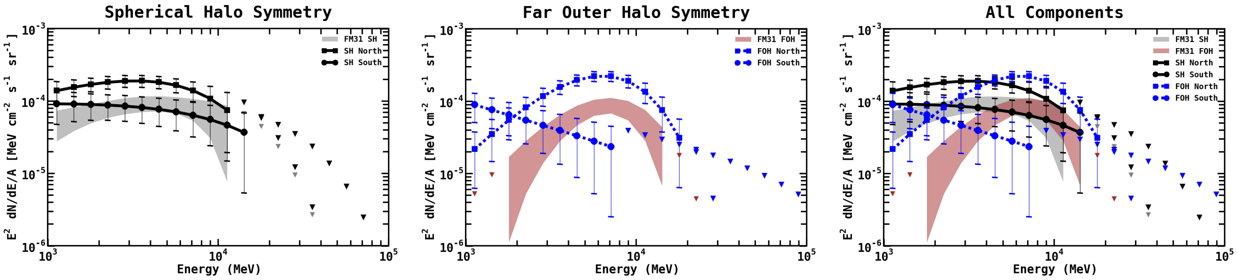

Figure 4.31 The best-fit spectra resulting from the symmetry test fit, where the spherical halo and far outer halo templates are divided into north and south components, and the spectral parameters for each component are allowed to vary independently. The cut is made at the midpoint of FM31 along the horizontal direction (parallel to the Galactic plane), corresponding to a latitude of $-21.5°$. The northern components are shown with square markers, and the southern components are shown with circle markers. Downward pointing triangles give upper limits. Also overlaid are the spectra for the full component fit (with arc north and south), as shown in Figure 4.28.

here. The corresponding best-fit parameters for the halo components are reported in Table 4.13. All components are significantly detected (with a significance $> 5\sigma$).

The spherical halo region is slightly brighter in the north than the south. The best-fit spectra for the two components have similar spectral shapes and are qualitatively consistent with that of the full template. We note that we have

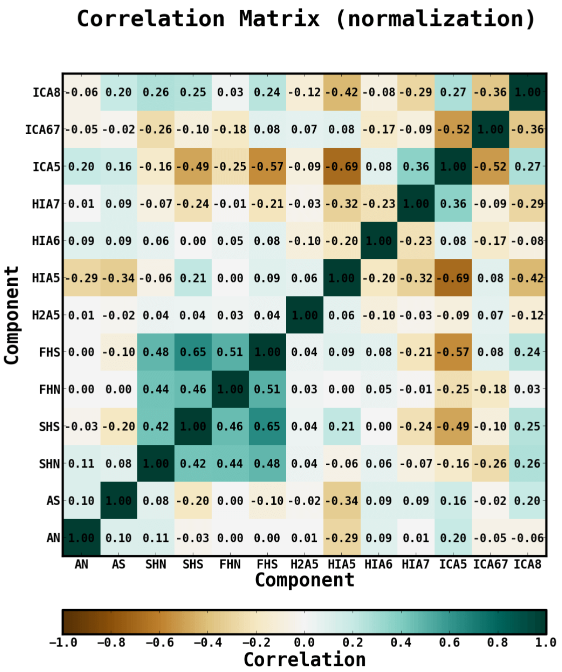

	AN	AS	SHN	SHS	FHN	FHS	H2A5	HIA5	HIA6	HIA7	ICA5	ICA67	ICA8
ICA8	-0.06	0.20	0.26	0.25	0.03	0.24	-0.12	-0.42	-0.08	-0.29	0.27	-0.36	1.00
ICA67	-0.05	-0.02	-0.26	-0.10	-0.18	0.08	0.07	0.08	-0.17	-0.09	-0.52	1.00	-0.36
ICA5	0.20	0.16	-0.16	-0.49	-0.25	-0.57	-0.09	-0.69	0.08	0.36	1.00	-0.52	0.27
HIA7	0.01	0.09	-0.07	-0.24	-0.01	-0.21	-0.03	-0.32	-0.23	1.00	0.36	-0.09	-0.29
HIA6	0.09	0.09	0.06	0.00	0.05	0.08	-0.10	-0.20	1.00	-0.23	0.08	-0.17	-0.08
HIA5	-0.29	-0.34	-0.06	0.21	0.00	0.09	0.06	1.00	-0.20	-0.32	-0.69	0.08	-0.42
H2A5	0.01	-0.02	0.04	0.04	0.03	0.04	1.00	0.06	-0.10	-0.03	-0.09	0.07	-0.12
FHS	0.00	-0.10	0.48	0.65	0.51	1.00	0.04	0.09	0.08	-0.21	-0.57	0.08	0.24
FHN	0.00	0.00	0.44	0.46	1.00	0.51	0.03	0.00	0.05	-0.01	-0.25	-0.18	0.03
SHS	-0.03	-0.20	0.42	1.00	0.46	0.65	0.04	0.21	0.00	-0.24	-0.49	-0.10	0.25
SHN	0.11	0.08	1.00	0.42	0.44	0.48	0.04	-0.06	0.06	-0.07	-0.16	-0.26	0.26
AS	0.10	1.00	0.08	-0.20	0.00	-0.10	-0.02	-0.34	0.09	0.09	0.16	-0.02	0.20
AN	1.00	0.10	0.11	-0.03	0.00	0.00	0.01	-0.29	0.09	0.01	0.20	-0.05	-0.06

Figure 4.32 Correlation matrix for the symmetry test fit. In addition to the standard components, the fit includes components for the arc north and south (AN and AS), inner galaxy (not shown here), spherical halo north and south (SHN and SHS), and the far outer halo north and south (FHN and FHS).

elected to define north and south with respect to the plane of the MW. However, if the spherical halo component is in fact physically associated with the M31-system, then it may be just as well to cut the two halves with respect to the major axis of M31 (38°), which may increase the symmetry between north and south. However, our primary objective here is to simply quantify the gross properties of the residual emission, and a more detailed determination of the morphology is left for a follow-up study.

The far outer halo region shows a significant spectral variation between the north and south. The northern component has a high spectral curvature, identical to the spectral shape that results when fitting the full template, and is generally brighter than the southern component.

The correlation matrix for the fit is shown in Figure 4.32. The southern components for both the spherical halo and far outer halo have a stronger anti-correlation with the IEM, compared to the northern components. In particular, the southern components have relatively strong anti-correlations with ICA5 and H I A7. We also note that the southern component of the spherical halo has some anti-correlation with the arc template, whereas the northern component does not. The normalizations of the diffuse components are mostly in agreement with those obtained for the fit with the full M31-related templates. However, the IC A6-A7 component obtains a best-fit normalization of 0.36 ± 0.40, which may not be very physical, and is in contrast to the values obtained for the other fits in FM31. These results highlight one major shortcoming of this test; that is, the northern and southern regions correlate differently with the IEM, and this can potentially lead to inaccuracies regarding the actual symmetry of the tentative signal. This is especially problematic for the excess in FM31, since the corresponding emission lies well below the foreground/background emission.

The fit with the north and south M31-related templates further shows the importance of the MW modeling and also that the excess is likely to contain a significant MW component. In particular, the excess emission associated with the far outer halo is likely to be related to the MW. Indeed, the Galactic disk region directly above FM31 has many complications, and it is known to contain extended excess γ-ray emission of unknown origin (Acero et al., 2016). In addition, the region (in projection) also contains an extended high-velocity cloud known as Complex H (Hulsbosch, 1975; Blitz et al., 1999; Lockman, 2003; Simon et al., 2006), which has been postulated to be either a dark galaxy of the Local Group or an example of a cold accretion flow onto the MW (Simon et al., 2006). Here we only point out a couple of these associated difficulties, but our primary goal is to quantify the rough properties of the excess emission.

A portion of the excess emission is also likely related to the M31 system, and in particular, the emission associated with the spherical halo region. We note that of the four halo components, the overall intensity is highest for the northern spherical halo. Given the significant modeling uncertainties, we make the simplifying conclusion that the excess emission in FM31 is significantly detected and has a total radial extension upwards of $\sim$120–200 kpc from the center of M31. The lower limit corresponds to the boundary of the spherical halo, and the upper limit corresponds to the boundary of the far outer halo. This conclusion encapsulates the possibility that the excess emission may have contributions from both M31 and the MW, and it also refers to the emission associated with the arc template, the nature of which remains unclear.

4.4 The Smooth Component of the Residual Emission in FM31 and Dark Matter

The dominant component of the residual emission in FM31 has a total radial extension upwards of $\sim$120–200 kpc from the center of M31, corresponding to the excess between $\sim$3–20 GeV in the fractional energy residuals. It is plausible that a portion of the signal may be related to M31's DM halo. In general, the exact properties of M31's DM halo remain highly uncertain, i.e. the geometry, extent, and substructure content. Here we make some simplifying assumptions to get a rough sense of the consistency between the observed signal and a possible DM interpretation. In particular, we check for consistency with the DM interpretation of the excess γ-ray emission observed in the Galactic center (Goodenough & Hooper, 2009; Hooper & Goodenough, 2011; Hooper & Linden, 2011; Abazajian &

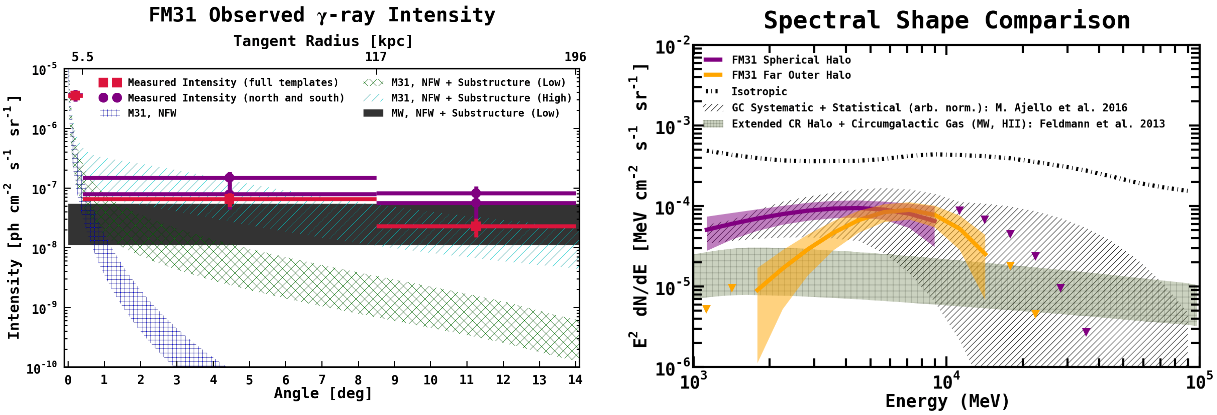

Figure 4.33 **Left:** Radial intensity profile for the M31-related components. Red square markers show the results from the north and south arc template with PLEXP. The profiles for the PL arc fit are basically the same. Purple circle markers show the results from the fit with the M31-related templates divided into north and south components (from Figure 4.31). For reference, we compare the radial profile to expectations for DM annihilation in the line of sight. Note that this also includes the contribution from the MW's DM halo in the line of sight, which has not been accounted for in our analysis, and may be at least partially embedded in the isotropic component and Galactic diffuse components. Likewise, the M31-related components may contain a significant contribution from the MW's extended halo. Details regarding the DM profiles are given in Appendix A.3. **Right:** Spectral shape comparison to the Galactic center excess (for an arbitrary normalization), as observed in Ajello et al. (2016). Also shown is a prediction for CRs interacting with the ionized gas of the circumgalactic medium from Feldmann et al. (2013). Note that the prediction is for a MW component, but we are primarily interested in a spectral shape comparison. We consider this because it is a possible source of γ-ray emission in the region, but based on the properties of the observed excess, we find it seemingly unlikely that the corresponding emission is dominated by these types of interactions. For reference, the isotropic component is plotted as well.

Kaplinghat, 2012; Hooper & Slatyer, 2013; Gordon & Macias, 2013; Huang et al., 2013; Abazajian et al., 2014; Zhou et al., 2015; Calore et al., 2015b; Abazajian et al., 2015; Calore et al., 2015a; Huang et al., 2016; Ajello et al., 2016; Daylan et al., 2016; Carlson et al., 2016; Ajello et al., 2017; Karwin et al., 2017; Ackermann et al., 2017a; Agrawal & Randall, 2017). This by no means encompasses all possibilities, and more detailed evaluations are left for future studies.

In addition to M31's DM halo, we also consider the contribution from the MW's DM halo along the line of sight, since this component has not been explicitly accounted for in our analysis. If such a component actually exists, then it may be at least partially absorbed by the isotropic component, as well as the other components of the IEM, but it will not necessarily be fully absorbed, and a portion of such a signal could be contained in the M31-related components.

The left panel of Figure 4.33 shows the radial profile of the γ-ray intensity for the M31-related components. Red square markers show the fit with the full M31-related templates, including the arc north and south with PLEXP. Purple circle markers show the fit with the M31-related templates divided into north and south components (from Figure 4.31). The individual intensities of the divided north and south components are a bit higher than the intensity of the combined template because of the different correlation of the tentative signal in these regions with the IEM components (see Figure 4.32 and the corresponding discussion in Section 4.3.5). The intensity of the M31-related emission is far less in the outer regions than it is towards the inner galaxy. Furthermore, the signal is not detected in the TR. This is consistent with the hypothesis that the emission originates (at least partially) from the M31 system.

In the Figure, we compare the radial dependence of the observed intensity to the predicted intensity for a DM signal. Plots of the corresponding J-factors and a description of all parameters for the predicted γ-ray flux due to DM annihilation are given in Appendix A.3. For the *DM attribute quantity*, Eq. (A.1), we use the best-fit values as determined from the GC excess in Karwin et al. (2017). The uncertainty bands for each of the three intensity profiles come from the uncertainty in the *DM attribute quantity* (as described in Appendix A.3). The black band shows the corresponding intensity profile for the MW DM component along the line of sight. Note that in general there is also expected to be an additional contribution from the local DM filament between M31 and the MW.

We find that the radial intensity profile of the positive residual emission in FM31 is roughly consistent with a cold DM scenario that includes a large boost factor due to substructures. Granted, however, the exact partitioning of individual contributions to the signal remains unclear, i.e. primary emission from M31's DM halo, secondary emission in M31, emission from the local DM filament between M31 and the MW, and emission from the MW's DM halo along the line of sight.

We again stress that the properties of the excess emission observed towards the outer halo have a strong dependence on the modeling of the IEM. This is partially reflected by the large uncertainty in the radial profile between the two different fit variations, as can be seen in the left panel of Figure 4.33. We also stress that the excess in FM31 is likely to contain a significant contribution from the MW. In particular, the emission associated with the far outer halo is more likely to be related to the MW than the M31 system. But still, the nature of this emission remains unclear.

The right panel in Figure 4.33 shows a spectral shape comparison with the excess emission observed in the Galactic center (Ajello et al., 2016). The band for the Galactic center excess shows the systematic + statistical uncertainty (although it is dominated by the systematics), and it is shown for an arbitrary normalization. We find that the spectra of the M31-related components are qualitatively consistent with the uncertainty band of the Galactic center excess. We note that the spectrum of the far outer halo component has a higher curvature at low energies. If this is indeed a real feature of the signal (and not just a systematic effect), then it could be related to secondary processes. If the DM produces some fraction of leptons, then the leptons may generate secondary γ-ray emission from IC and Bremsstrahlung, due to interactions with the interstellar radiation fields and gas (Cirelli et al., 2013b; Lacroix et al., 2014; Abazajian et al., 2015). For M31, the secondary emission may have a dependence on the radial distance from the center of M31, since the stellar halo and gaseous halo also have a radial dependence. However, this possibility would need to be quantified to get a better sense of the effect.

Also plotted in the right panel of Figure 4.33 is the isotropic component. The intensity of the M31-related components is below that of the isotropic component by a factor of ∼5. There is a bump in the isotropic spectrum around ∼10 GeV (as is more clearly seen in Figure 4.8), and this energy also somewhat corresponds to the peak emission of the M31-related components. This might suggest that the isotropic emission may include a contribution that originates from similar processes in the extended halo of the MW. As it pertains to DM in particular, this issue is significantly complicated and is beyond the scope of this work, but related discussions can be found in Cuoco et al. (2011), Cholis et al. (2014), Fornasa & Sánchez-Conde (2015), Ajello et al. (2015), and Ackermann et al. (2015c).

We note that the DM could be decaying (see Blanco & Hooper (2019) and references therein). In this case the γ-ray signal would be morphologically more consistent with the excess observed in FM31 without requiring a large boost from substructures, since it scales as the DM density, as opposed to the square of the density for annihilation. Here we restrict the interpretation to annihilating DM, also in the context of the GC excess. We leave a more complete DM study, including decaying DM, to a followup work.

We also note that aside from DM, another possible interpretation of the signal, if it truly originates from the M31 system, would be that it arises from CR interactions with the ionized gas of M31's circumgalactic medium. We do not rule out this possibility; however, if the emission is dominated by CR interactions with the ionized gas, then this would imply that the CR spectrum and distribution are significantly different in M31's outer galaxy than that measured locally in the MW.

Additionally, the observed intensity of the M31-related components would imply a relatively high emissivity in M31's outer regions compared to the local MW measurements. However, from a study of the γ-ray emission from a sample of high velocity clouds and intermediate velocity clouds in the halo of the MW, Tibaldo et al. (2015) concluded that the γ-ray emissivity per H atom of the clouds decreases as a function of distance from the disk, with indications of a ∼50%-80% decline of the CR density within a few kpc.

Likewise, from an analytical study of the MW, Feldmann et al. (2013) estimate that the CR density in the outer halo may be up to 10% of that found in the disk. Their predicted γ-ray spectrum is shown in Figure 4.33, right panel, with a green forward-hatch band. Note that the predicted intensity level in their model is based on the prediction for a MW signal, but we are mostly interested in a spectral shape comparison. The study in Feldmann et al. (2013) uses a distribution of H II gas derived using a high resolution hydrodynamical simulation, along with reasonable estimates for the distribution of CRs in the outer halo of the MW. The spatial extent of the CR halo is the greatest modeling uncertainty. The two CR distributions used in their calculation fall to half of their density (not including the density within the disk itself) by 60 kpc and 360 kpc, respectively. These distributions define their uncertainty band in the Figure.

Considering the radial extent, spectral shape, and intensity of the M31-related components, it is seemingly unlikely that the corresponding emission is dominated by CR interactions with the ionized gas of M31's circumgalactic medium.

4.5 The Structured γ-ray Emission in FM31 and Complementary M31-related Observations

Although the M31-related components are detected with high statistical significance and for multiple IEMs (Appendix A.2), the corresponding intensity lies below that of the isotropic emission, and therefore the signal has a strong dependence on the systematic uncertainties of the isotropic component. In addition, our analysis has demonstrated that the characterization of H I along the line of sight is a significant systematic uncertainty for analysis of the M31 field, including the contribution from the DNM. Overall, γ-ray observations of M31's outer halo are significantly complicated by confusion with the Galactic and isotropic emission, due to the halo's large extension on the sky.

To gauge the full extent of the uncertainty pertaining to the H I-related components, and to help mitigate the uncertainty pertaining to the isotropic component, in this section we supplement our analysis by observing the structured γ-ray emission in FM31 in a (semi) model-independent way. As a qualitative gauge, we also compare this emission to some of the main tracers of M31's outer disk and halo.

We observe the γ-ray emission in a (semi) model-independent way by removing the H I-related A5–A8 components from the model (including the Bremsstrahlung component). In addition, we remove the two point sources closest to the M31 disk (3FGL J0040.3+4049 and 3FGL J0049.0+4224), and we remove the new point sources that we find with our point source finding procedure, since most of these sources are found to correlate with the diffuse structures in the residuals (see Figure 4.13). All other sources are held fixed to their best-fit values obtained in the baseline fit (with IC scaled). This effectively amounts to removing only the known smooth diffuse sources and point sources from the data, or equivalently, observing only the structured emission.

The resulting count residuals (data − model) integrated between 1–100 GeV are shown in Figure 4.34. The color scale corresponds to counts/pixel, and the pixel size is $0.2^\circ \times 0.2^\circ$. The images are smoothed using a 1° Gaussian kernel. This value roughly corresponds to the PSF (68% containment angle) of *Fermi*-LAT, which at 1 GeV is $\sim 1^\circ$.

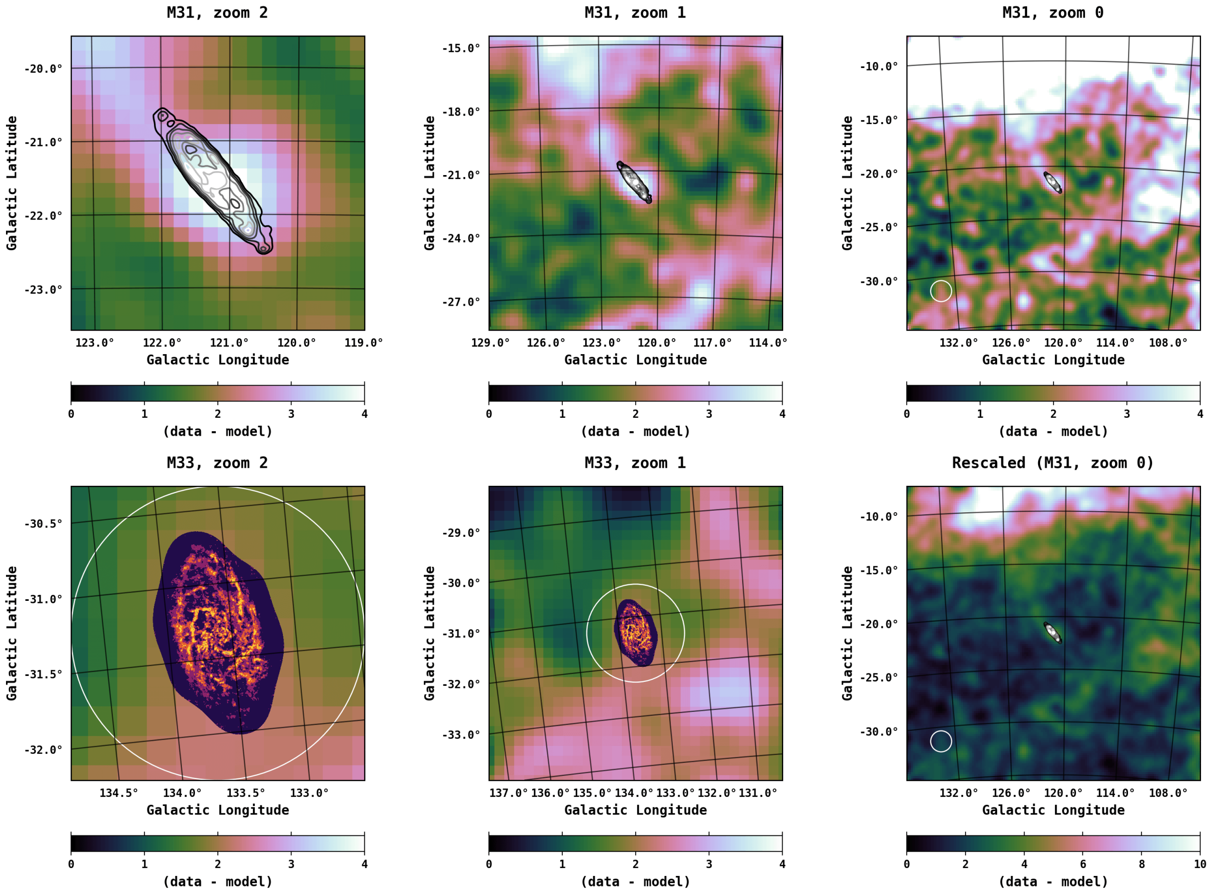

Figure 4.34 Residual maps showing the structured emission integrated in the energy range 1–100 GeV. The color scale corresponds to counts/pixel, and the pixel size is 0.2° × 0.2°. The images are smoothed using a 1° Gaussian kernel. This value corresponds to the PSF (68% containment angle) of *Fermi*-LAT, which at 1 GeV is ~1°. Maps are shown in the cubehelix color scheme (Green, 2011). In the top row contours for the IRIS 100 μm map of M31 are overlaid, and three zoom levels (2°, 7°, full field) centered at M31 are shown. The white circle (1°) shows the position of M33. The bottom row shows two zoom levels (1°, 3°) centered at M33, and the H I integrated intensity map (units of K) of M33 is overlaid. In the third panel we show the M31 zoom 0 map rescaled, in order to provide a sense of the relative intensity towards the MW disk. **We stress that these maps have not subtracted any Galactic H I-related emission.**

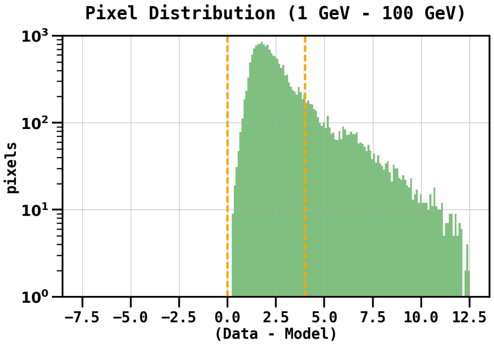

Figure 4.35 Pixel distribution of the smoothed residual map (1 GeV – 100 GeV) after removing the H I-related components, as shown in Figure 4.34. The yellow dashed lines are at 0 and 4 counts.

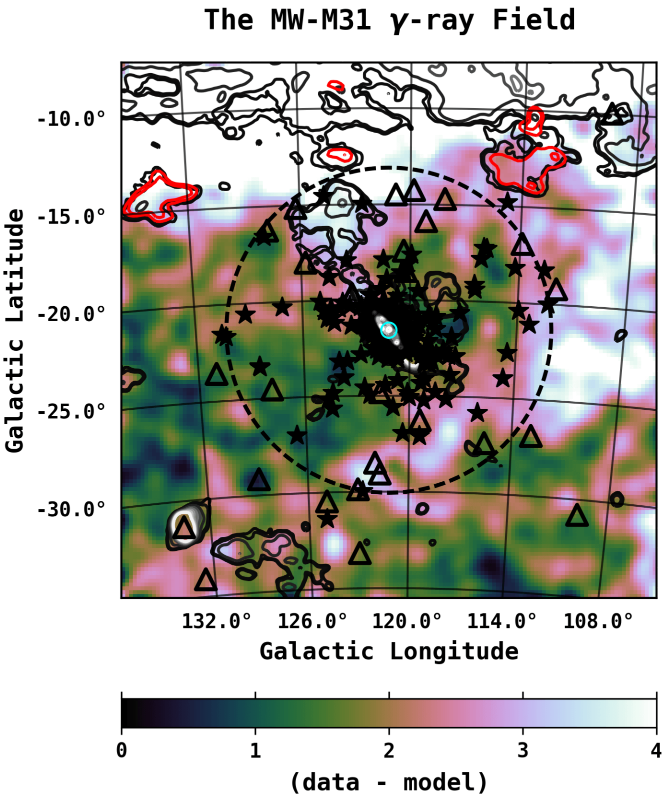

Figure 4.36 To the structured γ-ray emission in FM31 we overlay some M31-related observations from other wavelengths. We stress that this is only done as a qualitative gauge of M31's outer halo. In the figure we have not subtracted any Galactic H I-related emission, and we do not expect the M31-related observations to outshine the MW emission, as discussed in the text. Contours for the IRIS 100 μm map of M31 are overlaid. The solid cyan circle (0.4°) shows the boundary of the FM31 inner galaxy component, and the black dashed circle (8.5°) shows the outer boundary of the FM31 spherical halo component, as detailed in Section 4.3.4. H I emission contours from the HI4PI all-sky survey (based on EBHIS and GASS) (Bekhti et al., 2016), integrated over the velocity range $-600\ \mathrm{km\,s^{-1}} \leq V_{\mathrm{LSR}} \leq -95\ \mathrm{km\,s^{-1}}$ are overlaid. M31's confirmed globular clusters are shown with black stars. M31's population of dwarf galaxies is shown with open black triangles. The M31 cloud can be seen (although obscured by globular clusters). We note the serendipitous enclosure by the spherical halo of the M31 cloud, as well as a majority of M31's globular cluster population and dwarf galaxies. H I contours corresponding to M33 can be seen in the lower-left corner. The hook-shaped gas cloud to the right of M33 is Wright's cloud. The red gas contours towards the top of the map are clouds of Complex H. The black H I contours towards the top of the field correspond to the plane of the MW, and likewise for the bright (white) γ-ray emission. To the far right of the field a bright arm of emission extends to higher latitudes. Although not considered when making the overlay, the M31-related observations can be seen to trace the left boundary of the arm. This may be an observational bias, due to foreground gas and dust. **We stress that these maps have not subtracted any Galactic H I-related emission.**

The corresponding pixel distribution is shown in Figure 4.35. All of the pixels have positive counts, which is why we set the lower limit of the plot range to zero. Maps are shown in the cubehelix color scheme (Green, 2011). Contours for the disk regions of M31 and M33 (Gratier et al., 2010) are overlaid. Bright emission corresponding to M31's inner galaxy can be observed. The emission can be seen to extend continuously along M31's major axis in the north-east[11] direction, which then continues to extend upward until blending with the bright emission of the MW plane. This

---

[11] For M31-related directions, north points up, and east points to the left.

feature is lopsided, as the south-west side shows a more distinct cutoff away from the inner galaxy. The large arc feature observed in the residuals is also clearly visible in the emission.

We have found that the M31-related components are roughly consistent with arising from DM annihilation. Since there is still a high level of uncertainty regarding the actual nature of DM, especially on galactic scales, we cannot rule out the possibility that the smooth residual emission may in fact have a DM origin. The same also applies for some of the structured emission in FM31. We, therefore, consider the main tracers of M31's outer disk and halo, since these are some of the few observational handles available when searching for a DM signal from the outer regions of the M31 system.

In Figure 4.36 we overlay the boundaries for the M31 inner galaxy (solid cyan circle) and spherical halo (dashed black circle) components. We also overlay the M31 disk, the M31 cloud (Blitz et al., 1999; Kerp et al., 2016), M33, Wright's cloud (Wright, 1979), M31's population of globular clusters (Galleti et al., 2004; Huxor et al., 2008; Peacock et al., 2010; Mackey et al., 2010; Veljanoski et al., 2014; Huxor et al., 2014), M31's population of satellite galaxies (McConnachie, 2012; Martin et al., 2013; Collins et al., 2013), and clouds of Complex H (Hulsbosch, 1975; Blitz et al., 1999; Lockman, 2003; Simon et al., 2006). The spherical halo component is found to enclose 61% (22/36) of M31's dwarf galaxy population, which increases to 72% (26/36) if including the dwarfs which are within $\sim 1^\circ$ of the spherical halo boundary. We stress that this is only done as a qualitative gauge of M31's outer halo. We do not expect these systems to outshine the local MW emission. In particular, we do not expect to detect the individual M31 dwarfs, since they are mostly undetected in the MW. We also do not expect to detect the individual globular clusters. We do note, however, that we find features in the data that are positionally coincident with some of these tracers, and most prominently with the M31 cloud. Further investigation is left for a follow-up study.

4.6 Summary, Discussion, and Conclusion

The goal of this work is to search for extended γ-ray emission originating beyond the galactic disk of M31, and to examine the implications for CRs and DM. There are two primary motivations for this search. First, CR interactions with M31's circumgalactic medium and/or stellar halo could generate a detectable signal in γ-rays. Secondly, M31's DM halo has a large extension on the sky and could produce a detectable signal within currently allowed DM scenarios, which would be complementary to other targets, and specifically, the Galactic center. Our primary field of interest (FM31) is a $28^\circ \times 28^\circ$ square region, which amounts to a projected radius of $\sim$200 kpc from the center of M31. Our study complements previously published results on M31 (Abdo et al., 2010b; Ögelman et al., 2011; Pshirkov et al., 2016a,b; Ackermann et al., 2017b) and is the first to explore the farthest reaches of the M31 system in γ-rays.

Because of the extended nature of the signal we are investigating, modeling the bright foreground of the MW is the biggest challenge in performing this analysis. The IEM provided by the FSSC cannot be used as a primary foreground model for this study, as it *is not* intended for the analysis of extended sources[3] (Acero et al., 2016). We construct specialized interstellar emission models for the analysis of FM31 by employing the CR propagation code GALPROP, including a self-consistent determination of the isotropic component. Additionally, we use a template approach to account for inaccuracies in the foreground model relating to the neutral gas along the line of sight.

The parameters of the GALPROP model are tuned to the measured local interstellar spectra of CRs, including the latest AMS-02 measurements. We have adopted the best-fit parameters from the tuning procedure performed in Boschini et al. (2017, 2018a), where GALPROP and HelMod are implemented in an iterative manner, thereby accounting for solar modulation in a physically motivated way when fitting to the local CR measurements.

The total interstellar emission model consists of individual components for π^0-decay, IC, and Bremsstrahlung, and the components are defined in Galactocentric annuli. In total there are 8 annuli, but for FM31 only annulus 5 (the local annulus) and beyond contribute to the foreground emission. FM31 has a significant emission associated with H I gas, but there is very little emission from H_2 gas. A uniform spin temperature of 150 K is assumed for the baseline IEM. The foreground emission from H II and Bremsstrahlung are subdominant. Our model also accounts for the DNM. The anisotropic formalism is employed for the calculation of the IC component. To model the point sources in the region, we employ the 3FGL as a starting point, and because of the larger statistics of our data set, we account for additional point sources self-consistently with the M31 IEM by implementing a point source finding procedure, which is based on a wavelet transform algorithm.

We calculate the isotropic component self-consistently with the M31 IEM. The main calculation is performed over the full sky in the following region: $|b| \geq 30^\circ,\ 45^\circ \leq l \leq 315^\circ$. To better determine the normalization of the isotropic component we use a tuning region (TR) directly below FM31, outside of the virial radius. The best-fit normalization is found to be 1.06 ± 0.04, and this remains fixed for all other fits with the M31 IEM. The isotropic component anti-correlates with the IC components, and we also use the TR to initially constrain the normalizations of the IC components (A5 and A6-A7) for the fit in FM31. The fit in the TR yields a model that describes the data well across the entire region and at all energies. The best-fit normalizations of the IEM components in the TR are all in reasonable agreement with the GALPROP predictions.

For the initial baseline fit in FM31 we freely scale the normalizations of the H I and H_2 π^0-related components concurrently with the point sources. The normalizations of the isotropic and IC components (A5 and A6-A7) remain fixed to their best-fit values obtained in the TR. The top of FM31 has a minor contribution from IC A8, and it is also freely scaled in the fit. Lastly, the H II and Bremsstrahlung components remain fixed to their GALPROP predictions. Note that the Bremsstrahlung component possesses a normalization of 1.0 ± 0.6 in the TR, consistent with the GALPROP prediction.

The baseline fit in FM31 results in positive residual emission in the fractional energy residuals between ∼3–20 GeV. The residual emission in this corresponding energy range is fairly smooth and extends over the entire field. The spatial residuals also show structured excesses and deficits, primarily at lower energies (∼1–3 GeV). Because of this poor data-model agreement, additional freedom is given to the fit, including freely scaling the IC components in FM31 and rescaling the diffuse components in smaller subregions. The latter fit is performed in order to allow for any un-modeled spatial variation in the CR density, ISRF density, and/or spin temperature. We find that the general features of the residual emission persist even with these variations.

A significant fraction of the structured excess emission in FM31 is found to be spatially correlated with the H I column density and the foreground dust, including regions where the dust is relatively cold. This may be indicative of a spatially varying spin temperature, which is not properly accounted for by the rescaling in the smaller subregions. Correspondingly, the structured residual emission may be related to inaccuracies in the modeling of the DNM, which in general is determined as part of an all-sky procedure. A part of the shell of Loop III is also present in FM31, while Loops II and IIIs cover it completely. This may imply that some of the gas-related emission in the region is produced by a population of particles with the spectrum that is harder than that of the old CR population. Note that the H I π^0-related γ-ray component is dominant in FM31 for energies below ∼5 GeV.

We, therefore, refine the baseline IEM by constructing a template to account for potential mis-modeling of these components. The template is obtained by selecting the excess emission in FM31 that correlates with H I tracers. We refer to this as the arc template. This procedure accounts for any un-modeled H I (or other Galactic gas), as well as any mis-modeling in its line of sight distance, spin temperature, and spectral index variations.

We find that the specialized IEMs for the analysis of FM31, both the baseline model and the baseline model with the arc template, yield an extended excess at the level of ∼3–5% in the ∼3–20 GeV energy range. We have also tested a number of additional systematic variations to the fit. With the M31 IEM we allowed for additional freedom by varying the index of the IC components and the H I-related components using a PL scaling. The fit was also performed with two alternative IEMs, namely, the IG and FSSC IEMs. Each alternative IEM has its own self-consistently derived isotropic component and additional point sources. In addition, we tested systematic variations to the spectra of 3FGL sources (although the point sources are not a major uncertainty for this analysis). In total we perform 9 main variations of the fit (see Figure 4.29), using 3 different IEMs (although all IEMs share similar underlying H I maps). The excess is observed for all of the physically motivated IEMs intended for extended source analysis.

Using our benchmark model (the M31 IEM) we have demonstrated that the excess is robust against the systematic studies of the MW foreground emission that we have considered, and that it significantly decreases outside of FM31 (as evidenced by the lack of a similar excess in the TR). This indicates that the excess originates at least partially from outside of the MW and it is significant towards M31. However, we do not rule out the possibility that the signal may also include a MW component, as discussed below.

We note that apart from the structured residual emission correlated with the foreground gas and dust, which is accounted for with the arc template, other structured excesses and deficits in FM31 are found to be correlated with the major axis of the M31 disk. Likewise, a portion of the H I column densities in the outer Galaxy (A6 and A7) are found to be correlated with M31's major axis as well. This is an indication that some of the gas which is currently assigned to the MW may actually reside in the M31 system, as was also pointed out in Ackermann et al. (2017b). This will be fully addressed in a forthcoming work.

A component of the residual emission in FM31 is observed to be positionally coincident with the projected position of M33, and a portion of this emission may have an actual physical association; however, further investigation has been left for future studies. Aside from the structured excesses and deficits, which are observed primarily in the lower energy range (∼1–3 GeV), the majority of the excess emission is roughly uniformly distributed across FM31, corresponding to the positive residual emission observed in the fractional energy residuals between ∼3–20 GeV.

To determine whether the excess presents a spherically symmetric gradient about the center of M31, which would lend support to the hypothesis that it originates from there, we perform a further fit in FM31 by including three symmetric uniform templates centered at M31. This also allows us to quantify the spectrum and gradient of the positive residual emission. The templates are fit concurrently with the other components of the baseline IEM, including the arc template.

The inner disk (inner galaxy) has a radial extension of 0.4° (5.5 kpc projected radius). This is the best-fit morphology as determined in Ackermann et al. (2017b), and it corresponds to the bright γ-ray emission towards M31's inner galaxy. The intermediate ring (spherical halo) has a radial extension from $0.4^\circ < r \leq 8.5^\circ$ (117 kpc projected radius). This extension excludes most of the residual emission associated with the arc template, while also enclosing a majority of M31's globular cluster population and stellar halo, as well as the M31 cloud. The outer ring (far outer halo) covers the remaining extent of FM31, corresponding to a total projected radius of ∼200 kpc, and likewise it begins to approach the MW plane towards the top of the field. We find that all templates are significantly detected (with a significance of $\geq 5\sigma$). Furthermore, the M31-related components are able to flatten the positive residual emission in the fractional energy residuals.

For the fit with the arc template and M31-related components, the best-fit normalizations of the IEM components are overall in good agreement with the GALPROP predictions, and they also agree with the best-fit normalizations obtained for the all-sky fit in the determination of the isotropic component. The total integrated flux for the H I A5 component plus the arc north and south components is 185.6 ± 12.9 ph cm^{-2} s^{-1}, consistent with that of the baseline fit (with IC scaled). In turn, the corresponding local average emissivity is consistent with the measurements made in Abdo et al. (2009a), Ackermann et al. (2012d), and Casandjian (2015).

The normalization of the H I A6 component is consistent with the GALPROP prediction. The normalization of the H I A7 component is a bit high at 2.8 ± 0.4 (as for all fits in FM31), but this component may contain a fraction of gas that actually resides in the M31 system, as was already discussed, and will be further discussed below. The normalizations of the IC A5 and A6-A7 components are consistent with the all-sky average obtained in the isotropic calculation (Table 4.2). The normalization of the IC A8 component is high, which is true for all fits in FM31, but this component is subdominant and only contributes along the top of the field, corresponding to the Galactic plane.

The spectrum and intensity for the inner galaxy are consistent with previously published results. We note however that the spectrum derived between 1–100 GeV is softer than that derived between 300 MeV – 300 GeV (although consistent within errors). This is due to the energy range used for the calculation. The spherical halo and far outer halo have intensities that are much dimmer than the inner galaxy, and present a mild intensity gradient, tapering off with distance from the center of M31. Their spectra are significantly different from all the other extended components in FM31. They peak between ∼5–10 GeV, and drop off below and above these energies more steeply than all other contributions. We find it difficult to reconcile these spectra with the possibility that the excess emission originates solely within the MW, further setting it apart from known Galactic sources. Beyond these general features, the spectra for the two outer annuli differ from each other with the far outer halo presenting a harder spectrum at low energies.

To further test the symmetry of the residual emission in FM31, we also perform a fit in which we divide the spherical halo and far outer halo templates into north and south components, allowing the spectral parameters of each component to vary independently (although all components are fit simultaneously). The cut is made at the midpoint of FM31 along the horizontal direction (parallel to the Galactic plane), corresponding to a latitude of -21.5°. The fit is otherwise performed just as for the fit with the full M31-related templates (including the arc north and south). We find that all components are significantly detected (with a significance $> 5\sigma$). The results for this test further demonstrate the importance of the MW modeling and that the excess is likely to have a significant MW component. In particular, the emission associated with the far outer halo is more likely to be related to the MW than the M31 system. But even still, the nature of this emission remains unclear.

Given the approximately uniform spatial distribution of the excess emission (as most clearly indicated by the fit with the full M31-related templates), understanding its interplay with the isotropic component is crucial. We have investigated this issue and concluded that the excess emission is robust within the systematic uncertainties in the isotropic component we have considered. Our treatment of the isotropic component can primarily be found in Section 4.2.3, Figure 4.8, Appendix A.2.2, and Appendix A.2.3. We note, however, that the isotropic emission has a bump-like feature in the energy range that somewhat overlaps with the peak in the spectrum of the M31-related components (as is most clearly seen in Figure 4.8). This might suggest that the isotropic emission may include a component that originates from similar processes in the extended halo of the MW.

These results show that if the excess emission originates from the M31 system (at least partially), its extension reaches a distance upwards of $\sim$120–200 kpc from the center of M31. This is consistent with the expectation for a DM signal, as the virial radius for the DM halo extends at least this far. To test this interpretation, we compare these results with the predictions for a DM signal that originates from the M31 halo, with a spectrum and annihilation cross-section consistent with a DM interpretation of the GC excess. We also consider the contribution from the MW's DM halo along the line of sight, since this component has not been explicitly accounted for in this analysis. If such a component actually exists, then it may be at least partially embedded in the isotropic component, as well as the other components of the IEM, but it will not necessarily be fully absorbed. Note that in general there is also expected to be some contribution from the local DM filament between M31 and the MW.

We consider different assumptions for the amount of DM substructure in M31 (and the MW), and we find that if a cold DM scenario is assumed that includes a large boost factor due to substructures, the observed excess emission is consistent with this interpretation. Granted, however, the exact partitioning of individual contributions to the signal remains unclear, i.e. primary emission from M31's DM halo, secondary emission in M31, emission from the local DM filament between M31 and the MW, and emission from the MW's DM halo along the line of sight.

This is an intriguing finding, however, its implications are far reaching, and better understanding the MW foreground is crucial before drawing any stronger conclusions. Another crucial aspect is complementarity with other DM targets. Although these results are consistent with other observations in γ-rays, namely the GC excess and the constraints from dwarf spheroidal galaxies, they imply that a large boost factor from substructures would contribute to a DM signal from the MW halo. As already stated, this contribution has not been accounted for in this analysis and might be at least partially embedded in the isotropic component as well as other components of the MW foreground. Likewise, the M31-related components might contain some contribution from the MW DM halo along the line of sight, as well as some contribution from the local DM filament between M31 and the MW. From our substructure calculations we estimate that the intensity of a MW DM contribution in FM31 may be on the order of $\sim$1–10% of the isotropic intensity. Investigating this possibility in more detail requires a dedicated analysis which is beyond the scope of this work.

The CR halo of M31 might extend tens to hundreds of kpc from the center of M31. It is possible that some of the emission in FM31 results from CR interactions with the ionized gas of M31's circumgalactic medium and/or stellar halo, which also extend well beyond the galactic disk. However, based on the radial extent, spectral shape, and intensity of the M31-related components, it is seemingly unlikely that the corresponding emission is dominated by these types of CR interactions.

We have also investigated the structured residual emission in FM31, as well as the emission correlated with the H I γ-ray maps, and compared them to different tracers of M31's outer disk and halo. These tracers include the M31 cloud, and M31's populations of globular clusters and satellite galaxies. We find features in the data that are positionally coincident with some of these tracers, and most prominently with the M31 cloud. This is a further indication that some of the structured emission observed in FM31 originates from M31 rather than the MW. This in turn implies that the total γ-ray emission from the M31 system extends well beyond the inner regions of the galactic disk. The M31 system is very rich, and further analysis of these findings is beyond the scope of this paper. Our primary focus in this analysis is the more significant smoother component of the signal.

In summary, we present the first search for extended emission from M31 in γ-rays out to a distance of $\sim$200 kpc from its center. We find evidence for an extended excess that appears to be distinct from the conventional MW foreground, having a total radial extension upwards of 120–200 kpc from the center of M31. We discuss plausible interpretations for the excess emission but emphasize that uncertainties in the MW foreground, and in particular modeling of the H I-related components, have not been fully explored and may impact the results. The results also have a close link with the isotropic component (and likewise the IC components), which may be inevitable considering the nature of the signal under investigation. We find that a DM interpretation provides a good description of the observed emission and is consistent with the GC excess DM interpretation. However, better understanding of the systematics, and complementarity with other DM searches, as discussed in the paper, is critical to settle the issue.

Chapter 5

Summary and Conclusion

5.1 Summary

Detailed observations were made of the high-energy γ-ray emission towards the GC and the outer halo of M31. For the GC, an excess signal is detected. This excess was first reported in Goodenough & Hooper (2009), and has since been the subject of numerous studies (Hooper & Goodenough, 2011; Hooper & Linden, 2011; Abazajian & Kaplinghat, 2012; Hooper & Slatyer, 2013; Gordon & Macias, 2013; Huang et al., 2013; Abazajian et al., 2014; Zhou et al., 2015; Calore et al., 2015b; Abazajian et al., 2015; Calore et al., 2015a; Huang et al., 2016; Ajello et al., 2016; Daylan et al., 2016; Carlson et al., 2016; Ajello et al., 2017; Karwin et al., 2017; Ackermann et al., 2017a; Agrawal & Randall, 2017), including a confirmation of the excess by the *Fermi*-LAT Collaboration in Ajello et al. (2016), as summarized in Chapter 2. Possible explanations for the excess include inaccuracies in the foreground/background model, an unresolved population of millisecond pulsars, and/or DM annihilation. Note that it is likewise possible that the excess is due to some combination of all three.

Using the specialized IEMs and the First *Fermi*-LAT Inner Galaxy Point Source Catalog (1FIG) from Ajello et al. (2016), a DM interpretation of the GC excess was given in Chapter 3 (from Karwin et al. (2017)). The excess emission was characterized as annihilating DM in the framework of an effective field theory, where the annihilation process is mediated by either pseudoscalar or vector interactions, and all final states are allowed (up-type quarks, down-type quarks, and leptons). The spectral characteristics of the excess favor a DM particle in the range approximately from 50 to 190 (10 to 90) GeV and annihilation cross section approximately from 1×10^{-26} to 4×10^{-25} (6×10^{-27} to 2×10^{-25})

$\mathrm{cm}^3\ \mathrm{s}^{-1}$ for pseudoscalar (vector) interactions. For the lower mass models the annihilation goes primarily to down-type quarks, and for the higher mass models the annihilation goes primarily to up-type quarks. In each case a small fraction of the annihilation also goes to leptonic final states. The difference between the preference for the higher mass models and the lower mass models comes from the uncertainty in the modeling of the foreground/background γ-ray emission (index-scaled versus intensity-scaled). These intervals were mapped into the corresponding WIMP-neutron scattering cross sections and it was found that the allowed range lies well below current and projected direct detection constraints for pseudoscalar interactions, but are typically ruled out for vector interactions. For the pseudoscalar interactions, the lower mass models with annihilation to mostly down-type quarks may be in the reach of future direct detection experiments; however, the high mass models with annihilation to mostly up-type quarks lie just above the neutrino floor and may be difficult to probe.

It should be noted that although the exact particle physics description of the DM is of great interest, obtaining such a precise description is not the goal of this dissertation. For example, DM could annihilate to a combination of quarks and leptons, in which case secondary emission may contribute significantly to the total signal and may introduce a spatial dependence into the DM γ-ray spectrum. Such possibilities complicate the problem significantly. But more pragmatically, even determining an approximate range of the DM mass and cross section would mark tremendous progress in the DM problem.

The first search for extended γ-ray emission from M31's outer halo was presented in Chapter 4 (from Karwin et al. (2019)). An in-depth analysis was made of the systematic uncertainties related to the observations. Within the systematics considered, evidence was found for an extended excess that appears to be distinct from the conventional MW foreground, having a total radial extension upwards of ∼120–200 kpc from the center of M31. A DM interpretation (including a large boost factor due to substructures) was found to provide a good description of the observed emission and is consistent with the GC excess DM interpretation. Granted, however, the exact partitioning of individual contributions to the signal remains unclear, i.e. primary emission from M31's DM halo, secondary emission in M31, emission from the local DM filament between M31 and the MW, and emission from the MW's DM halo along the line of sight. It was also emphasized that uncertainties in the MW foreground, and in particular, modeling of the the H I-related components, have not been fully explored and may impact the results. The results also have a close link with the isotropic component (and likewise the IC component), which may be inevitable considering the nature of the signal under investigation.

Figure 5.1 summarizes the current state of DM annihilation indirect detection in the energy range 10 GeV - 300 GeV, corresponding to the GC excess. For simplicity only the representative case of annihilation to final state bottom quarks is shown. More generally, other final states are also possible, as well as more complicated models.

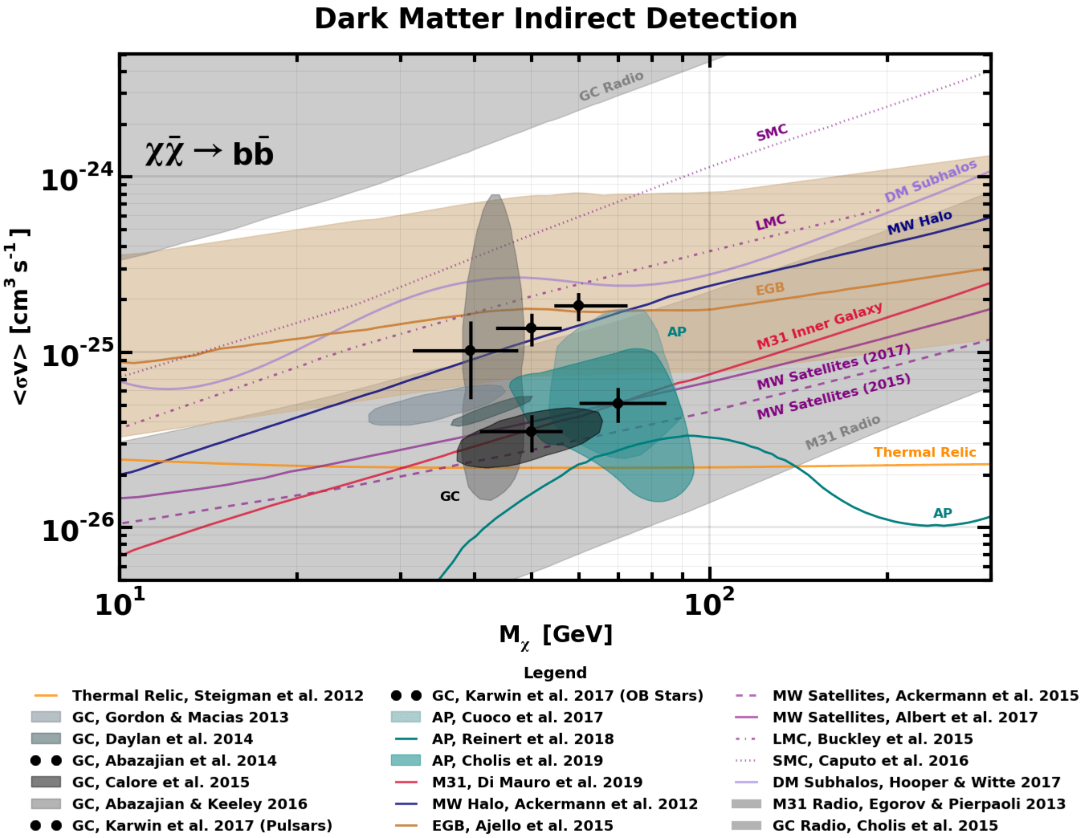

Figure 5.1 All results are shown for Dirac DM (which amounts to a factor of 2 compared to Majorana DM). See text for details of the different overlays.

The black data points in Figure 5.1 (furthest four to the right) are for a DM interpretation of the GC excess, as presented in Chapter 3. The two points at lower energy are for the OB stars index-scaled foreground model, and the points at higher energy are for the pulsars index-scaled foreground model. The NFW profile has $\gamma = 1.0$ (upper) and $\gamma = 1.2$ (lower). In addition, the NFW profile has $\mathrm{R_s} = 20$ kpc and $\rho_\odot = 0.4$ GeV cm^{-3}. Note that the final state goes to mostly bottom-type quarks, with a small fraction going to leptonic final states. Thus this model is not directly comparable to the other overlays which generally assume annihilation into a single final state.

The black contour that is highly elongated in the y-direction is for the GC excess from Abazajian & Keeley (2016). The contour represents the total uncertainty (3σ statistical + systematic). The uncertainty is dominated by the systematics, and in particular, the value of the local DM density (this study also considers uncertainties due to the index and scale radius of the DM profile, γ and R_s). The upper region of the contour corresponds to $\rho_\odot = 0.28$ GeV cm^{-3} (which is taken as the benchmark value), and the lower region of the contour corresponds to $\rho_\odot = 0.49$ GeV cm^{-3}. The shift occurs at a cross section value of $\sim 6 \times 10^{-26}$ cm^3 s^{-1}. See Abazajian & Keeley (2016) for details. Also plotted in Figure 5.1 is the best-fit point from Abazajian et al. (2014) (the black data point to the far left).

Other contours for the GC excess are also shown with different shades of grey. The lowest and darkest contour (2σ) is from Calore et al. (2015b), then above that is the contour (2σ) from Daylan et al. (2016), and above that is the contour from Gordon & Macias (2013). The NFW profiles for all of these contours have $\gamma = 1.2$, $R_s = 20$ kpc, and $\rho_\odot = 0.4$ GeV cm^{-3}.

The two lowest purple lines show limits for the MW satellite galaxies. The dashed line is from Ackermann et al. (2015a) and results from the combined analysis of 15 dwarf spheroidal galaxies using Pass-8 data. The solid line is from Albert et al. (2017) and results from the combined analysis of 45 stellar systems, including 28 kinematically confirmed dark-matter-dominated dwarf spheroidal galaxies, and 17 recently discovered systems that are dwarf candidates. Note that the dwarf limits are obtained by assuming spherical symmetry of the DM halos; however, if the halos are non-spheroidal then the limits may be weakened, as discussed in Klop et al. (2016).

The two highest purple lines are for the LMC and SMC. The dash-dot line shows 2σ limits from the LMC from Buckley et al. (2015), based on Pass-7 data. The dotted line shows 2σ limits from the SMC from Caputo et al. (2016).

The tan band shows the 2σ upper-limit from the extragalactic γ-ray background (EGB) from Ajello et al. (2015). The band reflects the uncertainties related to the modeling of DM subhalos. This analysis shows that blazars, star-forming galaxies, and radio galaxies can naturally account for the amplitude and spectral shape of the extragalactic γ-ray background (EBL) over the energy range 0.1–820 GeV, leaving only modest room for other contributions. We note that there is a slight bump in the upper limits right around the tentative detection region.

The blue line shows γ-ray limits (3σ) from the MW halo from Ackermann et al. (2012b). This is the limit obtained with modeling the MW diffuse emission using GALPROP, for an NFW profile, with $\gamma = 1$ and a local DM density of 0.43 GeV cm^{-3}. The limits are generally weaker without modeling the diffuse emission, and they have a strong dependence on the local DM density.

The light purple line is for DM subhalos from Hooper & Witte (2017). These limits are based on DM subhalo candidates from the unassociated point sources detected by *Fermi*-LAT. In total there are 19 subhalo candidates. The minimum subhalo mass for the upper limit calculation is assumed to be 10^{-5} $\mathrm{M}_\odot$.

The upper gray band in Figure 5.1 shows radio constraints for the GC from Cholis et al. (2015). The limits are derived using VLA observations at 330 MHz of the central 0.04 around Sgr A*. An NFW profile is used with $\gamma = 1.26$,

$R_s = 20$ kpc, a local DM density of 0.3 $\mathrm{GeV\ cm^{-3}}$, and a flat density core of 2 pc. The limits include energy losses due to IC and convection. The lower limit is for $V_C = 0\ \mathrm{km\,s^{-1}}$, and the upper limit (not shown) is for $V_C = 1000\ \mathrm{km\,s^{-1}}$. The limits can be much stronger (up to 3 or 4 orders of magnitude) when not including IC and convection, or for a core radius closer to zero. There is also a high uncertainty of the magnetic field strength in the innermost region of the GC.

The lower gray band shows radio limits from the central region of M31 ($\sim$1 kpc) from Egorov & Pierpaoli (2013). The band represents joint constraint from four different surveys: VLSS (74 MHz), WENSS (325 MHz), NVSS (1400 MHz), and GB6 (4850 MHz). An M31 signal is detected for all surveys but VLSS. The highest region is for a central magnetic field strength $B_0 = 5\ \mu$G and DM concentration of $c_{100} = 12$, the middle region is for $B_0 = 50\ \mu$G and DM concentration of $c_{100} = 20$, and the lowest region is for $B_0 = 300\ \mu$G and DM concentration of $c_{100} = 28$. An NFW profile is used for the DM density, with $\gamma = 1$, and a flat core for r<50 pc. The limits have a large uncertainty due to the uncertainties in the DM profile and magnetic field strength in the inner regions of M31. The magnetic field is modeled with an exponential dependence in galactocentric radius and height above the galactic plane. The analysis accounts for leptonic energy losses due to IC emission, synchrotron emission, Bremsstrahlung, and Coulomb scattering, with synchrotron emission being the dominant loss mechanism over most of the energy range. We note, however, that uncertainties in the astrophysical modeling of these processes may weaken the limits even further. In particular, the limits have a strong dependence on the relative strength of the IC losses compared to the synchrotron losses, which in turn depends on the energy density of M31's interstellar radiation field.

Also shown are contours for a recently reported excesses in the flux of antiprotons. The upper light teal contour (2σ) is from Cuoco et al. (2016). The lower dark contour (2σ) is from Cholis et al. (2019). The NFW profiles for these contours have $\gamma = 1.0$, $R_s = 20$ kpc, and $\rho_\odot = 0.4\ \mathrm{GeV\ cm^{-3}}$. The teal curve shows upper-limits from Reinert & Winkler (2018), where a less optimistic view of the excess is given (although the limits still clearly show an anomaly around the signal region).

The red line is for M31's inner galaxy from Di Mauro et al. (2019). These limits are obtained by assuming that all of the observed γ-ray emission from M31's inner galaxy arises from standard astrophysical emission, and therefore including a 0.3° disk template (which is derived directly from the bright γ-ray emission that is observed) in the DM fit. In addition, to account for the foreground/background emission, the FSSC IEM is fit directly to the γ-ray data in the signal region.

Given the properties of the observed excess towards M31's outer halo, as presented in Chapter 4, the corresponding data point should be consistent with the signal region in Figure 5.1, although the FM31 error bars may be pretty large, due to the uncertainty in the properties of the DM halos for both M31 and the MW. The work from this dissertation has allowed for the addition of the FM31 data point, and this will be presented in a forth-coming study.

5.2 Conclusion

There appears to be an emerging region in the DM parameter space that may prove to be of great significance (see Figure 5.1). The region corresponding to the GC excess is found to be consistent with a broad range of complementary observations. In particular, there is currently consistency with antiprotons, γ-ray constraints from the MW dwarfs, the LMC, the SMC, the MW halo, and the inner galaxy of M31, as well as radio constraints from the GC and M31. In addition, there now appears to be a complementary signal detected towards the outer halo of M31. It should be noted that for many of these upper limits, it is not the case that there is no γ-ray emission that is detected, and actually in some cases there is even tentative evidence for a DM signal (e.g. the LMC (Buckley et al., 2015) and the inner galaxy of M31 (Di Mauro et al., 2019)). The problem and difficulty is in unambiguously separating the tentative DM signal from the standard astrophysical emission, including the bright foreground/background of the MW and the truly isotropic emission. Among other things, this will require more detailed modeling of the foreground/background emission and better understanding of the corresponding systematics.

Bibliography

Aad, G., et al. 2013, JHEP, 04, 075, doi: 10.1007/JHEP04(2013)075

Aalbers, J., et al. 2016, JCAP, 1611, 017, doi: 10.1088/1475-7516/2016/11/017

Aartsen, M. G., et al. 2017, Eur. Phys. J., C77, 146, doi: 10.1140/ApJc/s10052-017-4689-9

Abazajian, K. N., Agrawal, P., Chacko, Z., & Kilic, C. 2010, JCAP, 1011, 041, doi: 10.1088/1475-7516/2010/11/041

Abazajian, K. N., Blanchet, S., & Harding, J. P. 2012, PhRv, D85, 043509, doi: 10.1103/PhysRevD.85.043509

Abazajian, K. N., Canac, N., Horiuchi, S., & Kaplinghat, M. 2014, PhRvD, 90, 023526, doi: 10.1103/PhysRevD.90.023526

Abazajian, K. N., Canac, N., Horiuchi, S., Kaplinghat, M., & Kwa, A. 2015, JCAP, 1507, 013, doi: 10.1088/1475-7516/2015/07/013

Abazajian, K. N., & Kaplinghat, M. 2012, PhRvD, 86, 083511, doi: 10.1103/PhysRevD.86.083511,10.1103/PhysRevD.87.129902

Abazajian, K. N., & Keeley, R. E. 2016, PhRvD, 93, 083514, doi: 10.1103/PhysRevD.93.083514

Abdo, A., Ackermann, M., Ajello, M., et al. 2009a, ApJ, 703, 1249

—. 2010a, A&A, 523, A46

Abdo, A., et al. 2010b, A&A, 523, L2, doi: 10.1051/0004-6361/201015759

Abdo, A. A. 2010, A&A, 512, A7, doi: 10.1051/0004-6361/200913474

Abdo, A. A., et al. 2009b, PhRvL, 103, 251101, doi: 10.1103/PhysRevLett.103.251101

—. 2009c, APh, 32, 193, doi: 10.1016/j.astropartphys.2009.08.002

—. 2010c, PhRvL, 104, 101101, doi: 10.1103/PhysRevLett.104.101101

—. 2010d, JCAP, 1004, 014, doi: 10.1088/1475-7516/2010/04/014

Abdullah, M., DiFranzo, A., Rajaraman, A., et al. 2014, PhRvD, 90, 035004, doi: 10.1103/PhysRevD.90.035004

Abeysekara, A. U., et al. 2014, PhRvD, 90, 122002, doi: 10.1103/PhysRevD.90.122002

Acero, F., et al. 2015, ApJS, 218, 23, doi: 10.1088/0067-0049/218/2/23

—. 2016, ApJS, 223, 26, doi: 10.3847/0067-0049/223/2/26

Ackermann, M., et al. 2012a, ApJ, 750, 3, doi: 10.1088/0004-637X/750/1/3

—. 2012b, ApJ, 761, 91, doi: 10.1088/0004-637X/761/2/91

—. 2012c, ApJS, 203, 4, doi: 10.1088/0067-0049/203/1/4

Ackermann, M., Ajello, M., Allafort, A., et al. 2012d, ApJ, 755, 22

Ackermann, M., et al. 2014, PhRvD, 89, 042001, doi: 10.1103/PhysRevD.89.042001

—. 2015a, PhRvL, 115, 231301, doi: 10.1103/PhysRevLett.115.231301

—. 2015b, ApJ, 799, 86, doi: 10.1088/0004-637X/799/1/86

—. 2015c, JCAP, 1509, 008, doi: 10.1088/1475-7516/2015/09/008

—. 2016, A&A, 586, A71, doi: 10.1051/0004-6361/201526920

—. 2017a, ApJ, 840, 43, doi: 10.3847/1538-4357/aa6cab

—. 2017b, ApJ, 836, 208, doi: 10.3847/1538-4357/aa5c3d

Ade, P. A. R., et al. 2015, A&A, 582, A28, doi: 10.1051/0004-6361/201424643

—. 2016, A&A, 594, A13, doi: 10.1051/0004-6361/201525830

Adriani, O., et al. 2009, Natur, 458, 607, doi: 10.1038/nature07942

Agrawal, P., Batell, B., Fox, P. J., & Harnik, R. 2015, JCAP, 1505, 011, doi: 10.1088/1475-7516/2015/05/011

Agrawal, P., & Randall, L. 2017, JCAP, 2017, 019

Aguilar, M., et al. 2013, PhRvL, 110, 141102, doi: 10.1103/PhysRevLett.110.141102

Aguilar, M., Aisa, D., Alpat, B., et al. 2014, PhRvL, 113, 221102, doi: 10.1103/PhysRevLett.113.221102

—. 2015a, PhRvL, 114, 171103, doi: 10.1103/PhysRevLett.114.171103

—. 2015b, PhRvL, 115, 211101, doi: 10.1103/PhysRevLett.115.211101

Aguilar, M., et al. 2016, PhRvL, 117, 091103, doi: 10.1103/PhysRevLett.117.091103

Ajello, M., et al. 2015, ApJ, 800, L27, doi: 10.1088/2041-8205/800/2/L27

—. 2016, ApJ, 819, 44, doi: 10.3847/0004-637X/819/1/44

—. 2017, Submitted to: ApJ. https://arxiv.org/abs/1705.00009

Akerib, D. S., et al. 2016. https://arxiv.org/abs/1608.07648

Albert, A., et al. 2017, ApJ, 834, 110, doi: 10.3847/1538-4357/834/2/110

Allgood, B., Flores, R. A., Primack, J. R., et al. 2006, MNRAS, 367, 1781, doi: 10.1111/j.1365-2966.2006.10094.x

Alves, A., Profumo, S., Queiroz, F. S., & Shepherd, W. 2014, PhRvD, 90, 115003, doi: 10.1103/PhysRevD.90.115003

Anand, N., Fitzpatrick, A. L., & Haxton, W. C. 2014, PhRvC, 89, 065501, doi: 10.1103/PhysRevC.89.065501

Anderson, L., et al. 2014, MNRAS, 441, 24, doi: 10.1093/mnras/stu523

Arp, H. 1964, ApJ, 139, 1045

Atwood, W., et al. 2013. http://inspirehep.net/record/1223837/files/arXiv:1303.3514.pdf

Atwood, W. B., et al. 2009, ApJ, 697, 1071, doi: 10.1088/0004-637X/697/2/1071

Babcock, H. W. 1939, Lick Observatory Bulletin, 19, 41

Bailin, J., & Steinmetz, M. 2005, ApJ, 627, 647, doi: 10.1086/430397

Balzs, C., & Li, T. 2014, PhRvD, 90, 055026, doi: 10.1103/PhysRevD.90.055026

—. 2016. https://arxiv.org/abs/1609.00113

Banerjee, A., & Jog, C. J. 2008, ApJ, 685, 254, doi: 10.1086/591223

—. 2011, ApJ, 732, L8, doi: 10.1088/2041-8205/732/1/L8

Barmby, P., Ashby, M., Bianchi, L., et al. 2006, ApJ Letters, 650, L45

Bartels, R., Krishnamurthy, S., & Weniger, C. 2016, PhRvL, 116, 051102, doi: 10.1103/PhysRevLett.116.051102

Bate, N. F., et al. 2014, MNRAS, 437, 3362, doi: 10.1093/mnras/stt2139

Beck, R., & Gräve, R. 1982, A&A, 105, 192

Bekhti, N. B., Flöer, L., Keller, R., et al. 2016, A&A, 594, A116

Beltran, M., Hooper, D., Kolb, E. W., Krusberg, Z. A. C., & Tait, T. M. P. 2010, JHEP, 09, 037, doi: 10.1007/JHEP09(2010)037

Beltran, M., Hooper, D., Kolb, E. W., & Krusberg, Z. C. 2009, PhRvD, 80, 043509, doi: 10.1103/PhysRevD.80.043509

Bennett, K., Bignami, G. F., Boella, G., et al. 1976, A&A, 50, 157

Bergstrom, L., Bringmann, T., Cholis, I., Hooper, D., & Weniger, C. 2013, PhRvL, 111, 171101, doi: 10.1103/PhysRevLett.111.171101

Berlin, A., Gratia, P., Hooper, D., & McDermott, S. D. 2014, PhRvD, 90, 015032, doi: 10.1103/PhysRevD.90.015032

Bernal, N., Necib, L., & Slatyer, T. R. 2016, JCAP, 1612, 030, doi: 10.1088/1475-7516/2016/12/030

Bernard, E. J., Ferguson, A. M., Richardson, J. C., et al. 2015, MNRAS, 446, 2789

Bertone, G., & Hooper, D. 2018, RvMP, 90, 045002, doi: 10.1103/RevModPhys.90.045002

Bett, P., Eke, V., Frenk, C. S., et al. 2007, MNRAS, 376, 215, doi: 10.1111/j.1365-2966.2007.11432.x

Billard, J., Strigari, L., & Figueroa-Feliciano, E. 2014, PhRvD, 89, 023524, doi: 10.1103/PhysRevD.89.023524

Binder, T., Covi, L., Kamada, A., et al. 2016, JCAP, 1611, 043, doi: 10.1088/1475-7516/2016/11/043

Bird, R. 2016, PoS, ICRC2015, 851. https://arxiv.org/abs/1508.07195

Blanchet, S., & Lavalle, J. 2012, JCAP, 1211, 021, doi: 10.1088/1475-7516/2012/11/021

Blanco, C., & Hooper, D. 2019, JCAP, 1903, 019, doi: 10.1088/1475-7516/2019/03/019

Blitz, L., Spergel, D. N., Teuben, P. J., Hartmann, D., & Burton, W. B. 1999, ApJ, 514, 818

Bloemen, J. B. G. M., Strong, A. W., Mayer-Hasselwander, H. A., et al. 1986, A&A, 154, 25

Boehm, C., Dolan, M. J., McCabe, C., Spannowsky, M., & Wallace, C. J. 2014, JCAP, 1405, 009, doi: 10.1088/1475-7516/2014/05/009

Boehm, C., Fayet, P., & Schaeffer, R. 2001, PhLB, 518, 8

Boehm, C., & Schaeffer, R. 2005, A&A, 438, 419

Bolatto, A. D., Wolfire, M., & Leroy, A. K. 2013, ARA&A, 51, 207, doi: 10.1146/annurev-astro-082812-140944

Boschini, M. J., Della Torre, S., Gervasi, M., et al. 2017, ApJ, 840, 115, doi: 10.3847/1538-4357/aa6e4f

—. 2018a, ApJ, 854, 94, doi: 10.3847/1538-4357/aaa75e

—. 2018b, ApJ, 858, 61, doi: 10.3847/1538-4357/aabc54

Bose, S., Hellwing, W. A., Frenk, C. S., et al. 2016, MNRAS, stw2686

—. 2017, MNRAS, 464, 4520, doi: 10.1093/mnras/stw2686

Bosma, A. 1978, PhD thesis, PhD Thesis, Groningen Univ., (1978)

Braun, R., & Burton, W. B. 1999, A&A, 341, 437. https://arxiv.org/abs/astro-ph/9810433

Braun, R., & Thilker, D. 2004, A&A, 417, 421, doi: 10.1051/0004-6361:20034423

Braun, R., Thilker, D., Walterbos, R., & Corbelli, E. 2009, ApJ, 695, 937

Brémond, A. G. 2009, JAHH, 12, 72

Bringmann, T., Ihle, H. T., Kersten, J., & Walia, P. 2016, PhRvD, 94, 103529

Brinks, E., & Burton, W. 1984, A&A, 141, 195

Buckley, M. R., Charles, E., Gaskins, J. M., et al. 2015, Phys. Rev., D91, 102001, doi: 10.1103/PhysRevD.91.102001

Buckley, M. R., Zavala, J., Cyr-Racine, F.-Y., Sigurdson, K., & Vogelsberger, M. 2014, PhRvD, 90, 043524

Bullock, J. S., Kolatt, T. S., Sigad, Y., et al. 2001, MNRAS, 321, 559, doi: 10.1046/j.1365-8711.2001.04068.x

Calore, F., Cholis, I., McCabe, C., & Weniger, C. 2015a, PhRvD, 91, 063003, doi: 10.1103/PhysRevD.91.063003

Calore, F., Cholis, I., & Weniger, C. 2015b, JCAP, 1503, 038, doi: 10.1088/1475-7516/2015/03/038

Campbell, S., Dutta, B., & Komatsu, E. 2010, PhRvD, 82, 095007, doi: 10.1103/PhysRevD.82.095007

Cao, Q.-H., Chen, C.-R., Li, C. S., & Zhang, H. 2011, JHEP, 08, 018, doi: 10.1007/JHEP08(2011)018

Caputo, R., Buckley, M. R., Martin, P., et al. 2016, Phys. Rev., D93, 062004, doi: 10.1103/PhysRevD.93.062004

Carignan, C., Chemin, L., Huchtmeier, W. K., & Lockman, F. J. 2006, ApJ Letters, 641, L109

Carlesi, E., et al. 2016, MNRAS, 458, 900, doi: 10.1093/mnras/stw357

Carlson, E., Linden, T., & Profumo, S. 2016, PhRvD, 94, 063504, doi: 10.1103/PhysRevD.94.063504

Carlson, E., & Profumo, S. 2014, PhRvD, 90, 023015, doi: 10.1103/PhysRevD.90.023015

Carpenter, L. M., Colburn, R., Goodman, J., & Linden, T. 2016, PhRvD, 94, 055027, doi: 10.1103/PhysRevD.94.055027

Casandjian, J.-M. 2015, ApJ, 806, 240, doi: 10.1088/0004-637X/806/2/240

Cherry, J. F., Friedland, A., & Shoemaker, I. M. 2014. https://arxiv.org/abs/1411.1071

Cholis, I., Evoli, C., Calore, F., et al. 2015, JCAP, 1512, 005, doi: 10.1088/1475-7516/2015/12/005

Cholis, I., Hooper, D., & Linden, T. 2015, PhRvD, 91, 083507, doi: 10.1103/PhysRevD.91.083507

Cholis, I., Hooper, D., & McDermott, S. D. 2014, JCAP, 1402, 014, doi: 10.1088/1475-7516/2014/02/014

Cholis, I., Linden, T., & Hooper, D. 2019. https://arxiv.org/abs/1903.02549

Cirelli, M., Del Nobile, E., & Panci, P. 2013a, JCAP, 1310, 019, doi: 10.1088/1475-7516/2013/10/019

Cirelli, M., Serpico, P. D., & Zaharijas, G. 2013b, JCAP, 1311, 035, doi: 10.1088/1475-7516/2013/11/035

Cirelli, M., Corcella, G., Hektor, A., et al. 2011, JCAP, 1103, 051, doi: 10.1088/1475-7516/2012/10/E01, 10.1088/1475-7516/2011/03/051

Clowe, D., Bradac, M., Gonzalez, A. H., et al. 2006, ApJ, 648, L109, doi: 10.1086/508162

Collins, M. L., Chapman, S. C., Rich, R. M., et al. 2013, ApJ, 768, 172

Colombi, S., Dodelson, S., & Widrow, L. M. 1996, ApJ, 458, 1, doi: 10.1086/176788

Conn, A. R., Ibata, R. A., Lewis, G. F., et al. 2012, ApJ, 758, 11

Conn, A. R., et al. 2013, ApJ, 766, 120, doi: 10.1088/0004-637X/766/2/120

—. 2016, MNRAS, 458, 3282, doi: 10.1093/mnras/stw513

Conrad, J., Cohen-Tanugi, J., & Strigari, L. E. 2015, J. Exp. Theor. Phys., 121, 1104, doi: 10.1134/S1063776115130099

Corbelli, E., Lorenzoni, S., Walterbos, R., Braun, R., & Thilker, D. 2010, A&A, 511, A89, doi: 10.1051/0004-6361/200913297

Cui, M.-Y., Yuan, Q., Tsai, Y.-L. S., & Fan, Y.-Z. 2016. https://arxiv.org/abs/1610.03840

Cummings, A. C., Stone, E. C., Heikkila, B. C., et al. 2016, ApJ, 831, 18, doi: 10.3847/0004-637X/831/1/18

Cuoco, A., KrŁmer, M., & Korsmeier, M. 2016. https://arxiv.org/abs/1610.03071

Cuoco, A., Sellerholm, A., Conrad, J., & Hannestad, S. 2011, MNRAS, 414, 2040, doi: 10.1111/j.1365-2966.2011.18525.x

Cyr-Racine, F.-Y., de Putter, R., Raccanelli, A., & Sigurdson, K. 2014, PhRvD, 89, 063517

Cyr-Racine, F.-Y., & Sigurdson, K. 2013, PhRvD, 87, 103515

Cyr-Racine, F.-Y., Sigurdson, K., Zavala, J., et al. 2016, PhRvD, 93, 123527

Dame, T. M., Hartmann, D., & Thaddeus, P. 2001, ApJ, 547, 792, doi: 10.1086/318388

Damiani, F., Maggio, A., Micela, G., & Sciortino, S. 1997, ApJ, 483, 350, doi: 10.1086/304217

Daylan, T., Finkbeiner, D. P., Hooper, D., et al. 2016, PDU, 12, 1, doi: 10.1016/j.dark.2015.12.005

de Boer, W., Sander, C., Zhukov, V., Gladyshev, A. V., & Kazakov, D. I. 2005, A&A, 444, 51, doi: 10.1051/0004-6361:20053726

de Heij, V., Braun, R., & Burton, W. B. 2002, A&A, 392, 417, doi: 10.1051/0004-6361:20020908

De Looze, I., Baes, M., Parkin, T., et al. 2012, MNRAS, 423, 2359

Demers, S., Battinelli, P., & Letarte, B. 2003, AJ, 125, 3037

Di Mauro, M., Hou, X., Eckner, C., Zaharijas, G., & Charles, E. 2019. https://arxiv.org/abs/1904.10977

Diemand, J., Kuhlen, M., & Madau, P. 2007, ApJ, 657, 262, doi: 10.1086/510736

Diemand, J., Zemp, M., Moore, B., Stadel, J., & Carollo, M. 2005, MNRAS, 364, 665, doi: 10.1111/j.1365-2966.2005.09601.x

Dugger, L., Jeltema, T. E., & Profumo, S. 2010, JCAP, 1012, 015, doi: 10.1088/1475-7516/2010/12/015

Egorov, A. E., & Pierpaoli, E. 2013, Phys. Rev., D88, 023504, doi: 10.1103/PhysRevD.88.023504

Einasto, J., Kaasik, A., & Saar, E. 1974, Natur, 250, 309

Eisenstein, D. J., et al. 2005, ApJ, 633, 560, doi: 10.1086/466512

Elsaesser, D., & Mannheim, K. 2005, PhRvL, 94, 171302, doi: 10.1103/PhysRevLett.94.171302

Escudero, M., Berlin, A., Hooper, D., & Lin, M.-X. 2016. https://arxiv.org/abs/1609.09079

Faber, S. M., & Gallagher, J. 1979, ARA&A, 17, 135

Falvard, A., et al. 2004, APh, 20, 467, doi: 10.1016/j.astropartphys.2003.07.001

Fan, J., Koushiappas, S. M., & Landsberg, G. 2016, JHEP, 01, 111, doi: 10.1007/JHEP01(2016)111

Fardal, M. A., et al. 2013, MNRAS, 434, 2779, doi: 10.1093/mnras/stt1121

Faria, D., Johnson, R. A., Ferguson, A. M., et al. 2007, AJ, 133, 1275

Feldmann, R., Hooper, D., & Gnedin, N. Y. 2013, ApJ, 763, 21, doi: 10.1088/0004-637X/763/1/21

Feng, J. L. 2010, ARA&A, 48, 495, doi: 10.1146/annurev-astro-082708-101659

Feng, J. L., Kaplinghat, M., Tu, H., & Yu, H.-B. 2009, JCAP, 2009, 004

Feng, J. L., & Kumar, J. 2008, PhRvL, 101, 231301

Ferguson, A., Irwin, M., Ibata, R., Lewis, G., & Tanvir, N. 2002, AJ, 124, 1452, doi: 10.1086/342019

Fichtel, C. E., Hartman, R. C., Kniffen, D. A., et al. 1975a, ApJ, 198, 163, doi: 10.1086/153590

—. 1975b, ApJ, 198, 163

Fitzpatrick, A. L., Haxton, W., Katz, E., Lubbers, N., & Xu, Y. 2013, JCAP, 1302, 004, doi: 10.1088/1475-7516/2013/02/004

Fornasa, M., & Sánchez-Conde, M. A. 2015, PhR, 598, 1, doi: 10.1016/j.physrep.2015.09.002

Fornengo, N., Pieri, L., & Scopel, S. 2004, PhRvD, 70, 103529, doi: 10.1103/PhysRevD.70.103529

Fortes, E. C. F. S., Pleitez, V., & Stecker, F. W. 2016, APh, 74, 87, doi: 10.1016/j.astropartphys.2015.10.010

Funk, S. 2015, ARNPS, 65, 245, doi: 10.1146/annurev-nucl-102014-022036

Gaensler, B., Madsen, G., Chatterjee, S., & Mao, S. 2008, PASA, 25, 184

Galleti, S., Federici, L., Bellazzini, M., Pecci, F. F., & Macrina, S. 2004, A&A, 416, 917

Gao, L., Frenk, C. S., Jenkins, A., Springel, V., & White, S. D. M. 2012, MNRAS, 419, 1721, doi: 10.1111/j.1365-2966.2011.19836.x

Garcia, M. R., Hextall, R., Baganoff, F. K., et al. 2010, ApJ, 710, 755, doi: 10.1088/0004-637X/710/1/755

Garrison-Kimmel, S., Wetzel, A., Bullock, J. S., et al. 2017, MNRAS, 471, 1709

Garrison-Kimmel, S., Hopkins, P. F., Wetzel, A., et al. 2018, arXiv preprint arXiv:1806.04143

Gaskins, J. M. 2016, ConPh, 57, 496, doi: 10.1080/00107514.2016.1175160

Génolini, Y., Maurin, D., Moskalenko, I. V., & Unger, M. 2018, PhRvC, 98, 034611, doi: 10.1103/PhysRevC.98.034611

Geringer-Sameth, A., & Koushiappas, S. M. 2011, PhRvL, 107, 241303, doi: 10.1103/PhysRevLett.107.241303

Geringer-Sameth, A., Walker, M. G., Koushiappas, S. M., et al. 2015, PhRvL, 115, 081101, doi: 10.1103/PhysRevLett.115.081101

Giesen, G., Boudaud, M., Gnolini, Y., et al. 2015, JCAP, 1509, 023, doi: 10.1088/1475-7516/2015/09/023, 10.1088/1475-7516/2015/9/023

Gil de Paz, A., et al. 2007, ApJS, 173, 185, doi: 10.1086/516636

Goodenough, L., & Hooper, D. 2009, arXiv preprint. https://arxiv.org/abs/0910.2998

Goodman, J., Ibe, M., Rajaraman, A., et al. 2010, PhRvD, 82, 116010, doi: 10.1103/PhysRevD.82.116010

—. 2011, NucPh, B844, 55, doi: 10.1016/j.nuclphysb.2010.10.022

Gordon, C., & Macias, O. 2013, PhRvD, 88, 083521, doi: 10.1103/PhysRevD.88.083521,10.1103/PhysRevD.89.049901

Gratier, P., Braine, J., Rodriguez-Fernandez, N., et al. 2010, A&A, 522, A3

Green, D. A. 2011, arXiv preprint arXiv:1108.5083

Grenier, I. A., Casandjian, J.-M., & Terrier, R. 2005, Sci, 307, 1292

Gresham, M. I., & Zurek, K. M. 2014, PhRvD, 89, 123521, doi: 10.1103/PhysRevD.89.123521

Gupta, A., Mathur, S., Krongold, Y., Nicastro, F., & Galeazzi, M. 2012, ApJ, 756, L8, doi: 10.1088/2041-8205/756/1/L8

Hammer, F., Yang, Y., Fouquet, S., et al. 2013, MNRAS, 431, 3543, doi: 10.1093/mnras/stt435

Hammer, F., Yang, Y. B., Wang, J. L., et al. 2010, ApJ, 725, 542, doi: 10.1088/0004-637X/725/1/542

Han, J., Cole, S., Frenk, C. S., & Jing, Y. 2016, MNRAS, 457, 1208

Hartman, R. C., et al. 1999, ApJS, 123, 79, doi: 10.1086/313231

Hayashi, E., Navarro, J. F., & Springel, V. 2007, MNRAS, 377, 50, doi: 10.1111/j.1365-2966.2007.11599.x

Hayashi, K., Ichikawa, K., Matsumoto, S., et al. 2016, MNRAS, 461, 2914, doi: 10.1093/mnras/stw1457

Helmi, A. 2004, MNRAS, 351, 643, doi: 10.1111/j.1365-2966.2004.07812.x

Henderson, A. 1979, A&A, 75, 311

Hinshaw, G., et al. 2013, ApJS, 208, 19, doi: 10.1088/0067-0049/208/2/19

Hooper, D., Cholis, I., Linden, T., Siegal-Gaskins, J., & Slatyer, T. 2013, PhRvD, 88, 083009, doi: 10.1103/PhysRevD.88.083009

Hooper, D., Finkbeiner, D. P., & Dobler, G. 2007, PhRvD, 76, 083012

Hooper, D., & Goodenough, L. 2011, PhL, B697, 412, doi: 10.1016/j.physletb.2011.02.029

Hooper, D., & Linden, T. 2011, PhRvD, 84, 123005, doi: 10.1103/PhysRevD.84.123005

Hooper, D., & Slatyer, T. R. 2013, PDU, 2, 118, doi: 10.1016/j.dark.2013.06.003

Hooper, D., & Witte, S. J. 2017, Journal of Cosmology and Astroparticle Physics, 2017, 018

Horiuchi, S., Kaplinghat, M., & Kwa, A. 2016. https://arxiv.org/abs/1604.01402

Howk, J. C., Wotta, C. B., Berg, M. A., et al. 2017, ApJ, 846, 141

Howley, K., Geha, M., Guhathakurta, P., et al. 2008, ApJ, 683, 722

Huang, W.-C., Urbano, A., & Xue, W. 2013, arXiv preprint. https://arxiv.org/abs/1307.6862

Huang, X., Enßlin, T., & Selig, M. 2016, JCAP, 1604, 030, doi: 10.1088/1475-7516/2016/04/030

Hubble, E. P. 1929, ApJ, 69

Hulsbosch, A. N. 1975, A&A, 40, 1

Hunter, S. D., et al. 1997, ApJ, 481, 205, doi: 10.1086/304012

Huo, R., Kaplinghat, M., Pan, Z., & Yu, H.-B. 2018, PhLB

Huxor, A., Tanvir, N., Ferguson, A., et al. 2008, MNRAS, 385, 1989

Huxor, A., Mackey, A., Ferguson, A., et al. 2014, MNRAS, 442, 2165

Ibata, R., Chapman, S., Ferguson, A., et al. 2005, ApJ, 634, 287

Ibata, R., Irwin, M., Lewis, G., Ferguson, A. M., & Tanvir, N. 2001, Natur, 412, 49

Ibata, R., Martin, N. F., Irwin, M., et al. 2007, ApJ, 671, 1591, doi: 10.1086/522574

Ibata, R. A., et al. 2013, Natur, 493, 62, doi: 10.1038/nature11717

Ichikawa, K., Ishigaki, M. N., Matsumoto, S., et al. 2016. https://arxiv.org/abs/1608.01749

Jóhannesson, G., Porter, T. A., & Moskalenko, I. V. 2018, ApJ, 856, 45, doi: 10.3847/1538-4357/aab26e

Jóhannesson, G., et al. 2016, ApJ, 824, 16, doi: 10.3847/0004-637X/824/1/16

Kachelrieß, M., & Ostapchenko, S. 2012, PhRvD, 86, 043004, doi: 10.1103/PhysRevD.86.043004

Kalberla, P. M., Burton, W., Hartmann, D., et al. 2005, A&A, 440, 775

Kalberla, P. M. W., & Kerp, J. 2009, ARA&A, 47, 27, doi: 10.1146/annurev-astro-082708-101823

Kamae, T., Karlsson, N., Mizuno, T., Abe, T., & Koi, T. 2006, ApJ, 647, 692, doi: 10.1086/505189

Kamionkowski, M., & Kinkhabwala, A. 1998, PhRvD, 57, 3256, doi: 10.1103/PhysRevD.57.3256

Karwin, C., Murgia, S., Campbell, S., & Moskalenko, I. 2019. https://arxiv.org/abs/1903.10533

Karwin, C., Murgia, S., Tait, T. M. P., Porter, T. A., & Tanedo, P. 2017, PhRvD, 95, 103005, doi: 10.1103/PhysRevD.95.103005

Keenan, O., Davies, J. I., Taylor, R., & Minchin, R. 2015, MNRAS, 456, 951

Kerp, J., Kalberla, P., Bekhti, N. B., et al. 2016, A&A, 589, A120

Khachatryan, V., et al. 2015, Eur. Phys. J., C75, 235, doi: 10.1140/ApJc/s10052-015-3451-4

Klop, N., Zandanel, F., Hayashi, K., & Ando, S. 2016. https://arxiv.org/abs/1609.03509

Klypin, A., Zhao, H., & Somerville, R. S. 2002, ApJ, 573, 597, doi: 10.1086/340656

Ko, P., & Tang, Y. 2015, JCAP, 1501, 023, doi: 10.1088/1475-7516/2015/01/023

Kolpak, M. A., Jackson, J. M., Bania, T. M., & Dickey, J. M. 2002, ApJ, 578, 868, doi: 10.1086/342659

Kopp, J., Liu, J., Slatyer, T. R., Wang, X.-P., & Xue, W. 2016. https://arxiv.org/abs/1609.02147

Kovesi, P. 2015, arXiv preprint arXiv:1509.03700

Kraushaar, W., & Clark, G. 1962, PhRvL, 8, 106

Kraushaar, W., Clark, G., Garmire, G., et al. 1972, ApJ, 177, 341

—. 1965, ApJ, 141, 845

Kraushaar, W. L., Clark, G. W., Garmire, G. P., et al. 1972, ApJ, 177, 341, doi: 10.1086/151713

Kroupa, P., Theis, C., & Boily, C. M. 2005, A&A, 431, 517, doi: 10.1051/0004-6361:20041122

Kuhlen, M., Diemand, J., & Madau, P. 2007, ApJ, 671, 1135, doi: 10.1086/522878

Kuhlen, M., Guedes, J., Pillepich, A., Madau, P., & Mayer, L. 2013, ApJ, 765, 10, doi: 10.1088/0004-637X/765/1/10

Kumar, J., & Marfatia, D. 2013, PhRvD, 88, 014035, doi: 10.1103/PhysRevD.88.014035

Lacroix, T., Boehm, C., & Silk, J. 2014, PhRvD, 90, 043508, doi: 10.1103/PhysRevD.90.043508

Lauer, T. R., Bender, R., Kormendy, J., Rosenfield, P., & Green, R. F. 2012, ApJ, 745, 121, doi: 10.1088/0004-637X/745/2/121

Law, D. R., Majewski, S. R., & Johnston, K. V. 2009, ApJ, 703, L67, doi: 10.1088/0004-637X/703/1/L67

Lee, S. K., Lisanti, M., & Safdi, B. R. 2015, JCAP, 1505, 056, doi: 10.1088/1475-7516/2015/05/056

Lee, S. K., Lisanti, M., Safdi, B. R., Slatyer, T. R., & Xue, W. 2016, PhRvL, 116, 051103, doi: 10.1103/PhysRevLett.116.051103

Lehner, N., Howk, J. C., & Wakker, B. P. 2015, ApJ, 804, 79

Lena, D., Robinson, A., Marconi, A., et al. 2014, ApJ, 795, 146, doi: 10.1088/0004-637X/795/2/146

Lewis, G. F., et al. 2013, ApJ, 763, 4, doi: 10.1088/0004-637X/763/1/4

Li, Z., Garcia, M. R., Forman, W. R., et al. 2011, ApJ, L10, doi: 10.1088/2041-8205/728/1/L10

Li, Z., Huang, X., Yuan, Q., & Xu, Y. 2016, JCAP, 1612, 028, doi: 10.1088/1475-7516/2016/12/028

Li, Z., & Wang, D. 2007, ApJ Letters, doi: 10.1086/522674

Liem, S., Bertone, G., Calore, F., et al. 2016, JHEP, 09, 077, doi: 10.1007/JHEP09(2016)077

Linden, T., Rodd, N. L., Safdi, B. R., & Slatyer, T. R. 2016. https://arxiv.org/abs/1604.01026

Lisanti, M., Mishra-Sharma, S., Rodd, N. L., & Safdi, B. R. 2018a, PhRvL, 120, 101101

Lisanti, M., Mishra-Sharma, S., Rodd, N. L., Safdi, B. R., & Wechsler, R. H. 2018b, PhRvD, 97, 063005

Lockman, F. J. 2003, ApJ Letters, 591, L33, doi: 10.1086/376961

Lovell, M. R., Frenk, C. S., Eke, V. R., et al. 2014, MNRAS, 439, 300

Lucero, D. M., & Young, L. M. 2007, AJ, 134, 2148

Ludlow, A. D., Bose, S., Angulo, R. E., et al. 2016, MNRAS, 460, 1214

Macciò, A. V., Paduroiu, S., Anderhalden, D., Schneider, A., & Moore, B. 2012, MNRAS, 424, 1105

Macias, O., Gordon, C., Crocker, R. M., et al. 2016. https://arxiv.org/abs/1611.06644

Mack, G. D., Jacques, T. D., Beacom, J. F., Bell, N. F., & Yuksel, H. 2008, PhRvD, 78, 063542, doi: 10.1103/PhysRevD.78.063542

Mackey, D., Huxor, A., Ferguson, A., et al. 2010, ApJ, 717, L11, doi: 10.1088/2041-8205/717/1/L11

Marleau, F., Noriega-Crespo, A., Misselt, K., et al. 2006, ApJ, 646, 929

Martin, A., Shelton, J., & Unwin, J. 2014, PhRvD, 90, 103513, doi: 10.1103/PhysRevD.90.103513

Martin, N. F., Ibata, R. A., McConnachie, A. W., et al. 2013, ApJ, 776, 80

Mattox, J. R., et al. 1996, ApJ, 461, 396, doi: 10.1086/177068

Mattox, J. R., Bertsch, D. L., Chiang, J., et al. 1996, ApJ, 461, doi: 10.1086/177068

Mayall, N. U. 1951, Publications of Michigan Observatory, 10

McConnachie, A. W. 2012, AJ, 144, 4, doi: 10.1088/0004-6256/144/1/4

McConnachie, A. W., Irwin, M. J., Ferguson, A. M. N., et al. 2005, MNRAS, 356, 979, doi: 10.1111/j.1365-2966.2004.08514.x

McConnachie, A. W., et al. 2009, Natur, 461, 66, doi: 10.1038/nature08327

McDermott, S. D., Fox, P. J., Cholis, I., & Lee, S. K. 2016, JCAP, 1607, 045, doi: 10.1088/1475-7516/2016/07/045

McMonigal, B., Bate, N., Conn, A., et al. 2015, MNRAS, 456, 405

Milgrom, M. 1983, ApJ, 270, 365, doi: 10.1086/161130

Miville-Deschenes, M.-A., & Lagache, G. 2005, ApJS, 157, 302, doi: 10.1086/427938

Moliné, Á., Sánchez-Conde, M. A., Palomares-Ruiz, S., & Prada, F. 2017, MNRAS, 466, 4974

Monaco, L., Saviane, I., Perina, S., et al. 2009, A&A, 502, L9

Moskalenko, I. V., & Strong, A. W. 1998, ApJ, 493, 694, doi: 10.1086/305152

—. 2000, ApJ, 528, 357, doi: 10.1086/308138

Navarro, J. F., Frenk, C. S., & White, S. D. M. 1997, ApJ, 490, 493, doi: 10.1086/304888

Ng, K. C. Y., Laha, R., Campbell, S., et al. 2014, PhRvD, 89, 083001, doi: 10.1103/PhysRevD.89.083001

Nolan, P. L., Abdo, A., Ackermann, M., et al. 2012, ApJS, 199, 31

Ögelman, H., Aksaker, N., Anılan, S., et al. 2011, AIP Conference Proceedings, 1379, 82

Olive, K. A., & Turner, M. S. 1982, PhRvD, 25, 213

Ostriker, J. P., Peebles, P., & Yahil, A. 1974, ApJ, 193, L1

Pagels, H., & Primack, J. R. 1982, PhRvL, 48, 223

Pawlowski, M. S. 2018, MPLA, A33, 1830004, doi: 10.1142/S0217732318300045

Pawlowski, M. S., Ibata, R. A., & Bullock, J. S. 2017, ApJ, 850, 132

Pawlowski, M. S., Kroupa, P., & Jerjen, H. 2013a, MNRAS, 435, 1928, doi: 10.1093/mnras/stt1384

—. 2013b, MNRAS, 435, 1928

Pawlowski, M. S., Pflamm-Altenburg, J., & Kroupa, P. 2012, MNRAS, 423, 1109, doi: 10.1111/j.1365-2966.2012.20937.x

Peacock, J. A., et al. 2001, Natur, 410, 169, doi: 10.1038/35065528

Peacock, M. B., Maccarone, T. J., Knigge, C., et al. 2010, MNRAS, 402, 803

Pease, F. 1918, Proceedings of the National Academy of Sciences of the United States of America, 4, 21

Peebles, P. 1982, ApJ, 263, L1

Perlmutter, S., Aldering, G., Goldhaber, G., et al. 1999, ApJ, 517, 565

Petrović, J., Serpico, P. D., & Zaharijaš, G. 2014, JCAP, 1410, 052, doi: 10.1088/1475-7516/2014/10/052

Pollock, A., Masnou, J., Bignami, G., et al. 1981, A&A, 94, 116

Porter, T. A., Johannesson, G., & Moskalenko, I. V. 2017, ApJ, 846, 23pp

Porter, T. A., Moskalenko, I. V., Strong, A. W., Orlando, E., & Bouchet, L. 2008, ApJ, 682, 400, doi: 10.1086/589615

Porter, T. A., & Strong, A. W. 2005, ICRC, 4, 77

Pshirkov, M., Postnov, K., & Vasiliev, V. 2016a, PoS, ICRC2015, 867

Pshirkov, M. S., Vasiliev, V. V., & Postnov, K. A. 2016b, MNRAS, 459, L76, doi: 10.1093/mnrasl/slw045

Ptuskin, V. S., Moskalenko, I. V., Jones, F. C., Strong, A. W., & Zirakashvili, V. N. 2006, ApJ, 642, 902, doi: 10.1086/501117

Recchia, S., Blasi, P., & Morlino, G. 2016, MNRAS: Letters, 462, L88

Reddy, N. A., & Yun, M. S. 2004, ApJ, 600, 695, doi: 10.1086/379871

Reinert, A., & Winkler, M. W. 2018, JCAP, 2018, 055

Richardson, J., Ferguson, A., Johnson, R., et al. 2008, AJ, 135, 1998

Riess, A. G., et al. 1998, AJ, 116, 1009, doi: 10.1086/300499

Roberts, I. 1893, A Selection of Photographs of Stars, Star-Clusters and Nebulae, together with Information concerning the Instruments and the Methods employed in the pursuit of Celestial Photography

Roberts, M. S., & Whitehurst, R. N. 1975, ApJ, 201, 327

Rubin, V. C., & Ford, Jr., W. K. 1970, ApJ, 159, 379, doi: 10.1086/150317

Rubin, V. C., Ford Jr, W. K., & Thonnard, N. 1978, ApJ, 225, L107

Saglia, R. P., Fabricius, M., Bender, R., et al. 2010, A&A, 509, A61, doi: 10.1051/0004-6361/200912805

Saha, K., Levine, E. S., Jog, C. J., & Blitz, L. 2009, ApJ, 697, 2015, doi: 10.1088/0004-637X/697/2/2015

Sánchez-Conde, M. A., & Prada, F. 2014, MNRAS, 442, 2271

Schlegel, D. J., Finkbeiner, D. P., & Davis, M. 1998, ApJ, 500, 525

Seigar, M. S., Barth, A. J., & Bullock, J. S. 2008, MNRAS, 389, 1911

Shull, J. M. 2014, ApJ, 784, 142, doi: 10.1088/0004-637X/784/2/142

Simon, J. D., Blitz, L., Cole, A. A., Weinberg, M. D., & Cohen, M. 2006, ApJ, 640, 270, doi: 10.1086/499914

Sjostrand, T., Mrenna, S., & Skands, P. Z. 2008, Comput. Phys. Commun., 178, 852, doi: 10.1016/j.cpc.2008.01.036

Slipher, V. M. 1913, Lowell Observatory Bulletin, 2, 56

Slipher, V. M. 1914, Lowell Observatory Bulletin, 2, 66

Smith, S. 1936, ApJ, 83, 23

Sofue, Y., & Rubin, V. 2001, ARA&A, 39, 137

Sohn, S. T., Anderson, J., & Van der Marel, R. P. 2012, ApJ, 753, 7

Springel, V., Wang, J., Vogelsberger, M., et al. 2008, MNRAS, 391, 1685, doi: 10.1111/j.1365-2966.2008.14066.x

Sreekumar, P., Bertsch, D., Dingus, B., et al. 1992, ApJ, 400, L67

—. 1994, ApJ, 426, 105

Stanek, K. Z., & Garnavich, P. M. 1998, ApJ, 503, L131, doi: 10.1086/311539

Stecker, F. W., Hunter, S. D., & Kniffen, D. A. 2008, Aph, 29, 25, doi: 10.1016/j.astropartphys.2007.11.002

Steigman, G., Dasgupta, B., & Beacom, J. F. 2012, PhRvD, 86, 023506, doi: 10.1103/PhysRevD.86.023506

Strong, A., & Mattox, J. 1996, A&A, 308, L21

Strong, A. W., Moskalenko, I., Reimer, O., Digel, S., & Diehl, R. 2004, A&A, 422, L47

Strong, A. W., & Moskalenko, I. V. 1998, ApJ, 509, 212, doi: 10.1086/306470

Strong, A. W., Moskalenko, I. V., & Ptuskin, V. S. 2007, ARNPS, 57, 285, doi: 10.1146/annurev.nucl.57.090506.123011

Strong, A. W., Moskalenko, I. V., & Reimer, O. 2000, ApJ, 537, 763, doi: 10.1086/309038

Strong, A. W., Moskalenko, I. V., & Reimer, O. 2004a, ApJ, 613, 962, doi: 10.1086/423193

Strong, A. W., Moskalenko, I. V., Reimer, O., Digel, S., & Diehl, R. 2004b, A&A, 422, L47, doi: 10.1051/0004-6361:20040172

Strong, A. W., Bloemen, J. B. G. M., Dame, T. M., et al. 1988, A&A, 207, 1

Tamm, A., Tempel, E., Tenjes, P., Tihhonova, O., & Tuvikene, T. 2012, A&A, 546, A4

Tanabashi, M., Hagiwara, K., Hikasa, K., et al. 2018, Phys. Rev. D, 98, 030001, doi: 10.1103/PhysRevD.98.030001

Thilker, D. A., Braun, R., & Walterbos, R. 2002, in Seeing Through the Dust: The Detection of HI and the Exploration of the ISM in Galaxies, Vol. 276, 370

Tibaldo, L., et al. 2015, ApJ, 807, 161, doi: 10.1088/0004-637X/807/2/161

Tinivella, M. 2016, arXiv preprint arXiv:1610.03672

Trimble, V. 1987, ARA&A, 25, 425, doi: 10.1146/annurev.aa.25.090187.002233

van den Aarssen, L. G., Bringmann, T., & Goedecke, Y. C. 2012, PhRvD, 85, 123512

Veljanoski, J., Mackey, A., Ferguson, A., et al. 2014, MNRAS, 442, 2929

Velliscig, M., et al. 2015, MNRAS, 453, 721, doi: 10.1093/mnras/stv1690

Vidal, M., Dickinson, C., Davies, R. D., & Leahy, J. P. 2015, MNRAS, 452, 656, doi: 10.1093/mnras/stv1328

Vladimirov, A. E., Digel, S. W., Johannesson, G., et al. 2011, Comput. Phys. Commun., 182, 1156, doi: 10.1016/j.cpc.2011.01.017

Welch, G. A., Sage, L. J., & Mitchell, G. F. 1998, ApJ, 499, 209

Wolleben, M. 2007, ApJ, 664, 349

Wright, M. 1979, ApJ, 233, 35

Yang, R., Aharonian, F., & Evoli, C. 2016, PhRvD, 93, 123007

Yun, M. S., Reddy, N. A., & Condon, J. J. 2001, ApJ, 554, 803, doi: 10.1086/323145

Yusifov, I., & Küçük, I. 2004, A&A, 422, 545

Zemp, M., Diemand, J., Kuhlen, M., et al. 2009, MNRAS, 394, 641, doi: 10.1111/j.1365-2966.2008.14361.x

Zhang, Y., Yang, X., Faltenbacher, A., et al. 2009, ApJ, 706, 747, doi: 10.1088/0004-637X/706/1/747

Zhou, B., Liang, Y.-F., Huang, X., et al. 2015, PhRvD, 91, 123010, doi: 10.1103/PhysRevD.91.123010

Zucker, D. B., Kniazev, A. Y., Bell, E. F., et al. 2004, ApJ Letters, 612, L117

Zwicky, F. 1933, Helv. Phys. Acta, 6, 138

Appendix A

Supplementary Material for the Analysis of M31's Outer Halo

A.1 Description of the Baseline IEMs

The baseline IEMs are built using GALPROP-based models (Ackermann et al. 2012a). The GALPROP code for CR propagation and diffuse emission (Moskalenko & Strong 1998; Strong & Moskalenko 1998) has been under development since 1996 and is a *de facto* standard in astrophysics of CRs. It solves the CR transport equation with a given source distribution and boundary conditions for all CR species. This includes all relevant processes, such as the Galactic wind (convection), diffusive reacceleration in the interstellar medium, energy losses, nuclear fragmentation, radioactive decay, and production of secondary particles and isotopes. The numerical solution of the transport equation is based on a Crank-Nicholson implicit second-order scheme. Diffusion of CRs in the Galaxy is assumed to be homogeneous and isotropic within a cylindrical volume, defined by the parameters z and r, which give the position along the longitudinal and polar axes. The spatial boundary conditions assume free particle escape. For a given halo size the diffusion coefficient, as a function of momentum and propagation parameters, is determined from secondary-to-primary ratios.

The GALPROP code computes a full network of primary, secondary, and tertiary CR production starting from input source abundances. Starting with the heaviest primary nucleus considered (e.g., ^{64}Ni, $A = 64$), GALPROP uses the dependency tree to compute the source terms for each propagated species, while production and propagation of secondary $e^{\pm}$ and $\bar{p}$ are calculated at the final steps. Calculations of nuclear fragmentation and production of secondary isotopes are detailed in Génolini et al. (2018). The inelastically scattered p and $\bar{p}$ are treated as separate components (secondary p, tertiary $\bar{p}$). GALPROP includes K-capture, electron stripping and pick up, and knock-on electrons.

The γ-ray and synchrotron emissivities are calculated using the propagated CR distributions, including a contribution from secondary $e^{\pm}$ (Strong et al. 2004a; Porter et al. 2008). Production of π^0 and secondary $e^{\pm}$ is calculated using parameterizations by Kamae et al. (2006) and Kachelrieß & Ostapchenko (2012). The inverse Compton scattering is treated using the formalism for an anisotropic photon field (Moskalenko & Strong 2000) with the full spatial and angular distribution of the interstellar radiation field (ISRF) (Porter et al. 2008; Porter & Strong 2005). The electron Bremsstrahlung calculations are described in Strong et al. (2000). Intensity skymaps are then generated using line-of-sight integrations where the gas-related γ-ray intensities (π^0-decay, Bremsstrahlung) are normalized to the column densities of H I and H_2 for Galactocentric annuli based on recent 21-cm and CO survey data. More details can also be found in Ptuskin et al. (2006), Strong et al. (2007), Vladimirov et al. (2011), and Jóhannesson et al. (2016) and in the description of the most recent version of GALPROP v.56 (**?**Porter et al. 2017, and references therein).

The interstellar gas distributions and gas-related γ-ray emission are the cornerstones of the analysis presented in this paper. The Galactic gas content is dominated by atomic (H I) and molecular hydrogen (H_2), which are present in approximately equal quantities ($\sim 10^9\ M_{\odot}$) in the inner Galaxy, but with very different radial distributions. Helium represents $\approx$10% by number and is usually assumed to be distributed similarly to the neutral gas. There is also a small fraction of low-density ionized hydrogen (H II). The H_2 gas is distributed within $R < 10$ kpc, with a peak at $\sim$5 kpc and a scale height of $\sim$70 pc. It is concentrated mainly in dense clouds of typical density $\sim 10^3$ atom cm^{-3} and masses $10^4 - 10^6 M_{\odot}$. The H_2 gas cannot be detected directly on large scales, but the 115 GHz emission of the molecule ^{12}CO is a good "tracer", because it forms in the dense H_2 clouds (Bolatto et al. 2013). The recent result obtained from a complete CO survey and infrared and H I maps gives $X_{\rm CO} \equiv N_{\rm H_2}/W_{\rm CO} = (1.8 - 2.0) \times 10^{20}$ cm^{-2} K^{-1} km^{-1} s (Dame et al. 2001; Bolatto et al. 2013). Observations of the diffuse γ-ray emission from the local medium and the whole Galaxy indicate that the local values are smaller and there are variations even in the local clouds $(0.63 - 1.0) \times 10^{20}$ cm^{-2} K^{-1} km^{-1} s (Ackermann et al. 2012d) while a gradual increase of $X_{\rm CO}$ toward the outer Galaxy is observed on the larger scale (Strong et al. 2004b; Ackermann et al. 2012a).

H I gas is mapped via its 21-cm emission line, which gives both distance (from the Doppler-shifted velocity and Galactic rotation models) and density information. The H I gas extends out to $\sim$35 kpc with a scale height of $\sim$200 pc in the inner Galaxy that increases considerably in the outer Galaxy (Kalberla & Kerp 2009). This results in an increase in the surface density with distance from the Galactic center that peaks at $10 - 20\ M_{\odot}$ pc^{-2} at $\sim$12 kpc before it starts falling exponentially with a scale length of 3.75 kpc. The H I disk is asymmetric with warping in the outer disk, and extends up to about 5 kpc above the Galactic plane in the north. The gas density is $\sim$1 atom cm^{-3} in the Galactic plane out to a Galactocentric radius of $\sim$14 kpc, beyond which it decreases quickly. Less studied is a cold component of H I, which does not emit at 21 cm and correlates with the H_2 distribution (Kolpak et al. 2002; Grenier et al. 2005). Its presence is detected using absorption spectra measured against bright radio sources or by using the dust reddening maps.

For the purposes of calculation of γ-ray skymaps, all interstellar gas (H I, H_2) is assigned to the Galactocentric annuli, providing column den/sity maps for each annulus (so-called gas maps). Since the kinematic resolution vanishes for directions near the Galactic center and Galactic anti-center, the gas maps are interpolated across the regions $|l| < 10°$ and $|180° - l| < 10°$. However, these regions do not overlap with the fields analyzed in this paper. The main uncertainty in deriving the H I column densities N(H I) is the H I spin temperature, which is used to correct for the opacity of the 21 cm line.

Infrared emission from cold interstellar dust is also employed in the determination of the H I and H_2 gas maps. Dust reddening maps, $E(B - V)$, are used to correct for uncertainties in N(H I) and W(CO), which may not trace all of the neutral gas. Because the quantity of dust traced by $E(B - V)$ cannot be reliably determined in regions with high extinction, two magnitude cuts (2 and 5 mag) are applied to the maps. The extinction is highest along the MW plane, and towards the inner Galaxy, but does not have a significant effect for the M31 field.

The ionized hydrogen (H II) averages only a few percent of the density of the neutral gas. However, because of its extended spatial distribution, it contributes significantly to the γ-ray emission at high latitudes. The modeling of H II is based on pulsar dispersion measurements (Gaensler et al. 2008).

The ISRF is a major component in calculation of the skymap distribution of the IC emission. The Galactic ISRF (optical, infrared, and cosmic microwave background) is the result of the emission by stars, and scattering, absorption, and re-emission of absorbed starlight by dust in the interstellar medium. Because dust is optically thick to starlight, one has to model the radiation transport to obtain the spatial distribution of the ISRF intensity and spectrum throughout the Galaxy. The major uncertainties in calculations of the ISRF include the distribution of stars and star classes in the Galaxy, and the distribution of dust and its properties.

A.2 Additional Systematic Checks

In this section we check some additional systematics pertaining to the observations. Using the M31 IEM we vary the index of the IC components and the H I-related components. In addition, we repeat the analysis with two different IEMs, namely, the IG IEM and the FSSC IEM. We also take a closer look at the 3FGL point sources in FM31. Lastly, we check the systematics relating to CR contamination in the detector. Note that both of the additional IEMs employ the same underlying gas maps (H I and H_2), which are also used for the M31 IEM, and so these tests do not address the systematics relating to the 3D gas distribution in the line of sight. In particular, the H I maps for all IEMs use the same cuts in velocity and space for M31.

A.2.1 The M31 IEM

Using the M31 IEM we perform additional variations of the fit. First, we vary the index of the IC components using a PL scaling. Otherwise, the fit is performed in the standard way, including iterating over all the point sources. Table A.1 reports the normalizations and indices of the diffuse components for the fit in the TR, and the resulting fractional count residuals are shown in the left panel of Figure A.1. The IC components show a hardening towards the outer Galaxy. The normalization of the isotropic component is higher than the value found in the main analysis, but still consistent within 1σ. The energy residuals are qualitatively consistent with what is found in the main analysis. The improvement in the fit is $-2\Delta\text{LogL}=6$.

Table A.2 reports the normalizations and indices of the diffuse components for the fit in FM31, and the resulting fractional count residuals are shown in the right panel of Figure A.1. The IC components show a hardening towards the outer Galaxy, consistent with the results for the TR. The normalization of H I A5 is 1.22 ± 0.04, compared to its baseline value of 1.04 ± 0.04. The fractional energy residuals still show a clear excess between ∼3–20 GeV, with the data being over-modeled above and below this range. For this particular fit the isotropic normalization was held fixed to its original value of 1.06. We also tested repeating the fit with the isotropic normalization fixed to 1.12 (from the TR with IC index scaled), but the results where essentially the same. To verify, we also repeated the arc fit with the M31 components, and the results are qualitatively consistent with the results found in the main analysis.

We also test varying the index of the H I-related components using a PL scaling. The best-fit normalizations and indices for the fit in the TR are reported in Table A.3. The best-fit index for H I A5 is consistent with zero, thereby returning the original spectral shape. The H I A6 component shows a significant change in index, but this component has a minimal contribution in the TR, and likewise it's normalization is also very high. The contribution from H I A7

Table A.1. Scaling the Index for the IC Components in the TR

Component	Normalization	Index, $\Delta\alpha$
H I π^0, A5	1.09 ± 0.03	···
H I π^0, A6	5.2 ± 1.33	···
H I π^0, A7	0.00 ± 0.06	···
H_2 π^0, A5	2.10 ± 0.12	···
IC, A5	2.11 ± 0.15	0.07 ± 0.04
IC, A6-A7	3.7 ± 0.4	–0.21 ± 0.09
Isotropic	1.12 ± 0.06	···

Note. — We vary the index of the IC components using a PL scaling $dN/dE \propto E^{-\Delta\alpha}$. The new effective index is the original index plus the best-fit index, i.e. add the exponents.

Table A.2. Scaling the Index for the IC Components in FM31

Component	Normalization	Index, $\Delta\alpha$
H I π^0, A5	1.22 ± 0.04	···
H I π^0, A6	0.35 ± 0.2	···
H I π^0, A7	2.43 ± 0.4	···
H_2 π^0, A5	2.74 ± 0.3	···
IC, A5	1.86 ± 0.1	–0.07 ± 0.03
IC, A6-A7	1.35 ± 0.4	–0.32 ± 0.08
IC, A8	43.3 ± 15.8	–0.6 ± 0.1

Note. — We vary the index of the IC components using a PL scaling $dN/dE \propto E^{-\Delta\alpha}$. The new effective index is the original index plus the best-fit index, i.e. add the exponents.

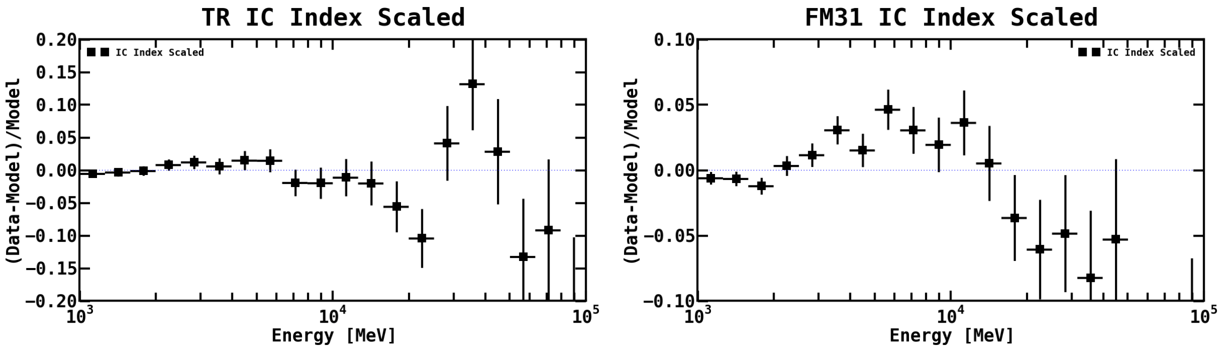

Figure A.1 Fractional energy residuals resulting from varying the index of the IC components using a PL scaling. Otherwise, the fit is performed in the standard way. The left shows the results for the TR and the right is for FM31.

is also minimal in the TR, and its normalization goes to zero.

Table A.3. Scaling the Index for the H I-Related Components in the TR

Component	Normalization	Index, $\Delta\alpha$
H I π^0, A5	1.12 ± 0.01	–0.01 ± 0.01
H I π^0, A6	6.05 ± 0.69	–0.56 ± 0.12
H I π^0, A7	0.00 ± 0.1	0± 0
H_2 π^0, A5	2.1 ± 0.07	···
IC, A5	2.31 ± 0.02	···
IC, A6-A7	3.34 ± 0.15	···
Isotropic	1.01 ± 0.01	···

Note. — We vary the index of the H I-related components using a PL scaling $dN/dE \propto E^{-\Delta\alpha}$. The new effective index is the original index plus the best-fit index, i.e. add the exponents.

We next scale the index for the H I-related components in FM31. Results for this fit are reported in Table A.4. The H I-related emission shows a significant hardening towards the outer Galaxy. The H I A5 component obtains a best-fit index $\Delta\alpha$ of –0.13 ± 0.02, in direct contrast to the result from the TR. For the outer Galaxy the H I A7 component obtains a best-fit index of –0.39 ± 0.11, which corresponds to an effective index of 2.37, compared to its GALPROP prediction of 2.76.

The left panel of Figure A.2 shows the index as a function of Galactocentric radius. Note that the values reported from this analysis are obtained by fitting a PL to the γ-ray spectrum for energies above 2 GeV (i.e. the photon index). Also shown are the results of the template fits from Acero et al. (2016) and Yang et al. (2016), as well as a model interpretation from Recchia et al. (2016). The index of the gas-related emission from these other studies shows evidence of a gradual softening towards the outer Galaxy, which may also provide a hint to the origin of the flat CR gradient in the outer Galaxy (Strong & Mattox 1996; Strong et al. 2004; Recchia et al. 2016). The results obtained in FM31 clearly show an anomaly with respect to these other measurements, as well as an anomaly with respect to the results in the TR and the GALPROP predictions. The anomaly is most clearly evident for the outer Galaxy rings, A6 and A7, and it is also these rings which are found to be partially correlated with the M31 system, as is clearly seen in Figure 4.17. Because of this we also tested the fit with the IG IEM, which only has one outer ring (see Table 4.1). The results for the IG IEM are qualitatively consistent with the M31 IEM. These results support our conclusion that the MW IEM may be holding a fraction of gas that actually resides in the M31 system, as already discussed in the main text.

The fractional count residuals that result from this fit are shown in the right panel of Figure A.2. The fit does a better

Table A.4. Scaling the Index for the H I-Related Components in FM31

Component	Normalization	Index, $\Delta\alpha$
H I π^0, A5	1.39 ± 0.04	-0.13 ± 0.02
H I π^0, A6	0.61 ± 0.27	-0.24 ± 0.35
H I π^0, A7	3.01 ± 0.42	-0.39 ± 0.11
H_2 π^0, A5	2.83 ± 0.26	$\cdots$
IC, A5	1.6 ± 0.11	$\cdots$
IC, A6-A7	1.13 ± 0.29	$\cdots$
IC, A8	0.00 ± 0.01	$\cdots$

Note. — We vary the index of the H I-related components using a PL scaling $dN/dE \propto E^{-\Delta\alpha}$. The new effective index is the original index plus the best-fit index, i.e. add the exponents.

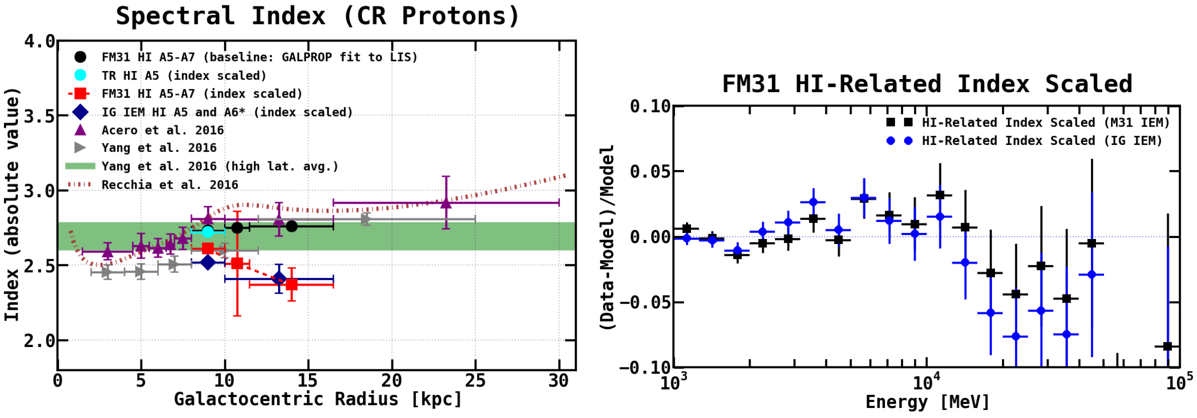

Figure A.2 **Left:** The index of the H I-related emission as a function of Galactocentric radius. The black circles give the baseline index for the M31 IEM corresponding to the GALPROP prediction (∼–2.75). The cyan circle is the best-fit index for the local annulus obtained in the TR (using the M31 IEM), which is consistent with the GALPROP prediction. The red squares show the results for scaling the index of the H I-related components in FM31. The middle ring, A6, has the smallest radial extension, and likewise it has the largest error bars. We also repeat the fit using the IG IEM, which only has one outer ring. The results for the IG IEM are shown with blue diamonds, and they are qualitatively consistent with the M31 IEM. For comparison, we also show other measurements. The purple upward-pointing triangles are from Acero et al. (2016). For the local ring the fit includes all longitudes and $10^\circ < |b| < 70^\circ$ and for the outer Galaxy (last two rings) the fit includes all latitudes and $90^\circ < l < 270^\circ$. The grey rightward-pointing triangles are from Yang et al. (2016). The fit is performed in the latitude range $|b| < 5^\circ$. The green dashed band is also from Yang et al. (2016), and it shows the 1σ average photon index (above 2 GeV) in the region $10^\circ < |b| < 15^\circ$ and $90^\circ < l < 150^\circ$, which corresponds to the M31 direction. Lastly, the brown dashed curve is a model fit from Recchia et al. (2016), which is based on non-linear CR propagation in which transport is due to scattering and advection off self-generated turbulence. **Right:** Fractional energy residuals resulting from scaling the index of the H I-related components, for both the M31 IEM and the IG IEM.

job at flattening the residuals, however, excess emission still remains. To quantify the remaining excess we fit the M31-related components. All other diffuse components are held fixed to the values obtained in the baseline fit, except for the normalizations of the gas components which are rescaled. We also iterate through all the point sources. In this case the spherical halo component is detected at $\sim 3\sigma$ and 4σ, for the M31 and IG IEMs, respectively. The spectrum remains qualitatively consistent with the results obtained in the main analysis. The far outer halo is not significantly detected.

The purpose of this test was to allow for a gradual softening towards the outer Galaxy, as has been reported in other studies. We instead found a significant hardening. This result is included here only as a systematic check, but we do not consider this to be a proper description of the foreground gas-related emission. However, it does further support the conclusion that there is some significant anomaly in FM31.

A.2.2 The Inner Galaxy IEM

The analysis is repeated with the IG IEM. Like the M31 IEM, the IG IEM is also a GALPROP-based model. There are, however, some important differences between the two, as summarized in Table 4.1. The IG IEM was initially tuned to Pass 7 data, whereas in this analysis we use Pass 8 data. This is fine for the diffuse components, since we retune their normalizations in FM31; however, the isotropic spectrum needs to be recalculated self-consistently with the data set. The isotropic spectrum for the IG IEM recalculated with Pass 8 data is shown in Figure A.3, where we show it calculated for the all-sky analysis and separately for specific regions. We use the same data selection as for the main analysis. For the fit in FM31 we use the high latitude spectrum fixed to its nominal value (1.0). This is in contrast to the M31 IEM which uses the all-sky spectrum tuned directly to a TR region south of FM31. Also, the IG IEM uses the isotropic approximation for the IC component, whereas the M31 IEM uses the anisotropic formalism.

The baseline fit is performed just as it is in the main analysis. Results for the baseline fit are shown in Figure A.4. The top panel in Figure A.4 shows the best-fit spectra and the bottom panel shows the resulting fractional energy residuals. The blue band shows the corresponding residuals for the M31 IEM (baseline with IC scaled). Results for the two IEMs are very similar. Overall, the M31 IEM performs better over the entire energy range, showing marginal improvements compared to the IG IEM. The spatial residuals are shown in Figure A.5, and they are also qualitatively similar to those found with the M31 IEM. The best-fit normalizations and corresponding flux and intensities for the diffuse components are reported in Table A.5. The table includes the original best-fit normalizations from Ajello et al. (2016), as well as the corrected value, which is obtained by taking the product of the original value with the updated value.

In addition to the positive residual emission between ∼3–20 GeV, the fractional energy residuals for both IEMs also show a high energy deficit (HED) in the last few energy bins, reaching as high as ∼20%. Note, however, that the data

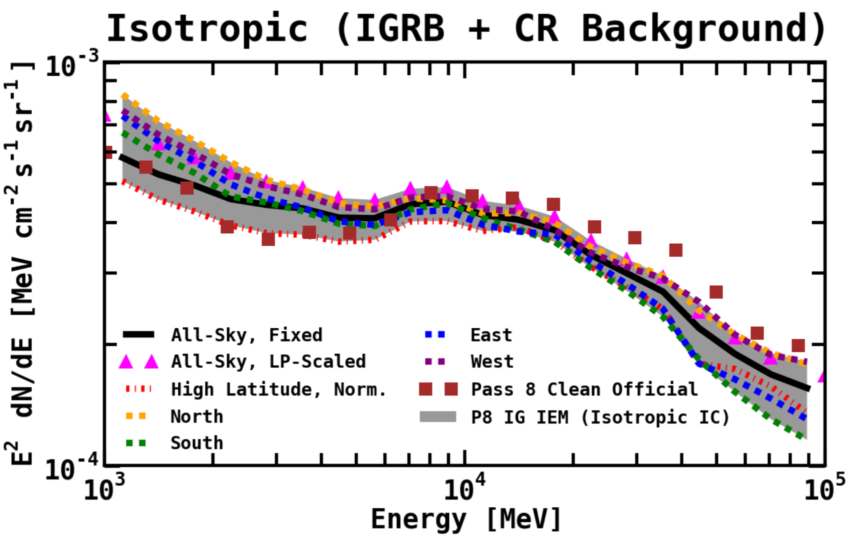

Figure A.3 The isotropic component includes unresolved diffuse extragalactic emission, residual instrumental background, and possibly contributions from other Galactic components which have a roughly isotropic distribution. The spectrum has a dependence on the IEM and the ROI used for the calculation, as well as the data set. For the IG IEM (which uses the isotropic IC sky maps) we calculate the **All-Sky** (solid black line) isotropic component in the following region: $|b| \geq 30°,\ 45° \leq l \leq 315°$. We also calculate the isotropic component in the different sky regions: **North**: $b \geq 30°,\ 45° \leq l \leq 315°$ (orange dashed line); **South**: $b \leq -30°,\ 45° \leq l \leq 315°$ (green dashed line); **East**: $|b| \geq 30°,\ 180° \leq l \leq 315°$ (blue dashed line); and **West**: $|b| \geq 30°,\ 45° \leq l \leq 180°$ (purple dashed line). The calculations are performed using a log parabola (LP) scaling for the diffuse components. In addition, we calculate the isotropic spectrum at high latitudes ($|b| > 50°$), scaling just the normalizations of the diffuse components. The brown squares show the official FSSC isotropic spectrum (iso_P8R2_CLEAN_V6_v06). The grey band is our calculated isotropic component systematic uncertainty for the IG IEM, as shown in Figure 4.8.

in these higher bins are limited, and the error bars are fairly large. Likely related to a portion of the HED are the point sources in the field. Most of the 3FGL sources in FM31 are active galactic nuclei, and are modeled with power law spectral models. Many of these sources are over-modeling in the lower and higher energy bins, and under-modeling in the intermediate range, as seen in Figure 4.16. This is an indication that some of the sources may be more consistent with a different spectral model, such as a log parabola (LP). We have tested this by replacing the PL spectral models of all 3FGL sources with LP models. The spectral parameters for each source (norm, α, β, E_b) are initially set to the corresponding values for the respective PL spectra, with β initially set to 0. The fit is otherwise performed in the standard way. Figure A.6 shows the difference in the spatial residuals for the baseline fit and the optimized fit. In bins 1 and 3 the 3FGL over-modeling is deeper for the baseline fit, resulting in the surrounding blue regions, and in bin 2 the 3FGL under-modeling is more severe for the baseline fit, resulting in the surrounding red regions.

The fractional energy residuals resulting from the optimized fit are shown in Figure A.7, and the corresponding difference between the optimized fit and the baseline fit is reported in Table A.6. The optimized 3FGL improve the HED in the last few energy bins by 6–12%. However, the optimization does not have a significant impact on the positive residual emission between ~3–20 GeV.

Table A.5. Normalizations of the Diffuse Components and Integrated Flux

Component	IG IEM	Original Value	Corrected Value	Flux ($\times 10^{-9}$) (ph cm^{-2} s^{-1})	Intensity ($\times 10^{-8}$) (ph cm^{-2} s^{-1} sr^{-1})
H I π^0, A5	0.78 ± 0.02	1.21	0.94	179.4 ± 5.8	76.3 ± 2.5
H I π^0, A6	0.75 ± 0.08	1.74	1.3	25.8 ± 2.7	11.0 ± 1.1
H_2 π^0, A5	1.1 ± 0.2	1.4	1.5	2.3 ± 0.4	1.0 ± 0.2
IC, A5	1.8 ± 0.1	1.5	2.7	86.4 ± 5.4	36.7 ± 2.3
IC, A6	2.0 ± 0.3	1.8	3.6	54.5 ± 6.9	23.1 ± 2.9

Note. — Diffuse normalizations and flux for the IG IEM. The original values are from Ajello et al. (2016), and they give the initial scaling with respect to the GALPROP predictions. The corrected value is then the product of the original value with the current value (second column). Intensities are calculated by using the total area of FM31, which is 0.2352 sr. The fit uses the high latitude isotropic spectrum fixed to 1.0.

Table A.6. Difference in Fractional Energy Residuals

Energy Bin	Baseline – Optimized
1	–0.004
2	–0.004
3	0.0004
4	0.003
5	0.005
6	0.007
7	0.008
8	0.009
9	0.008
10	0.006
11	0.004
12	0.0003
13	–0.004
14	–0.01
15	–0.02
16	–0.03
17	–0.05
18	–0.06
19	–0.08
20	–0.12

Note. — The corresponding plot is shown in Figure A.7.

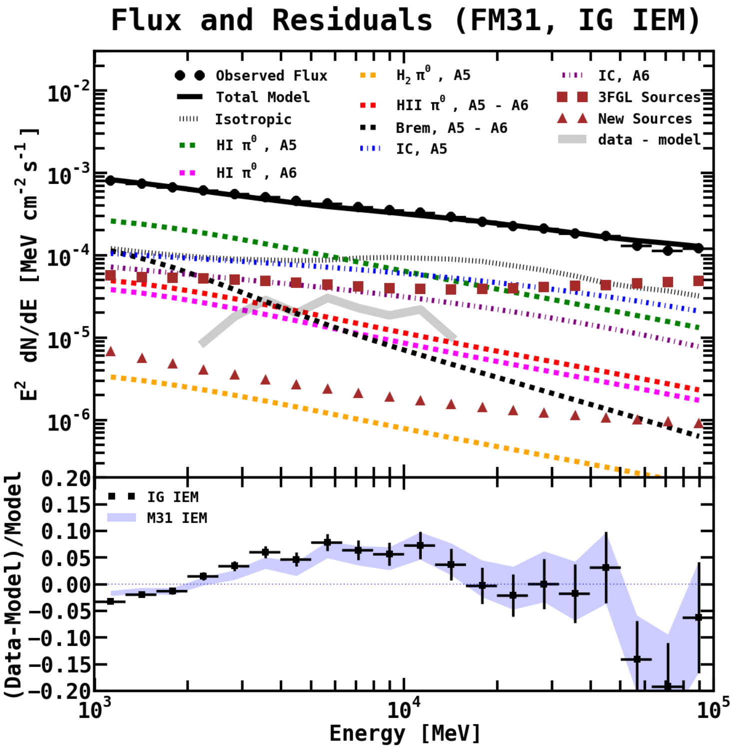

Figure A.4 Flux (upper panel) and fractional count residuals (lower panel) for the fit in FM31 with the IG IEM. The H II and Bremsstrahlung components are fixed to their GALPROP predictions. The normalizations of the IC, H I-related, and H_2-related components are fit to the γ-ray data in FM31, as well as 3FGL sources within 20° of M31, and additional point sources which we find using our point source finding procedure. The fit is performed with the high latitude isotropic component fixed to its nominal value (1.0). The blue band in the bottom panel shows the corresponding fractional residuals for the baseline fit (with IC scaled) with the M31 IEM.

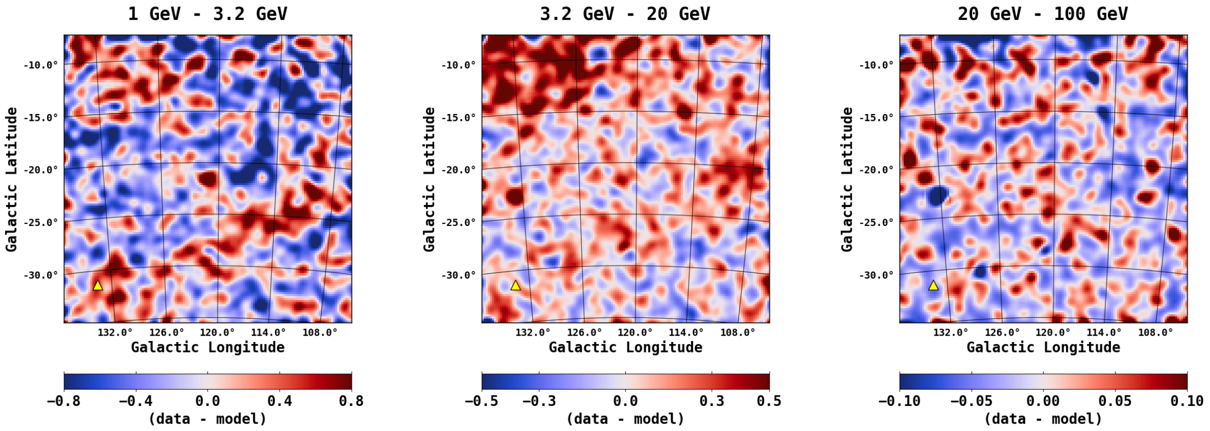

Figure A.5 Spatial count residuals (data – model) resulting from the fit in FM31 with the IG IEM for three different energy bands, as indicated above each plot. The energy bins are chosen to coincide with the excess observed in the fractional residuals. The color scale corresponds to counts/pixel, and the pixel size is 0.2° × 0.2°. The images are smoothed using a 1° Gaussian kernel. This value corresponds to the PSF (68% containment angle) of *Fermi*-LAT, which at 1 GeV is ∼1°. For reference, the position of M33, (l,b) = (133.61°,−31.33°), is shown with a yellow triangle.

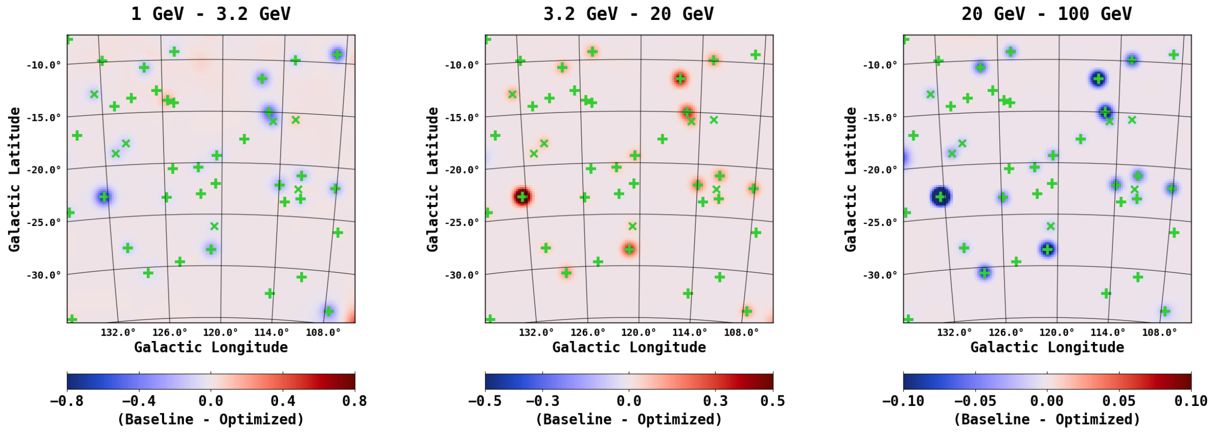

Figure A.6 The maps show the difference between the spatial residuals resulting from the baseline fit and the spatial residuals resulting from the 3FGL optimized fit. For the optimized fit the PL spectral models are replaced with LogParabola spectral models. Three energy bins are shown, just as in Figure 4.15. Green crosses show 3FGL sources with TS$\geq$25 and slanted green crosses show 3FGL sources with 9$\leq$TS$<$25. For the baseline fit, numerous 3FGL sources with PL spectral models were over-modeling in bins 1 and 3, and under-modeling in bin 2, as seen in Figure 4.16. And as seen here, in bins 1 and 3 the 3FGL over-modeling is deeper for the baseline fit, resulting in the surrounding blue regions, and in bin 2 the 3FGL under-modeling is more severe for the baseline fit, resulting in the surrounding red regions, i.e. numerous 3FGL sources show improvement in the spatial residuals with the optimized fit.

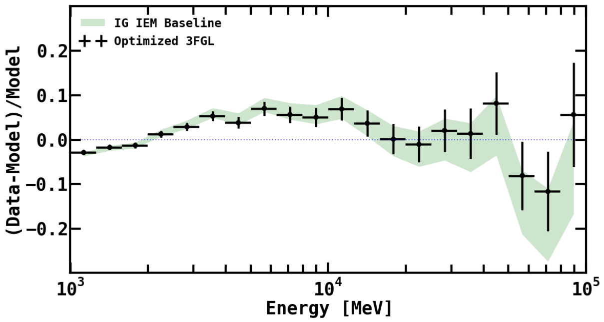

Figure A.7 All 3FGL sources in FM31 with a PL spectral model are fit with a LogParabola spectral model. The spectral parameters for each source (norm, α, β, E_b) are initially set to the corresponding values for the respective PL spectra, with β initially set to 0. Optimization of the 3FGL sources leads to marginal improvement in the fractional energy residuals, and most notably for the high energy deficit in the last few energy bins. The corresponding differences for each energy bin are reported in Table A.6. For the baseline fit the likelihood value is $-\log L$=143349, and for the optimized 3FGL fit it is $-\log L$=143308.

A.2.3 The FSSC IEM

We also repeat the analysis using the official IEM provided by the Fermi Science Support Center (FSSC IEM) for point source analysis. We note, however, that in general the FSSC IEM *is not* intended for extended source analysis[3] (Acero et al. 2016). Construction of the FSSC IEM is based on a template fitting approach. In this approach, the intensities of the model components are not calculated based on CR data and propagation models, as they are for the GALPROP-based IEMs; rather, a linear combination of gas and IC components is fit to the γ-ray data, based on corresponding spatial correlations (Acero et al. 2016). The different gas column density maps offer spatial templates for γ-ray photons originating mainly from π^0-decay and Bremsstrahlung emission. For the IC component, there is no direct observational template, and so it must be calculated. The FSSC IEM employs an IC template from the GALPROP code. We note that the FSSC IEM contains patches to account for extended excess emission (EEE) of unknown origin, also referred to as the "rescaled IC component". The region towards the north of FM31 (primarily in the MW plane) contains such a patch.

Figure A.8 shows results for the baseline fit with the FSSC IEM. The fit is performed over the energy range 300 MeV – 300 GeV, using the same ROI as for the main analysis. The normalizations of the diffuse components, Galactic and isotropic, are freely scaled in FM31, as well as the 3FGL point sources, and additional sources that we find with our point source finding procedure. Note that the index of the Galactic diffuse component is held fixed. The best-fit normalizations of the isotropic and Galactic diffuse components are 1.04 ± 0.005 and 0.98 ± 0.0002, respectively. The top panel in Figure A.8 shows the best-fit spectra using the Clean data class. The bottom panel shows the fractional count residuals. Black squares are for the Clean selection. The best-fit normalizations and flux for the isotropic and Galactic diffuse components are reported in Table A.7. The spatial residuals resulting from the baseline fit are shown in Figure A.9. They are qualitatively consistent with the results for the GALPROP IEMs.

We also repeated the fit with freeing the index of the Galactic diffuse component.The best-fit indices and normalizations are reported in Table A.8 and the fractional energy residuals are shown with green circles in the bottom panel of Figure A.8. As can be seen, this variation is able to flatten the excess between $\sim$3–20 GeV. We again stress that the FSSC IEM is not intended for extended source analysis, especially for weak sources, and this result illustrates how an application of an improper IEM can alter the physical results.

Using the FSSC IEM we also repeat the observations with the UltraCleanVeto data selection. The isotropic background was found to be enhanced by a factor of $\sim$2 at 1–3 GeV within 20° of the Ecliptic/Equator compared to the poles, ascribed to primary CRs misclassified as photons[1]. The UltraCleanVeto data selection removes this anisotropy. More generally, the UltraCleanVeto selection is the cleanest of all data classes, with respect to CR contamination in the detector. Shown in the bottom panel of Figure A.8 are the fractional residuals resulting from the UltraCleanVeto (UCV) selection (blue triangles). The brackets in Table A.7 give the best-fit normalizations for the fit. Note that the index of the Galactic diffuse component is held fixed. The results are qualitatively consistent with the clean data selection.

We fit the M31-related components (not including the arc template) using the FSSC IEM. The best-fit spectra are shown

---

[1] For a discussion regarding the enhanced isotropic emission within 20° of the Ecliptic/Equator see `https://fermi.gsfc.nasa.gov/ssc/data/analysis/LAT_caveats.html`

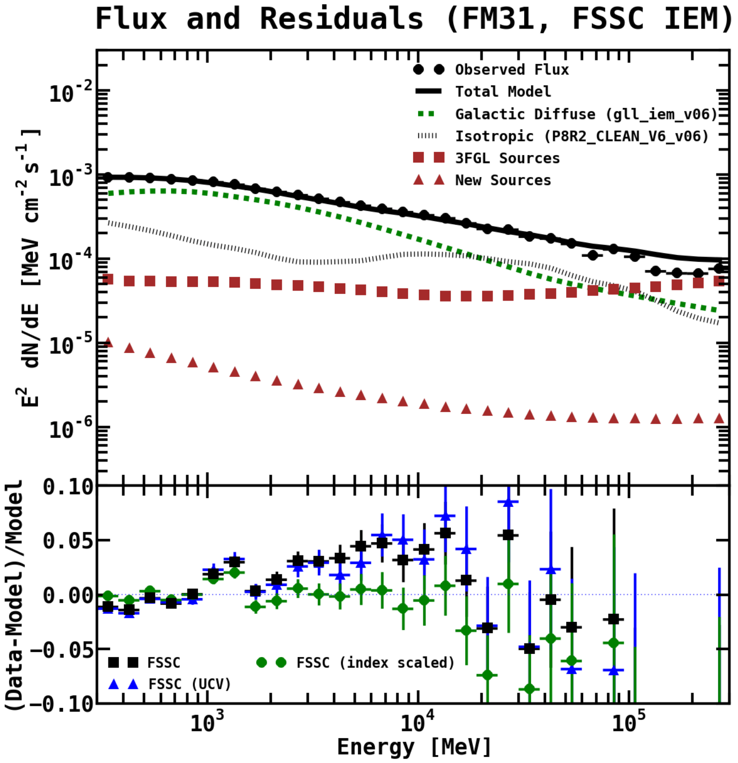

Figure A.8 The top panel shows the best-fit spectra resulting from the FSSC IEM using the Clean data class (with the Galactic diffuse index fixed). The bottom panel shows the resulting fractional count residuals. Black squares are for the Clean class (with the Galactic diffuse index fixed), green circles show the same fit but with the index of the Galactic diffuse component freed, and blue triangles are for the UltraCleanVeto (UCV) class (with Galactic diffuse index fixed). All components are fit in FM31, including the isotropic.

in Figure A.10. For this fit the normalization of the isotropic component is held fixed to its best-fit value obtained in the baseline fit (1.04). The fit can also be performed by freeing the normalization of the isotropic component, but in this case the M31-related components are assigned more counts, and the isotropic normalization is decreased. All other components are fit simultaneously in the standard way. Note that the index of the Galactic diffuse component is held fixed. Two variations of the fit are performed. In one variation the M31-related components are given PL spectral models. In the second variation the M31-related components are fit with a power law per every other energy band (EB) over the range 0.3–300 GeV. The free parameters include an overall normalization, as well as the index in each respective energy bin. Note that for the extended energy range a PLEXP spectral model does not provide a good fit.

The inner galaxy component shows a harder spectrum when fitting over the energy range 300 MeV – 300 GeV, compared to 1 GeV – 100 GeV. Interestingly, the EB spectrum for the inner galaxy component appears to show two distinct features, one bump near 7 GeV and a second bump near 1 GeV. However, the data becomes limited as the energy approaches 10 GeV, and for higher energies only upper limits are obtained.

Table A.7. Normalizations of the Diffuse Components and Integrated Flux for the FSSC IEM

Component	FSSC IEM	Flux ($\times 10^{-9}$) (ph cm^{-2} s^{-1})	Intensity ($\times 10^{-8}$) (ph cm^{-2} s^{-1} sr^{-1})
Galactic Diffuse	0.98 ± 0.0002 [1.002 ± 0.004]	1861.1 ± 0.4	791.1± 0.2
Isotropic	1.04 ± 0.005 [1.04 ± 0.02]	635.0 ± 3.3	270.0 ± 1.4

Note. — Diffuse normalizations and flux for the FSSC IEM with the Clean data selection (with the Galactic diffuse index fixed). For reference, the normalizations in brackets are for the UltraCleanVeto data selection (with the Galactic diffuse index fixed). Intensities are calculated by using the total area of FM31, which is 0.2352 sr.

Table A.8. Scaling the Index of the Galactic Diffuse Component for the FSSC IEM

Component	Normalization	Index, $\Delta\alpha$
Galactic Diffuse	0.900 ± 0.007	–0.033 ± 0.002
Isotropic	1.07 ± 0.01	$\cdots$

Note. — For this fit we free the index of the Galactic diffuse component $dN/dE \propto E^{-\Delta\alpha}$. The fit is otherwise performed in the standard way.

The spectra for the spherical halo component are pretty consistent for the two IEMs. For the far outer halo component, the FSSC IEM shows a bump near 1 GeV. For this fit we do not include the arc template, and the bump at $\sim$1 GeV may be related to inaccuracies in the foreground model, akin to that which is accounted for using the arc template. Otherwise, the spectra for the far outer halo are consistent for the different IEMs. Both the spherical halo and far outer halo components show a sharp spectral cutoff at lower energies.

A.2.4 The Inner Galaxy

The inner galaxy of M31 has previously been detected, and as a consistency check we compare our results with the results from these other studies. To be consistent with the other studies, we use the FSSC IEM and a $14^\circ \times 14^\circ$ ROI. We use an energy range of 0.3–300 GeV, with the P8R2_SOURCE event class, and the same time range as for the main analysis. Our baseline model consists of the FSSC isotropic (iso_P8R2_SOURCE_V6_v06), Galactic diffuse (gll_iem_v06), and 3FGL point sources. The model includes all 3FGL sources within 20° of M31, but only sources within 10° are freely scaled in the fit (normalization and index).

We also find new sources using our point source finding procedure. The procedure is employed self-consistently with

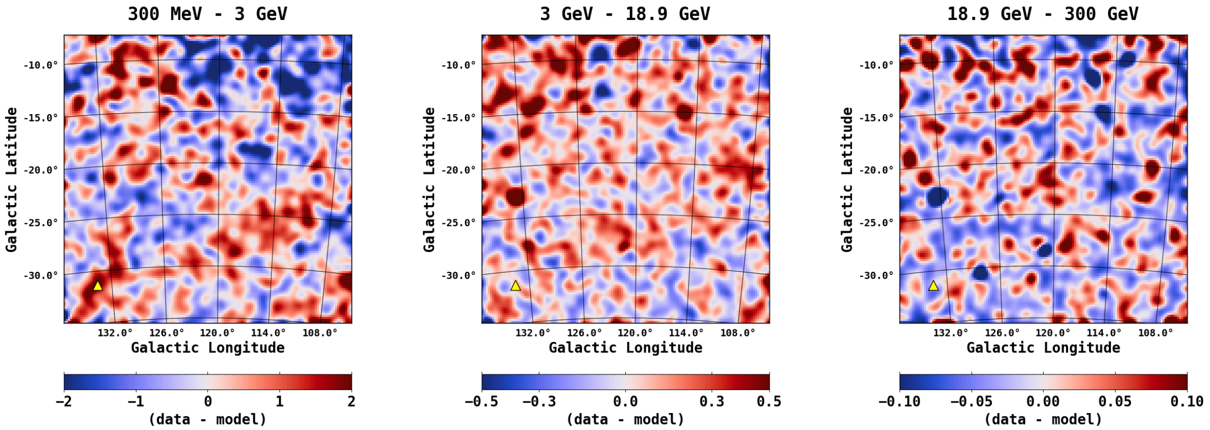

Figure A.9 Spatial count residuals (data – model) resulting from the fit in FM31 with the FSSC IEM for three different energy bands, as indicated above each plot. The energy bins are chosen to coincide with the excess observed in the fractional residuals. The color scale corresponds to counts/pixel, and the pixel size is $0.2° \times 0.2°$. The images are smoothed using a 1° Gaussian kernel. This value corresponds to the PSF (68% containment angle) of *Fermi*-LAT, which at 1 GeV is ∼1°. For reference, the position of M33, (l,b) = (133.61°,−31.33°), is shown with a yellow triangle.

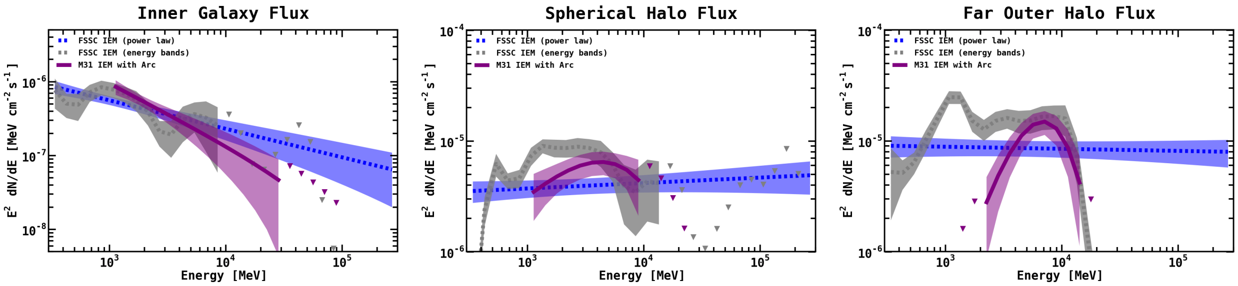

Figure A.10 The M31-related components (not including the arc template) are added to the model and fit with the FSSC IEM. For this fit the normalization of the isotropic component is held fixed to its best-fit value obtained in the baseline fit (1.04). All other components are fit simultaneously in the standard way. Two variations of the fit are performed. In one variation the M31-related components are given PL spectral models (dashed blue curves). In the second variation the M31-related components are fit with a power law per every other energy band over the range 0.3–300 GeV (dashed gray curves). The free parameters include an overall normalization, as well as the index in each respective energy bin. Corresponding results for the M31 IEM are shown with solid purple curves.

the FSSC IEM, and we include an M31 template based on the IRIS 100 μm map of the galaxy. TS maps for the region with and without the additional sources are computed using the *gttsmap* package (included in the *Fermi*–LAT ScienceTools) and are shown in Figure A.11. The additional point sources are overlaid. Point sources with TS $\geq$ 25 are shown with red crosses, while sources with $9 \leq$ TS < 25 are shown with red angled crosses. We find that the agreement between the data and the model significantly improves with the additional point sources, i.e. the initial TS map shows a bright extended region in the lower right-hand corner. The point source finding procedure models this region as three point sources (all with very soft spectra), and as can be seen in the final TS map, these sources do a fairly good job in absorbing the excess. However, this structure is more likely part of a larger extended component, as discussed in the main analysis. We also find that the peaks in the initial TS map are in good agreement with the

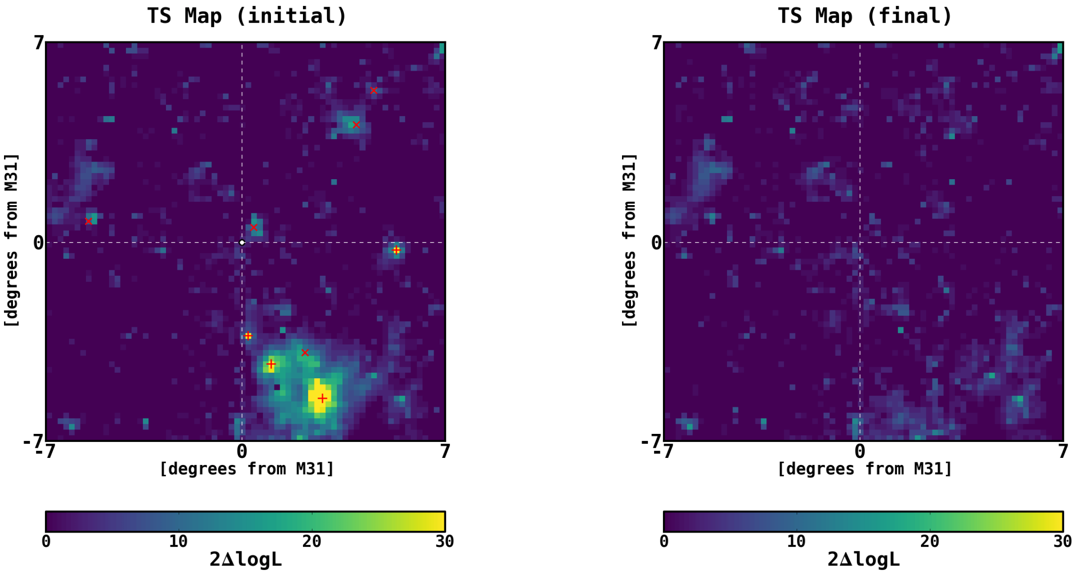

Figure A.11 TS map before and after the additional point sources are included in the model. Note that M31 is modeled with an elliptical template based on the IRIS 100 μm map of the galaxy The region shown is a $14^{\circ} \times 14^{\circ}$ square, centered at M31 (white circle). The color scale corresponds to the TS value ($2\Delta \log L$), as calculated by *gttsmap*. Overlaid on the initial TS map are the positions of the additional point sources that we find with our point source finding procedure. Point sources with TS $\geq$ 25 are shown as red crosses, and sources with 9 $\leq$ TS $<$ 25 are shown as angled red crosses.

positions of the additional point sources.

One of the new point sources is located close to M31, as seen in Figure A.11. Other studies have observed a source at a similar location (Pshirkov et al. 2016b; Ackermann et al. 2017b). In Pshirkov et al. (2016b) the source is detected with TS $= 11.2$, and is attributed to a nearby AGN (FSRQ B3 0045+013). In Ackermann et al. (2017b) the source was found to have a TS = 12, where the TS map is calculated for energies between 1–100 GeV, in a $3.5^{\circ} \times 3.5^{\circ}$ region around M31, with M31 modeled as a point source. From our point source finding procedure we find this source to have a TS = 14. We point out here, for the first time, that this source is spatially coincident with NGC 205, having an angular separation of $\sim 0.16^{\circ}$. NGC 205 is an irregular dwarf elliptical galaxy of M31, and it has a number of open issues that are associated with its star formation history, total gas content, and its orbital history (Welch et al. 1998; Demers et al. 2003; Marleau et al. 2006; Howley et al. 2008; Monaco et al. 2009). Theoretical arguments support a history of violent supernova explosions in NGC 205; however, no supernova remnants have been detected (Lucero & Young 2007; De Looze et al. 2012). We leave further discussion to a forthcoming analysis.

The initial analysis by the *Fermi*-LAT collaboration modeled the emission in M31 both as a point source and using an elliptical template. All of the relevant measurements from that analysis are given in Table A.9. Also shown in Table A.9 are the updated measurements from Ackermann et al. (2017b), the measurements from Pshirkov et al.

Table A.9. Comparison of measured values for the inner galaxy of M31

Template	$-\log(L)$	TS	Index	Flux ($\times10^{-9}$) (ph cm^{-2} s^{-1})	Isotropic Normalization	Galactic Normalization
M31 IEM	···	54	2.8 ± 0.3	0.5 ± 0.1	···	···
Baseline FSSC	–4745	···	···	···	0.970 ± 0.002	1.0167 ± 0.0009
Point FSSC	–4771	52	2.75 ± 0.15	2.16 ± 0.35	0.96 ± 0.03	1.02 ± 0.01
IRIS FSSC	–4776	62	2.46 ± 0.07	3.29 ± 0.24	0.96 ± 0.01	1.017 ± 0.003
Fermi Point	···	25.5	2.5 ± 0.3	···	···	···
Fermi IRIS	···	29	2.1 ± 0.3	11.0 ± 6.7	···	···
Fermi 0.4° Disk	···	97	2.4 ± 0.1	10.0 ± 2.0	···	···
Pshirkov Point	···	62	2.64 ± 0.15	1.9 ± 0.3	···	···
Pshirkov IRIS	···	79	2.4 ± 0.12	2.6 ± 0.4	···	···

Note. — Comparison of the γ-ray emission when modeling M31 both as a point source and an extended source, where the extended source is based on estimates from the IRIS 100 μm map of the galaxy. The first four rows are our values, the next three rows are from Abdo et al. (2010b) and Ackermann et al. (2017b), and the last two rows are the values obtained by Pshirkov et al. (2016a,b). Our baseline model consist of the FSSC isotropic (iso_P8R2_SOURCE_V6_v06), Galactic diffuse (gll_iem_v06), and 3FGL point sources. For this calculation we use a $14^\circ \times 14^\circ$ ROI, in order to be consistent with the other studies. The reported flux is integrated over the entire energy range. The energy ranges are as follows: our energy range (with FSSC IEM): 0.3–300 GeV; Abdo et al. (2010b): 0.2–20 GeV; Ackermann et al. (2017b): 0.1 – 100 GeV; Pshirkov et al. (2016a,b): 0.3–100 GeV. The TS is defined as $-2\Delta \log L$.

(2016a,b), and our current measurements (using the FSSC IEM). When M31 is modeled as a point source using a power law spectrum, the best fit index has a value of –2.75 ± 0.15, the total flux integrated over the energy range 0.3–300 GeV is 2.16 ± 0.35 ph cm^{-2} s^{-1}, and the significance is TS = 52. When modeled using the IRIS elliptical template the spectrum is harder, having an index of –2.46 ± 0.07, the total flux is 3.29 ± 0.24 ph cm^{-2} s^{-1}, and the statistical significance is TS = 62.

The seeming discrepancies could be attributed to the different energy ranges and exposure times. With our GALPROP-based IEM, and using the energy range 1–100 GeV, the index for the inner galaxy template (0.4° uniform disk) is –2.8 ± 0.3. This is a somewhat softer spectrum than that measured in Ackermann et al. (2017b) (–2.4 ± 0.1), although the two values are still consistent within 1σ. This is likely attributed to the energy range used for the fit. The spectral analysis in Ackermann et al. (2017b) shows a flattening of the flux below 1 GeV, which would result in a hardening of the spectrum. When repeating the fit with the FSSC IEM between 300 MeV – 300 GeV, we obtain a best-fit index of –2.4 ± 0.1 for the inner galaxy component.

Evidence of a spherical γ-ray halo around M31 with a 0.9° extension is reported in Pshirkov et al. (2016a). In Pshirkov et al. (2016b) the morphology of the extended γ-ray emission is reported to consists of two bubbles symmetrically located perpendicular to the M31 disk, akin to the MW Fermi bubbles. We have tested both these templates. We found

Table A.10. Comparison for the gas and bubble templates

Template	$-\log(L)$	TS	Index	Flux ($\times 10^{-9}$) (ph cm^{-2} s^{-1})	Isotropic Normalization	Galactic Normalization
Baseline FSSC	–4875	···	···	···	0.91 ± 0.01	1.017 ± 0.004
Gas FSSC	–4880	10	2.30 ± 0.05	2.8 ± 0.3	0.909 ± 0.005	1.016 ± 0.002
Bubbles FSSC	–4880	10	2.33 ± 0.07	1.96 ± 0.20	0.910 ± 0.006	1.017 ± 0.003
Pshirkov Gas	···	22	2.3 ± 0.1	3.2 ± 1.0	···	···
Pshirkov Bubbles	···	28	2.3 ± 0.1	2.6 ± 0.6	···	···

Note. — The first three rows are our values, and the last two rows are the values reported by Pshirkov et al. (2016b). Our baseline model consists of the FSSC isotropic (iso_P8R2_SOURCE_V6_v06), Galactic diffuse (gll_iem_v06), 3FGL point sources, new sources determined from our point source finding procedure, and an M31 template based on the IRIS 100 μm map of the galaxy. For this calculation we use a $14^\circ \times 14^\circ$ ROI. We use an energy range of 300 MeV – 300 GeV. The gas template is a uniform 0.9° disk centered at M31, and the bubble template consists of two uniform 0.45° disks perpendicular to the M31 disk. For each respective fit, the respective template is added in addition to the IRIS template. Note that Pshirkov et al. (2016b) find an additional source (TS $= 11.2$) near M31, and when including this source in the fit the TS for the gas template reduces to 15, and the change in TS for the bubble template was not reported. We found a source in a similar location with TS $= 14$. The TS is defined as $-2\Delta \log L$.

that there is evidence of an extended γ-ray halo around M31. However, we found no statistical preference between the disk template and the bubble template. The corresponding measured values are given in Table A.10. In their analysis they used a disk (bubble) template + the IRIS template. Performing the fit in this way we found that both templates, disk and bubbles, have a TS $= 10$. Moreover, the characterization of the H I along the line of sight is a significant systematic uncertainty when it comes to determining the actual morphology of the extended emission from M31.

A.3 Details for the Dark Matter Radial Profiles

Observational evidence for DM in M31 comes from measurements of its rotational velocity curve. Some of the earliest of these measurements were published by Babcock (1939), Rubin & Ford (1970), and Roberts & Whitehurst (1975). These observations provide coarse-grained properties of the dark matter distribution near the central regions of the halo where the galaxy resides. With the existing data, the fine-grained structure of DM and its distribution outside of the galaxy is primarily inferred from simulated halos.

In 1997 a variety of studies culminated in the realization that the spherically averaged mass distribution of DM halos can be accurately described by an approximately universal profile, determined by the halo mass and halo characteristic density, as introduced by Navarro, Frenk, and White (NFW) (Navarro et al. 1997; Hayashi et al. 2007). However, individual DM halos are not necessarily expected to be smooth, nor spherically symmetric, especially on galactic scales (Kamionkowski & Kinkhabwala 1998; Braun & Burton 1999; Blitz et al. 1999; de Heij et al. 2002; Helmi 2004; Braun & Thilker 2004; Bailin & Steinmetz 2005; Allgood et al. 2006; Hayashi et al. 2007; Bett et al. 2007; Diemand et al. 2007; Kuhlen et al. 2007; Springel et al. 2008; Banerjee & Jog 2008; Law et al. 2009; Zemp et al. 2009; Saha et al. 2009; Banerjee & Jog 2011; Velliscig et al. 2015; Bernal et al. 2016; Moliné et al. 2017; Pawlowski et al. 2017).

DM halos can form irregular shapes depending on their environment and formation history. In general, the geometry may either be spherical, ellipsoidal with an allowed minor to major axis ratio c/a as low as $\sim$0.4, or even lopsided. In addition, the local filament structure of the cosmic web may also affect the halo geometry (Zhang et al. 2009; Carlesi et al. 2016; Pawlowski et al. 2017). Moreover, M31 and the MW cannot necessarily be considered as two isolated halos, as, in fact, it is possible that they are interacting and may be connected by a DM filament (Carlesi et al. 2016; Pawlowski et al. 2017), and such a feature would predict additional DM substructures in the M31 field of view.

Simulations of cold DM, extended to smaller scales with semi-analytic models of hierarchical structure formation, indicate that halo substructure amounts to as much as $\sim$10–40% of the total (MW-size) halo mass; however, simulation resolution remains a limiting factor in these studies (Diemand et al. 2007; Kuhlen et al. 2007; Springel et al. 2008; Zemp et al. 2009; Moliné et al. 2017). The presence of substructure is especially important for indirect detection, as it provides a significant boost to the annihilation intensity, such that the substructures dominate over the NFW profile, except near the halo center. Note that the flux enhancement is most important for more massive halos, as they enclose more hierarchical levels of structure formation (Ng et al. 2014; Sánchez-Conde & Prada 2014). Thus, in the case of dwarf galaxies, a boost factor is not expected to be as important for indirect searches. The main uncertainty pertaining to the boost factor is the low mass behavior of the halo substructures, which includes the number of low-mass halos and their individual density profiles. In addition, the presence of the galactic disk is predicted to have an effect on the substructure content. Tidal forces near the disk may act to break apart the substructure, resulting in a smaller substructure fraction within a radial distance of $\sim$50 kpc (Garrison-Kimmel et al. 2017).

The prompt γ-ray flux for DM annihilation is given by

$$\frac{dN_\gamma}{dE} = \left[\sum_f \frac{\langle\sigma_f v\rangle}{4\pi\eta m_\chi^2}\frac{dN_\gamma^f}{dE}\right]J, \tag{A.1}$$

where the summation is over annihilation final states f (i.e. up-type quarks, down-type quarks, leptons, etc.), dN_γ^f/dE is the number of photons produced for a single annihilation into final state f, $\langle\sigma_f v\rangle$ is the thermally averaged cross section for final state f, m_χ is the DM particle mass, and $\eta = 2(4)$ for self-conjugate (non-self-conjugate) DM. The total cross section $\langle\sigma v\rangle$ is the sum of the cross sections for all final states $\langle\sigma_f v\rangle$. The quantity in large brackets depends on the particle nature of the DM and is referred to as the *DM attribute quantity*. Note that we take all annihilation channels to be s-wave dominated (for which σv does not depend on v) over the kinetic energies found in the M31 halo. Other velocity-dependent scenarios can be considered, but in these cases the velocity distribution of M31 must be modeled and the average $\langle \sigma v \rangle$ must be included in the line-of-sight integration of J (Campbell et al. 2010).

The J-factor (J) characterizes the spatial distribution of the DM, and is given by the integral of the mass density squared, over the line of sight. When describing the dark matter distribution as an ensemble of disjoint dark matter halos, the J-factor is:

$$J = \sum_i \int_{\Delta\Omega} d\Omega \int_{\mathrm{LoS}} ds \rho_i^2(\mathbf{r}_i(s, \mathbf{n})), \tag{A.2}$$

summed over all halos in the line of sight (LoS), where $\rho_i(\mathbf{r})$ is the density distribution of halo i, and $\mathbf{r}_i(s, \mathbf{n})$ is the position within that halo at LoS direction $\mathbf{n}$ and LoS distance s. The spherically-averaged DM halo density profile $\rho(r)$ for each halo is often taken to be a generalized NFW profile (however, other profiles are also possible):

$$\rho(r) = \rho_s \left(\frac{r}{R_s}\right)^{-\gamma} \left(1 + \frac{r}{R_s}\right)^{\gamma - 3}. \tag{A.3}$$

Here, γ specifies the inner spectral slope of the profile, R_s is the scale radius, and ρ_s is the scale density, often determined for the MW halo from the local DM density.

J-factors determined from these spherically-averaged profiles (denoted J) are an underestimate of the total J-factor (denoted J') because of the effect of the non-spherical structure. This underestimate is typically encoded with a boost factor (B) such that

$$J' = BJ, \tag{A.4}$$

with B determined from the model of halo substructure.

To give a sense of the DM properties typically implicated by the GC excess, for the *DM attribute quantity* we use the results from Karwin et al. (2017) (the pseudoscalar interaction model), which is based on the IG IEM. The spectral characteristics for this model favor a DM particle with a mass in the range ∼50–190 GeV and annihilation cross section $\langle \sigma v \rangle$ in the range $\sim 1 \times 10^{-26} - 4 \times 10^{-25}$ cm^3 s^{-1}. For masses above ∼175 GeV the annihilation final state is mostly up-type quarks, and below 175 GeV the annihilation final state is mostly down-type quarks. For each case, a small fraction ($\lesssim$5%) of the annihilation also goes to leptonic final states. Note that other DM scenarios are also possible, but the corresponding DM mass and annihilation cross section typically fall in the ranges given above.

The hatched regions in Figure 4.33 show predicted intensity profiles for DM annihilation in M31 corresponding to three different DM substructure scenarios. The blue (slanted hatch) region shows a smooth NFW halo appropriate for

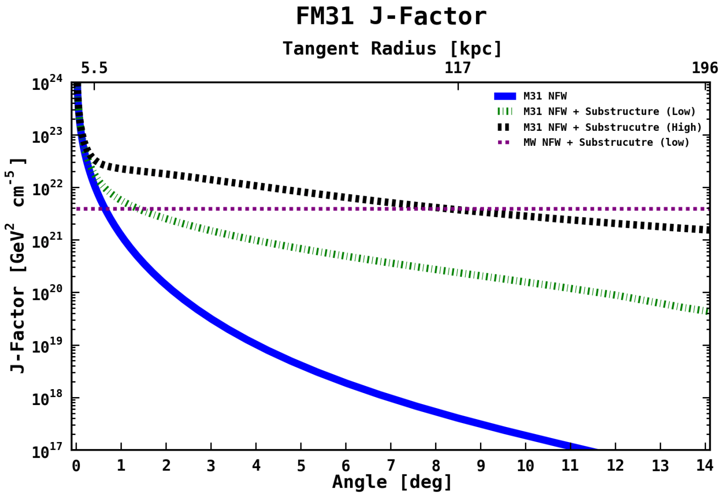

Figure A.12 The blue solid line shows a smooth NFW halo appropriate for warm DM models that do not produce significant structure below the dwarf galaxy scale. The parameters of the NFW profile are as follows: mass $= 10^{12} M_{\odot}$, concentration = 11.2, $R_{\text{virial}} = 210$ kpc, $R_{\text{scale}} = 18.9$ kpc, $\gamma = 1.0$. The green (lower) dashed line, labeled NFW + Substructure (Low), shows the expected DM for a typical ΛCDM cosmology with thermal WIMP DM. For the NFW + Substructure (Low): overall boost factor = 4.2, substructure fraction = 13%, minimum halo mass $= 10^{-6} M_{\odot}$. The black (upper) dashed line, labeled NFW + Substructure (high), shows a scenario in which DM is produced very cold such that the minimum mass structures form with very high concentrations. These smallest structures would dominant the annihilation signal. For the NFW + Substructure (High) we use results from (Gao et al. 2012).

warm DM models that do not produce significant structure below the dwarf galaxy scale (Pagels & Primack 1982; Peebles 1982; Olive & Turner 1982; Colombi et al. 1996; Macciò et al. 2012; Lovell et al. 2014; Bose et al. 2016, 2017). Other alternatives to warm DM are the scenarios of late kinetic decoupling (Bringmann et al. 2016) and dark acoustic oscillations through self-interactions, through interactions with the standard model (Boehm et al. 2001; Boehm & Schaeffer 2005; Hooper et al. 2007), or interactions with a dark sector thermal bath (Feng et al. 2009; Cyr-Racine & Sigurdson 2013; van den Aarssen et al. 2012; Cyr-Racine et al. 2014; Buckley et al. 2014; Cherry et al. 2014; Cyr-Racine et al. 2016; Binder et al. 2016; Huo et al. 2018). The parameters of the NFW profile are as follows: mass = $10^{12} M_{\odot}$, concentration = 11.2, $R_{\text{virial}} = 210$ kpc, $R_{\text{scale}} = 18.9$ kpc, $\gamma = 1.0$.

The presence of a (DM) γ-ray halo around M31 would likely indicate that the line of sight extends through a similar halo surrounding the MW. To obtain a simple estimate for this scenario, we model M31 and the MW as two isolated spherical halos separated by 785 kpc, both described by the same NFW mass profiles (as given above), and both with the same substructure content. We calculate J-factors for an observer inside the MW halo at a distance of 8.5 kpc from the Galactic center. Our standard cold DM halo substructure is modeled with a radial dependent subhalo mass function with tidally truncated density profiles, as described in Ludlow et al. (2016) and Han et al. (2016). The relevant parameters are as follows: overall (M31) boost factor = 4.16, substructure mass fraction = 13%, minimum halo mass = $10^{-6} M_{\odot}$. This scenario corresponds to the expected DM signal for a typical ΛCDM cosmology with thermal WIMP

DM. The corresponding intensity profiles are plotted in Figure 4.33, and labeled as NFW + Substructure (Low). The green (slanted cross-hatch) region shows the M31 component, and the black band shows the corresponding MW component in the line of sight.

The black (vertical cross-hatch) region, labeled NFW + Substructure (High), shows a scenario in which DM is produced very cold such that the smallest substructures around $10^{-6} M_{\odot}$ have large concentrations which dominate the J-factor, as described in Gao et al. (2012). Corresponding J-factors are given in Figure A.12.